Synchronization of spin trasnsfer nano-oscillators

Abbass Hamadeh

UNIVERSITÉ DE PARIS-SUD

UFR Scientifique d'Orsay

Ecole Doctorale de Physique en Ile-de-France (ED-564)

CEA SACLAY

Thèse de Doctorat

présentée pour obtenir
le grade de Docteur en sciences
de l'UNIVERSITÉ PARIS XI, ORSAY

Spécialité:
Physique

par

Abbass Hamadeh

Synchronization of spin transfer nano-oscillators

Soutenue le 3 Octobre 2014 au CEA Saclay devant le jury composé de :

Rapporteurs	Mme.	Ursula Ebels
	M.	Stéphane Mangin
Examinateurs	M.	André Thiaville
	M.	Andrei Slavin
	M.	Vincent Cros
Directeur de thèse	M.	Olivier Klein
Co-encadrant	M.	Grégoire de Loubens

Synchronization of spin transfer nano-oscillators

Abstract

Spin transfer nano-oscillators (STNOs) are nanoscale devices capable of generating high frequency microwave signals through spin momentum transfer. Although they offer decisive advantages compared to existing technology (spectral agility, integrability, etc.), their emitted power and spectral purity are quite poor. In view of their applications, a promising strategy to improve the coherence and increase the emitted microwave power of these devices is to mutually synchronize several of them. A first step is to understand the synchronization of a single STNO to an external source. For this, we have studied a circular nanopillar of diameter 200 nm patterned from a Cu60|Py15| Cu10|Py4|Au25 stack, where thicknesses are in nm. In the saturated state (bias magnetic field > 0.8 T), we have identified the auto-oscillating mode and its coupling to an external source by using a magnetic resonance force microscope (MRFM). Only the uniform microwave field applied perpendicularly to the bias field is efficient to synchronize the STNO because it shares the spatial symmetry of the auto-oscillation mode, in contrast to the microwave current passing through the device. The same sample was then studied under low perpendicular magnetic field, with the two magnetic layers in the vortex state. In this case, it is possible to excite a highly coherent mode ($F/\Delta F$ > 15000) with a linewidth below 100 kHz. By analyzing the harmonic content of the spectrum, we have determined that the non-linear amplitude-phase coupling of the excited mode is almost vanishing, which explains the high spectral purity observed. Moreover, the oscillation frequency can still be widely tuned thanks to the Oersted field created by the dc current. We have also shown that the synchronization of this mode to a microwave field source is very robust, the generation linewidth decreasing by more than five orders of magnitude compared to the autonomous regime. From these findings we conclude that the magneto-dipolar interaction is promising to achieve mutual coupling of vortex based STNOs, the dipolar field from a neighboring oscillator playing the role of the microwave source. We have thus experimentally measured a system composed of two STNOs laterally separated by 100 nm. By varying the different configurations of vortex polarities, we have observed the mutual synchronization of these two oscillators.
Keywords: Magnetism; spintronics; microwave; oscillators; synchronization MRFM-magnetic resonance force microscopy; magnetic vortex state; dipolar coupling.

Synchronisation de nano-oscillateurs à transfert de spin

Résumé

Les nano-oscillateurs à transfert de spin (STNOs) sont des dispositifs capables d'émettre une onde hyperfréquence lorsqu'ils sont pompés par un courant polarisé grâce au couple de transfert de spin. Bien qu'ils offrent de nombreux avantages (agilité spectrale, intégrabilité, etc.) pour les applications, leur puissance d'émission et leur pureté spectrale sont en général faibles. Une stratégie pour améliorer ces propriétés est de synchroniser plusieurs oscillateurs entre eux. Une première étape est de comprendre la synchronisation d'un STNO unique à une source externe. Pour cela, nous avons étudié une vanne de spin Cu60|NiFe15|Cu10|NiFe4|Au25 (épaisseurs en nm) de section circulaire de 200 nm. Dans l'état saturé perpendiculaire (champ appliqué > 0.8 T), nous avons déterminé la nature du mode qui auto-oscille et son couplage à une source externe grâce à un microscope de force par résonance magnétique (MRFM). Seul un champ micro-onde uniforme permet de synchroniser le mode oscillant de la couche fine car il possède la bonne symétrie spatiale, au contraire du courant micro-onde traversant l'échantillon. Ce même échantillon a ensuite été étudié sous faible champ perpendiculaire, les deux couches magnétiques étant alors dans l'état vortex. Dans ce cas, il est possible d'exciter un mode de grande cohérence ($F/\Delta F > 15000$) avec une largeur de raie inférieure à 100 kHz. En analysant le contenu harmonique du spectre, nous avons déterminé que le couplage non-linéaire amplitude-phase du mode excité est quasi nul, ce qui explique la grande pureté spectrale observée, et qu'en parallèle, la fréquence d'oscillation reste ajustable sur une grande gamme grâce au champ d'Oersted créé par le courant injecté. De plus, la synchronisation de ce mode à une source de champ micro-onde est très robuste, la largeur de raie mesurée diminuant de plus de cinq ordres de grandeur par rapport au régime autonome. Nous concluons de cette étude que le couplage magnéto-dipolaire entre STNOs à base de vortex est très prometteur pour obtenir une synchronisation mutuelle, le champ dipolaire rayonné par un STNO sur ses voisins jouant alors le rôle de la source micro-onde. Nous sommes donc passés à l'étape suivante, à savoir la mesure expérimentale de deux STNOs similaires séparés latéralement de 100 nm. En jouant sur les différentes configurations de polarités des vortex, nous avons réussi à observer la synchronisation mutuelle de ces deux oscillateurs.
Mots-clés : Magnétisme; éléctronique de spin; hyperfréquence; oscillateurs; MRFM; synchronisation; MRFM-microscopie de force à résonance magnétique; état vortex magnétique; couplage dipolaire.

Remerciements

Enfin, le navire qui avait quitté son port il y a 3 ans, est revenu, regorgeant d'informations et de résultats inscrits dans cette thèse. Mon bonheur ne connaît point de limite, ma reconnaissance aussi à l'égard de toutes les personnes qui m'ont assuré de leur soutien et de leur aide durant ce périple.

En premier lieu, mes remerciements s'adressent à Olivier Klein et Grégoire de Loubens qui m'ont inculqué le goût et la passion de la physique que j'ai découverte sans limite ni réserve. Je vous remercie pour avoir été mes "pagaies", me propulsant toujours vers l'avant. Je vous remercie pour avoir été "la boussole" qui me montrait le chemin. Vous m'avez permis de grandir en amour et en passion pour la physique. J'aimerais également vous dire à quel point j'ai apprécié vos grandes disponibilités et vos respects sans faille des délais serrés de relecture ma thèse que je vous ai adressés. Enfin, j'ai été extrêmement sensible à vos qualités humaines d'écoute et de compréhension tout au long de ce travail de thèse.

Mes remerciements vont également à Vladimir Naletov. Son aide et son soutien aura été sans faille durant une grande partie de ma thèse, et j'ai grandement apprecie sa réactivité et sa gentillesse.

Je remercie chaleureusement Ursula Ebels et Stéphane Mangin d'avoir accepté d'être rapporteurs de ce manuscrit, ainsi les menbres du jury de thèse Andrei Slavin, André Thiaville et Vincent Cros pour leurs remarques.

Ce travail de thèse a été effectué au SPEC au sein de Laboratoire Nano-magnétisme et Oxydes (LNO). Je remercie tous les personnes de SPEC qui ont attribué dune façon ou dune autre à ce travail, en particulier Claude Fermon de m'avoir accueilli dans leur laboratoire. Je remercie également Michel Viret pour toutes les discussions et la préparation des contact de échantillons de disques de YIG. Grand merci.

Evidemment ces années passées au sein de LNO n'auraient pas été sans la gentillesse de l'ensemble des membres du Groupe. Je remercie sincèrement tous les permanents du groupes . Je souhaite remercier aussi mes collèges de LNO (Thesards, Post-docs, Ingenieurs, Stagiéres ..), avec lesquels j'ai partagé de bons moments, Merci donc à, Christian, Benjamin, Pierre-andré, Camille, Jean-Yves, Laure, Quentin, Amala, Elodie, Aurélie, Olivier, Paolo, Soraya, Hugo, Remy, Damien, Ruben, Vincent ... pour leur soutien inconditionnel aussi je les remercie pour leur sympathie. Je noublie pas de

remercier mes amis, de SPEC ainsi que en dehors du Laboratoire, qui mont soutenu durant ces trois ans, avec eux j'ai partagé de bons moments ainsi que des moments difficiles.

Je tiens aussi à remercier les personnes du l'unité mixte CNRS Thales avec qui j'ai collaboré pour mon travail. Tout d'abord Vincent Cros pour les fructueuses discussions que nous avons eues. Mes remerciements vont également à Julie Grollier, Madjid Anane, Nicolas Locatteli, Romain Lebrun (bon courage pour la suite), Eva Grimaldy, ALex Jenkis et Olivier Dallivykelly.

Je ne saurai oublier de remercier tous mes professeurs qui mont appris de leur savoir faire, en particulier Monsieur Jean-Jacques Greffet, responsable de Master 2 nanophysique et Monsieur Jérome Leygnier responsable de Master 1 physique fondamentale pour les différents conseils. Je ne les oublierai jamais.

Enfin ma reconnaissance va à ceux qui ont plus particulièrement assuré le soutien affectif de ce travail : ma famille ainsi que ma cherie.

Table of Contents

Introduction

0.1. Context

Technological progress in the fabrication of hybrid nanostructures incorporating magnetic metals has allowed the emergence of spintronics. This field of research capitalizes on the spin degree of freedom of electron [1]: spin currents are generated and manipulated at the nanometer scale in order to achieve novel functionalities.

An elementary device of spintronics consists of two magnetic layers separated by a normal layer. It exhibits the well-known giant magnetoresistance (GMR) effect [2, 3], that is, its resistance depends on the relative angle of $\overrightarrow{M}$ between the magnetic layers. Nowadays, this useful property is extensively used in magnetic sensors [4, 5]. The converse effect is that a direct current can transfer spin angular momentum between two magnetic layers separated by either a normal metal or a thin insulating layer [6, 7]. More generally, a spin current exerts on a ferromagnetic material a spin transfer torque, that can compensate the damping and lead to the destabilization of the magnetic moment [8]. Practical applications are the possibility to control the digital information in magnetic random access memories (MRAMs) [9, 10] or to produce high-frequency signals in spin-transfer nano-oscillators (STNOs) [11, 12].

Owing to their tunability, agility, compactness, and integrability, STNOs are promising candidates for various high frequency applications such as frequency generation [13, 14],

frequency detection [15, 16], signal processing [17, 18] and dynamic recording [19, 20, 21]. As far as microwave applications are concerned, spectral purity and tuning sensitivity are two key characteristics for STNOs. A particularity of such devices compared to other oscillators is their strong nonlinear properties, which are inherited from the equation of motion of magnetization [22]. On one hand, they confer interesting properties to STNOs, as for instance their large frequency tunability [11, 12, 13, 14]. On the other hand, they lead to a severe broadening of the generation linewidth [23]: due to nonlinear phase-amplitude coupling, the phase noise of STNOs is indeed rather large [24, 25], which is the main limiting factor to their practical applications. Hence, non-linearities affect both the agility and spectral purity in a way such that both quantities cannot be optimized independently and a compromise must be found. Moreover, STNOs being nanoscale microwave generators, their emitted power is very tiny, typically in the range of pico- or nano-Watts. In that context, mutual phase-locking of several STNOs has been proposed as means to reduce the phase noise and increase the power generated of such oscillators [26, 22]. To date, there are a few experimental realizations of this idea, based on specific systems with $2 \leq \mathcal{N} \leq 4$ mutually-synchronized STNOs [27, 28, 29, 30]. The main limitations in developing large arrays of synchronized STNOs are: the dispersion of dynamical properties due to uncertainties in the fabrication process, the strength of the dynamical coupling, and its symmetry, which might prevent synchronization of large arrays. For example, for the same reason why the dipolar coupling alone cannot be responsible for a spontaneous magnetization (ferromagnetism), one cannot build a closed-packed 3D array of oscillators synchronized through the dipolar coupling.

0.2. Motivations

This thesis work has been motivated by understanding better the microwave properties of STNOs, a prerequisite if one wants to optimize their performance at the level of single device or several mutually coupled oscillators. To achieve this goal, a spectroscopic point of view has been adopted, because the knowledge of the spectrum of spin-wave eigenmodes in hybrid magnetic nanostructures, namely of their symmetries, energies, relaxation rates, and nonlinear properties, is crucial in many aspects. On one side, the spin-wave energies, relaxation rates, and nonlinear properties determine at which frequencies and with which spectral linewidth STNOs can emit [22]. On the other side, the spatial symmetry of the modes gives a fundamental insight about their selection

rules (how they couple to external sources) and about the mutual coupling mechanisms that might exist intra- or inter-STNOs.

The spin-wave eigenmodes can be considered as a fingerprint of a magnetic nanostructure and are deeply linked to its ground state [31, 32]. Moreover, due to interactions between the different magnetic layers in a STNO (*e.g.*, the dipolar interaction), these eigenmodes often have a collective character, *i.e.*, they involve several layers in the stack. A few years ago, it was experimentally shown that spin transfer torque could excite the gyrotropic mode of a magnetic vortex [33], which is the lowest energy mode of this topological ground state [34]. The remarkably narrow generation linewidths (about 1 MHz or less) and the large output power in the case of magnetic tunnel junctions (MTJs) demonstrated by UMR CNRS/Thales in collaboration with AIST (Japan) [35], are extremely promising for applications[1]. In parallel, it was realized in the Spintec lab of CEA that the excitation of coupled modes in uniformly magnetized standard MTJs could improve the linewidth by up to one order of magnitude [38, 39]. Shortly before the beginning of this thesis, my lab in CEA/SPEC and the UMR CNRS/Thales combined these two ideas to minimize even more the auto-oscillation linewidth. By operating a STNO based on two coupled vortices in a spin-valve nanopillars, they obtained a record low linewidth of $\Delta f = 46$ kHz (for a generated frequency $f \simeq 780$ MHz, *i.e.*, $f/\Delta f \approx 17\,000$) [40]. Importantly for applications, a high coherence was kept even at zero magnetic field, and a large frequency tunability on dc current (≈ 10 MHz/mA) was measured.

In order to define a strategy to optimize the microwave characteristics (in particular the coherence) of individual STNOs and to efficiently couple several STNOs together, the following questions have to be addressed:

1. What is the nature of the auto-oscillating eigenmode(s) in a STNO?
2. What is the influence of other modes in the system on the spectral emission?
3. What are the nonlinearities in the system? Which other properties can influence the spectral linewidth and the tunability?
4. What is the optimal coupling mechanism to phase-lock the auto-oscillation to an external source?

[1] Recently, up to a few micro-Watts have been reported in optimized stacks having large magnetoresistance ratio and supporting large dc currents[36]. The low phase noise in vortex MTJs has also been directly measured and analyzed [37]

5. What is the best strategy to mutually synchronize several STNOs in a scalable way?

The goal of this thesis is to bring some insights to these different points, with a special focus to understand the interesting properties of vortex-based STNOs. In particular, the interplay between the different non-linearities and the limitations has been so far extensively studied in the case of uniformly magnetized state. The role of the magnetic configuration and its influence on the non-linear properties were still an open question at the beginning of my thesis.

0.3. Methods

To tackle these open questions, an experimental approach has been followed. Therefore, detailed high-frequency studies of well characterized STNOs have to be conducted. If one wants to be able to understand with sufficient accuracy their microwave properties, it is important to work with STNO samples having a simple design and high symmetry.

The work has thus been focused on a standard circular nanopillar composed of only two ferromagnetic layers having different thicknesses and separated by a normal metal layer. When magnetized by a large perpendicular magnetic field applied along its normal, the axial symmetry of this STNO allows for a simplified identification of its spin-wave eigenmodes [41]. Moreover, the same device exhibits the double vortex configuration (one vortex in each magnetic layer) with outstanding microwave properties [40]. This sample, an archetype of STNO, is thus particularly adapted to bring useful answers to the questions raised by the motivations of this thesis. To be consistent with our road map, the same STNO device, but duplicated, will be used in the studies of mutual synchronization.

An originality of this work is its spectroscopic perspective. One thus needs spectroscopic tools to investigate the magnetization dynamics in STNOs. A natural mean to probe spin-wave modes in hybrid nanostructures is to use their magnetoresistance properties [42, 43, 44, 45, 46]. Since its first application to STNOs [11], spectral analysis of the emitted signals has widespread. However, these high-frequency transport techniques are not sensitive to all spin-wave modes, because some can be hidden to them due to selection rules [41]. Moreover, they do not provide a direct access to the spatial mode profiles. Experimental methods independent of transport have recently brought

useful insights to magnetization dynamics in hybrid nanostructures [47, 48, 49, 50, 51, 52]. In particular, optical techniques such as time-resolved magneto-optical Kerr microscopy (TR-MOKE) [53], micro Brillouin Light Scattering (μ−BLS) [54], or X-ray magnetic circular dichroism (XMCD) [55] were recently successfully applied to probe spin transfer driven dynamics. However, these experimental techniques all require an optical access to the active part of the sample. In that respect, magnetic resonance force microscopy (MRFM) [56, 57, 58, 59, 60], which relies on the dipolar interaction between the sample and a magnetic probe attached at the free end of a soft cantilever, is well adapted to the study of STNOs [41]. In fact, this very sensitive technique can detect the magnetization dynamics in nanostructures buried under thick metallic electrodes [61], which in STNOs are required to pass the large current densities needed to compensate the damping. Moreover, it is sensitive to all spin-wave modes, because it directly measures the longitudinal component of the magnetization [62].

In this thesis, both MRFM and high frequency transport techniques will be employed to probe the magnetization dynamics in a STNO where magnetic layers are either in the saturated and or in the vortex state. They will bring complementary information to address the open questions listed above.

0.4. Outline of the manuscript

This manuscript is divided in three main parts.

The first part is dedicated to the introduction of the physical concepts and of the background required for the analysis of the experimental results. In Chapter 1, I introduce the equation of motion of magnetization in the presence of spin transfer torque and the state-of-the-art of STNOs. The description of the vortex state will also be included. In Chapter 2, I explain the classification of spin-wave eigenmodes in isolated and coupled magnetic nanostructures. In particular, the influence of the dipolar interaction between magnetic layers is emphasized. In Chapter 3, I present the universal nonlinear auto-oscillator theory in the single mode approximation and mention its extension to the multi-mode case.

In the second part, I describe the experimental setups and the studied samples. Details on the high frequency transport measurements and MRFM microscope are given in

Chapter 4. The studied samples are described in Chapter 5, and their preliminary characterization is also reported there.

The third part is dedicated to the presentation of the main experimental results obtained during my thesis.

In Chapter 6, the power emitted by a STNO in the normally saturated state is measured using an MRFM in the autonomous and forced regimes. This provides a quantitative estimate of the threshold current, spin torque efficiency acting on the thin layer and noise level, as well as the nature of the mode which first auto-oscillates: the lowest energy, spatially most uniform spin-wave mode. It is also demonstrated that in order to phase lock this mode, the external source must have the same spatial symmetry. Then, by breaking the perfect axial symmetry of the system, a bi-modal excitation regime is observed using spectrum analyzer and MRFM measurements. Studying this regime in the presence of a small external driving force, a nonlinear interaction between the two auto-oscillating modes is evidenced. At large dc current, it is shown that the coupled dynamics between the thick and thin magnetic layers that is excited greatly improves the generation linewidth to the detriment of frequency tunability.

In Chapter 7, I study the same STNO device, but in the double-vortex state. First, its microwave characteristics are investigated as a function of the perpendicular magnetic field $H_\perp$. By analyzing the harmonic content of the spectrum, this vortex-based oscillator is found to be quasi-isochronous, which means that the severe nonlinear broadening usually observed in STNOs is suppressed. The generation linewidth is found to display strong variations on $H_\perp$ (from 40 kHz to 1 MHz), while the tunability remains constant (7 MHz/mA). This demonstrates that these two quantities are not necessarily correlated. The frequency tunability is ascribed to the current induced Oersted field, while the variations of linewidth are attributed to the coupling of the auto-oscillating mode to an overdamped mode in the system. I will present how these two modes can influence the emission spectrum. Then, I will study the synchronization of this double-vortex STNO to a uniform microwave field. In particular, conditions for a perfect phase-locking to the external source will be demonstrated.

Built on these results, mutual coupling of adjacent vortex-based STNOs through the dipolar interaction will be demonstrated in Chapter 8. Here, the idea is to replace the external microwave field source by a second STNO. By controlling the frequency mismatch between the two oscillators, evidence of mutual synchronization when the latter becomes smaller than the interacting energy will be presented.

Part I.

Background

CHAPTER 1

Spin transfer nano-oscillators

This chapter is dedicated to introduce the physics at play in spin transfer nano-oscillators (STNOs) in order to understand well the results obtained in this thesis. In the first part, we introduce the equation of motion of magnetization in the presence of spin transfer torque. Then the static and dynamic properties of the vortex state are discussed. Finally, we review results from literature on STNOs that were obtained before or at the start of this thesis.

1.1. Equation of motion of magnetization

The archetypal structure of spin transfer nano-oscillators is a non-magnetic layer sandwiched between two ferromagnetic layers. One of the magnetization is usually considered fixed, whereas the second one is free to move. Then, the equation of motion for the magnetization of the free layer (with magnetization vector referred by $\vec{M}$) in the presence of magnetic dissipation and the spin-torque effect can be described by collecting contributions from three terms. The two first terms are given by the classical Landau-Lifshitz-Gilbert (LLG) equation [63, 64] and the third one accounts for the spin transfer torque (STT) [6, 7]:

$$\frac{\partial \vec{M}}{\partial t} = \left[\mathcal{T}_{LL}\right]_{Conservative} + \left[\left[\mathcal{T}_{G}\right]_{damping} + \left[\mathcal{T}_{S}\right]_{spin}\right]_{Non-conservative}. \tag{1.1}$$

The conservative term determines possible types of magnetization precession trajectories (in-plane precession, clamshell, out-of-plane precession...). It also determines the dynamics on a qualitative level. On the other hand, non-conservative terms determine which of many possible trajectories will be stable and the dynamics on a quantitative level.

1.1.1. Conservative terms

In equation 1.1 (referred by Landau-Lifshitz-Gilbert-Slonczewski (LLGS) equation) the first right term $\mathcal{T}_{LL} = -\gamma \vec{M} \times \vec{H}_{\text{eff}}$ is conservative and represents the Larmor precession of the magnetization $\vec{M}$ about the direction of the effective field $\vec{H}_{\text{eff}}$, here γ corresponds to the gyromagnetic ratio of the electron ($\gamma = g\mu_B/\hbar$) [1], g is Landé factor, μ_B is Bohr magneton and $\hbar = h/2\pi$ is Planck's constant. The effective field $\vec{H}_{\text{eff}}$ is the functional derivative with respect to the magnetization vector of the continuous magnetic energy density:

$$\mu_0 \vec{H}_{\text{eff}} = -\frac{\delta \mathcal{W}(\boldsymbol{r})}{\delta \vec{M}}. \tag{1.2}$$

The main contributions to the energy $\mathcal{W}$ are:

[1] $\gamma = g\mu_B/\hbar = 1.87 \times 10^7$ rad.s^{-1}.G^{-1} for Permalloy = Py = $Ni_{80}Fe_{20}$

1. *Zeeman energy*: it corresponds to the interaction between the magnetization and the external magnetic field $\mathcal{H}_{\text{ext}}$ which includes the Oersted magnetic field created by the current I as well as the stray field produced by nearby layers. This energy can be written as:
$$E_z = -\mu_0 \int \mathcal{M}(\boldsymbol{r}).\mathcal{H}_{\text{ext}} \mathrm{d}^3\mathrm{r}\,. \tag{1.3}$$
Where the integral is performed over the volume of the magnetic body.

2. *Exchange energy*: This energy is of purely quantum mechanical origin, and derived from the competition between the Coulomb's interaction and the principle of exclusion of Pauli. This favors the alignment of the magnetic moment and depends on the spatial inhomogeneity of the magnetization.
$$E_{\text{exch}} = \frac{A}{\mathcal{M}_s^2} \int \Sigma_i \mid \frac{\partial}{\partial \alpha_i} \mathcal{M} \mid^2 \mathrm{d}^3\mathrm{r}\,, \tag{1.4}$$
where α_i = x, y, z. A is the exchange constant and $\mathcal{M}_s$ is the saturation magnetization value.

3. *Demagnetizing energy*: it is generated by the surface charges, and associated to the dipolar interaction between each individual magnetic moment. This energy can be written as follows :
$$E_d = -\mu_0 \frac{1}{2} \int \mathcal{M}.\mathcal{H}_d \mathrm{d}^3\mathrm{r}\,, \tag{1.5}$$
where $\mathcal{H}_d = -\hat{\mathcal{N}}_{ij}.\mathcal{M}$ is the demagnetizing field, with $\hat{\mathcal{N}}_{ij}$ a demagnetization tensor which strongly depends on the shape of the sample.

4. *Magneto-crystalline anisotropy energy*: it originates from the spin-orbit interaction and tends to align the magnetization M with particular lattice directions. It can be expressed as follows:
$$E_a = -\frac{K_u}{\mathcal{M}_s^2} \int (\hat{\boldsymbol{n}}.\mathcal{M}(\boldsymbol{r}))^2 \mathrm{d}^3\mathrm{r}\,, \tag{1.6}$$
where K_u is the magneto-crystalline anisotropy constant.

5. *Magneto-elastic energy*: it tends to align the direction of the magnetization along the axis of the mechanical strains. Often, this effect is negligible, in particular in permalloy, in which the magnetostriction is minimized.

As a consequence, the effective field is composed of the total external applied field $\mathcal{H}_{\text{ext}}$ and the magnetic self-interactions :

$$\vec{H}_{\text{eff}} = \vec{H}_{\text{ext}} + \frac{2A}{\mu_0 M_s^2}\Delta.\vec{M} - \hat{N}_{ij}.\vec{M} + \frac{2K_u}{\mu_0 M_s^2}\hat{n}(\hat{n}.\vec{M}(r)) . \tag{1.7}$$

It is clear that $\vec{H}_{\text{eff}}$ depends strongly in $\vec{M}$, this leads to the *nonlinearity* of the equation of motion.

1.1.2. Non-conservative terms

In order to take into account the dissipation effect, Gilbert has proposed to add a phenomenological damping term $\vec{T}_G = -\frac{\alpha}{M_s}\vec{M} \times \frac{\partial \vec{M}}{\partial t}$ which acts as a viscous restoring force on $\vec{M}$[64]. This non-conservative term describes the energy dissipation of the system, where α is a dimensionless dissipation parameter. The origin of this damping factor is the interaction of spin waves with each other from one side and with lattice vibrations and conduction electrons from other side. In the absence of current (I=0) or external force, the magnetization precesses with a spiral around the effective field. $\vec{M}$ reaches its equilibrium position after a certain relaxation time $\mathcal{T} \sim \frac{1}{\alpha\omega}$ and aligns with $\vec{H}_{\text{eff}}$ (see figure 1.2 (a)).

In the presence of a polarized electric current, an additional torque may act on the magnetization vector $\vec{M}$, arising primarily from the transmission and reflection of incoming electrons with moments at arbitrary angles to the magnetization. Indeed, when an unpolarized electric current I is passed through a spin valve structure. the thick layer filters the spin component in the opposite direction, and the counterpart with the same direction goes through it. As a result, the electric current becomes polarized i.e the spin angular momentum of the current is changed from the natural direction to the direction of the magnetization. Due to the conservation of angular momentum, the loss of angular momentum of the current in the interface is absorbed by the thin layer, and thus this layer receives a torque (see figure 1.1). This torque represent the third term of equation 1.1 and it is the Slonczewski spin transfer torque (STT) and is given by :

$$\vec{T}_s = \tau_S[\vec{M} \times (\vec{M} \times \vec{p})] , \tag{1.8}$$

where $\tau_S = \frac{\sigma_0 I}{M_s}$ is the Slonczewski factor. $\sigma_0 = \frac{\epsilon g \mu_B}{2eM_s LS}$ with L is the thickness of the layer, S is the area of the current-carrying region, ϵ is the spin polarization efficiency ($\epsilon \leq 1$), p is the direction of the spin polarization of the current and e is the charge of electron. The

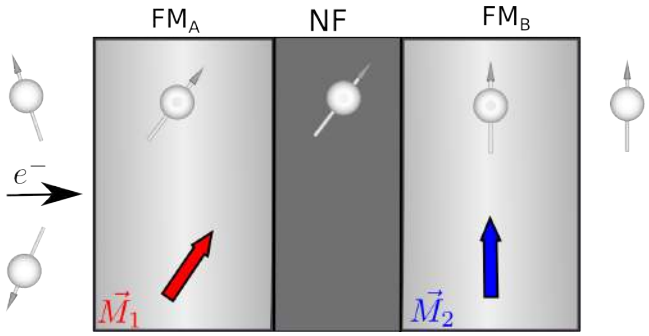

Figure 1.1: *A simplified illustration of spin transfer torque process, FM_A and FM_B refers to ferromagnetic film with magnetization $\mathcal{M}_1$ and $\mathcal{M}_2$ respectively, whereas NF refers to nonmagnetic spacer. The thick magnetic layer is used to produce a polarized electric current which in turns produces a torque on $\mathcal{M}_2$.*

additional Slonczewski term describes the torque acting on the magnetization due to spin transfer and depends on the current density J ($J = I/S$). It can be either parallel or anti-parallel to the damping term (see figure 1.2), depending on the direction of the current. In our convention for a positive current (electron flow from the fixed layer to the free layer), STT torque is in the same direction as the damping torque. So the current increases the value of the effective damping and as a result, the STT torque accelerates the relaxation of the magnetization. On the other hand, for negative current (electron flow from the free layer to the fixed layer), the STT torque is opposite to the damping. Then, the current reduces the effective damping. Thus, the torque reduces the relaxation or even excites the dynamics of the magnetization depending on its strength relative to the damping torque.

All the terms contributing to the magnetization motion are sketched in the figure 1.2. The magnetization, represented as a black arrow, precesses around $\mathcal{H}_{\text{eff}}$ in a way defined by the balance between all the different magnetic torques (Larmor+Damping+STT).

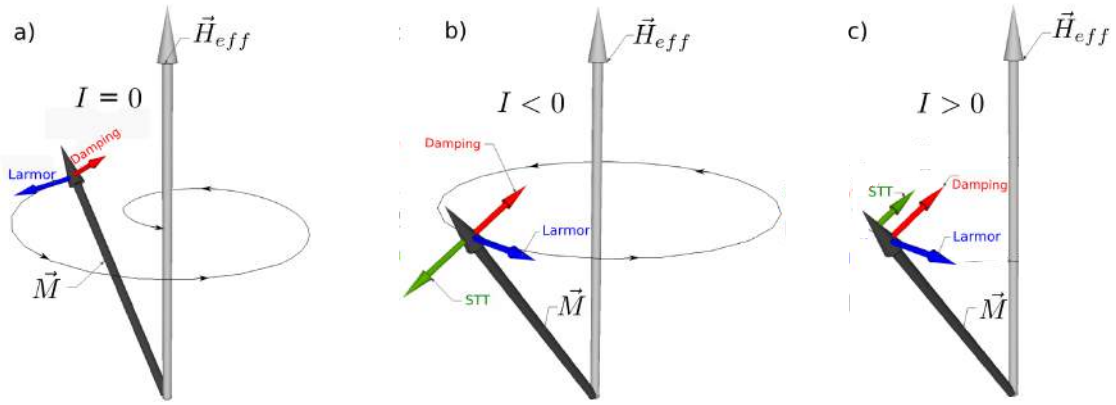

Figure 1.2.: *Sketch of the magnetization motion in ferromagnetic object: the Larmor term or (adiabatic torque) induces the precession of the magnetization $\vec{M}$ about the effective field whereas the damping term pushes magnetization in the direction of the effective field. Then, in absence of STT (I=0) the magnetization is a spiral motion around the effective field. In the presence of STT (I≠0), for $I < 0$ (b) the torque is opposite to the damping and therefore decreases its effect leads to a precession motion of the magnetization around the effective field, for $I > 0$ (c) STT is parallel to the damping and therefore increases it, then the magnetization aligns faster with $\vec{H}_{eff}$.*

1.1.3. Critical current

Now to completely compensate the effective damping of the ferromagnetic layer, in order to start the oscillation of magnetization $\vec{M}$ of this layer, it is necessary that the current density exceeds a threshold current J_{th} which can be calculated by equaling the Gilbert damping term with the STT term i.e ($[T_G]_{damping} = [T_S]_{spin}$). Then, the amplitude of the critical current density J_{th} is expressed as [22]:

$$J_{th} = \frac{2eM_sL}{\epsilon g \mu_B}\alpha\omega\,, \tag{1.9}$$

where ω is the angular frequency of the magnetization around the equilibrium position. Then, according to this expression, it is clear that the threshold current is proportional to the magnetization and the free layer thickness because spin transfer is an interfacial effect. It is inversely proportional to spin-polarization coefficient ϵ which depends in particular on the relative angle of the magnetizations of the fixed and free layers. Then, we can control the critical current by varying the thickness of the free layer and by choosing the material with small damping. For example, the current density required

for spin transfer effect for Permalloy of a few nm of thickness (α = 0.01, ω = 10 GHz, and $\epsilon \sim 0.5$) is $\sim 10^7 A/cm^2$.

1.2. The vortex state

The magnetic configuration at remanence inside a nanodot usually corresponds to a spatially non-uniform ground state. In certain conditions the magnetic configuration could be in a vortex state. Indeed, the vortex state is often found to be the ground state of magnetic nanodots, in which the dot size is larger than the exchange length L_E of the material [65]. In the vortex state, the in-plane magnetization M curls along the disk border and in the center (the vortex core) the magnetization turns out-of-plane (see figure 1.3). In fact, due to the finite size of a ferromagnetic disk the magnetization adopts a vortex configuration at remanence to minimize the exchange and dipolar energies. In general, vortex nucleation can be favored in a ferromagnetic layer whose thickness exceeds the exchange length L_E and provided that the aspect ratio (thickness/lateral size) is kept small, otherwise magnetic domain walls appear. The magnetic vortex is characterized by its *chirality* and *polarity*.

- The *chirality* C: this quantity defines the in plane direction of the magnetization curling and is either clockwise or counterclockwise ($C = \pm 1$).
- The *polarity* p: It defines the relative orientation of the vortex core with respect to the plane of the ferromagnet. This quantity can be $p = \pm 1$.

1.2.1. Static properties

To describe the vortex magnetization distribution, an analytical model has been proposed by Usov [66] which describes a rigid vortex core at the center of the disk. Indeed, for a circular dot of thickness L and radius R, the static magnetization distribution of the vortex can be parameterized as follows:

$$m_x + i m_y = \sin\Theta(\boldsymbol{\rho}) e^{i\Phi(\boldsymbol{\rho})}, \quad m_z = p\cos\Theta(\boldsymbol{\rho}), \quad \Phi(\phi,\rho) = q\,\phi + C\,\frac{\pi}{2}. \tag{1.10}$$

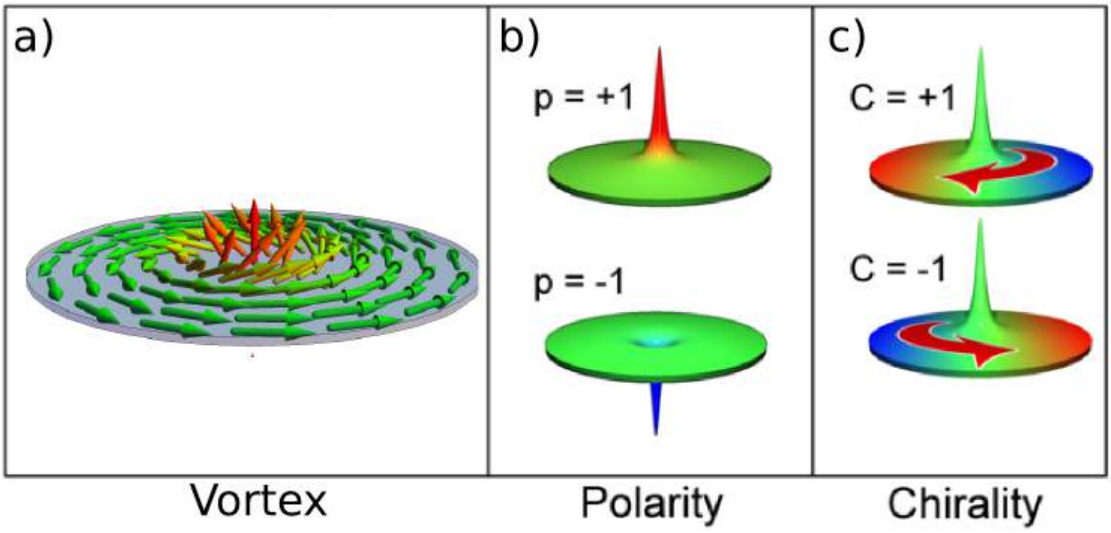

Figure 1.3.: *Figure (a) shows a sketch of a magnetic vortex of counterclockwise chirality and positive polarity. Here the magnetization is curling in the plane of the disk, except at the center where it is pointing out-of-plane, This is called the vortex core. (b) and (c) shows the characteristics of a ferromagnetic vortex: polarity (b) and chirality (c).*

Here ρ, ϕ, Θ and Φ are the polar coordinates that define the magnetization vector. Then, the common ansatz for the magnetization distribution in the core is [66]:

$$\sin\Theta(\boldsymbol{\rho}) = \frac{2\rho R_c}{R_c^2 + \rho^2} \text{ if } \rho < R_c \text{ and } \Theta(\boldsymbol{\rho}) = \frac{\pi}{2} \text{ if } \rho > R_c\,. \tag{1.11}$$

Where R_c corresponds to the vortex core radius which is a few exchange length (~ 10- 20 nm). In order to describe properly the evolution of magnetization distribution of the magnetic vortex and its dynamic properties, it is necessary to introduce an analytical description of the vortex shifted from its equilibrium position. Several different analytic models of magnetic vortices in confined geometries were developed (see references [67, 65]). Thus, the magnetization of equation (1.10) is rewritten as:

$$m_x + im_y = \frac{2w(\zeta,\bar{\zeta})}{1 + w(\zeta,\bar{\zeta})\bar{w}(\zeta,\bar{\zeta})},\quad m_z = \frac{1 - w(\zeta,\bar{\zeta})\bar{w}(\zeta,\bar{\zeta})}{1 + w(\zeta,\bar{\zeta})\bar{w}(\zeta,\bar{\zeta})},\quad \boldsymbol{m}^2 = 1\,, \tag{1.12}$$

where ζ is a dimensionless variable and $w(\zeta,\bar{\zeta})$ is a function which gives the position of the vortex core and it has the form:

$$w(\zeta,\bar{\zeta}) = \begin{cases} f(\zeta) & \text{if } |f(\zeta)| < 1 \\ \frac{f(\zeta)}{|f(\zeta)|} & \text{if } |f(\zeta)| \geqslant 1 \end{cases} \tag{1.13}$$

Where $f(\zeta)$ is an analytical function given by different forms, depending on the analytical model.

- *The rigid vortex model*: this model describes the cases when the vortex is shifted without any deformation of the original distribution according to a translational movement. The distribution of the magnetization is given by this function:

$$f(\zeta) = \frac{i}{c}(\zeta - s)\,, \tag{1.14}$$

  where $s = \frac{X+iY}{R}$ is the relative vortex center shift and $c = R_c/R$ is the relative core radius. In this approach, the magnetization is not tangent to the surface at the edges of the disc. The displacement of the vortex is then accompanied by the formation of the magnetic charges on the side of the dot. This distribution of the magnetization corresponds to the minimization of the magnetic energy of the disk. This model describe the dipolar confinement potential of a vortex core position inside a nanodisk subject to a static external magnetic field.

- *The double vortex model:* it takes into account the deformation of the vortex core and satisfies the magneto-static boundaries condition ($\boldsymbol{M}.\boldsymbol{n} = 0$ with $\boldsymbol{n}$ representing the normal vector to the surface) on the side borders. In this case $f(\zeta)$ is given by:

$$f(\zeta) = \frac{1}{c}\left[iC\zeta + \frac{a - \bar{a}\zeta^2}{2}\right], \tag{1.15}$$

  where the parameter a is related to the core displacement as $a = -2is/C$. This model is applicable to describe the vortex low frequency dynamics because the vanishing deformation at the boundary satisfies the boundary and pinning conditions of the precession profile.

The study of the stability of the vortex state compared to the uniform state for in plane magnetic field have been realized experimentally [68, 69] and theoretically [66, 65, 70]. Indeed, when the dot size is comparable to the exchange length, there is a competition between the vortex state and the uniform state. The ratio between the radius and the

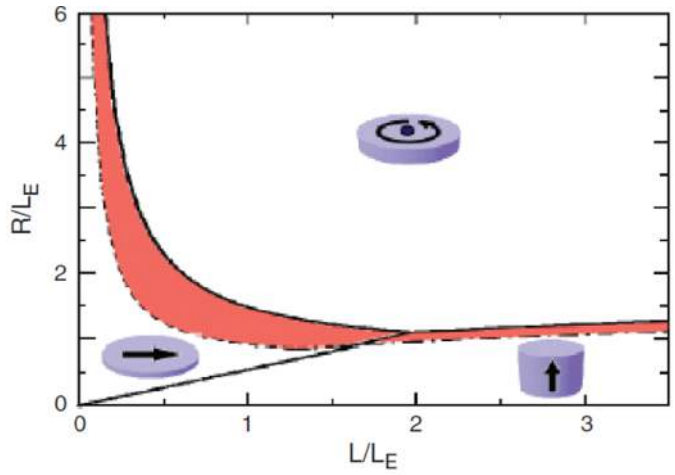

Figure 1.4.: *Diagram of stability of the vortex state (from[34]) when varying the dot radius R and thickness L (L_E is the material exchange length). Three different ground state can be fonded. (I) vortex state, (II) magnetized uniformly in-plane and (III) magnetized uniformly parallel to the cylinder axis. The red area is a region of bi-stability.*

thickness of the dot is the main parameter that is responsible to the transition between these states. The boundaries between these states correspond to lines of equal magnetic energy. Then, the stability of a magnetic vortex in a soft ferromagnetic material was calculated by Metlov et al. [65]. The calculation of energy for each dot aspect ratio L/R is shown in figure 1.4. These calculations show that there are three stable magnetic states: the vortex state and the uniform states with the magnetization either in or out of the dot's plane. Qualitatively, the phase diagram shows that if L or R is too small, the magnetization is saturated in the plane in the case of flat disk and the magnetization is saturated along the dot axis in the case of thick cylinder . Otherwise the vortex state is stable in soft magnetic cylinder with lateral size greater than the exchange length except in the bi-stability regions which corresponds to the red area in the figure 1.4.

Finally it should be mentioned that the phase diagram presented in figure 1.4 is universal for soft magnetic dots if the geometrical sizes (R, L) are normalized to the material exchange length L_E.

1.2.1.1. Vortex stability under applied magnetic field

The stability of the vortex state as a function of magnetic field was studied in details in these references [71, 72, 67, 61]. The main effect of the external magnetic field is to deform the vortex configuration, and leading to its annihilation.

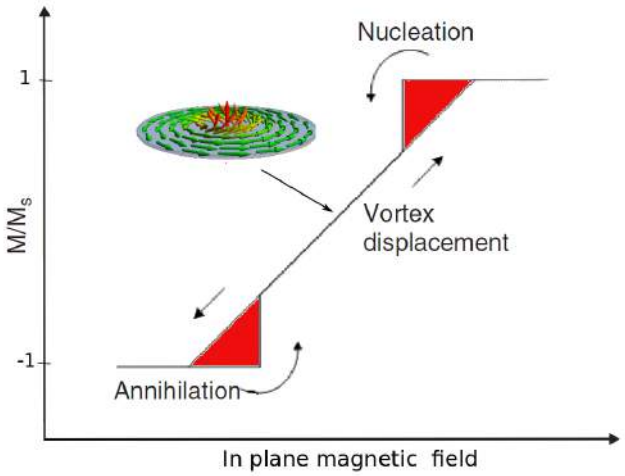

Figure 1.5.: *Diagram of the reversal process of the normalized magnetization M/Ms as function of in plane applied magnetic field of a magnetic disk. The remanent state corresponds to a centered vortex. The filled area represents the region of bi-stability between the vortex and the uniform state.*

- *In plane magnetic field:* The stability of the vortex state as a function of in plane magnetic field was experimentally investigated for the first time by using magneto-optical measurements [69]. Indeed, when a strong magnetic field is applied in the dot's plane, the magnetization aligns with the field direction and thus the vortex is expulsed. In a magnetic disk with vortex state at zero field, the saturation magnetization in the direction of the field is described by a process of vortex core displacement, and the vortex annihilation. The displacement of the vortex core occurs perpendicularly to the direction of the applied field due to the growth of the in-plane domain parallel to the applied field. The displacement of the core was calculated by minimizing the total magnetic energy which consists of the magneto-static energy exchange and the Zeeman energy due to the external field. Figure 1.5 shows a typical behavior of the evolution of the magnetic vortex in a disk. When the magnetic field is decreased from the saturation, a magnetic vortex is nucleated, accompanied by an abrupt decrease in magnetization. The reversible linear part of the loop corresponds to the vortex core movement perpendicular to the applied field. Then, when the magnetic field reaches the annihilation field, the vortex vanishes completely and the disk stabilizes in a uniform state. The field annihilation (H_{an}) of the vortex is greater than the field nucleation (H_n) of the vortex. There is also a region where the magnetic fields of the disk are in the bi-stable state (red area of figure 1.5). The values of characteristic fields (H_{an} and

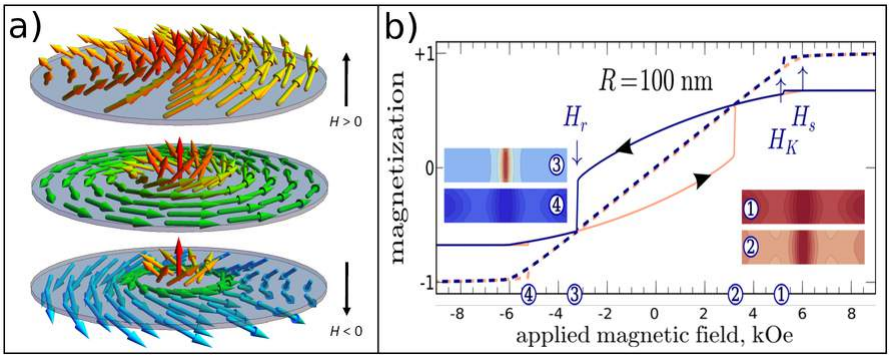

Figure 1.6.: *a) Sketch of the vortex magnetization under a perpendicular bias field. b) Numerically calculated field dependence of the static magnetization of a NiMnSb disk (thickness 44 nm, radius 100 nm). The solid lines show the averaged magnetization over the core only. The insets show the spatial distribution of M_z at four progressively decreasing values of $H_\perp$ [61].*

H_n) and the slope of the linear part of hysteresis loop depends strongly on the size of the disk. The nucleation and annihilation fields decrease with increasing the disk diameter [73].

- *Out of plane magnetic field:* The application of perpendicular field $H_\perp$ to the disk will also modify the distribution of magnetization. Mainly, the magnetization lying in the plane at remanence will progressively go out of plane to follow the increase of the $H_\perp$ field (see figure 1.6 (a)). It was demonstrated that the behavior of the evolution of the vortex is a linear increase of M_z with field [61]. Then, depending on the field direction compared to the core polarity two cases have to be deliberated:

  – The field is parallel to the core polarity (P).

  – The field is anti-parallel to the core polarity (AP).

  In the first case, when the field is applied parallel to the core polarity, its volume will be increased and covers most of the dot as H_z reaches the perpendicular saturation field H_s. On the other hand, when the field is applied anti-parallel to the core, its lateral size is reduced until it is energetically more favorable for the polarity to be reversed. Figure 1.6 (b) shows a micromagnetic simulation for a magnetic disk of diameter 200 nm and thickness 44 nm in order to present the influence of a perpendicular field on the vortex stability. Similarly to what we have shown before for H in plane, we can see the transition between the vortex and the saturated states.

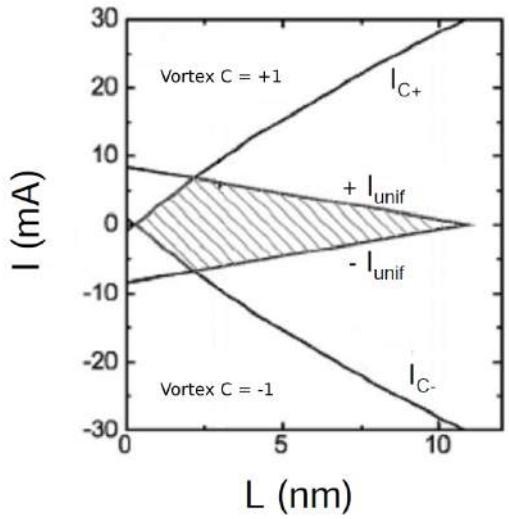

Figure 1.7.: *Stability diagram of current (I) versus thickness L for Py discs with radius 100 nm. From [74]. The three states are stable in the shaded region.*

1.2.1.2. Vortex stability under applied DC current

The influence of the DC current on the stability of the vortex was investigated in this reference [74]. The main effect of a DC current on a ferromagnetic layer in the vortex state is due to the Oersted field created by the current which is oriented in an ortho-radial direction and its amplitude increases linearly from the center of the disk to its extremity. The Oersted field has a circular symmetry which is identical to the symmetry of the distribution of the magnetization in the vortex state. Thus, for an Oersted field having the same chirality (direction of rotation) of the vortex, the magnetic state is favored, and vice versa in case of the opposite chirality (when the sign of the current is reversed). The stability of the vortex state, taking into account the effects of the Oersted field was calculated by S. Urazhdin et al. [74]. Figure 1.7 shows the stability diagram calculation for a permalloy disk (M_s = 800 emu/cm^3) with a radius of 100 nm, varied thickness L, and current I. Three different states can be distinguished. The state with positive chirality (C=+1), negative chirality (C=-1) and uniform state or single domain state. In this diagram the polarity I >0 is taken for the Oersted field of the current favoring the C=+1 state. The main conclusion of the phase diagram is as follows: although the initial configuration of a magnetic thin film (L<8nm) is uniform, it is possible to nucleate a vortex by increasing the current amplitude. Then, if the thickness is sufficient, the vortex will be stable even at zero current.

1.2.2. Gyrotropic mode

Several types of dynamic modes of magnetic vortices have to be distinguished, These modes can be classified to two main types:

- The gyrotropic mode or translational mode which is excited at low frequency.
- The higher order modes (radial and azimuthal modes) which are excited at high frequency (see section 2.3.2 of chapter 2).

The experiments performed in the vortex state in this thesis deal exclusively with the gyrotropic mode. In the following, we will provide some background on this mode.

The lowest energy excitation mode of a magnetic vortex is the so-called gyrotropic mode. It corresponds to a gyration of the vortex core around its equilibrium position at the center of the disk (see figure 1.8). In order to describe theoretically this mode, it is possible to use an analytical model developed by Thiele [75]. Starting from the LLG equation, it can be linearized and rewritten with the ansatz ($\mathcal{M}(\boldsymbol{\rho},t) = \mathcal{M}(\boldsymbol{\rho} - \mathcal{X}(t), \dot{\mathcal{X}}(t))$ and in the presence of spin transfer torque, the full equation of motion is given :

$$\boldsymbol{G} \times \dot{\mathcal{X}} - \frac{\partial \mathcal{W}(\mathcal{X})}{\partial \mathcal{X}} - D\dot{\mathcal{X}} + \boldsymbol{F_{STT}} = 0\,. \tag{1.16}$$

Where $\mathcal{X}$ parameterizes the vortex core position within the dot. In this equation the first term is a force acting perpendicular to the velocity. The gyrovector can be expressed as $\boldsymbol{G} = -G.\boldsymbol{e}_z$, where $G = 2\pi p L \mathcal{M}_s/\gamma$, this vector is directed perpendicular to the disc plane, and is responsible for the vortex core oscillation. The second term is the reversible force on the magnetic structure. This force is equal to a potential energy (W) that confines the core in the middle of the disk. The variation of the total potential energy associated with a small displacement of the vortex core from the center can be expressed as :

$$\mathcal{W}(\mathcal{X}) = \mathcal{W}(0) + \frac{\kappa \mathcal{X}^2}{2} + \mathcal{O}(\mathcal{X}^4)\,, \tag{1.17}$$

the variation of the energy (W) is mainly due to the variation of the magnetostatic energy ($\mathcal{W}_{ms}$) and influence of the Oersted field induced by the current ($\mathcal{W}_{Oe}$) [76].

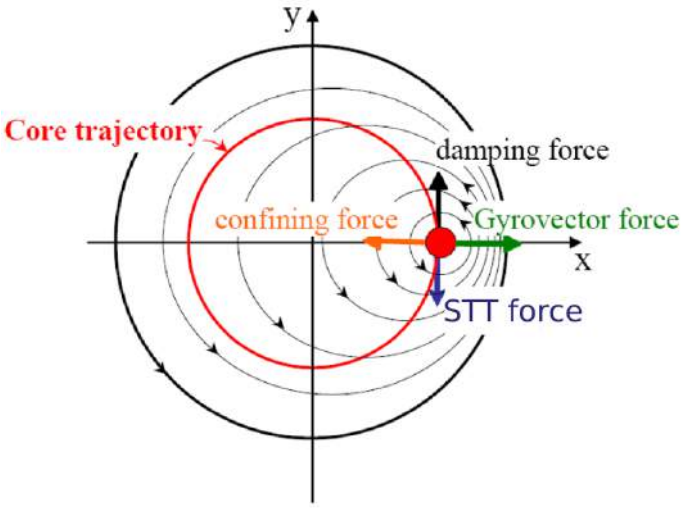

Figure 1.8.: *Scheme of the different forces acting on a vortex core which is represented by the red dot.*

The third term is a dissipative force opposed to the velocity, responsible for the return to equilibrium of the shifted vortex core. It can be shown that the tensor damping D is diagonal [77] and that:

$$D \simeq \frac{\alpha \pi M_s L}{\gamma}\left[\frac{5}{4} + \ln\frac{R}{R_c}\right]. \tag{1.18}$$

The last term is the force due to the spin current which acts so as to compensate the damping leading to steady precession of the core upon application of a dc current bias. In the case of a uniformly perpendicular polarized [2] current this torque has the form:

$$\boldsymbol{F_{STT}} = \kappa_\perp p_z J(\vec{e_z} \times \vec{X}) \quad , \kappa_\perp = \frac{\epsilon M_s}{\gamma}\pi L\,. \tag{1.19}$$

The different forces contributing to the gyrotropic motion of the vortex core are presented in the figure 1.8. Here the vortex core is represented by red dot, which gyrates around an equilibrium orbit (red), defined by the balance between all the forces.

[2] These calculations of the terms of the equation have been done for the case of a uniformly polarized current [78, 76, 79]. For the other type of the polarizer orientation example vortex polarizer where certain simplifying assumptions can be made we can find the calculations in this reference [80].

Approximations for the gyrotropic-frequency

The calculation of eigen-frequency of the vortex oscillations can be done by solving the Thiele equation. The first calculation is given by Konstantin Guslienko, only the gyro-force and the confining potential are taken into account. Then, it predicts an oscillation frequency in the absence of applied magnetic field and zero current takes the approximate form [81] :

$$\omega_G(0) \simeq \frac{20}{9}\gamma M_s \frac{L}{R}, \tag{1.20}$$

which is a good approximation for disk with small thickness compared to the radius. Taking into account the presence of the applied current (the frequency of the oscillations is modified due to the Oersted field created by the current [76, 82, 83]) and external perpendicular magnetic field $H_\perp$(See next chapter) [61], the frequency of the oscillations is modified with respect to $\omega_G(0)$ by two current and field dependent terms, so it takes the form:

$$\omega(H_\perp) = \omega_0(H_\perp) + \omega_{Oe}(H_\perp) \text{ with } \begin{cases} \omega_0(H_\perp) = \omega_0(0)[1 + p\frac{H_\perp}{H_s}]. \\ \omega_{Oe}(H_\perp) = \omega_{Oe}(0)\sqrt{\frac{1+[\frac{H_\perp}{H_s}]}{1-[\frac{H_\perp}{H_s}]}}. \end{cases} \tag{1.21}$$

Where $\omega_{Oe}(0) \simeq \frac{0.85}{2\pi}\gamma\mu_0 R$.

1.3. State-of-the-art of STNOs experimental results

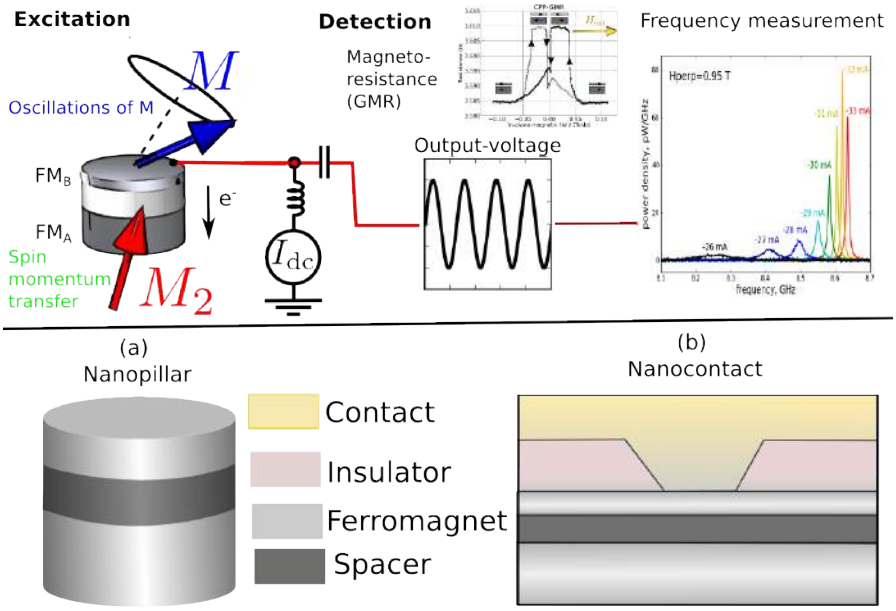

Figure 1.9.: *Upper panel: principle of spin transfer effect. Bottom panel : Two types of typical spintronic devices (a) Nanopillar or (b) Nanocontact. In these typical devices two types of magnetic configurations can exist: homogeneous or vortex.*

As mentioned in the introduction, the STNO microwave spintronic devices are based on a magneto-resistive heterostructure of the type $FM_A/NM/FM_B$. Spin momentum transfer from a current polarized by the polarizer FM_A, to the local magnetization of the free layer FM_B can drive the latter into large angle self-sustained oscillations (see figure 1.9). This occurs when the spin polarized current is larger than a given threshold value, necessary to overcome intrinsic losses (see equation 1.9). These self-sustained oscillations are converted into voltage oscillations through magneto-resistive (MR) effects and are at the base of the spin transfer nano-oscillator (STNO) used for microwave high frequency generation. After the first demonstration in 2003 by the Cornell group [11] , many studies were realized in the following years to understand the magnetic excitations for different magnetic stack configurations, with varying magnetic and transport properties, confirming the new phenomenon of spin momentum transfer and its role for the magnetization dynamics. Several classes of configurations are used that are characterized by different excitation modes and frequency ranges. We give here a few examples of theses configuration in multi-layered nano-structures.

1.3.1. Individual STNOs

Homogeneous nanopillar: Here, the basic configuration is a circular or elliptical nanopillar structure (see figure 1.9 (a)), with a homogeneous magnetization for both layers. The first direct observation of microwave emission in this structure with a magnetic field applied in the plane of the layers was given by Kiselev et al. [11]. This research group has shown that when the applied DC current is above the threshold, the microwave spectrum of the nano-pillar is strongly modified by the appearance of the emission peak whose frequency and amplitude depend on the current (see figure 1.10 (a)). When the magnetizations of both ferromagnetic layers FM_A and FM_B are in-plane, the corresponding uniform excitation mode (all spins precess in-phase), makes use of only 30% of the full magneto-resistive signal. This can be enhanced to 100%, when the magnetization of FM_A is out-of-plane (perpendicular polarizer) as first demonstrated by D. Houssamedine et al. [13]. These structures are thus of great importance for reaching the required output level. Furthermore they operate in zero external magnetic field. To conclude, the frequency of this device class for single layers is between 2-25 GHz with typical linewidths in the range of 10-200 MHz, depending on current, field amplitude, orientation and temperature.

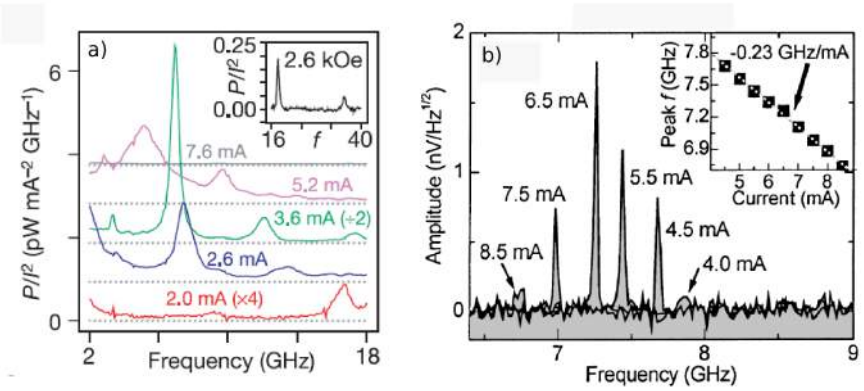

Figure 1.10.: *direct measurements of STT driven magnetic dynamics in (a) for nano-pillar geometry from [11] and (b) for nano-contact from [12]*

Nanocontact: Another important configuration of devices have been proposed which are nano-contacts (see figure 1.9 (b)), first introduced by Tsoi et al.[84] and then in 2004 by the NIST group [12], where only the volume under a 10-100nm diameter sized metallic injection point is excited in an otherwise continuous magnetic film (see figure 1.10 (b)). The advantage of nano-contacts is the possibility of reaching very high frequencies (up

to 65 GHz) as has been demonstrated by Bonetti et al .[14] and to easily realize coupling of individual oscillators via spin waves (see next section).

Vortex based STNOs: The ability to induce steady oscillations in a ferromagnet by using a DC current, has firstly been reported only for a uniform magnetization. Subsequently, a second case of dynamics that was foretold to be possible as a result of STT are steady oscillations of non-uniform magnetic structure (magnetic vortex) under excitation by a direct DC current. Several experiments have indeed demonstrated this phenomenon in different geometries. The initial experiments was given by the group from Cornell university [33] in a nanopillar device. In this geometry, the microwave signals were observed for out-of-plane applied fields (required to have a polarized layer which is here essential for the vortex to be excited into steady motion). Here the spin transfer torque acts as a source of anti-damping, canceling out the damping torque on average an thus leading to the oscillation of the vortex. Then, thanks to the magneto-resistance, the oscillations of the voltage at frequencies below 2 GHz are observed, corresponding to oscillations of the gyrotropic mode (see figure 1.11). This vortex mode, first introduced in nano-pillar geometry followed in 2008 by [79] in nano-contact geometry. These outcomes, quickly aroused great interest of the scientific community because the vortex mode offers important advantages compared the homogenous modes, to mention are a lower threshold current a lower linewidth (<1MHz) , easier stabilization of modes in zero field [85] and up to 100% use of the magnetoresistance (thus large output power) due to the large radius of the trajectory [76, 35].

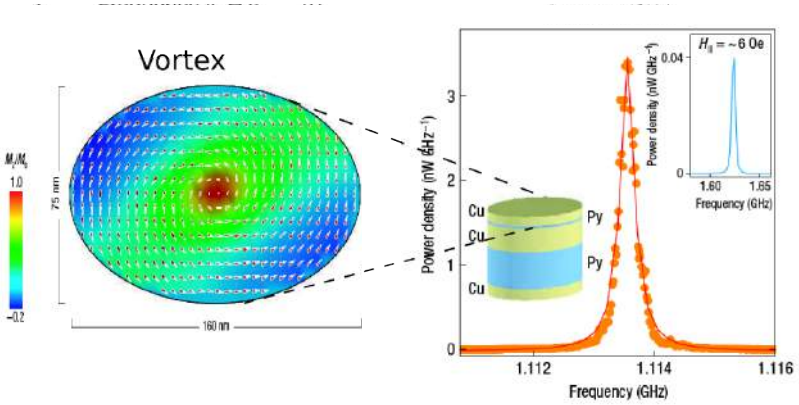

Figure 1.11.: *Experimental measurement of the microwave signal resulting from the motion of the gyro-tropic vortex core under the influence of the spin transfer torque. Sample layout (left inset). Microwave peak which can be obtained at ~ 6 Oe (right inset). From [33].*

Single STNOs with improved performance

The integration of STNOs in high frequency circuits depends on various conditions. The important parameters are linewidth, and the generated power signal. Further research efforts are being devoted to optimization of these parameters. In the last 6 years, the state of the art for STNO power performances has increased by more than 40dB, mainly through the use of magnetic tunnel junctions (MTJ). To date, the largest power output obtained in a single MTJ device in the vortex state is close to the μW range for a TMR hybrid device [35, 36, 86].

A remaining key issue is the phase noise directly related to linewidth. Using special nanocontact geometry, subsequent reports showed a reduction from GHz down to a few MHz by using a strong out-of-plane field [87]. A recent research allowed identifying two main origins of the spectral linewidth. First, as the active magnetic volume in such spin transfer devices is extremely small ($<< \mu m^3$), the magnetic energy at stake is of the order of the thermal energy, meaning that thermal noise determines for the most part the generation linewidth [88, 23]. Second, the high nonlinear character of STNOs (i.e. the dependence of the frequency on the precession amplitude and with this on the spin polarized current) is extremely important for achieving high frequency tunability unreachable for any other types of oscillators, but in turn, is a source of phase noise [89, 90, 25].

Although the understanding of the linewidth broadening is still a subject of intense research, it was recently identified an important way for linewidth reduction, which makes use of collective excitations. Going beyond excitations in a single magnetic layer as done in the large majority of studies, the use of magnetic multilayer stacks is an innovative point proposed in several studies. In such structures like FM/NM/FM, all layers interact directly via spin transfer torque as well as dipolar interactions. Recently, Houssameddine et al . have shown that the linewidth in an anti-ferromagnetic exchange coupled bilayer is by a factor of 10 narrower than the one of a single layer [38]. Then CNRS/Thales in collaboration with CEA/SPEC have shown that in spin transfer oscillators based on coupled vortices, the linewidth drops down to a minimum of 50 kHz [40] as compared to 1 MHz in a single layer.

Finally, Naletov et al. [41] have succeeded to identify selection rules for the excited modes for a single nano-pillar that are of importance when coupling the oscillations of different layers or when synchronizing to an external signal source. This fundamental aspect

is vital for improving the spectral purity via synchronization of different oscillators or inside a phase locked loop.

1.3.2. Phase-locking and mutual synchronization

Besides understanding and improving the performances of single types of STNOs, enormous progress has also been concentrated on the coherent coupling between oscillators in order to synchronize a large array of nano-oscillators. Indeed, improvements of the performance are expected from the phase-coherence which leads to an increase of the power output that varies as $\mathcal{N}^2$ and the emission linewidth as $1/\mathcal{N}$ where $\mathcal{N}$ is the number of elements [91]. To date three different coupling mechanisms between STNOs have been proposed (see figure 1.12).

- *Coupling mediated by spin-waves (SWs):* is associated with the SWs created by one STNO in the extended magnetic medium (thin layer) that then propagate towards the other STNO . The range of this coupling is controlled by the SW decay length in the thin magnetic layer and is expected to lie in the range of 200nm to $1\mu m$. This mechanism has been first demonstrated experimentally in 2005 [28, 27] and recently studied in detail by the Akerman group who have successfully fabricated multi-nanocontact STNOs with strong lateral coupling. While the state-of-the-art in the literature is limited to two nanocontacts, Sani et al.[30] have recently demonstrated synchronization of both 3 and 4 nanocontacts STNOs with a 10× increase in total microwave power and a 20× increase in the efficiency (microwave power/supplied power) compared to the best available literature values [92].

- *Coupling through the common self-generated microwave current:* this coupling mechanism has been successfully demonstrated on a system very close to the STNO, the Josephson junction [93]. One of the main advantages of this approach to the synchronization of STNOs is that it is a global coupling, which provides a key advantage for phase-locking of large arrays. Another important point is that no technological breakthrough is needed, such as reduction of the distance between oscillators. In this case, and for the frequencies under consideration that lie in the GHz range, the coupling length scale is several hundreds of micrometers. To date, several studies (experimental [94, 95, 90, 96] and theoretical [97, 98]) have attempted to demonstrate that a single STNO can be locked to an external injected microwave current. Recently, Grollier et al. have developed theoretical simulations

[26], within the macro-spin approximation, which show that synchronization of an assembly of STNOs is achievable through the common stimulated microwave current. These calculations, performed at zero temperature, provide evidence that the efficiency of phase-locking is strongly linked to the MR ratio of each oscillator and to the delay of microwave current transmission between STNOs. To date there is no experimental verification of this coupling mechanism, because of the too small rf emitted power and the too large phase noise of individual STNOs.

- *Coupling through the dipolar magnetic field:* when the separation between STNOs is reduced to approximately their diameter, the oscillations in the individual oscillators can couple via the dynamic magnetic dipolar fields radiated from each STNO. Several experimental studies have demonstrated that a single STNO can be locked to the rf magnetic field produced by an external microwave antenna [99]. Then, in the resonance mode (below threshold excitation) this coupling has recently been demonstrated by Pigeau et al. using the MRFM technique [100]. It might proof to be more efficient than electrical coupling and spin-waves coupling, this is why we decided to perform a first experimental study using only two STNOs placed nearby laterally. The experimental result of this study will be presented in chapter 8.

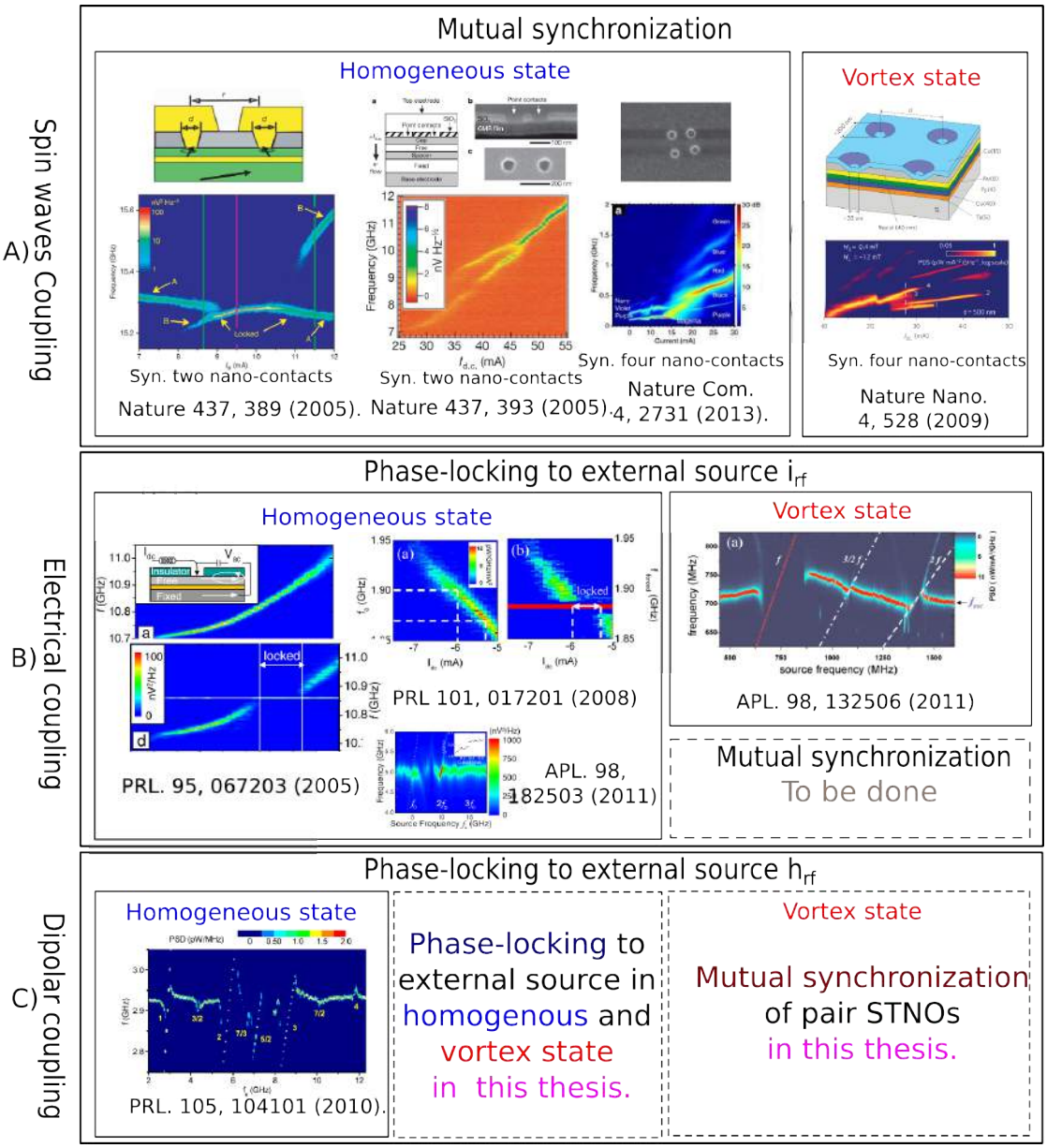

Figure 1.12.: *Summary of state of art of phase locking and mutual synchronization.*

In conclusion, we have presented in this chapter the basic operating concepts of STNOs. They offer many capabilities for applications, but many challenges remain in order to optimize the microwave performances of these spintronic devices. In particular, vortex based STNOs, STNOs operating on coupled modes, and the coupling of several STNOs are promising ways to achieve this goal.

CHAPTER 2

Classification of spin-wave modes in magnetic nanostructures

In this chapter, we first introduce the basics of a general theoretical approach of linear spin-wave excitations. We then present the classification of spin-wave modes in two particular cases of interest in this thesis, which both preserve the axial symmetry: the normally saturated disk, and the vortex-state disk, in the presence of a perpendicular magnetic field. We then discuss the influence of dipolar interaction on the collective dynamics of adjacent magnetic disks.

2.1. General approach

The general theoretical framework to determine linear spin wave modes in magnetic nanostructures, developed by Vasyl Tiberkevich and Andrei Slavin, is presented in details in references [41, 101] and in the thesis of Benjamin Pigeau [102]. Below, we briefly recall the general idea of this approach.

The first step is the linearization of the Landau-Lifshitz equation of motion of magnetization

$$\frac{\partial \mathbf{M}}{\partial t} = \gamma \mathbf{H}_{\text{eff}} \times \mathbf{M} , \tag{2.1}$$

in which the non-conservative terms are disregarded, and where the effective field, introduced in equation (2), can be conveniently written in the following form:

$$\mathbf{H}_{\text{eff}} = \mathbf{H}_{\text{ext}} - 4\pi \widehat{\boldsymbol{G}} * \mathbf{M} . \tag{2.2}$$

In this notation, $\widehat{\boldsymbol{G}}$ is a linear tensor self-adjoint operator that regroups all the internal magnetic interactions (exchange, demagnetizing and magneto-crystalline anisotropy energies).

In the equilibrium state, the effective field $\mathbf{H}_{\text{eff}}$ is parallel everywhere to the local magnetization direction $\boldsymbol{u}_{\mathbf{M}}$. To find the linear magnetization excitations, the out-of-equilibrium component of the magnetization $\boldsymbol{m}$ is defined by the following ansatz:

$$\mathbf{M}(\boldsymbol{r}, t) = M_s\big(\boldsymbol{u}_{\mathbf{M}} + \boldsymbol{m}(\boldsymbol{r}, t)\big) + \mathcal{O}(\boldsymbol{m}^2) . \tag{2.3}$$

The norm of the magnetization vector is a constant of motion, hence $\boldsymbol{m} . \boldsymbol{u}_{\mathbf{M}} = 0$. Thus, $\boldsymbol{m}$ is the small component of the magnetization ($|\boldsymbol{m}| \ll 1$) oscillating in the plane transverse to the local $\boldsymbol{u}_{\mathbf{M}}$.

Substituting $\boldsymbol{m}$ in equation (2.1) and keeping only the linear terms, a linear equation describing the transverse magnetization precession at the Larmor frequency is obtained:

$$\frac{\partial \boldsymbol{m}}{\partial t} = \boldsymbol{u}_{\mathbf{M}} \times \widehat{\boldsymbol{\Omega}} * \boldsymbol{m} , \tag{2.4}$$

where the sign $*$ denotes the convolution product. The self-adjoint tensor operator $\widehat{\boldsymbol{\Omega}}$ represents here the Larmor frequency:

$$\widehat{\boldsymbol{\Omega}} = \gamma\big(H_{\text{eff}}\widehat{\mathbb{I}} + 4\pi M_s \widehat{\boldsymbol{G}}\big) . \tag{2.5}$$

Here, $\widehat{I}$ is the identity matrix and H_{eff} is the norm of the effective field.

Considering only linear excitations of the spin system, $\boldsymbol{m}$ is developed in the eigen-basis of the spin wave eigenmodes, labeled by ν:

$$\boldsymbol{m}(\boldsymbol{r},t) \approx \sum_{\nu} c_\nu(t)\boldsymbol{m}_\nu(\boldsymbol{r}) + c.c. \tag{2.6}$$

where $c.c.$ stands for complex conjugate. In this formulation, $c_\nu(t)$ are the amplitudes of the eigenmodes and $\boldsymbol{m}_\nu(\boldsymbol{r})$ represents their spatial profile. This eigen-basis must be orthonormal and obey the closure relation:

$$i\langle\overline{\boldsymbol{m}}_\nu.(\boldsymbol{u}_{\mathcal{M}} \times \boldsymbol{m}_{\nu'})\rangle = \mathcal{N}_\nu\delta_{\nu,\nu}\,, \tag{2.7}$$

where $\overline{\boldsymbol{m}}$ is the $c.c.$ of $\boldsymbol{m}$, δ the Kronecker delta function, and the bracket denotes the spatial average over the volume of the magnetic body. $\mathcal{N}_\nu$ are normalization constants of the basis.

Assuming an oscillatory dependence of the spin wave magnetization vector $\boldsymbol{m}_\nu$ at the eigen-frequencies ω_ν, the eigen-modes labeled by ν are solutions of equation (2.4):

$$-i\omega_\nu\boldsymbol{m}_\nu = \boldsymbol{u}_{\mathcal{M}} \times \widehat{\boldsymbol{\Omega}} * \boldsymbol{m}_\nu\,. \tag{2.8}$$

The main properties of spin wave excitations follow from the eigen-problem equation (2.8) and the fact that the operator $\widehat{\boldsymbol{\Omega}}$ is self-adjoint and real. In particular, if the equilibrium magnetization along $\boldsymbol{u}_{\mathcal{M}}$ corresponds to a local minimum of the energy, the operator $\widehat{\boldsymbol{\Omega}}$ is positive-definite. The "physical" (positive) eigen-frequencies are then simply given by the formula:

$$\omega_\nu = \frac{\langle\overline{\boldsymbol{m}}_\nu.\widehat{\boldsymbol{\Omega}} * \boldsymbol{m}_\nu\rangle}{\mathcal{N}_\nu}\,. \tag{2.9}$$

The importance of this relation is that the frequenciesω_ν calculated using equation (2.9) are variationally stable with respect to perturbations of the mode profile $\boldsymbol{m}_\nu$. Thus, injecting some trial vectors inside equation (2.9) allows one to get approximate values of ω_ν with high accuracy.

2.2. Normally magnetized thin disk

In this section, we consider a thin magnetic disk (thickness L, radius R) saturated by a strong magnetic field applied exactly along the normal $\boldsymbol{u}_z$ of the disk. Due to the finite size of the system, we expect a discrete spin-wave mode spectrum. Moreover, as the disk is considered to be thin, the magnetization is uniform along its thickness, and the 2D approximation holds. Therefore, two indices are expected to be required to label the eigen-modes: $\nu = (\ell, n)$. Due to the axial symmetry of the system, ℓ should be related to the azimuthal symmetry of the spin-wave modes, whereas n should be a radial index.

2.2.1. The eigen-modes

From symmetry arguments, it can be shown that the spin-wave mode profiles can be written as [41]:

$$\boldsymbol{m}_\ell = \frac{1}{2}(\boldsymbol{u}_x + i\boldsymbol{u}_y)e^{-i\ell\phi}\psi_\ell(\rho)\,, \tag{2.10}$$

where (ρ, ϕ) are the cylindrical coordinates, and $\boldsymbol{u}_x$, $\boldsymbol{u}_y$ orthogonal unit vectors in the plane of the disk.

The calculation of the radial functions $\psi_\ell(\rho)$ involves to solve complicated integro-differential equations. An approximation consists of using a reasonable set of known mathematical trial functions. Here, the Bessel functions of the first kind $J_\ell(x)$ are well adapted, since they have the appropriate radial and azimuthal symmetry. Moreover, they reproduce well the strong pinning of the magnetization at the lateral boundaries due to the magneto-dipolar interaction [81]. Therefore, we use radial profiles of the form $\psi_\ell(\rho) = J_\ell(k_{l,n}\rho)$. The eigenmodes wave numbers $k_{l,n}$ are determined from the pinning conditions at the disk boundary. For very thin disks, this pinning is found to be almost complete [81], so that $k_{\ell,n} = \kappa_{\ell,n}/(R + L)$, where $\kappa_{\ell,n}$ is the nth root of the Bessel function of the ℓth order.

The spatial profiles of such functions are presented in figure 2.1, with the rows corresponding to the azimuthal index ℓ and the columns to the radial index n. The phase (or direction) of the magnetization precession $\phi = \arg(\boldsymbol{m}_\nu)$ is displayed in color code using the hue, while the amplitude $|\boldsymbol{m}_\nu|^2$ is given by the brightness (we will use consistently the same color code to show the precession pattern). One can easily identify the $(\ell = 0, n = 0)$ mode as the "uniform" mode: the magnetization precesses in-phase uniformly in the disk. The first azimuthal mode $(\ell = +1, n = 0)$ corresponds to a spin

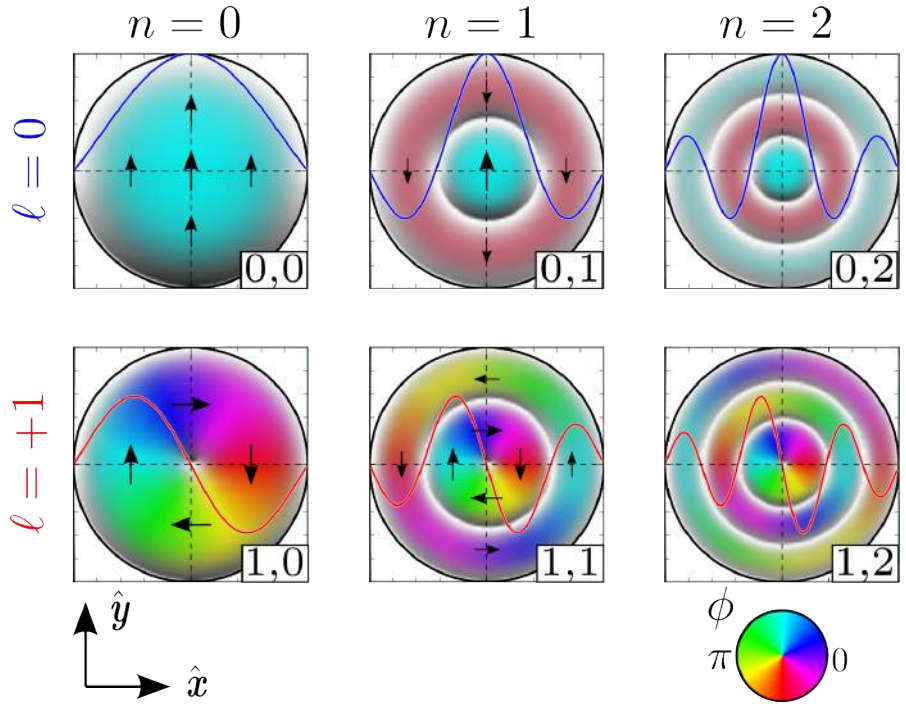

Figure 2.1.: *Color representation of the Bessel spatial patterns for different values of the azimuthal mode index ℓ (by row) and radial mode index n (by column). The arrows are a snapshot of the transverse magnetization $\boldsymbol{m}_\nu$, labeled by the index $\nu = (\ell, n)$. All arrows are rotating synchronously in-plane at the spin-wave eigen-frequency. The hue indicates the phase $\phi = \arg(\boldsymbol{m}_\nu)$ (or direction) of $\boldsymbol{m}_\nu$, and the brightness the amplitude of $|\boldsymbol{m}_\nu|^2$. The nodal positions ($|\boldsymbol{m}_\nu| = 0$) are marked in white.*

wave that is rotating around the disk in the same direction as the Larmor precession. The corresponding phase is in quadrature between two orthogonal positions and this mode has a node at the center of the disk (the nodal positions are marked in white). Then, increasing the index n results in an increase of the number of nodes in the radial direction.

2.2.2. Selection rules

The spatial symmetry of the source is crucial to determine which spin-wave eigen-modes can be excited [41]. The overlap integral between the excitation field $\boldsymbol{h}_{rf}$ and the mode profile governs the selection rules:

$$h_{\ell,n} = \frac{\langle \overline{\boldsymbol{m}}_{\ell,n}.\boldsymbol{h}_{rf} \rangle}{\mathcal{N}_{\ell,n}} . \tag{2.11}$$

It can be easily shown that a uniform microwave magnetic field can only excite ($\ell = 0, n$) spin wave modes, because in this case overlap integrals with azimuthal modes ($\ell \neq 0$) vanish. In order to excite azimuthal spin wave modes with $\ell = +1$, a field with an orthoradial symmetry can be used, as the one produced by an rf current flowing vertically through the disk [41]. We will come back on this point in section 5.5 of chapter 5

2.2.3. Influence of symmetry breaking

In the case of a small symmetry breaking from the perfect axial symmetry, introduced either by a small tilt of the perpendicular applied field [59, 41] or a deviation from a perfect circular shape of the disk [41], it is still possible to use the same eigen-basis of equation (2.10) to decompose the new spin-wave modes. The so-called "uniform" mode will not be affected, as it will always correspond to an in-phase precession of all the spins around the local effective field. But in general, the eigen-modes will now be a superposition of $\ell = 0$ and $\ell \neq 0$ modes of the basis, therefore, the selection rules might also be affected [59, 41].

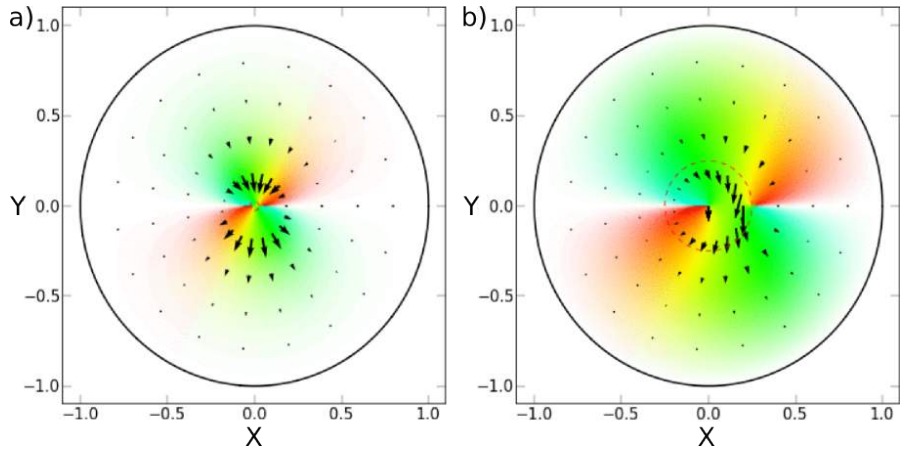

Figure 2.2.: *Profile of the vortex gyrotropic mode in the regime of small (a) and large (b) amplitude. The dashed circle displays the vortex core orbit, which is smaller and larger than the core radius in (a) and (b), respectively.*

2.3. Disk in the vortex state

We have already introduced in section 1.2 the particular dynamics of the gyrotropic mode in the vortex state with no applied magnetic field. Although the Thiele equation is very convenient to describe the dynamics of the vortex core, it is interesting to note that this gyrotropic mode can be treated in the same general framework as presented in section 2.1, see *e.g.* reference [103]. In particular, similarly to equation 2.3, the profile of the gyrotropic mode can be defined as the dynamical deviation from equilibrium configuration, $\boldsymbol{m} = \boldsymbol{M}(x,y) - \boldsymbol{M}(x,y)_{\text{eq}}$, where x, y are the cartesian coordinates in the disk. Using the same color code as in figure 2.1, we have plotted in figure 2.2 (a) this profile in the linear regime, where the deviation of the vortex core from its equilibirum position at the center of the disk is smaller than the core radius. From this snapshot at a particular phase of the vortex core gyration, it is clear that the gyrotropic mode has the $\ell = 0$ symmetry, as the arrows displaying the dynamical magnetization are pointing on average in a particular direction (mainly along −Y). At larger radius of gyration (figure 2.2 (b)), we observe that the magnetization in the central region enclosed by the core orbit (see dashed circle) operates a full rotation in the plane over one period. This feature was also clear from the Thiele approach presentend in section 1.2.2 and is a very interesting point for the power emitted by STNOs based on the gyrotropic mode. It is also interesting to note that the dynamical magnetization profile extend far outside the region enclosed by the core orbit, until the boundaries of the disk.

In the following, we will briefly discuss two cases of spin-wave modes in the vortex state relevant to the experimental situations in this thesis: the behavior of the gyrotropic mode and the description of the full spin wave mode spectrum under a perpendicular field preserving the axial symmetry of the system.

2.3.1. Gyrotropic mode in the cone state

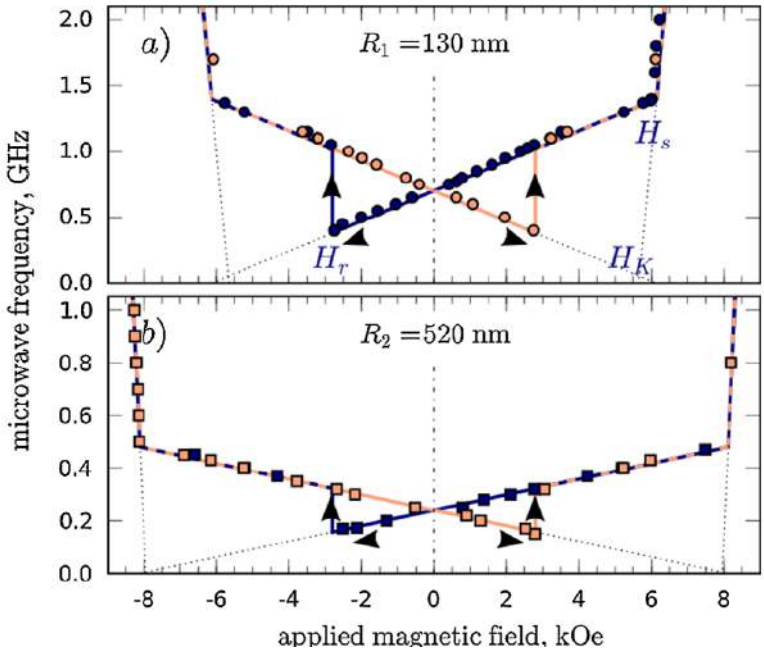

Figure 2.3.: *Frequency of the lowest excitation mode in a magnetic disk as a function of the perpendicular bias magnetic field for two sizes: (a) R_1 = 130 nm, (b) R_2 = 520 nm. Dark blue (light red) dots are experimental points corresponding to the field variation starting from large positive (negative) values. From [61].*

When a perpendicular magnetic field H_z is applied to the vortex structure, the latter will deform as sketched in figure 1.2 (a). This deformed vortex state is called "cone state", and exhibits interesting magnetization dynamics [104]. In particular, it was shown experimentally and analyzed theoretically that the gyrotropic frequency ω_G varies linearly with the bias perpendicular field field [61]:

$$\omega_G(H_z) = \omega_G(0)\left[1 + p\frac{H_z}{H_s}\right], \tag{2.12}$$

where H_s is the perpendicular saturation field of the disk. Two different frequency branches can be observed, depending on the the vortex core polarity p, as shown in figure 2.3. When p is anti-parallel to H_z ($p.H_z < 0$) equation (2.12) is valid only if the perpendicular field is below the static reversal field H_r, which is indicated in figure 1.6 (a) of chapter 1 and figure 2.3.

From equation (2.12), it is interesting to note that the vortex core polarity is directly given by the slope of $\omega_G(H_z)$ vs. H_z. If $\omega_G(H_z)$ increases (decreases) as H_z increases, then $p = +1$ ($p = -1$), *i.e.*, the vortex core is along $+z$ ($-z$). This useful property will allow us to determine the orientation of the vortex core in our experimental results presented in chapters 7 and 8.

2.3.2. Higher order spin-wave modes

The gyrotropic mode is the lowest energy mode of the vortex state, and in this thesis, we will operate STNOs based on this mode. However, there are of course many other spin-wave modes at higher energy [105, 106, 107, 108]. Here, we briefly mention the nature of these modes, and we comment on the large frequency gap which exists between the gyrotropic mode and higher order spin-wave modes in the vortex state.

The general approach presented in section 2.1 can be applied to classify the spin-wave modes in the vortex state. The obtained spin wave spectrum is similar to the normally saturated state, with the existence of radial and azimuthal modes. However, some qualitative differences exist due to the presence of the vortex core at the center of the disk, and to the orthoradial symmetry of the equilibrium magnetization in the vortex state (see figure 1.3 of chapter 1).

1. *Radial spin waves* ($\ell = 0, n$). Similarly to the case of a normally saturated disk, radial spin waves develop in the disk plane, leading to a varying angle of precession in the radial direction [108]. In the limit of thin disks, the amplitude of the dynamical magnetization is well described by Bessel functions [105, 108]. The presence of the vortex core does not break the symmetry, but imposes a vanishing angle of precession at the center of the disk. Therefore, J_1 rather than J_0 is appropriate to describe the mode profiles, because $J_1(0) = 0$. Compared to the saturated state, the symmetry of the background in which the spin wave modes develop is inverted. Out of the core, the magnetization follows an orthoradial symmetry, while it was axial in the saturated case. Therefore, the selection rules for these spin

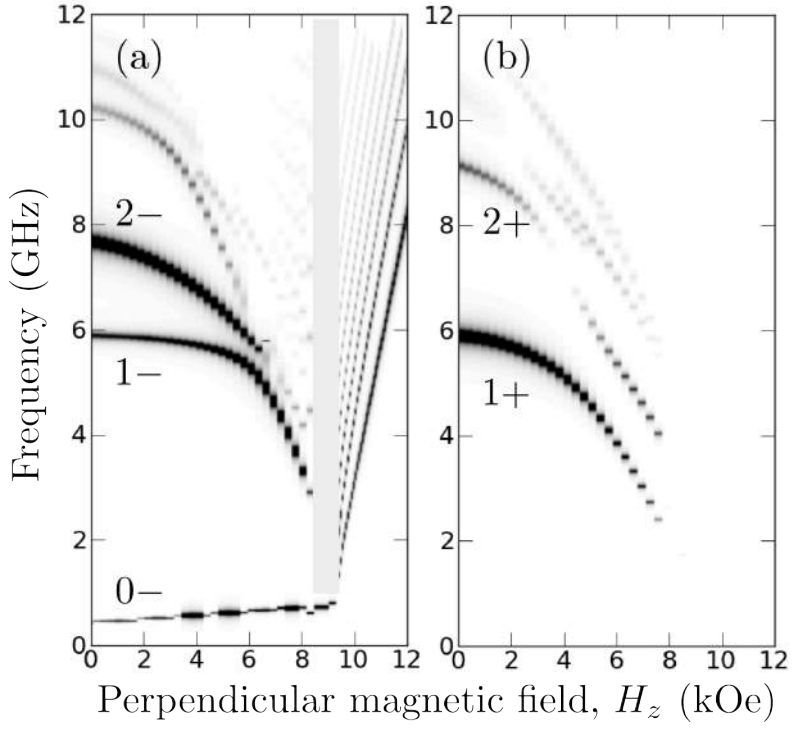

Figure 2.4.: *In plane dynamical susceptibilities a)χ_- and b) χ_+ for a downward field sweep and a positive field branch ($p = +1$). The high values are in black and the low ones in light gray.*

waves are reversed: to couple to the radial modes in the vortex state, the excitation has to follow an azimuthal symmetry. For instance, a microwave field applied perpendicularly to the plane of the disk is effective [108].

2. *Azimuthal spin waves* $(\ell, n = 0)$. Waves traveling around the vortex core can also be excited. The profiles of these modes are proportional to $m_\ell(\rho)\cos(\ell\phi + \omega_{\ell,0}t)$. In a saturated disk, azimuthal spin waves with indices $\pm\ell$, traveling in opposite directions, are degenerate in energy. The presence of the vortex core lifts this degeneracy [109]. In fact, the gyrotropic mode can interact with the azimuthal modes by dynamic dipolar coupling [103], leading to a lower (higher) frequency for waves rotating with (against) the gyrotropic mode. The selection rules for these modes are also reversed compared to the saturated state, as they can only be excited by a spatially homogeneous in-plane microwave field.

In figure 2.4, we present the results of micro-magnetic simulations which illustrate the qualitative modification of the spin-wave spectrum between the normally saturated and the vortex (cone) states [110]. Here, the dynamic susceptibility tensor $\chi_{i,j}(\boldsymbol{r}, \omega)$

($i,j = x,y,z$) of a Permalloy disk ($L = 50$ nm, $R = 500$ nm) is calculated using a 3D micro-magnetic code [110]. Due to the rotational symmetry of the element, the in-plane susceptibility spectra are expressed using the circular polarization basis resulting in $\chi_{\pm} = 1/2[(\chi_{xx} + \chi_{yy}) \pm i(\chi_{yx} - \chi_{xy})]$. The imaginary part of both quantities are plotted versus the perpendicular field H_z in figure 2.4.

In the saturated state ($H_z > H_s \simeq 9.5$ kOe), the radial modes ($\ell = 0, n$) described in the section 2.2 are seen in the χ_- component. Azimuthal modes ($\ell, n = 0$) are not observed because they do not couple to the homogeneous in-plane microwave excitation field. In the vortex state ($H_z < H_s$), the low frequency gyrotropic mode is identified as $0-$. It has the expected dependence versus field for a $p = +1$ core polarity and couples only to χ_- because of the particular sense of rotation of the core. At higher frequency, several spin wave modes can be seen. They exhibit an opposite dependence with H_z. In contrast to the saturated state, they correspond to azimuthal modes. The magnetization of the vortex is curling in-plane, hence, the in-plane excitation field cannot couple to the radial modes. The azimuthal modes can travel either clockwise or counter-clockwise around the disk, this is the reason why they can be observed both in χ_- and χ_+. Moreover, the modes having indices $l = \pm 1, 2$ are not degenerate in energy.

A particularly interesting observation is the existence of a large gap between the fundamental gyrotropic mode and higher order spin-wave modes in the vortex state (in this example, more than 5 GHz at zero field), in contrast to the saturated case (where this gap is lower than 0.5 GHz). This well isolated fundamental mode makes it an ideal candidate to operate STNOs [33, 35], as the presence of neighboring spin-wave modes in the spectrum is known to affect negatively the coherence of auto-oscillations [88, 111, 112].

2.4. Collective spin-wave modes induced by the dipolar interaction in a pair of magnetic disks

In this section, we introduce the notion of coupled dynamics between neighboring disks interacting through dipolar magnetic fields. Due to the different experimental cases met in this thesis, we will discuss the particularities due to the geometry (vertical vs. lateral arrangement of the disks) and to the ground state (normally saturated vs. vortex) in a first step, by explaining how to evaluate the strength of the magneto-dipolar coupling. In a second step, we will treat the coupled equations of motion from a general point of view in order to describe the basics of the resulting collective dynamics.

2.4.1. Strength of the dynamic magneto-dipolar coupling

The goal here is to evaluate the strength of the dynamic dipolar coupling between adjacent disks. The general expression of the effective demagnetizing stray field produced by the dynamic magnetization of the jth disk projected along the local dynamical magnetization vector inside the ith disk and averaged over its volume is given by

$$h_{i\to j} = \frac{M_s}{\mathcal{N}_j}\langle \overline{\boldsymbol{m}}_j . \widehat{\boldsymbol{G}^{\mathrm{d}}} * \boldsymbol{m}_i \rangle_{V_j} , \tag{2.13}$$

where $\widehat{\boldsymbol{G}^{\mathrm{d}}}$ is the contribution of the demagnetizing interaction of the linear tensor self-adjoint operator introduced in equation (2.2).

The overlap defined in equation (2.13) is maximum for modes having the same wave numbers in each disk [113]. In the following, we will thus only consider the dynamic dipolar coupling between similar spin-wave modes. Hence, $\overline{\boldsymbol{m}}_j$ and $\boldsymbol{m}_i$ correspond to the dynamical magnetization in each of the disks, but they have the same set of mode indices (ℓ, m). Two cases are particularly interesting to us: the uniform mode in the normally saturated state (with spatial profile $J_0(k_{0,0}\rho)$) and the gyrotropic mode in the vortex state (in this case, the spatial profile of the gyrotropic mode defined in reference [103] should be employed).

This dynamical field is an in-plane rotating field that is able to couple to the dynamical part of magnetization in both disks. Its calculation is in general non trivial, but can be derived in some simple cases [114, 41, 115, 116]. Generally, it can be calculated from

the demagnetizing tensor $\widehat{\mathcal{N}}$. In the case of two discs on top of each other, this field is isotropic since $\mathcal{N}_{xx}^{i\to j} = \mathcal{N}_{yy}^{i\to j}$, hence

$$h_{i\to j} = \mathcal{M}_s\{\mathcal{N}_{xx}^{i\to j}\}\,, \tag{2.14}$$

where the curly brackets indicate that the spatial average is weighted by the mode profile. But in the case of two disks placed side by side, the axial symmetry is broken and:

$$h_{i\to j} = \frac{\mathcal{M}_s}{2}\left(\{\mathcal{N}_{xx}^{i\to j}\} + \{\mathcal{N}_{yy}^{i\to j}\}\right)\,. \tag{2.15}$$

Finally, we would like to point out the strong dependence of the dynamic magneto-dipolar coupling on the geometry. Roughly, it indeed scales with the thickness of the magnetic layers L and decays as $1/d^3$, where d is the spacing between magnetic elements.

2.4.2. Coupled equations of motion and collective dynamics

Denoting the spin wave amplitudes in both disks by $c_{1,2}$ and their isolated frequencies by $\omega_{1,2}$, the coupled equations neglecting the damping terms read:

$$\frac{dc_1}{dt} = -i\omega_1 c_1 + i\gamma h_{2\to 1} c_2 \tag{2.16a}$$

$$\frac{dc_2}{dt} = -i\omega_2 c_2 + i\gamma h_{1\to 2} c_1 \tag{2.16b}$$

By diagonalizing this system, the eigenvalues of the coupled frequencies $\omega_{A,B}$ are found to be:

$$\omega_{A,B} = \frac{\omega_1 + \omega_2}{2} \pm \sqrt{\left(\frac{\omega_1 - \omega_2}{2}\right)^2 + \left(\frac{\Omega}{2}\right)^2}\,, \tag{2.17}$$

where the coupling strength is:

$$\Omega^2 = 4\gamma^2 h_{1\to 2} h_{2\to 1}\,. \tag{2.18}$$

The anti-crossing (or avoided crossing) behavior of equation (2.17), shown in figure 2.5 (a), is typical of two oscillators coupled by conservative terms.

The collective eigen-modes are given by the eigen-vectors of the system, and are linear

combinations of the isolated spin-wave modes in each disk:

$$C_A = c_1 + \frac{\omega_1 - \omega_A}{\gamma h_{2\to 1}} c_2 \tag{2.19a}$$

$$C_B = \frac{\omega_2 - \omega_B}{\gamma h_{1\to 2}} c_1 + c_2 \,. \tag{2.19b}$$

The ratio of hybridization is given by

$$\left.\frac{c_i}{c_j}\right|_{\omega_{A,B}} = \left(\frac{(\omega_i - \omega_j) \mp \sqrt{(\omega_i - \omega_j)^2 + \Omega^2}}{\Omega} \right)^{\mp 1} \,. \tag{2.20}$$

In the case of lateral neighboring disks displayed in figure 2.5 (b), the anti-binding mode A with higher energy has $c_i = -c_j$, *i.e.*, a precession with equal weight in both disks and out-of-phase (optical mode), and the binding mode B with lower energy has $c_i = +c_j$ which denotes an in-phase precession (acoustic mode). Due to the reversed sign of the dipolar interaction, the situation is opposite in the case of vertically stacked disks.

To conclude, the dynamic dipolar interaction between neighboring magnetic disks has two main consequences:

1. It renormalizes the eigen-frequencies following equation (2.17).
2. It hybridizes the spin-wave modes, which become delocalized in both magnetic elements (see equation (2.20)).

To experimentally observe these effects, however, the dynamic dipolar coupling Ω has to be large with respect to the mismatch $\omega_2 - \omega_1$ between the isolated (uncoupled) frequencies, but also with respect to the linewidth of the resonance line [100].

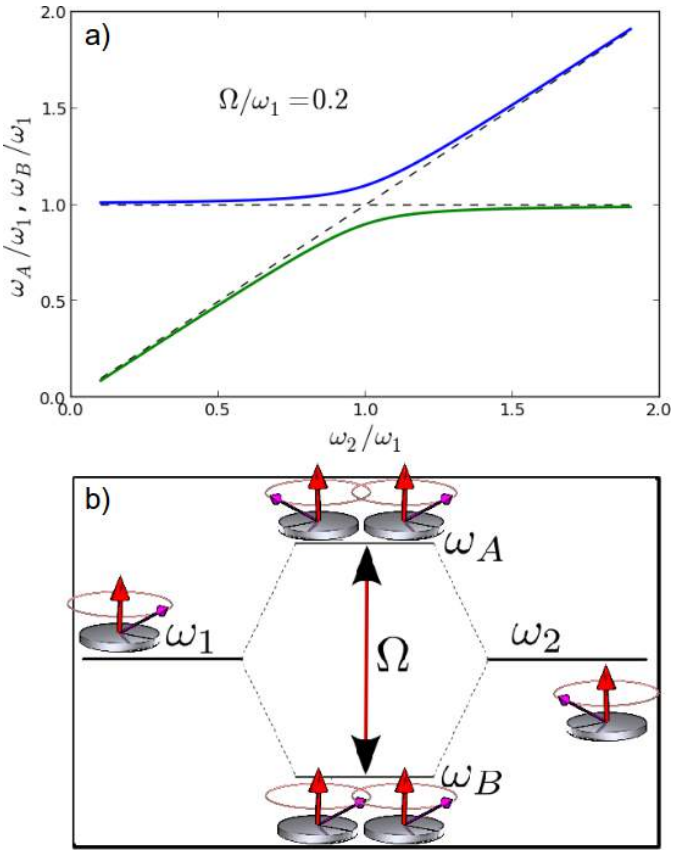

Figure 2.5.: *(a) Eigen-frequencies vs. mismatch between isolated frequencies. (b) Energy level diagram when $\omega_1 = \omega_2$. The magneto-dipolar interaction hybridizes the system in binding and anti-binding coupled modes separated in frequency by the dynamical splitting Ω.*

To summarize, we have presented a general analytical theory which enables to calculate the frequencies of the spin-wave eigen-modes in the linear regime and to classify them according to their symmetry. In a normally magnetized disk, azimuthal and radial indices (ℓ, n) are required to label the spin-wave modes. We have also described the influence of a perpendicular magnetic field on the spin-wave modes in the vortex-state. Finally, we have highlighted that the dynamic dipolar interaction between neighboring magnetic elements hybridizes the spin-wave modes, which become coupled, and renormalizes their eigen-frequencies.

CHAPTER 3

Nonlinear auto-oscillator theory

The purpose of this chapter is to present the formalism for the STNO proposed by A. Slavin and V. Tiberkevich [22]. We start in the first section by giving the basics and the notions of oscillator. Next we give the analytic theory of STNO based on the universal model of nonlinear auto-oscillator. Then, the amplitude and phase fluctuations of this oscillator is discussed and the output power and the generation linewidth expressions are given. Finally we give examples of theoretical and exprimental results for the non-autonomus regime of STNOs.

3.1. Harmonic oscillator : introduction to useful concepts

Before discussing the model of the spin transfer nano-oscillators, we will review the simple example of the oscillator (mass attached to a spring) shown in figure 3.1, to introduce the basic concepts to be used in the next section of this chapter. This section is meant to be educational to show the most simple equations which we can refer to later. Briefly, we will develop the equations of motion of a $free$, $damped$ and $driven$ oscillator. Then we will show a small description of the notion of $self\text{-}sustained$ oscillator.

3.1.1. Free, damped and driven oscillator

An oscillator is a system which produces a desired oscillation and characterized by a periodic output in time domain. The study of the dynamical behavior of an oscillator, is a central issue in physics and mathematics. The spring is a model that allows an easy visualization and understanding of the behavior of an oscillator. Let's consider a single mass attached to a spring and allowed to slide on a horizontal surface (top of figure 3.1). First, we will ignore any damping forces acting on the mass. We can describe the state of our system at any time in terms of the displacement x(t) of the mass. According to Newton's laws of motion, in this case the x(t) has to obey the following dynamical law:

$$\ddot{x} + \omega_0^2 x = 0\,. \tag{3.1}$$

It is a linear second order differential equation describing the motion of the mass. Here ω_0=$\sqrt{\frac{k}{m}}$ is known as the resonance frequency of the mass. The general solution of equation 3.1 is :

$$x_f(t) = A\sin(\omega_0 t + \phi)\,. \tag{3.2}$$

This solution is characterized by an amplitude A, an angular frequency ω_0 (period of oscillation T=$2\pi\sqrt{\frac{m}{k}}$), and a phase shift of ϕ radians. A graph for this solution is shown in figure 3.1 (a). In addition to x(t), we have plotted (x, $\dot{x}$) the phase portrait of the system. This variable is important to describe the state of the oscillator where it displays the qualitative concepts of the trajectory. The point on the phase portrait is called a phase point and is represented in polar coordinates by A and ϕ. Figure 3.1 (b) shows that the evolution of the system is a closed trajectory which is called a limit cycle.

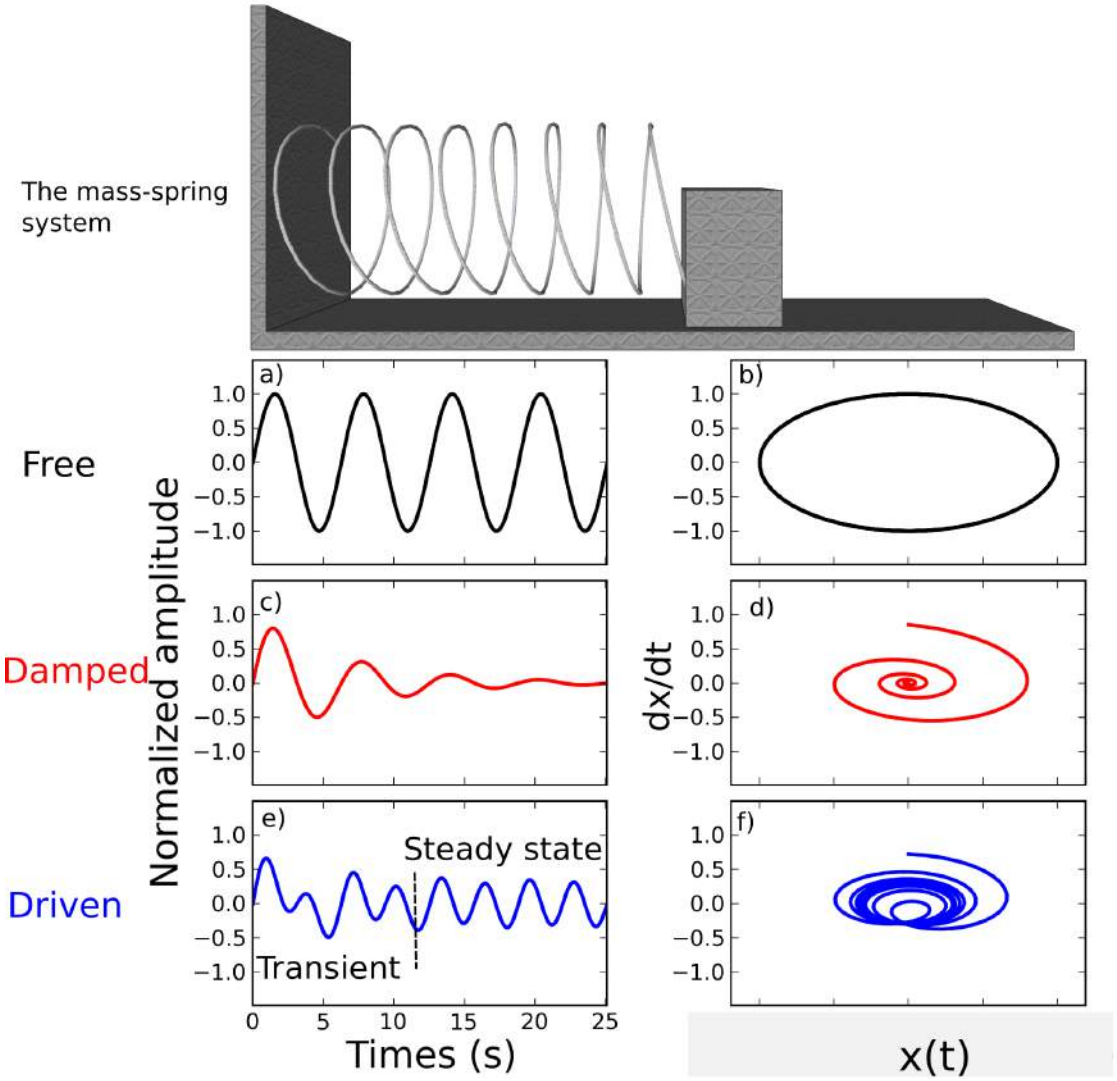

Figure 3.1.: *(a), (c) and (e) Time series for a free, damped and driven harmonic oscillator respectively. (b), (d) and (f) phase portrait of free, damped and driven oscillator. We note here that the initial behavior of a driven oscillator depends on the initial conditions and the nature of the driving force.*

We are going now to introduce a real case where the system is dissipative and thus undergoes a loss in energy. According to the previous example, we will now take into account the presence of friction or some other dissipative effect. The dissipation is an effect which opposes to the motion of the mass. So, considering the simplest form of damping, i.e loss that is proportional to $\dot{x}$ (like friction force). Equation 3.1 becomes:

$$\ddot{x} + 2\lambda\dot{x} + \omega_0^2 x = 0\,, \tag{3.3}$$

where λ is a positive parameter that measures the intensity of the dissipation. The solution of this equation is written as:

$$x_d(t) = A e^{-\lambda t}\cos\left(\omega_1 t - \phi\right). \tag{3.4}$$

With $\omega_0 > \lambda$ and $\omega_1 = \sqrt{\omega_0^2 - \lambda^2}$. We conclude that the effect of a small amount of damping (λ) on a system which exhibits simple harmonic oscillation about a stable equilibrium state is to reduce the angular frequency of the oscillation from its undamped value ω_0 to ω_1, and to reduce the amplitude of the oscillation exponentially at the rate λ. This type of time evolution is illustrated in figure 3.1 (c). In particular, if the damping is sufficiently large ($\lambda \geq \omega_0$), then the system does not oscillate. Figure 3.1 (d) shows that the trajectory of the phase portrait is a spiral along which the point of functioning moves in time until reaching zero.

To study the case of a damped oscillator affected by an external periodic force, let's consider the same system investigated before with attaching a moving piston to the end of the spring. The piston executes simple harmonic oscillation of angular frequency ω_e and amplitude A_e. Here, x(t) is described by the linear second order differential equation which is expressed as follows:

$$\ddot{x} + 2\lambda\dot{x} + \omega_0^2 x = A_e \sin\left(\omega_e t\right), \tag{3.5}$$

where $A_e \sin\left(\omega_e t\right)$ is the external periodic force. The general solution is simply demonstrated graphically in figures 3.1 (e) and (f) and denoted analytically as:

$$x(t) = x_d(t) + x_A(\omega_e)\cos\left(\omega_e t + \beta\right), \tag{3.6}$$

where A(ω_e) and β are respectively the amplitude and the phase shift with respect to the external force such that:

$$A(\omega_e) = \frac{A_e}{\sqrt{(\omega_0^2 - \omega_e^2)^2 + (2\lambda\omega_e)^2)}}\,, \tag{3.7}$$

$$\beta = \tan^{-1}\left(\frac{2\lambda\,\omega_e}{\omega_0^2 - \omega_e^2}\right). \tag{3.8}$$

The behavior of x(t) presented in figure 3.1 (e) shows that for small t there is a transient behavior due to the presence of $x_d(t)$ in equation 3.6 and after, there is a periodic oscillation (stationary behavior because t is large), and the phase presented in figure 3.1 (f) shows that after a transitory evolution, the system settles down in a motion on cycle similar to that presented in figure 3.1 (b).

3.1.2. Self-sustained oscillator

A self-sustained oscillator has the capacity to oscillate forever if we isolate it from the environment. This oscillator is different from the forced oscillator whose amplitude and period are determined by the characteristics of the external source. In contrary to the free oscillator, the trajectory in the phase plane of a self-sustained oscillator is independent of the initial conditions (see figure 3.2). The oscillator reaches the limit cycle from the initial position. In figure 3.2 (a), dissipative damping (called D_+) restores the limit cycle by reducing the trajectory towards the limit cycle. Here the oscillation varies the amplitude slowly due to the dissipated energy. In contrary, in figure 3.2 (b) anti-damping (called D_-) restores the limit cycle and extends the trajectory. Here, the amplitude of oscillations is larger, due to the extra energy taken from the source. We can conclude that the equilibrium between these two dissipative terms determines the amplitude of the oscillation as illustrated in figure 3.2 (c). In the case of zero amplitude, there is no dissipated and supplied energy taken from the source, thus the two functions pass through the origin. The amplitude A_0 of the steady oscillations is determined by the intersection of the two functions where the energy supplied compensates the dissipated energy.

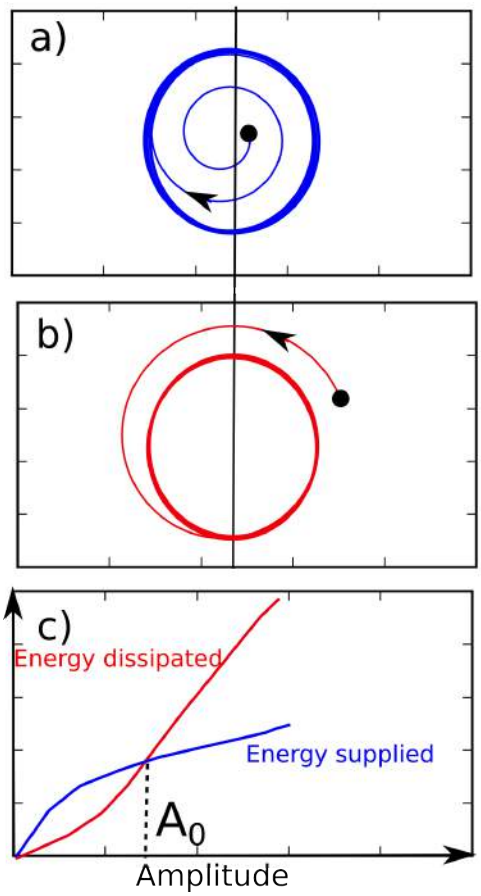

Figure 3.2.: *(a) and (b) limit cycles for self-subtained oscillations. The initial states are marked with a dot. (a) correspond for the initial condition $A(t=0) < A_O$ and (b) $A(t=0) > A_O$ (c) The intersection between the dissipative (V_+) and supplied (V_-) determines the amplitude A_0 of the oscillations*

To summarize, in this section we have introduced the notations and basic concepts of an oscillator. We have included the notions of equilibra, dissipation, forcing, self-substained, limit cycle, and phase portrait. Theses notations will be used later.

3.2. Non-linear auto-oscillator model

We present in this section the nonlinear auto-oscillator (NAO) model that is formulated from equation of motion of magnetization which is presented in chapter 1. This model is based on the classical quasi-Hamiltonian formalism for spin wave [22] and it consider that only a $single$ mode is excited at the auto-oscillation threshold. A similar approch of the case of multi-mode will be discussed in section 3.5.

It can be shown that the dynamics of the dimensionless complex amplitude c (given by $c = \frac{M_x - iM_y}{\sqrt{2M_s(M_s+M_z)}}$ where M_s is the length of the magnetization saturation vector in the free magnetic layer, and M_x, M_y and M_z, are the projection of this vector on the equilibrium magnetization direction x, y and z respectively) which describes magnetization precession in a STNO, is given by the following universal form:

$$\frac{\partial c}{\partial t} + i\omega(|c|^2)c + \Gamma_+(|c|^2)c - \Gamma_-(|c|^2)c = 0\,. \tag{3.9}$$

To recall the different terms used in this equation:

- c: the complex amplitude of auto-oscillations with the power and phase are denoted $p = |c|^2$ and $\phi = \arg(c)$ respectively.
- $\omega(p)$: is the resonance frequency.
- $\Gamma_+(p)$: is the damping rate for the energy dissipation.
- $\Gamma_-(p)$: is the effective negative damping introduced into the system by the spin-polarized current.

For a simple geometry, when the external magnetic field is applied along the normal of the free layer, the dependences of the frequency $\omega(p)$ and damping rates $\Gamma_{\pm}(p)$ on the power p can be expressed as a first order series expansion:

$$\omega(p) = \omega_0 + N p \tag{3.10a}$$

$$\Gamma_+(p) = \Gamma_G(1 + Qp + Q'p^2) \tag{3.10b}$$

$$\Gamma_-(p) = \sigma_0 I (1 - p)\,, \tag{3.10c}$$

where $\omega_0=\gamma(H_{ext} - 4\pi M_s)$, N is the coefficient of the nonlinear frequency shift for the normally magnetized layer given by $N = 2\omega_M = 2\pi\gamma M_s$, $\Gamma_G = \alpha_G\omega_0$ (Gilbert damping), $Q = 2\omega_M/\omega_0$ and $Q' = -2\omega_M/\omega_0$ represent the nonlinearity of the damping.

The form of equation (3.9) makes easy the analysis and the interpretations of the dynamics of magnetization. So, we will use this model along the manuscript and we will start by seeking the solution of this equation.

Stationary regime : The solutions of equation 3.9 is given by the form: $c = p\exp(i\phi)$. Then, we will separate the real and imaginary parts to obtain a system of two equations for the power (p) and the phase (ϕ):

$$\frac{\partial p}{\partial t} + 2[\Gamma_+(p) - \Gamma_-(p)]p = 0\,, \tag{3.11}$$

$$\frac{\partial \phi}{\partial t} + \omega(p) = 0\,. \tag{3.12}$$

Two stationary solutions ($dp/dt = 0$) can be obtained from equation 3.11. The first stationary solution corresponds to $p = 0$ for which the linearization of equation 3.11 yields this solution:

$$\frac{\partial p}{\partial t} + 2[\Gamma_+(0) - \Gamma_-(0)]p = 0\,. \tag{3.13}$$

Based on this equation, it's clear that when $\Gamma_+(0) > \Gamma_-(0)$, the solution $p = 0$ is stable. Then, the condition $\Gamma_+(0) = \Gamma_-(0)$ gives the critical current I_{th} to obtain auto-oscillation.

From equations 3.10b and 3.10c, the expression of the critical current is given by (see equation 1.9) :

$$I_{th} = \frac{\Gamma_G}{\sigma_0} . \tag{3.14}$$

In order to establish the second type of stationary solution when $p = p_0$, the damping terms should cancel exactly at $p = p_0$ such that $\Gamma_+(p) = \Gamma_-(p_0)$. This means that the energy lost by damping ($\Gamma_+(p_0)$) should be compensated by the energy supplied ($\Gamma_-(p_0)$) via spin transfer. Using equations 3.10b and 3.10c and with super-criticality $\xi = I/I_{th}$, one can obtain the stationary power (p_0) for the STNO:

$$p_0 = \frac{\xi - 1}{\xi + Q} . \tag{3.15}$$

Two different regimes can be defined for the oscillator: the sub-critical regime ($I < I_{th}$) for which the system does not oscillate and the supercritical regime ($I > I_{th}$) for which the spin torque driven self-sustained oscillations exist. Then, for small power deviation $\delta p = p - p_0$, we can get a damping rate $\Gamma_p = G_+ - G_- = (\xi - 1)\Gamma_G$ where ($G_+ = d\Gamma_+/dp$ and $G_- = d\Gamma_-/dp$). Morever, from equation 3.15 , it is possible to describe the frequency, damping and spin transfer term as function of the current as follows:

$$\omega = \omega_0 + N \frac{\xi - 1}{\xi - Q} \tag{3.16a}$$

$$\Gamma_-(p) = \sigma_0 I \frac{Q + 1}{\xi + Q} \tag{3.16b}$$

$$\Gamma_+(p) = \Gamma_G \frac{\xi(1 + Q)}{\xi + Q} , \tag{3.16c}$$

Using the expression of the frequency ω, we can also find the relation between the agility in the current, which is defined by $d\omega/dI$ and the nonlinearity factor N :

$$\frac{d\omega}{dI} = \frac{N}{I} \frac{1 + Q}{(\xi + Q)^2} . \tag{3.17}$$

The non-linear frequency shift coefficient for STNO strongly depends on the direction of the external magnetic field and can be negative or positive. It is possible to introduce the

normalized dimensionless nonlinear frequency shift ν which characterizes the relative influence of frequency shift $\mathcal{N}$ in comparison on damping rate and its can given as:

$$\nu = \frac{\mathcal{N}}{\Gamma_p} p_0 \,, \tag{3.18}$$

$\nu >> 1$ for STNOs which make them unique compared to other oscillators. The NAO model has many advantages, because it has transformed the LLGS equation into a one simple equation. So, now we can describe the autonomous regime (i.e: the expression of frequency, damping, ...). In the next section, we will describe the influence of the thermal noise in the NAO model which leads to an amplitude and phase fluctuation consequence to $linewidth$ broadening.

3.3. The noise in the NAO Theory

Beside describing the NAO model without external source in section 3.2 , a theory of non-autonomous dynamics of a STNO in the presence of thermal noise was developed. This theory is based on the nonlinear oscillator equation for the complex amplitude c(t) of a spin wave exited by spin current. When a force $f(t)$ acts on the STNO, equation 3.9 becomes:

$$\frac{\partial c}{\partial t} + i\omega(|\,c\,|^2)c + \Gamma_+(|\,c\,|^2)c - \Gamma_-(|\,c\,|^2)c = f(t)\,. \tag{3.19}$$

It should be noted here that when $f(t)$ is due to a periodic external source, the model describes the synchronization or modulation [90] of STNO to an external source and we will present this formalism later. In the case of the action of thermal noise, the function f(t) is a stochastic force. Before we discuss the contribution of phase and amplitude fluctuations to the emitted power and generation linewidth, we will first discuss the origin of these fluctuations.

3.3.1. Amplitude and phase fluctuations

Due to the small size of an STNO, the thermal fluctuations acting along the trajectory of the oscillation, cause a spread in the time it takes to complete every orbit by making

the magnetization precession slower or faster. The phase of the movement of oscillation was defined by the variable $\phi(t)$. The phase fluctuation is $\phi(t) = \delta\phi(t) + \phi_0$, where $\delta\phi(t)$ is a variable random phase. In order to see clearly how phase fluctuations lead to a contribution of the linewidth, let's consider an example of an ensemble of N identical oscillators [117] (with this example we will try to elucidate the role of phase fluctuations). At t=0, all the oscillators are assumed to be at the same phase and rotate on the limit cycle (see figure 3.3 (a)). In this case, the time domain signal from the ensemble is identical at t=0. Then due to the fluctuation along the direction of the limit cycle, the signals becomes incoherent (see figure 3.3 b). Finally, based on the evolution of the probability distribution of the phase p(ϕ,t) with time, we can see that all oscillators have the same initial distribution delta function. As times goes, all the oscillators start to have a different phase, so the probability distribution spreads out (figure 3.3 c). The width of p is proportional to the phase diffusion constant D which indicates how the phase diffusion accurs.

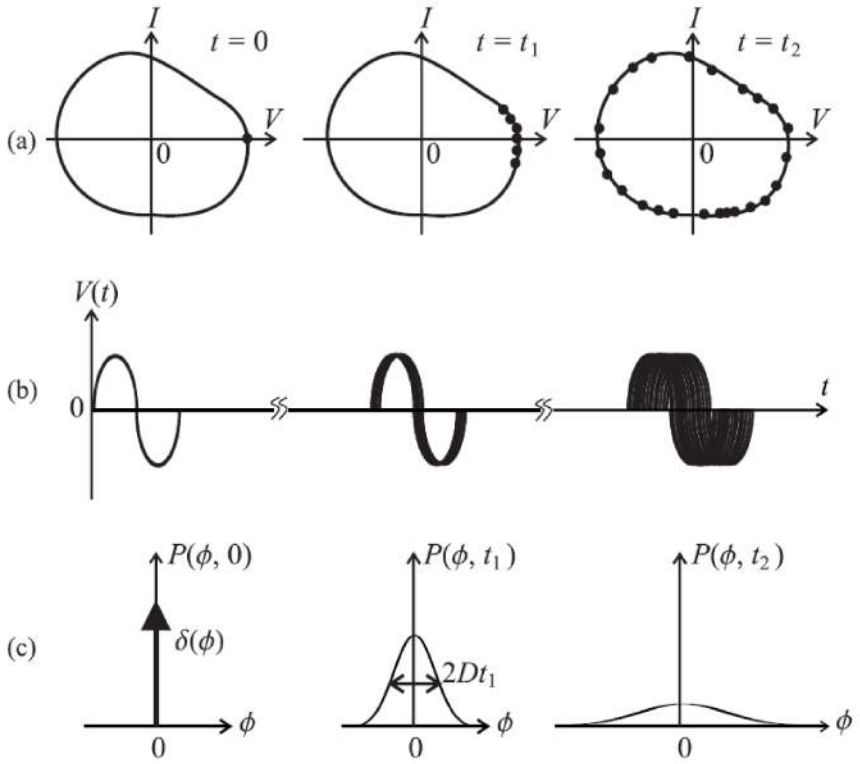

Figure 3.3.: *Figure From [117]: (a) limit cycle (b) Time domain signal of any one oscillator (c) Probability distribution of the phase.*

In addition to the phase noise, the amplitude of the oscillation is affected by the thermal

fluctuation. Here the later act perpendicular to the trajectory of the oscillation which lead to a fluctuation on amplitude.

3.3.2. Power generated by a STNO

We have presented in details the meaning of amplitude and phase fluctuation. Now the goal is to solve equation 3.19 in order to derive the expression of the microwave power generated by the STNO in the presence of thermal noise. For this purpose we can consider that the function $f(t)$ which describes the noise caused by temperature is a stochastic white Gaussian process [118] with the correlator:

$$\langle f(t)f^*(t')\rangle = 2D(p)\delta(t-t')\,, \tag{3.20}$$

Where $D(p) = \Gamma_+(p)\eta(p)$ is the diffusion coefficient constant that characterizes the noise amplitude of the oscillator with power p, $\eta(p) = \gamma k_B T/V_{eff}M_0\omega(p)$ is the effective noise power which depends on the effective volume V_{eff} of the ferromagnetic material involved in the oscillation. Note that equation 3.19 is nonlinear and stochastic and thus, this equation is difficult to solve. After writing the corresponding Fokker-Planck equation, we come down to a linear and deterministic problem, consequently simple to solve. The system is described by a function $\mathcal{P}(t,p,\phi)$ which gives the probability of finding the system with state (p,ϕ) at time t. The function that describes the system 3.19 is a solution of [119] :

$$\frac{\partial\mathcal{P}}{\partial t} = \frac{\partial}{\partial p}\left[2p(\Gamma_+ - \Gamma_-)\mathcal{P}\right] + \omega\frac{\partial\mathcal{P}}{\partial\phi} + \frac{\partial}{\partial p}\left(2pD\frac{\partial\mathcal{P}}{\partial p}\right) + \frac{\partial}{\partial\phi}\left(\frac{D}{2p}\frac{\partial\mathcal{P}}{\partial\phi}\right). \tag{3.21}$$

To calculate the power in the presence of thermal fluctuations, we can limit to the stationary case. The stationary solution is independent of the phase ϕ. Now, we provide the analytic expression of the power distribution going from thermal equilibrium as follows:

$$\mathcal{P}_0(p) = \mathcal{N}_0\exp\left[-\int_0^p\left(\frac{\Gamma_+(p') - \Gamma_-(p')}{D(p')}\right)\mathrm{d}p'\right]. \tag{3.22}$$

With $\mathcal{N}_0$ is the normalization constant which depends on the normalization condition of the distribution. The mean power ($\bar{p} = \int_0^\infty \mathrm{d}p\mathcal{P}_0 p$) has two expressions, one below the threshold current I_{th}:

$$\bar{p}^{<} = \eta(0)\frac{I_{th}}{I_{th} - I}, \tag{3.23}$$

and the other above I_{th}:

$$\bar{p}^{>} = p_0 = \frac{I - I_{th}}{I - QI_{th}}. \tag{3.24}$$

In this regime, $\mathcal{P}_0$ has a maximum power at $p = p_0$. Then an approximate expression for $\mathcal{P}_0$ can be given by expanding the integrand in equation 3.22 in a Taylor series, $\mathcal{P}_0(p) \sim exp\left[-(p-p_0)^2/2\Delta p^2\right]$ with $\Delta p^2 = \eta(p_0)(1+Q)\bar{\xi}/(\bar{\xi}+Q)^2$ is the level of power fluctuation of STNO. This formulation leads finally to what is shown in figure 3.4. As one can see in the case of $\bar{\xi}$=0, the thermal noise makes the mean power non-zero. Based on our measurements, that will be shown in chapter 6, we will compare the mean power experimentally to the one predicted by the NAO model and found a good agreement with the theory. In addition from the dependence of the inverse of the power on the bias current in the sub-critical (equation 3.23) regime we will determine the critical current from our experimental work.

3.3.3. Generation linewidth of an STNO

Another important parameter characterizing a STNO is the oscillator's full with at half maximum (FWHM) linewidth of the power spectra. As we mentioned before, the main contribution to the linewidth of generation comes from the thermal fluctuations that perturb the amplitude and phase of the orbit. For aplications it is important that the microwave signal has a frequency spectrum with a narrow linewidth at room temperature. As a result, understanding the physical process that affect the linewidth has generated considerable interest, both theoretically and experimentally. For example, there have been several experiments done to study the linewidth dependence on temperature [88] and magnetic field [120, 12, 121, 122, 123]

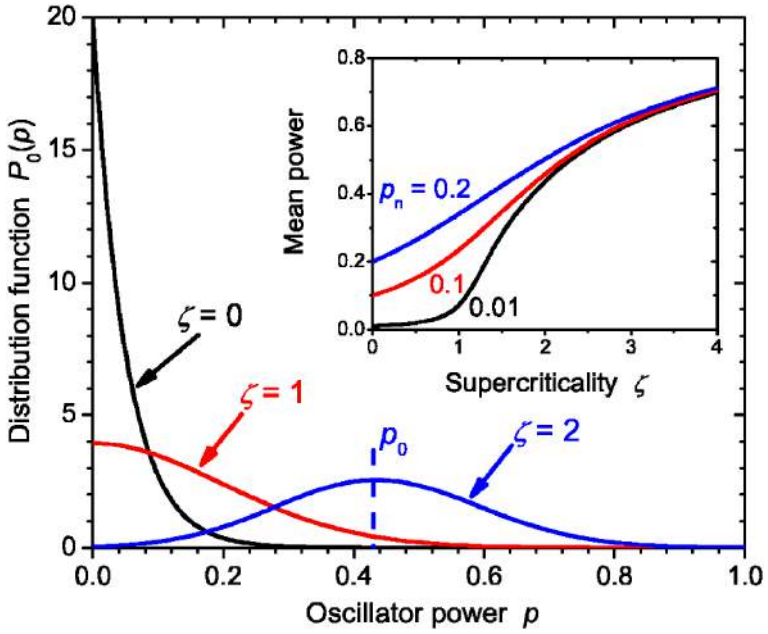

Figure 3.4.: *Figure From [119]: Probability distribution $\mathcal{P}_0$ for different $\bar{\xi}$ with Q=0.03 and η=0.05. Inset: dependence of $\bar{p}$ for different noise level $\bar{\xi}$ values.*

How to calculate linewidth in NAO model? The value of linewidth generated depends on the properties of the specific STNO. Its was first calculated in the seminal work of Kim et al [23]. Here we present the derivation of the general formula for the STNO linewidth. This formula relates the linewidth to a nonlinear factor ν, and its calculation is based on the NAO theory. Indeed the power spectrum of an auto-oscillator in the presence of thermal noise is given by:

$$S(\omega) = \int \mathcal{K}(t) e^{i\omega t} dt \,. \tag{3.25}$$

Where $\mathcal{K}(t)$ is the correlation function can be evaluated as:

$$\mathcal{K}(t) = \langle c(t) c^*(t') \rangle \,. \tag{3.26}$$

In the regime where phase fluctuations dominate, the correlation function corresponding to phase noise contribution can be written as:

$$\mathcal{K}(t) = p_0 \langle e^{i[\phi(t)-\phi(0)]} \rangle = p_0 e^{i\langle \phi(t)-\phi(0) \rangle} \exp[-\Delta\phi^2(t)/2] \,. \tag{3.27}$$

Where $\Delta\phi^2(t)$ is the phase variance and in the case of a nonlinear (or non-isochronous) auto-oscillator its given by:

$$\Delta\phi^2(t) = \langle\phi^2(t)\rangle - [\langle\phi(t)\rangle]^2 = 2\pi\Delta F_0\left[(1+\nu^2)t + \nu^2\frac{1-e^{-2\Gamma_p t}}{2\Gamma_p}\right], \tag{3.28}$$

where ΔF_0 is the linewidth of the main frequency in an linear (or isochronous) [1] auto-oscillator (in the absence of frequency nonlinearity). $\Delta F_0 = \frac{k_B T}{E_s}\frac{\Gamma_+}{2\pi}$ where k_B is the Boltzmann constant, T is the temperature, E_s is the energy stored in the auto-oscillation and Γ_+ is the natural energy dissipation rate. Now from equation 3.28 it is possible to calculate the linewidth of the non-linear auto-oscillator in two different regimes, depending on temperature T, the generation linewidth $\Delta\omega$ and the the amplitude fluctuations Γ_p:

- $\Delta\omega << \Gamma_p$: in this case the exponential factor in the variance (equation 3.28) can be neglected, then the linewidth becomes:

$$\Delta F = \frac{k_B T}{E_s}\frac{\Gamma_+}{2\pi}(1+\nu^2), \tag{3.29}$$

- $\Delta\omega >> \Gamma_p$ in this case the exponential factor in the variance (equation 3.28) can be developed into Taylor series, then the linewidth becomes:

$$\Delta F = \frac{|\nu|}{2\pi}\sqrt{\Gamma_+\Gamma_P}\sqrt{\frac{k_B T}{E_s}}. \tag{3.30}$$

It is clear that the linewidth scales with temperature and nonlinearity, as the temperature increases, the ratio of the noise energy increases leading to increase of linewidth. In particular, one can see in expression 7.4 that the nonlinear frequency shift coefficient ν, leads to the increase of the linewidth by factor of $(1+\nu^2)$. For linear auto-oscillator, where $\nu = 0$, this increase is negligible. In this thesis we will use the first approximate expression for the non-linear auto-oscillator linewidth, since $\Delta\omega << \Gamma_p$ in our oscillator. Moreover, the nanoscale size of STNOs, although it confers to these devices high agility, broadens substantially the spectral purity since the linewidth depends inversely on

[1] In an isochronous auto-oscillator, the auto-oscillation frequency f does not depend on the oscillation amplitude.

E_s, which is proportionnal to the sample volume. This is an intrinisc compromise. Synchronization provides a mean to improve the spectral purity by increasing E_s.

3.4. Phase-locking and mutual synchronization

A formalism for STNO in terms of nonlinear dynamical equation in the presence of external source or by synchronizing two STNOs were also described within the NAO model. In this section we summarize results from literature that used the NAO theory in order to provide the experimental results in phase-locking and synchronizing STNOs.

Phase-locking to an external source

We mention here the injection locking experiments of STNOs to an external signal. Indeed, these experiments are described by the NAO model where in the equation 3.19, f(t) is a term represents an external harmonic signal ($f(t) = f_{source}e^{-i\omega_{source}t}$). Starting from this equation, and following Adler's formalism [124], it is possible to calculated the relevant uniformly rotating phase for the auto-oscillator $\tilde{\Phi}$, that depends on the non-linearity ν ($\tilde{\Phi} = \Phi - \nu\frac{\delta p}{2p_0}$), to end up with the equation driving the phase dynamics of the spin transfer oscillator in the presence of noise:

$$\frac{\partial\tilde{\Phi}}{\partial t} + \omega_{oscillator} = -\frac{\sqrt{1+\nu^2}\mid f_{source}\mid}{\sqrt{p_0}}\sin\left(\omega_{source}t + \tilde{\Phi} - \psi_{source} + \arctan(\nu)\right). \quad (3.31)$$

Where $\tilde{\Phi}$ is the phase difference between the oscillator and the source, $\mid f_{source}\mid$ is the real amplitude of the external source, and $\psi_{source} = \arg(f_{source})$ is the initial phase of the external source. The oscillator is synchronized if $\tilde{\Phi}$ is constant. Then the phase-locking bandwidth Δ is given by [97]:

$$\Delta = \sqrt{1+\nu^2}\frac{\mid f_{source}\mid}{\sqrt{p_0}}. \quad (3.32)$$

One can see, that the nonlinearity of the STNO leads to the increases of the phase-locking range by ($\sqrt{1+\nu^2}$) times. We note here that the nonlinearity isn't required to phase

lock an oscillator to an external source. From equation 3.32 it's clear that for linear oscillator where $\nu = 0$ the phase locking bandwidth of this linear oscillator has the form $\Delta = \mid f_{source} \mid / \sqrt{\mathcal{P}_0}$.

The first experimental studies of phase-locking to external source was performed in [94] and [90]. Since in this section we present experiments that have used NAO model, we show in figure 3.5 an experimental result (black squares) together with the theoretical curves giving the frequency mismatch ($f_{forced} - f_{source}$) versus the detuning ($f_{free} - f_{source}$) between the oscillator and the source for an oscillator with a finite linewidth of 17 MHz. It appears that the locking range, i.e. the frequency range where the mismatch is zero, can be fitted and it appears also that the phase locking is small compared to the case when the linewidth is zero, because the fluctuating phase (i.e. a large linewidth) is detrimental for synchronization (this proves the important role played by the noise that induces fluctuations in the phase dynamics of STNOs and therefore weakens the synchronization, we will come back on this point in section 7.3.4 of chapter 7). We have also shown in figure 3.5 (b) the evolution of the phase locking with the amplitude of the external rf signal. One can see that the frequency bandwidth Δ increases with the amplitude of external source I_{rf} increase, this behavior is expected from expression 3.32. The quantitative agreement between experimental results and theoretical prediction demonstrates the validity of the analytical approach which is based on the NAO model.

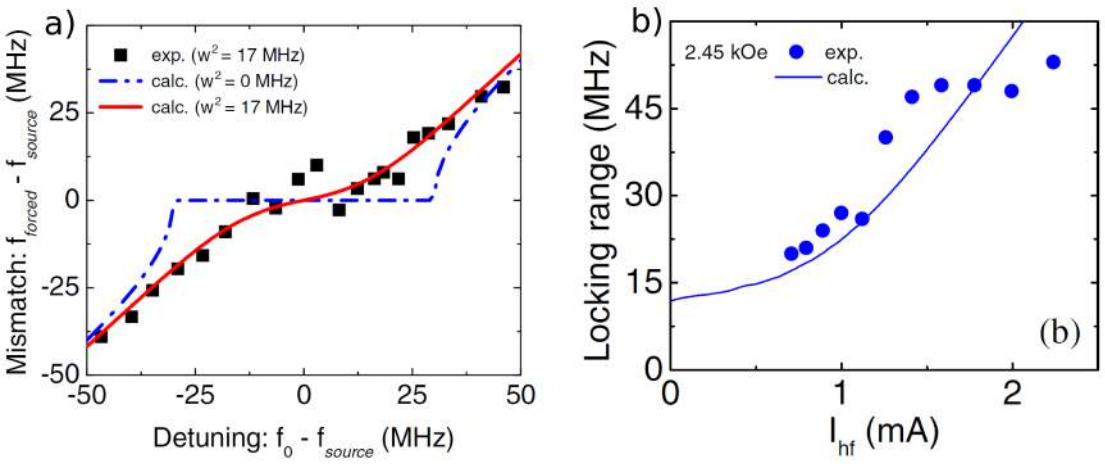

Figure 3.5.: *(a) Frequency mismatch versus frequency detuning. The black dots are the experimental data. The lines are a calculation for zero linewidth (blue) and 17 MHz corresponding to the experimental value (red). (b) locking range as a function of the external amplitude current (blue dots), plain blue line is fit to the experimental data. From [90].*

Another example of experimental results to be mentioned is the injection locking experiment by Bonetti [125] where the locking range has been measured as a function of out of plane magnetic field angle in nano-contact STNOs geometries. It was shown in this work that the angular dependence of the locking strength (or phase locking interval), can be explained by using the NAO model. Indeed, as already mentionned in section 3.2 that the nonlinear frequency $\mathcal{N}$ for STNO strongly depends on the direction of the external magnetic field (see figure 6.1 of chapter 6). Since $\nu = \mathcal{N}/(G_+ - G_-)$ then, it is understandable why the phase locking range Δ depends on the magnetization field angle of the oscillation layer (see figure 3.6).

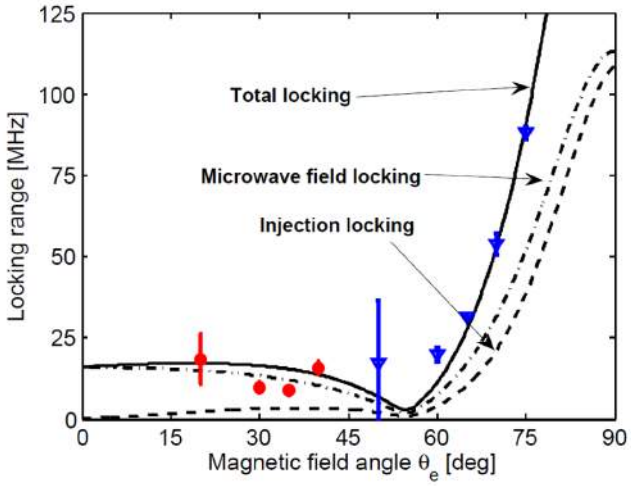

Figure 3.6.: *locking range versus out of plane field angle. the dots represented the experimental Data. The lines are calculated from the NAO model. The dependence of the locking range versus the out of plane field angle is explained by the variation of the nonlinear frequency shift $\mathcal{N}$ with the external magnetic field. From [125]*

Mutual synchronization of two oscillators

Besides injection locking experiments to an external source, the spin-wave formalism of the NAO theory explains as well the mutual synchronization. Indeed, the equations for the complex precession amplitudes c_j $(j = 1, 2)$ in two generating coupling STNOs

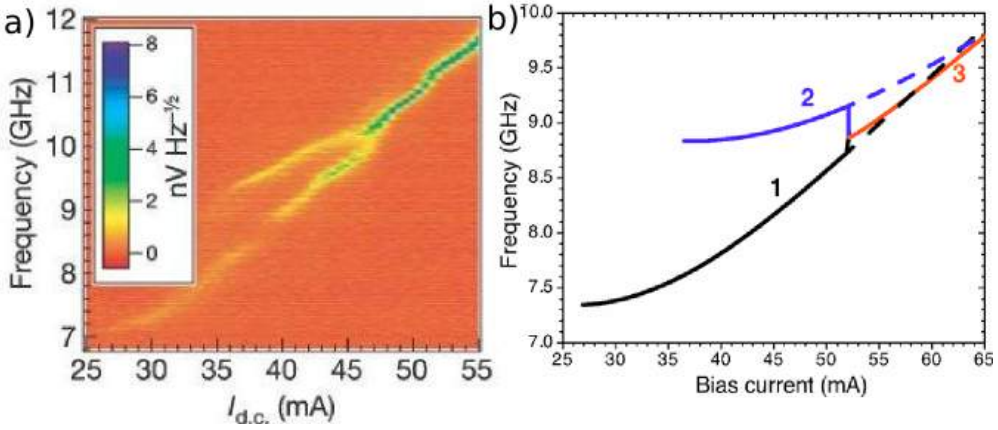

Figure 3.7.: *(a) Power spectra observed when increasing the bias DC current to the structure composed of two nano-contacts [28]. (b) Theoretical model which use the NAO theory from [126]*

can be written using the formalism of equation 3.9 by introducing a coupling factor $\Omega_{j,k}$ such that [126]:

$$\frac{\partial c_j}{\partial t} + i\omega_j(\mid c_j \mid^2)c_j + \Gamma_+(\mid c_j \mid^2)c_j - \Gamma_-(\mid c_j \mid^2)c_j = \Omega_{j,k}e^{i\beta_{j,k}}c_k \,. \tag{3.33}$$

Where $\Omega_{j,k}$ describe the strength of the coupling between the oscillators, and $\beta_{j,k}$ describe the coupling phases between the jth and kth oscillator. Theses quantities depend on several parameters according to the nature of the coupling between oscillator. For example, they depend on the distance between the oscillators, and on the orientation, amplitude of the external magnetic field in the case of dipolar coupling.

In particular, it was predicted theoretically that the locking range Δ_{syn} for two identical oscillators with different frequencies depends on the nonlinearity of the oscillators ν and on the coupling phase β as [22]:

$$\Delta_{syn} = 2\Omega\sqrt{1+\nu^2}\mid cos(\beta - \arctan(\nu))\mid \,. \tag{3.34}$$

For comparison to the theoretical model with experiment, figure 3.7 (a) shows an example of the mutual phase-locking of two spin-torque oscillators and figure 3.7 (b) shows the solution of the theoretical equation 3.33. It is clear, that the oscillator mutual synchronization theory gives a reasonably good qualitative description of the experiment.

3.5. Multi-mode oscillator

Usually, only one spin wave mode is excited by the spin-polarized current in STNO [2]. Then the NAO model describe several experiments among them [12, 111, 87, 90, 28, 27, 42, 123]. However, recent experiments have shown STNOs multi-mode generation [127, 128, 129, 130, 131]. In STNOs exhibiting more than one mode, it is very important to know if there are interactions between these modes. The distinction between intra-mode coupling (different modes of the same layer) and inter-mode coupling (modes of different layers) can also be significant. This is why a general multi-mode theory is needed to describe the dynamics in STNO in the presence of two or more modes, and describe the nature and the physical origin of the coupling between theses modes [127, 130, 132, 133, 134, 135]. In nano-contact MTJ STNO, Muduli et al. [128] have shown that the mode generated by this device can exhibit jumbs between two and three frequencies when either current or temperature is varied. By extending the NAO theory, and taking into account the action of thermal noise, Slobodianiuk et al. [135] have shown that two-mode generation is possible to be described analytically. Indeed, we have already mentioned that the magnetization dynamics in STNO's of a $single$ spin wave mode excited by the bias current can be described by the dimensionless complex c which related to the mode power. Now for $double$ mode, the equation of motion for the amplitude c_i $(i = 0, 1)$, whereby the thermal noise is taken into account can be described as:

$$\frac{\partial c_0}{\partial t} + i\omega_0(c_0, c_1)c_0 + \Gamma_0(c_0, c_1)c_0 = f_0(t) \tag{3.35a}$$

$$\frac{\partial c_1}{\partial t} + i\omega_1(c_0, c_1)c_1 + \Gamma_1(c_0, c_1)c_1 = f_1(t)\,. \tag{3.35b}$$

Where the frequency ω_i and the action of the spin-polarized current $\Gamma_i = \Gamma_i^+ - \Gamma_i^-$ are nonlinear functions of the spin wave power p_i. $f_i(t)$ is the random white Gaussian process that describes the influence of the thermal noise.

[2] This effect is a direct consequence of the nature of the STT process, which is stimulated emission. Stimulated emission efficiency is proportionnal to magnon occupation of a particular eigen-mode. Thus the first mode that goes unstable has the highest probability to couple to the dc source of angular momentum in the STT process. This is similar to the process that leads to laser.

Then the mean-mode generation power p_i is calculated as (see [135] for detailed calculation):

$$\bar{p_0} = \int_0^\infty \int_0^\infty p_0 \mathcal{P}(p_0, p_1) \mathrm{d}p_0 \mathrm{d}p_1 \tag{3.36a}$$

$$\bar{p_1} = \int_0^\infty \int_0^\infty p_1 \mathcal{P}(p_0, p_1) \mathrm{d}p_0 \mathrm{d}p_1 \, . \tag{3.36b}$$

Where $\mathcal{P}(p_0, p_2)$ is the probability distribution function. The results of calculations performed using equations 3.36b are presented in figure 3.8. Here the integrals are calculated numerically for a value of χ (constant proportional to the temperature in the system) of 0.2 and 1.2. As one can see, in the case of $\chi = 0.2$ which correspond to a small power of thermal noise, the dependence of the mean power mode c_0 versus supercriticality ξ does not change compared to the solution without thermal noise (black dashed line). In this case the second mode power which presented in blue is very small. Then, by increasing χ the thermal noise promotes the oscillation of the second mode.

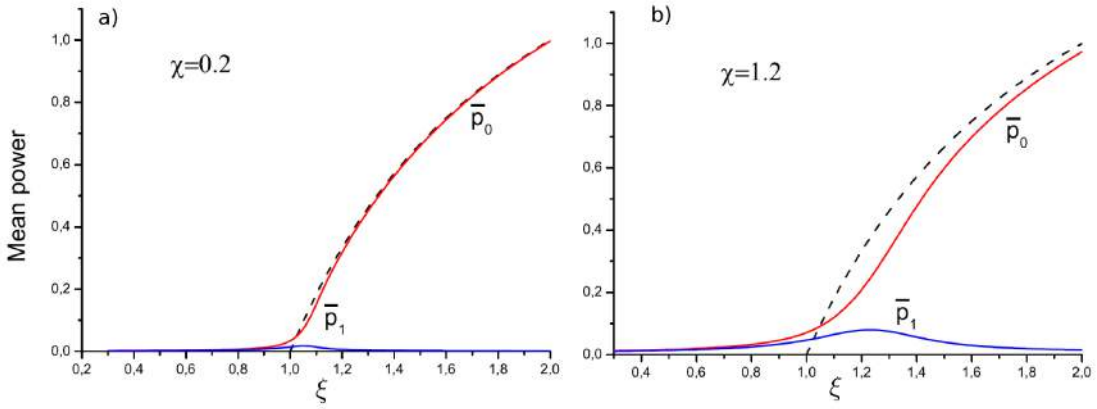

Figure 3.8.: *Dependence of the mean-mode powers dependence on supercriticality Δ. for different amplitude of phase noise. Dashed line corresponds to the one-mode solution. From [135].*

In sum, we have presented in this chapter the main results of a formalism for STNOs in terms of a universal nonlinear dynamical equation. This theory enables to predict all the useful characteristics of STNOs: generation frequency and linewidth, tunability, locking range, synchronization properties. Finally, it deserves to be noted that the validity of the NAO model for the description of a STNO is not limited to the case of a uniform magnetization precession. The spin wave mode excited in an STNO can have an arbitrary spatial distribution, and the NAO model can still be used in the vortex state [37, 136].

Part II.

Experimental setup and samples

CHAPTER 4

High frequency transport and MRFM

This chapter describes the experimental setups used during this thesis to characterize the STNO samples. The first part presents briefly the key aspects of the SATM (Spectrum Analyzer Transport Measurement) setup. In the second part a brief description of the MRFM (Magnetic Resonance Force Microscopy) instrument will be given.

4.1. Transport measurement

A natural mean to study STNOs is to use their magneto-resistance properties. Indeed, the resistance of a GMR junction depends on the relative angle between the two layers. Then when steady-state oscillations occur, it will generate an oscillating voltage. The first direct measurements of the high-frequency oscillations were undertaken at Cornell and the measurement technique is presented also in the same paper [11]. In this thesis, we measure the spectra of microwave power that result from magnetic motions by using SATM (Spectrum Analyzer Transport Measurement) technique. A schematic of this technique is shown in figure 4.1. In this approach, a DC current is injected through the magneto-resistive device to excite the precession of magnetization and because of the GMR effect, there is an oscillation change in resistance and then, a time varying voltage.

In this setup the sample is mounted on a support between the poles of an electromagnet (cooled down by water) with its power supply to apply a magnetic field up to 1.1 T. The contact to the sample is realized by means of GGB industries microwave probes, with 150 μm pitch and with nominal maximum operating frequency of 20 GHz and nominal impedance Z_c = 50 Ω. The probes were custom built in all-non-magnetic parts, in order to avoid movements induced by the external magnetic field generated by the electromagnet. After the probe, a coaxial cables adapted to high frequency are used with SMA connectors for the connection between the probe and a bias-tee which allows the injection of AC and DC into the sample simultaneously. Since the determination of the static magnetic configuration is based on the measurement of giant magnetoresistance effect, an experimental access to the resistance of the device is necessary. For this purpose, the sample is connected to a dc current source and to a voltmeter through the same contact electrodes, which can be used for standard current perpendicular to the plane (CPP-GMR) transport measurements. The AC part of the voltage produced by the sample is sent through a low-noise amplifier having gain + 30 dBm to an Agilent Spectrum Analyzer (SA) with a working range of [9 KHz - 26 GHz] for frequency domain analysis.

In order to detect voltage oscillations, the relative orientation of the static magnetizations of the two layers constituting in our spin-valve have to be misaligned in order for the magnetization precession to produce a voltage, because highly symmetric magnetization trajectories do not produce any variation of resistance with time.

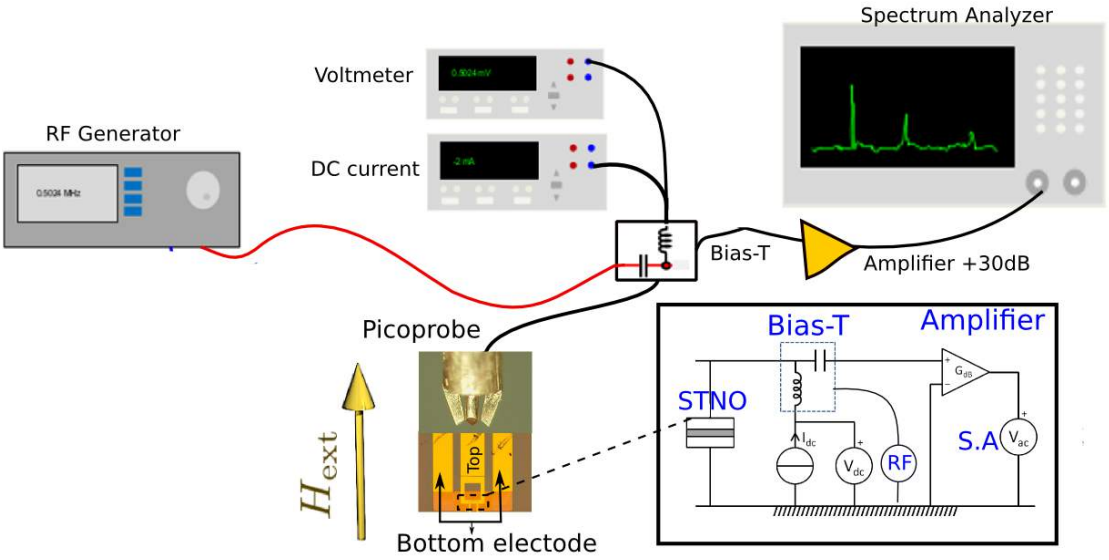

Figure 4.1.: *Experimental setup spectrum analyzer transport measurement (SATM) for electrical measurement. A DC current is applied to the STNO. A bias-tee allows the AC component of the current to be extracted, which is then amplified and has measured with an SA. Here the field is applied by an electromagnet which control the local field on the STNO. In addition this setup allows monitoring the DC voltage produced across the nanopillar when it is excited by an external source. A lock-in amplifier (not shown here) is used in these voltage-FMR measurements. Inset: schematics of an equivalent circuit to the setup.*

In our experimental setup it is also possible to monitor the dc voltage produced across the nanopillar by the precession of the magnetization in the sample structure when a rf current is injected in this structure (voltage-FMR). To do this, a lock-in detection is used to measure the difference of voltage across the nanopillar when the rf is turned ON and OFF: $V_{dc} = V_{ON} - V_{OFF}$.

4.2. Magnetic Resonance Force Microscopy

In addition to the SATM technique, we will use another independent method of detecting the magnetic resonance inside our device. We decided to use a mechanical detection of the FMR with a ferromagnetic resonance force microscope (MRFM)[59], which was constructed in the laboratory. This method has several advantages:

- A first decisive advantage is that the detection scheme does not rely on the spin wave spatial symmetry because it measures the change of the static component

(time average) of the magnetization (i.e the component along the precession axis or longitudinal component).

- A second decisive advantage is that the dipolar coupling used in MRFM permits the study of buried objects. Importantly, the dynamics of the thin layer underneath the top contact electrode can be studied.

- A third decisive advantage is that in MRFM, a quantitative measurement ofΔM_z, can be obtained. Thus one can obtain the power of the signal emitted by the STNO (p=$\Delta M_z/2M_s$).

4.2.1. Introdution

The dynamics of magnetization in ferromagnetic bodies can be studied using a variety of different experimental techniques. Among them, Brillouin light scattering (BLS)[137, 138], time-resolved scanning Kerr microscopy (TRSKM)[139], X-ray magnetic circular dichroism (XMCD) transmission microscopy [55] and spin-torque driven ferromagnetic Resonance (ST-FMR)[15, 140].

Magnetic Resonance Force Microscopy (MRFM)[141, 57, 142, 143, 144, 145, 49, 102] which was used in this work, is a powerful technique that can detect any change in the magnetization of a ferromagnetic sample. This technique was proposed in 1991 by Sidles who was searching for a precise technique of measurement to study the structure of biological objects and to achieve this goal he came up with the intriguing idea which is to couple a highly sensitive force detector like a micrometer sized cantilever to the longitudinal component of magnetic moment of either nuclear or electronic spins. The capabilities of the MRFM to detect the electron spin resonance (ESR) was given by Rugar team (1992) in the DiphenylPicrylhydrazyl (DPPH) molecule [146], the nuclear magnetic resonance (NMR) [147], ferromagnetic resonance (FMR) experiments [56]. In the following section, we will give a brief overview of our MRFM experiment.

4.2.2. MRFM operating principles

The principles of MRFM are the same as that of the magnetic force microscope (MFM) technique, which measures the magnetic interaction between the probe and the sample. In fact, when a magnetic moment m is placed in a gradient field ∇B, it will experience a

force $F = (m.\nabla)B$. In MRFM, the gradient B is supplied by a very small probe magnet or ferromagnetic nano-particle mounted at the end of a very soft mechanical resonator (cantilever) and the moment m is produced by the spins of the sample. For an orientation of the external magnetic fields (produced by an electromagnet) along the unit vector z and the cantilever shown in figure 4.2 the force on the cantilever is :

$$\mathbf{F_z} = (\mathbf{m_z}.\nabla)\mathbf{B_z}\,. \tag{4.1}$$

Here the cantilever can detect the force in the z direction only, i.e, the forces in the x and y direction are neglected. Indeed, the mechanical oscillator (cantilever and probe) is not sensitive to the rapid oscillation of the transverse component in the sample, which occurs at the Larmor precession frequency. As a result, the force on the cantilever probe is proportional to the static component of the magnetization inside the sample which is equal to M_z. When a resonance is excited in the sample, it opens up a precession movement at a cone angle θ, it is the deviation of static magnetization M_z from M_s, $\Delta M_z = M_s - M_z = M_s(1-\cos(\theta))$, that leads to changes of the force acting on the cantilever. This force is measured through the detection of the oscillation amplitude of the cantilever using a laser beam on a four-quadrants photodiode. Here the detection noise is ultimately limited by the Brownian motion of the cantilever. This noise depends on the temperature T and the detection bandwidth B, as well as mechanical characteristics of the harmonic oscillator (resonator) like quality factor Q, spring constant k and mechanical resonance frequency of the first flexural mode of the cantilever f_c. Thus the minimal detectable force follows the relation:

$$F_{min} = \sqrt{\frac{4k_BTB}{\omega_c Q}}\,. \tag{4.2}$$

In order to obtain a sensitivity gain, the dynamics of the magnetic moments are excited at f_c. This is achieved by the modulation of the microwave excitation at this frequency. As a result, the amplitude of vibration will be multiplied by Q, the quality factor of the mechanical resonator.

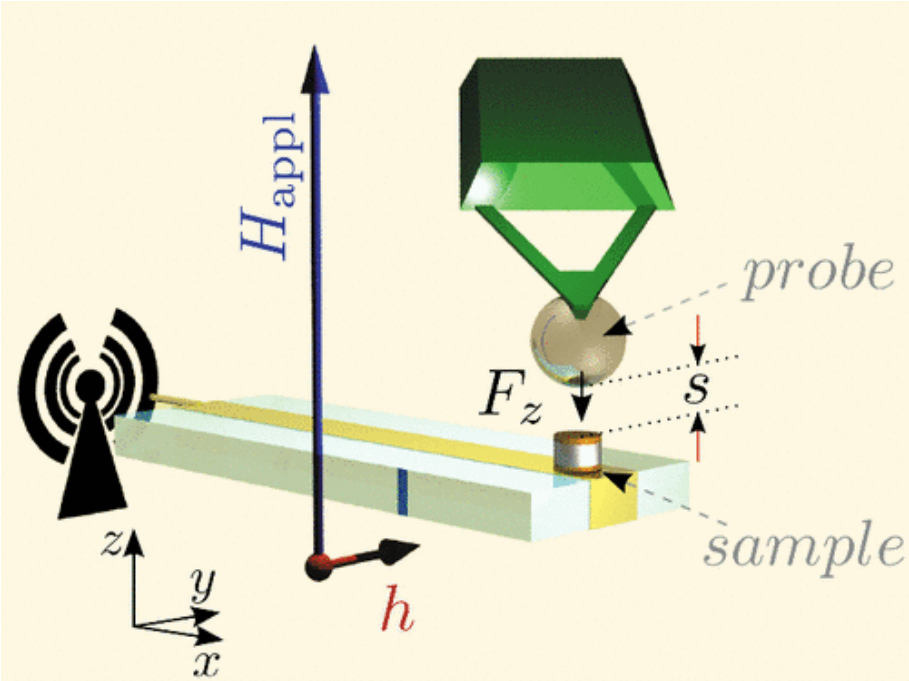

Figure 4.2.: *A schematic of a MRFM apparatus : the electromagnet (not shown) provides an external field $\vec{H}_{ext}$ perpendicular to the cantilever axis. A small probe magnet is attached at the end of cantilever and is coupled dipolarly to the sample placed underneath. The excitation comes from a microwave strip-line placed underneath the sample which produces an RF modulation field. The displacement of the cantilever is measured optically. Image taken from [59].*

4.2.3. Experimental realization

Figure 4.3 displays our MRFM in graph and computer design drawing. The system is set between the poles of an electromagnet which produces an external magnetic field ($\vec{H}_{ext}$) oriented out of plane i.e. along the sample axis. This electromagnet can reach 1.1 T at room temperature. In our setup it's very important to set the alignment of our MRFM cantilever because the later has to be brought into close proximity of the sample in order to maximize the dipolar interaction. For this purpose, we first manually align the cantilever to within a few micrometers. Then, we mount the experiment in a vacuum chamber (10^{-6} mbar) in order to achieve the detection sensitivity. At this stage, the cantilever isn't placed exactly over the sample. Thus, for the fine alignment, the sample is placed on a piezoelectric tube (see figure 4.3 (c)). The tube has a nanometer accuracy and can be distorted in a sufficiently large range (micrometer range) in the three dimension (XYZ). This positioning system is driven by applying high voltage on its electrodes. Then, for positioning the magnetic probe precisely above the center of the

sample, we search for the minimum of the cantilever frequency which corresponds to the maximum dipolar interaction between the sample and the probe [61].

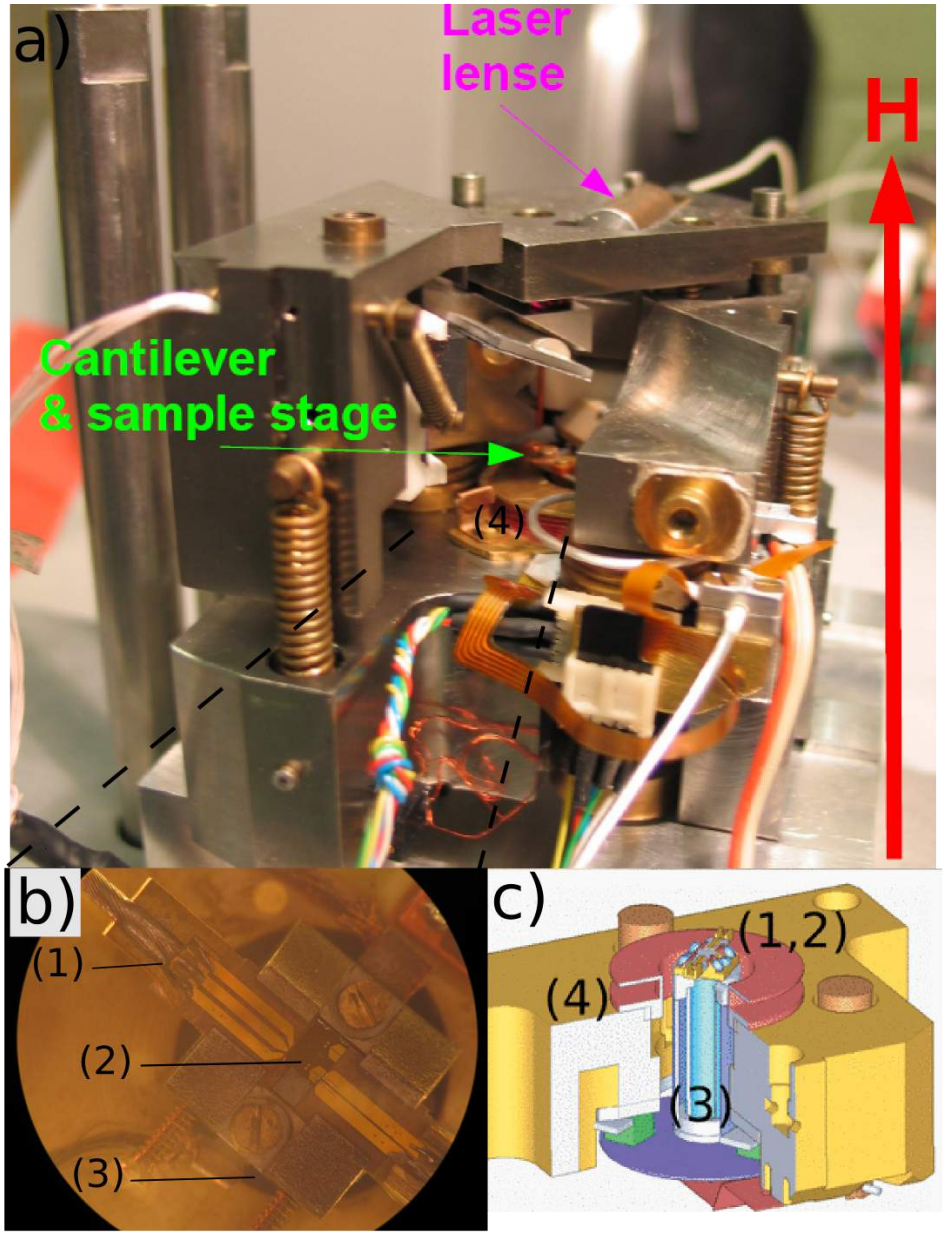

Figure 4.3.: *(a) General view of the MRFM microscope used during this thesis. The MRFM is placed in the middle of a 1.1 T electromagnet.(b) Photograph of the MRFM bottom. (c) Schematic drawing of the above elements. The top part with the cantilever and the optical detection is not shown. The numbers indicate the visible parts that are shown in (b) (1) the microwave circuit, (2) the substrate is the sample (3) the piezoelectric scanner, and (4) the magnetic coil used for a calibrated modulation of the applied field.*

4.2.3.1. Cantilever

It is evident from equation 4.2 that in order to improve the force sensitivity, one should choose a cantilever with a high quality factor Q, high resonant frequency f_c and low spring constant k. In our experiments, we have chosen the commercial cantilever (Olympus BioLever) that has a small spring constant. This cantilever is made of crystalline Silicon Nitride (Si_3N_4) coated by 30 nm of gold, and with dimensions w × t × l = 30 μm 160 nm 100μm. Table 4.1 contains the typical parameters for our unloaded cantilever:

Frequency (Hz)	Spring constant k ($N.m^{-1}$)	Quality factor under vacuum
12000	6×10^{-3}	3000

Table 4.1.: *Typical parameters of the cantilever used in this setup*

For instance, after gluing the magnetic particle on the cantilever, the resonant frequency changes. Then, at room temperature we characterize the cantilever resonance by studying its response to an excitation AC voltage on a piezoelectric bimorph located on the cantilever chip holder. In figure 4.4, we show a typical curve of the amplitude response of our cantilever (with probe attached) as a function of the frequency. A Lorentzian fit to the data in figure 4.4 (a) yields a resonant frequency of 11745 Hz and ΔF of 4.3 Hz from which the quality factor can be determinate $Q = F/\Delta F \sim 2500$. From equation 4.2 we can find the minimum detectable force ($F_{min} = 0.7f N/\sqrt{Hz}$) which gives us a excellent force sensitivity. Also, we can measure the noise of this cantilever. This measurement is performed in the absence of external excitations, and it is a way to determine the thermally activated amplitude which is about 300 pm.

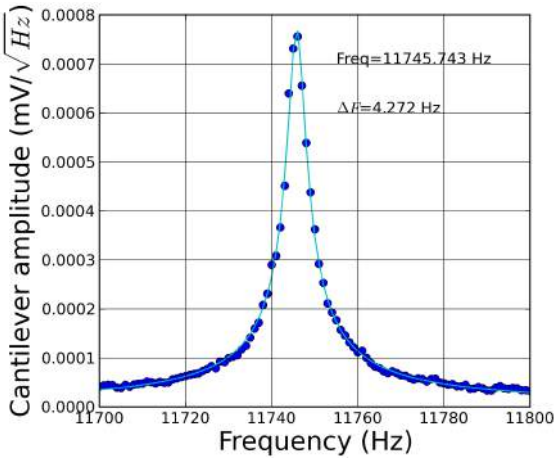

Figure 4.4: *sweep frequency measurement of cantilever with a dimension w × t × l = 30 μm 160 nm 100μm , equipped with a sphere magnet of diameter equal to 800 nm. This measurements were performed under vacuum ($10^{-6}mbar$) at room temperature (300 K).*

4.2.3.2. Probe magnet

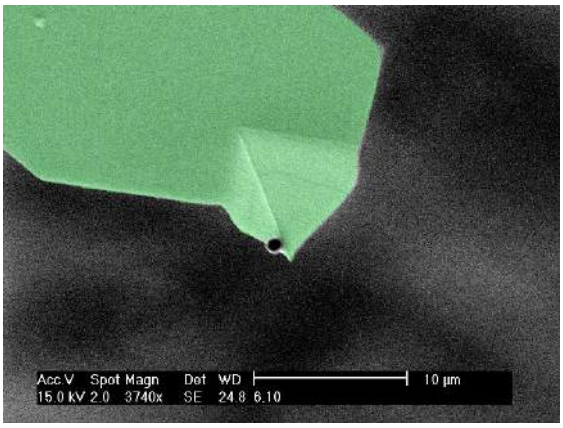

Figure 4.5: *Scanning electron microscopy image of the magnetic probe (FeSi) glued at the top of a BioLever cantilever.*

We have already mentioned in equation 4.1 that the force is created if the magnetic moments of the sample interact with a field gradient. In order to increase the probe-sample interaction and hence MRFM sensitivity we need to increase the magnetic field gradient of the probe. In our case, the probe itself is an 800 nm diameter sphere of amorphous Fe (with 3 % Si) glued at the apex of the cantilever (see figure 4.5). The choice of the spherical shape, small size and the material for the magnetic probe is due to several reasons. First, the spherical shape preserves the axial symmetry of the nano-pillar and this geometry does not has any shape anisotropy [1] which decreases the influence of the applied magnetic field on the mechanical resonance frequency of the cantilever. Secondly, a small probe magnet provides larger magnetic field gradient. Finally, FeSi was chosen to provide a high magnetization $\mathcal{M}_s$ to maximize the field gradient.

To characterize this sphere, we have performed a magnetometry measurement by measuring the cantilever frequency f_c as a function of the applied magnetic field. In this experiment the magnetic probe is placed 13 μm above the center of a magnetic cylinder which produces a known source of field gradient. The resulting cantilever frequency is shifted due to the presence of the magnetic moment and can be obtained with the following equation:

$$\frac{\Delta fc}{fc} = -\frac{m}{2k}\left(\frac{\partial^2 B_z}{\partial z^2}\right)_{z_0}, \tag{4.3}$$

where z_0 is the equilibrium position of the nanomagnet in the field gradient. The experi-

[1] The shape anisotropy could induce parasitic torques which can disturb the motion of the cantilever.

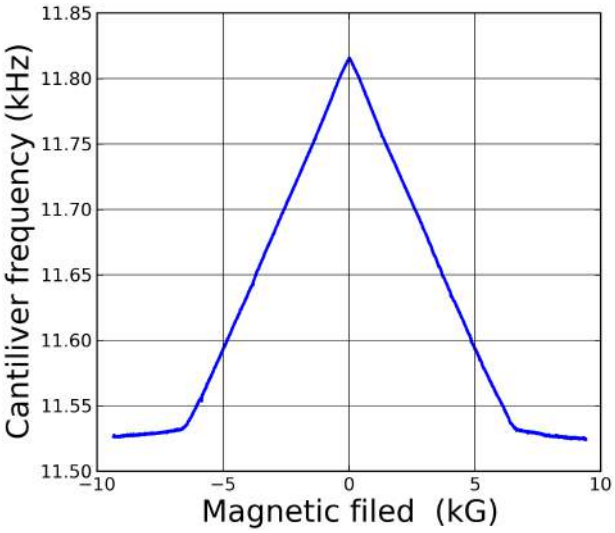

Figure 4.6: *The cantilever frequency as a function of the applied magnetic field in a field gradient of* $\frac{\partial^2 B_z}{\partial z^2} = 10^9 G/cm^2$.

ment shows a linear dependence of the frequency shift with the particle magnetization, since it has a change of the slope at 0.65 T which indicates the magnetic saturation of the probe. We have indicated in table 4.2 the final extracted values of the radius R, magnetic moment m, and saturation magnetization Ms of the (FeSi) probe with the experimental error bars.

Radius (nm)	Magnetic moment (emu)	Magnetization (emu/cm^3)
350 ± 30	(2.8 ± 0.7)×10^{-10}	1550 ± 70

Table 4.2.: *Summary of the cantilever magnetometry measurements performed to characterize the probe on the cantilever [148]*

4.2.4. Experimental precision

4.2.4.1. Tip stray field

Exhaustive past studies [144, 59], have already demonstrated that, in the weak perturbation regime, the influence of the magnetic probe of the MRFM is mostly reduced to a uniform shift to lower field of the whole spectrum of the studied sample by an offset field:

$$\{R_{sph}\}_{l,n} = \frac{1}{\langle M_\perp^2(r)\rangle} \int_v R_{sph}(r) M_\perp^2(r) d^2(r) dz \,. \tag{4.4}$$

where $\{H_{sph}\}$ is the magnetic stray field generated by the sphere. Although the exact shift value in equation 4.4 depends on the mode index [81], it turns out that within the experimental precision, this offset can be approximated to a constant [144]. Performing a numerical application for the uniform precession profile , we calculate $\{H_{sph}\}_{0,0}$ = 180 Oe when our magnetic sphere with magnetic moment m = 2.8 $\times 10^{-10}$ emu is set at a distance s = 1.3 μm from the sample (all the MRFM spectra are recorded with magnetic sphere at the same exact position above the sample 1.3μm). Notice that another way to directly measure the value of H_{sph} can be done by measuring the voltage-FMR detection with the sphere above the sample. In this case, it is possible to compare the FMR spectra with and without the presence of the spherical magnetic probe above the sample. We find experimentally that the two spectra are homogeneously shifted from each other, and that the shift $\{H_{sph}\}$ = 190 Oe is in a good agreement with the estimation based on equation 4.4.

4.2.4.2. Calibration of ΔM_z

As we mentioned previously, the MRFM experiment consists of detecting mechanically the diminution of spontaneous magnetization in the sample associated with the Larmor precession. The mechanical oscillator is not sensitive to the rapid oscillations of the transverse component in the sample, which occurs at the Larmor precession frequency, i.e. several orders of magnitude faster than its mechanical resonance. Thus, the magnetization of the sample acting on the cantilever probe reduces to the static component M_z. The measured MRFM quantity is given by :

$$\langle M_z \rangle \equiv \frac{1}{V} \int_V M_z(r) d^3r \,, \tag{4.5}$$

where the chevron brackets stand for the spatial average over the volume of the magnetic body. A calibration of $\langle M_z \rangle$ is possible by using the same experimental foldover phenomenon as in the RF calibration. In fact for the special case of a sample magnetized perpendicular to the plane, the amplitude of the uniform mode is a solution of the operational foldover equation :

$$[(2(H - H_{res})/\Delta H + \beta A^2)^2 + 1] A^2 = 1 \,. \tag{4.6}$$

In equation 4.6, H is the applied static field, H_{res} is the resonance field at low power, ΔH is the linewidth measured in the linear regime, β is a parameter proportional to the microwave power level and A is the amplitude. MRFM profiles with power = +9 dBm is shown in figure 4.7. The spectra are fitted with equation 4.6. From the parameters ΔH = 0.1 kOe and H_r= 10.7 kOe we obtain $\beta = \frac{8}{3\sqrt{3}}$. Hence, the maximal amplitude of the resonance, which is equal to the longitudinal change of the magnetization is [149]:

$$4\pi\langle\Delta M_z\rangle = \frac{4}{3\sqrt{3}}\Delta H \,. \tag{4.7}$$

A numerical application of equation (4.7) yields $4\pi\langle\Delta M_z\rangle = 36 \pm 4$ G, which corresponds to the critical angle of precession $\langle\theta_c\rangle = 5°$. We have used this calibration of the cantilever vibration amplitude to evaluate the change of the longitudinal magnetization ΔM_z.

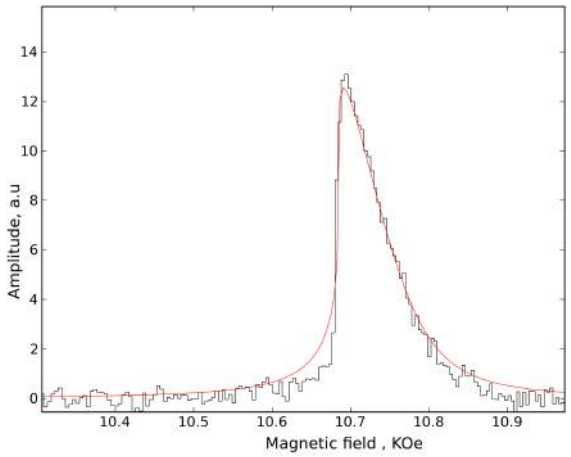

Figure 4.7: *The resonance curve at different microwave power in the non linear regime. The foldover threshold (red curve) gives a fit of the experimental data in order to give a direct calibration of the measured amplitude.*

In this chapter we have presented the experimental techniques that will be used to study the STNO samples. Our study will be done by two independent methods of detecting the magnetization dynamics inside a spin-valve nano-structure. The first tool is MRFM, which detects all the excited spin wave modes independently of their phase. In particular, it allows us to perform a study in the exact normal configuration, which is the simplest possible geometry for a STNO as it coincides with the universal auto-oscillator model. The second tool is the SATM where we detect the voltage produced across the STNO. It deserves to be mentioned that in the MRFM setup, the magnetization dynamics can also be simultaneously detected via SATM technique. In this case the device electrodes are not directly connected to the microwave synthesizer through a picoprobe but are wire bounded to a microwave cable and the circuit contains more connections. Thus, the MRFM spectra can be directly compared to transport measurements in order to better understand the experimental results.

CHAPTER 5

Studied samples

As mentioned previously, the current density required for spin transfer effect is high ($\sim 10^7 A/cm^2$). As a result, nano-scaled device would require several mA. Thus, nanofabrication is necessary to make a STNO. This chapter starts with a description of the sample structure and fabrication , followed by a description of the magnetic properties and DC caracterization. Then, a precise identification of the spin-wave eigen-modes inside the sample will be given.

5.1. Nano-pillar structure and sample design

5.1.1. The lithographically patterned nanostructure

The spin-valve structure used in this thesis is a standard Permalloy ($Ni_{80}Fe_{20}$=Py) bi-layer structure sandwiching a 10 nm copper (Cu) spacer: the thicknesses of the thin Py_a and the thick Py_b layers are respectively t_a = 4 nm and t_b = 15 nm. The samples are fabricated in laboratoire de photonique et nanostructures (LPN) and CNRS-Thales. We present in this section the process of the production of these metallic nano-pillars.

We can describe the different steps of the fabrication process as follow (see figure 5.1).

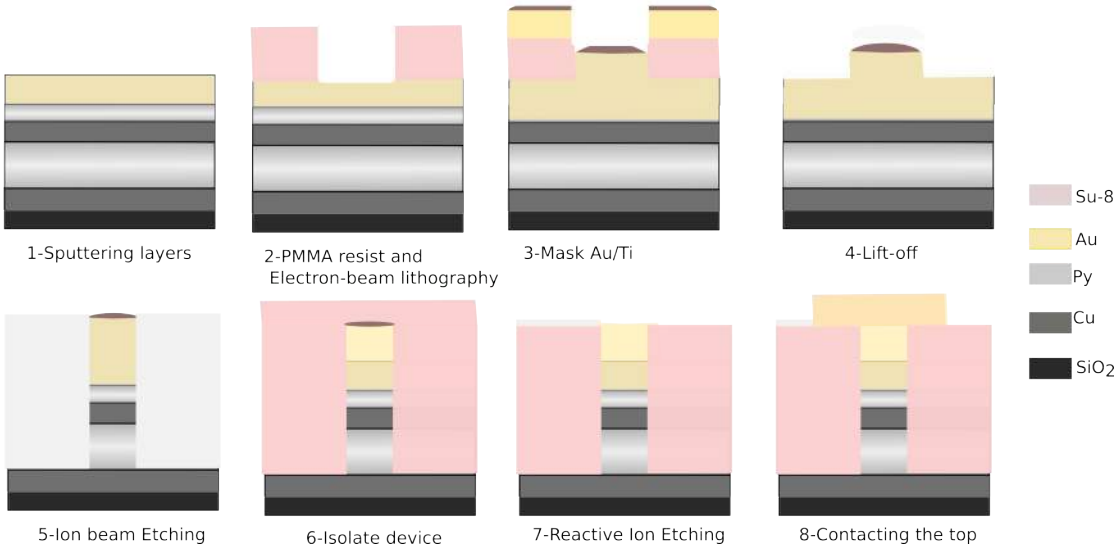

Figure 5.1.: *Fabrication processes for the production of a nanopillar*

1. *Sputtering magnetic layers* : the first step in the fabrication process is sputtering thin films of all the layers. The metal stack chosen for the samples studied is still the same where the metallic layers were deposited onto oxidized Si substrates: Cu(60nm)/Py(15nm)/Cu(10nm)/Py(4nm)/Au(25nm).

2. *Electron-beam lithography* : after sputtering all the layers, the nanopillar device is defined to be circular with dimension of the order of several hundreds of nanometers by electron-beam lithography. The layer of PMMA resist is used to give a good undercut.

3. *Mask Au/Ti*: after developing the e-beam resist, an etching mask Au/Ti is deposited.

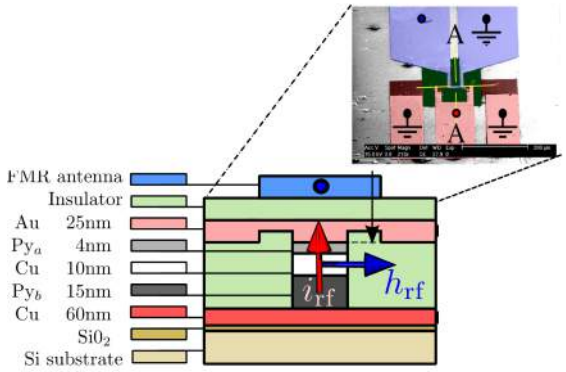

Figure 5.2: *Schematic representation of the sample which is a circular nano-pillar comprising a thin Py_a and a thick Py_b magnetic layers separated by a Cu spacer. The inset is a top view microscopy image of the sample showing the two independent circuits in different colors. The electrodes in blue represent the antenna circuit which enables to produce an RF in-plane magnetic field. The electrodes in red represent the contact circuit that allow for injecting a DC or/and RF current through the nano-pillar.*

4. *Lift-off*: the resist and the Au/Ti is removed except above the device by lift-off in order to define the etching mask of the nano-pillar. .

5. *Ion beam etching* : Then the multilayer is etched as a nano-pillar by Ion Beam Etching (IBE).

6. *Isolate devices* : In order to isolate the device an insulating SU-8 is deposited to cover the whole pillar.

7. *Reactive ion etching and planarization* : at this point of the fabrication process, there is SU-8 above everything on the wafer, the next step involve selectively removing SU-8 above the devices. This is done by Reactive Ion Etching (RIE). Then, the surface is planarized to flatten the bump above the pillar. This is done using the ion-milling technique.

8. *Contacting the top* : Finally, optical lithography is used to make the contact in the top of the nanopillar by depositing Au over the top-lead.

In addition, an independent top microwave antenna is deposited , with the aim of producing an in-plane rf magnetic field h_{rf} at the nanopillar location. This is followed by two steps :

1. *Isolate devices*: a polymer layer that provides electrical isolation from the rest of the structure is deposited.

2. *Antenna* : Then, a broadband strip-line antenna that consists of a 300-nm-thick Au layer is evaporated on the top. The width of the antenna constriction situated above the nanopillar is 10 μm. The microwave antenna circuit is shown in blue in figure 5.2 .

Finally it deserves to be mentioned here that the design of the contact electrodes (top and bottom) is done in a specific form (see red circuit in figure 5.2) to minimize the Oe field created by the current which prevents parasitic torques, which may disturb the motion of the cantilever.

5.1.2. The different samples

In this thesis, two batches of samples were produced. The first batch of devices having only single nano-pillar. The STNO in this series is a circular nanopillar of nominal diameter 200 nm patterned from the stack which is discribed previously. The thicknesses of the two magnetic layers have been chosen in order to observe the effects of spin transfer on both layers. Moreover, the spacer layer, of thickness only 10 mm is thin enough to have a dynamic coupling between the two magnetic layers in dipol interaction . Thus, in these samples which contain only one pillar, we will focus to the dynamics of magnetization of the coupled two magnetic layers. We note that, the selected material Permalloy and the dimensions of each magnetic disks are also with the aim of having stable uniform and vortex states. Indeed, it will be possible to change on the stability of different magnetic configurations by applying a current or an external magnetic field.

A second series of samples was prepared for which the electron beam lithography mask was modified to prepare for each sample several nano-pillars. We will study only samples that are of pair of spin valve nanopillars, processed using the same steps of e-beam and UV lithography and the same stack described previously. The structure of each pillar is the same as that described previously and the separation distance is 100 nm. The top and bottom electrodes are common to the two pillars. The characterization of this sample will be presented in chapter 8.

In this thesis two classes of configurations will be studied, these configurations are characterized by different excitation modes and frequency ranges:

- Homogeneous nano-pillar: Here the basic configuration is a circular nanopillar structure which has been presented previously, with a homogeneous magnetization for the thin Py_a and the thick Py_b. When the magnetizations of both layers are out-of-plane (a strong perpendicular magnetic fields is applied), the frequency of the uniform excitation mode is between 2-25 GHz

- Vortex nano-pillar: Here in the vortex state, the in-plane magnetization curls along the pillar border, leading to a singularity in the center (the vortex core), where the magnetization turns out of plane . The dynamics of the vortex state which is very different from the one of the homogeneous state, since the very narrow region of the soliton-like vortex core (a few nanometers) leads to very different unique dynamical modes. The lowest energy mode, excited by spin transfer, is the gyrotropic mode (frequency range 200 MHz - 2 GHz) where the vortex core is orbiting on a circular trajectory around its equilibrium position. In this thesis, we will study the dynamic behavior of vortex when excited in a coupled dynamics between the thick and the thin layers.

5.2. The microwave circuit: design and calibration

The microwave circuit has been designed specially for the MRFM setup. A special care has been put in the design of the microwave circuit and the electrodes around the nano-pillar. The circuit is adapted at 50 Ω to minimize the parasitic reflexions. The microwave antenna is close as possible from the samples to get the maximum of amplitude and to generate homogeneous microwave field. It should be noted that for the microwave antenna an anti-node is created at the end which leads to a total reflexion of the microwave current to the source (Anritsu synthesiser, 100 kHz to 20 GHz). The constriction is 10 μm wide and 25 μm long and creates an orthoradial microwave field h_{rf} that is linearly polarized. Simulations have been performed with the Sonnet microwave software in order to validate the properties of the design of this circuit.

5.2.1. Modulation of the microwave source

The goal of MRFM is to detect ferromagnetic resonance at high frequency. To enable this, a microwave field at these frequencies has to be created in the near field of the sample. For this purpose, two different circuits have been designed to excite the magnetization dynamics and perform spectroscopy. The figure 5.3 shows the first circuit allowing the generation of an rf in-plane magnetic field h_{rf} and the circuit allowing the injection of an rf current perpendicular to the plane through the nanopillar i_{rf}. The microwave circuit was carefully designed to minimize the crosstalk between the RF field and RF current excitation parts.

As discussed in the previous chapter, the DC current can cause steady state oscillations of the magnetization in the microwave frequency range. For this we will inject a finite DC current I_{dc} in the sample, and study our device in the two regimes: autonomous regime which corresponds to study the sample under the action of only the DC current and forced regime which correspond to study the sample under the action of the DC current and its response to external perturbations created by rf circuit. It is also possible to do spectroscopic study where there is no dc current flowing through the device in order to identify (excite) the eigen-modes in the STNO. Finally, we mention that in all these excitations a source modulation is applied at the cantilever frequency in order to get rid of spurious contributions and to enhance the signal by increases the quality factor of the mechanical oscillator. This modulation does not affect the line shape of the linear regime, because the relaxation time of the ferromagnetic system is very small compared to the period of the modulation $1/f_c$.

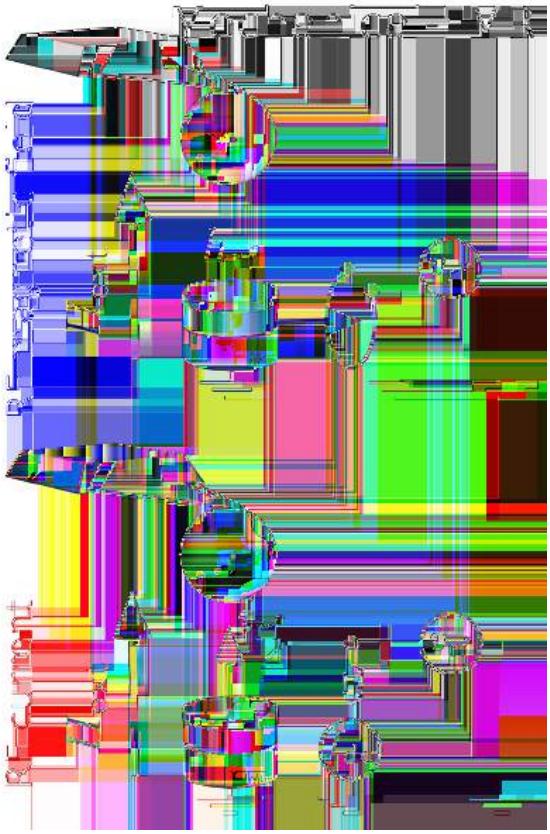

Figure 5.3.: *Schematic representation of the different excitation circuit available in our setup. Three different means are available to put the system out of equilibrium: Firstly an RF magnetic field applied parallel to the layers (blue arrow) secondly an RF current flowing perpendicularly to the layers (red arrow). Finally a DC current I_{dc} flowing through the nano-pillar.*

5.2.2. Calibration of microwave setup

5.2.2.1. Calibration of rf field

The amplitude of the RF magnetic field produced by the microwave antenna can be calibrated based on intrinsic nonlinear properties of the sample. In fact, it was pointed out by Anderson and Suhl [149] that the resonance curve at high power should be skewed, because the static change of the magnetization M_z, which also shifts the resonance frequency. This is the foldover phenomenon (see figure 4.7) which is characterized by a critical power, for which the resonance curve becomes infinite on the low field side of the resonance:

$$h_c = 2\Delta H \sqrt{\frac{2\Delta H}{3\sqrt{3}[\{N_{zz}\} - \{N_{xx}\}]4\pi M_s}}\,. \tag{5.1}$$

Where $\{N_{xx}\}$ and $\{N_{zz}\}$ are the demagnetizing factors in the transverse and longitudinal directions respectively. ΔH is the linewidth measured in the linear regime. Experimentally, we find that h_{rf} = 4.2 ± 0.8 Oe for an amplitude power of +9 dBm.

It is also possible to estimate the amplitude of hrf from Maxwell-Ampere law :

$$h_{rf} = \frac{\mu_0}{w}\sqrt{\frac{P_{rf}}{2Z}}\,. \tag{5.2}$$

Where $Z = 50\Omega$ is the impedance matched to the synthesizer and w is the width of the constriction. The value estimated by this method is $h_{rf} = 5.5 \pm 1$ Oe for P_{rf} = +9 dBm which is a good agreement with the estimation made in equation 5.1.

5.2.2.2. Calibration of rf current

Here we detail the experimental protocol used to calibrate the RF current flowing through the device with respect to the synthesizer output power injected into the contact electrodes. We have first used the voltage-FMR technique, in which the sample electrodes are connected to the microwave synthesizer through a picoprobe to perform voltage-FMR spectroscopy. In this experiment, the amplitude of i_{rf} flowing through the sample can be accurately determined, owing to the determination of losses and reflexions in

the microwave circuit using a network analyzer. Then, the same experiment is repeated inside the MRFM setup, in which the contact electrodes are wire bounded to a microwave cable and the circuit contains more connections. The comparison with the SATM setup yields an estimation of the rms amplitude of the RF current in the mechanical-FMR setup: $i_{\mathrm{rf}} = 170 \pm 40$ μA for an output power of -22 dBm injected at 8.1 GHz through the contact electrodes.

5.3. The magnetic properties of the sample

First of all, the magnetic properties of the Py layers (thick and thin) have to be determined. A precise extraction of the material properties (for the two layers) like the saturation magnetization, the damping parameter and the effective gyro-magnetic ratio γ are given by by cavity FMR and MRFM measurements. In summary the obtained values of the magnetic parameters are the ones reported in table 5.1. More details about the extraction of these parameters can be found in [41].

Table 5.1.: *Fundamental magnetic parameters of the thin Py_a and thick Py_b layers measured by cavity-FMR on the reference film (top row) and by MRFM (bottom row) in the p3460 sample*

$4\pi M_a$ (G)	α_a	$4\pi M_b$ (G)	α_b	γ (rad $\cdot$ s^{-1} $\cdot$ G^{-1})
8.2×10^3	1.5×10^{-2}	9.6×10^3	0.9×10^{-2}	1.87×10^7
8.0×10^3	1.4×10^{-2}	9.6×10^3	0.85×10^{-2}	1.87×10^7

5.4. DC and high frequency characterization

5.4.1. DC characterization

To characterize the DC properties of our devices, we have reported in figure 5.4 the measurement of the GMR in our sample in the CPP geometry (current perpendicular to the plane). The curve represents the hysteric behavior on the magneto-resistance of the spin valve under an in-plane magnetic field bias. Dark symbols (respectively light) are

used to show the behavior for sweep down (respectively up) in field. The low and high resistance states correspond to the uniformly magnetized state in both the thin and the thick layers, respectively parallel or anti-parallel to each other. The intermediate state observed around zero magnetic field corresponds to the formation of a vortex state in the thick layer. In our device, the average resistance is about 3.6 Ω and the $\Delta R = 25m\Omega$ which corresponds to a GMR ~ 0.7%.

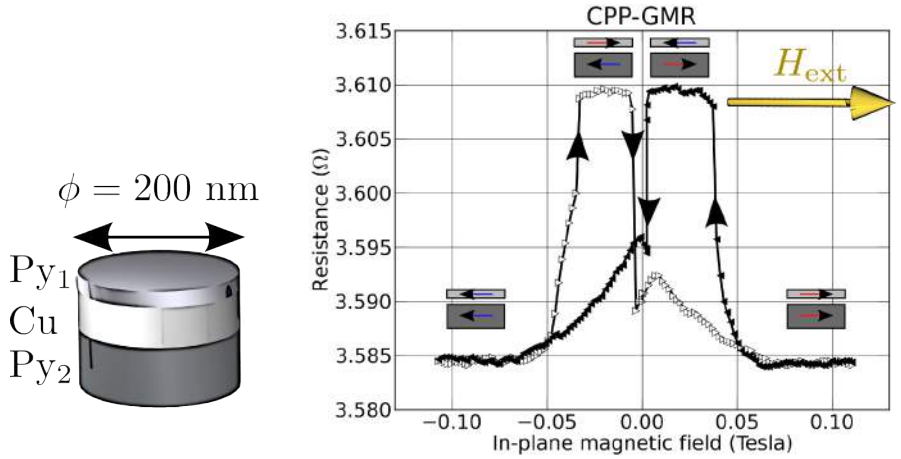

Figure 5.4.: *GMR hysteresis curve of the nano-pillar for in plane magnetic field. The field is swept from positive values to negative (dark symbols) values and back to positive saturation (light symbols). On the left: cartoon of the sample structure.*

5.4.2. RF characterization

The goal of our experiment is to study the magnetization dynamics in the STNO, by means of the STT effect. For this purpose, we aim to perturb the magnetization equilibrium with a DC current. The effect of the current was checked firstly by using the SATM technique. In figure 5.5 we show the power spectral density acquired for an external field H_{perp} = 0.95 T applied out of plane of the layers with $\theta_H = 2^0$. For a fixed negative current corresponds to a flow of electrons from the Py_B thick layer to the Py_A thin layer and stabilizes the parallel configuration due to the spin transfer effect [6, 7]. This test validates that our sample is ready to be studied.

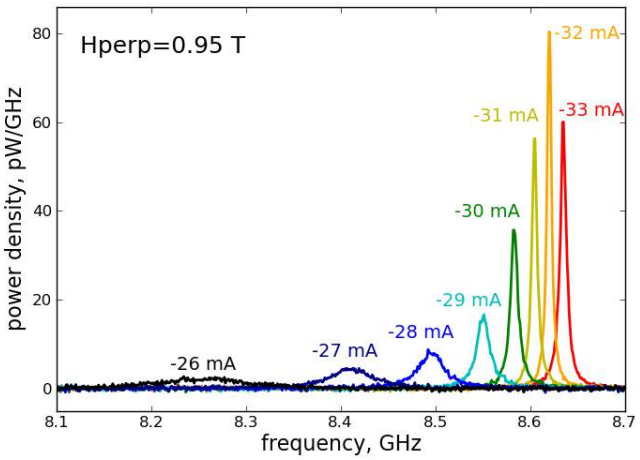

Figure 5.5: *Typical power spectral density of the nano-pillar at room temperature for different values of current. Here the field angle $\theta_h = 2^0$ and H_{perp}=0.95 T. As we can see that the measured microwave frequency spectrum showing a spectral Lorentzian peak whose frequency depend on the current.*

5.5. Eigen-modes in the saturated state

The purpose of performing MRFM experiments is to understand and characterize the nature of the auto-oscillation modes in STNOs. However, an accurate identification of the SW eigen-modes is necessary. Naletov et al. [41] have obtained experimentally this identification from a comparative spectroscopic study of the SW eigen-modes excited either by a homogeneous RF in-plane magnetic field or by an RF current flowing perpendicularly through the nano-pillar which is the same sample as that studied in this thesis. Furthermore, their work contributed to the roadmap of study which is displayed in the next chapter. Typical results are shown in the figure 5.6 for the two different excitation circuits. On the top, the SW spectrum is obtained by varying the perpendicular magnetic field while the sample is excited by an in plane microwave field h_{rf} at fixed frequency 8.1 GHz. As we can see, several modes can be detected, here only SW modes with the azimuthal index $\ell = 0$ can be excited (due to the homogeneous RF magnetic field it's coupled only with the axially symmetric modes (see section 2.2.2 of chapter 2)). The lowest energy mode occurs at the largest magnetic field, so the right mode corresponds to the uniform mode ($\ell = 0, n = 0$) with n is the number of nodes in the precessing magnetization.

On the bottom of the figure 5.6, the SW spectrum is acquired by varying the perpendicular magnetic field while the sample is excited by an RF current of same frequency 8.1 GHz flowing perpendicularly through the nano-pillar. Different spin wave modes can be seen in the same frequency. This is due to the fact that the RF current, creating a circular RF Oersted field, excites only the modes having azimuthal index $\ell = +1$.

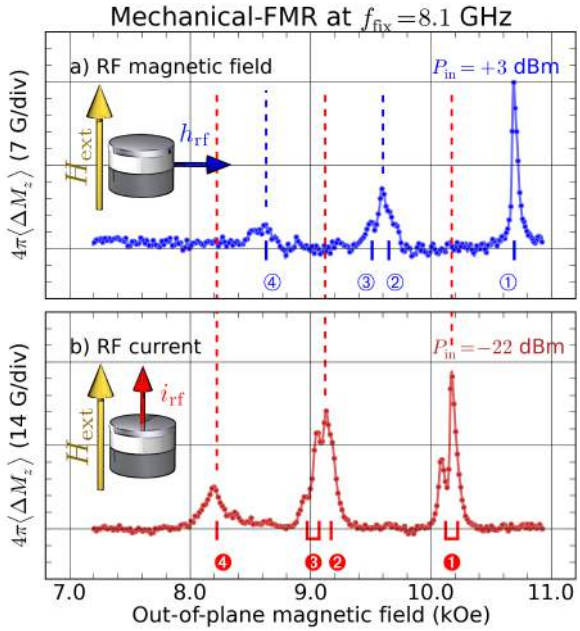

Figure 5.6.: *Comparative spectroscopic study performed by MRFM. (a) and (b) panels show the spin-wave mode spectra excited by a uniform microwave field and a microwave current flowing through the nano-pillar, respectively. The positions of the peaks are reported in table 5.2.*

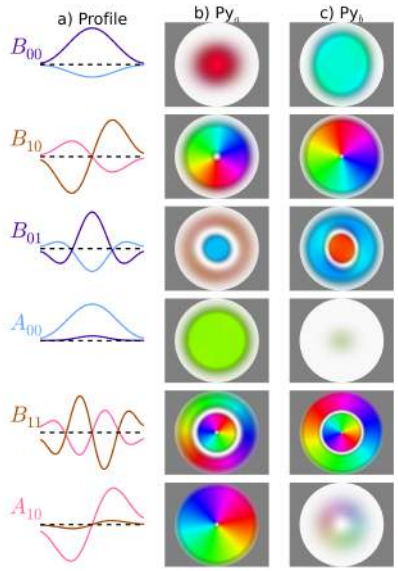

Figure 5.7.: *Simulated precession patterns of the eigen-vectors. (a) shows the precession profiles across the thin (light color) and thick (dark color) layers. (b) and (c) show the dynamics in the thin Py_a and thick Py_b layers, respectively. (see chapter 2 for the color code)*

In order to identify which layer (thick or thin) contributes mostly to each resonant mode a direct current is added through the nano-pillar, because it produces opposite spin transfer torques on each magnetic layers [41]. In addition the experimental results are compared to theoretical prediction of the nanopillar spin-wave spectra calculated both analytically (see section 2.2.2 of chapter 2) and numerically. Figure 5.7 (a) shows the relative amplitudes of precession in each layer to identify the dynamic coupling between the disks. From the profiles shown in figure 5.7, one can then determine which layer (thin A_{ij} or thick B_{ij}) contributes mostly to each dynamic mode. The summary of the precise identification is presented in table 5.2.

①	②	③	④
10.69 kOe	9.65 kOe	9.51 kOe	8.64 kOe
B_{00}	B_{01}	A_{00}	A_{01}
❶	❷	❸	❹
10.22 kOe	9.17 kOe	9.07 kOe	8.22 kOe
B_{10}	B_{11}	A_{10}	A_{11}

Table 5.2.: *The resonance field values for the spin wave modes. The blue and red indices are the location of the SW modes measured experimentally in figure 5.6. Second line represents the experimental field peaks measured at f=8.1 GHz by sweeping the field. Third refers to the Eigen-modes indexed with label $j_{\ell n}$ where $j = A, B$ indicates the layer (respectively the thin and thick Permalloy layer) and the pair ℓ, n indicates the azimuthal and radial index of the mode.*

In summary we have presented in this chapter the samples that we will study in this thesis. The most important information in order to understand the results of chapter 6 is summarized in table 5.2. Here we have presented the precise identification of SW spectrum excited by either a homogeneous rf magnetic field or a rf current flowing through the nanopillar. These experimental results have important consequences regarding the identification of the auto-oscillation mode of STNOs, as we will see in the next chapter.

Part III.

Experimental results

CHAPTER 6

Nanopillar in the normally magnetized state

The MRFM and SATM techniques presented in the previous chapter will be used to study a spin transfer nano-oscillator consisting of a normally magnetized Py|Cu|Py circular nanopillar in the autonomous and forced regimes. The nature of the mode which first auto-oscillates will be identified in the high symmetric perpendicular configuration and in breaking this axial symmetry. Moreover, the influence of the external source on the auto-oscillating mode will be highlighted in these two cases. Finally, we present measurements of high frequency magnetic dynamics excited by large current.

6.1. Perfect axial symmetry

The main question to be addressed here is: which is the nature of the mode that auto-oscillates in a STNO when the current exceeds the critical threshold ? This question is crucial, because the spectroscopic identification of the auto-oscillating mode is usually a challenge. In fact it is possible to excite a large variety of dynamic modes in STNOs by changing their geometrical and magnetic parameters and tuning the bias conditions. Moreover, the precise determination of the auto-oscillating mode is important for the synchronization of several STNOs. In fact, a promising strategy to improve the coherency and increase the emitted microwave power of these devices is to mutually synchronize several of them [27, 28, 97, 26, 29]. In order to optimize the coupling mechanism between STNOs, one has thus to understand the symmetries associated with the particular SW mode which auto-oscillates due to spin transfer.

So we decided to study a STNO in the simplest configuration: a circular nanopillar saturated by a strong magnetic field applied along its normal. Indeed, the trade-off between agility and spectral purity depends on the non-linear frequency shift coefficient $\mathcal{N}$. As shown in figure 6.1 for homogeneously magnetized layer, this trade-off can be tuned by rotating the magnetization direction in the azimuthal direction with an out-of-plane angle θ. There is a particular orientation (θ about $10°$) where the coefficient $\mathcal{N}$=0, which means that the oscillator has the highest spectral purity but also the lowest agility, which is not good for synchronization. In the opposite, in the exact perpendicular orientation ($\theta = 0°$), the STNO has the highest agility but also the lowest spectral purity. We will concentrate on this case since it corresponds to an optimum configuration for synchronization, it has a maximal nonlinear frequency shift (see figure 6.1), which provides a large ability for the STNO to lock its phase to an external source [97]. Moreover, the perpendicular configuration coincides with the universal oscillator model, for which an exact analytical theory can be derived [22]. Also, this configuration corresponds to an optimal orientation for the spin polarized current to compensate the damping, as a result a minimal current threshold to produce auto-oscillation [6, 121]. Last but not least, this highly symmetric case allows for a simplified classification of the SW eigenmodes inside the STNO [41] .

In this section we use the room temperature MRFM setup to monitor directly the power emitted by our device vs. the bias DC current and perpendicular magnetic field. Indeed, it should be noted that the SATM technique cannot be used here to probe the auto-

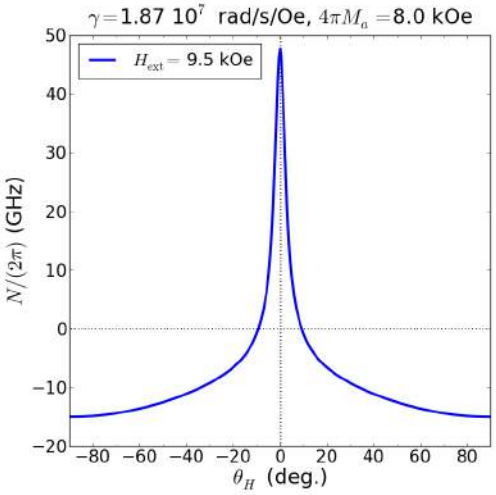

Figure 6.1: *Nonlinear frequency shift N calculated using equation (105a) of reference [22] and our sample parameters.*

oscillations in the normally magnetized nanopillar because no oscillatory voltage is produced due to the perfect axial symmetry.

6.1.1. Autonomous regime

6.1.1.1. Phase diagram of autonomous dynamics

First, we measure the phase diagram corresponding to the STNO autonomous dynamics as a function of I_{dc} (between +10 and -25 mA) and H_{ext} (between 8.5 and 10.5 kOe), see figure 6.2. In this experiment, I_{dc} is fully modulated at the cantilever frequency, $f_c \approx 12$ kHz. As we mentioned before, the MRFM provides a spectroscopic detection scheme, which measures the variation of the longitudinal magnetization M_z over the whole volume of the magnetic body, a quantity *directly* proportional to the normalized power p emitted by the STNO [22]. Indeed, it was shown in section 3.2 of chapter 3 that the dynamics of the dimensionless complex amplitude c is given by $c = \frac{M_x - i M_y}{\sqrt{2M_s(M_s+M_z)}}$ then,

$$p = |c|^2 = \frac{|M_x - iM_y|^2}{2M_s(M_s+M_z)} = \frac{M_x^2 + M_y^2}{2M_s(M_s+M_z)} = \frac{M_s^2 - M_z^2}{2M_s(M_s+M_z)} = \frac{(M_s - M_z)(M_s+M_z)}{2M_s(M_s+M_z)} = \frac{\Delta M_z}{2M_s}, \quad (6.1)$$

where M_s is the saturation magnetization of the precessing layer.

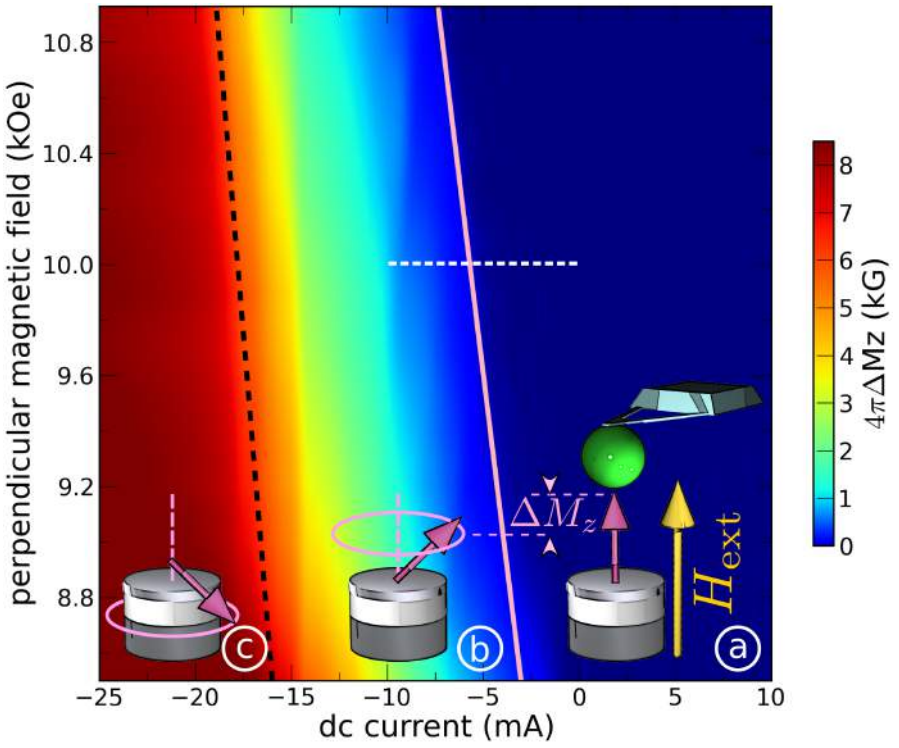

Figure 6.2.: *Phase diagram of the autonomous dynamics measured by MRFM. The change in the longitudinal component ΔM_z of the nanopillar is plotted as a function of the dc current through it and the magnetic field applied along its normal. The solid and dashed lines are guides to the eye.*

The quantitative measurement of ΔM_z is displayed using the color scale indicated on the right of figure 6.2 . The diagram can be divided into three different regions delimited by solid pink and dashed black lines with different dynamics of the free layer .

- Region ⓐ, at low negative or positive current (dark blue tone). In this region the change in M_z is negligible, because in the sub-critical region, the spin transfer torque is not sufficient to destabilize the magnetization in the thin or thick layer away from the perpendicular applied field direction.

- Region ⓑ, from -3 to -7 mA as H_{ext} increases from 8.5 to 10.5 kOe (light blue tone). In this region the MRFM signal starts to smoothly increase. From our current sign convention, we can deduce that it corresponds to the onset of spin transfer

driven oscillations in the thin layer, which will be analyzed in details in the next subsection.

- Region ©, starts around -15 mA (dark red tone). As I_{dc} is further decreased towards negative values, the angle of precession increases in the thin layer, until it eventually reaches 90°. At this point, $4\pi\Delta M_z$ reaches the full saturation magnetization in the thin layer, $4\pi M_s$ = 8 kOe This is also corroborated by transport measurements, as the increase of the dc resistance measured at this boundary equals 11 mΩ, *i.e.*, half of the full GMR of the spin-valve nanopillar see figure 6.3 (a).

Indeed, it is possible to measure both the dc resistance R_{dc} and the magnetization change ΔM_z of the STNO as a function of I_{dc} and H_{ext}. These two sets of data are complementary, as R_{dc} varies due to the GMR effect (of interfacial nature), whereas the MRFM measurement yields the averaged ΔM_z in the total volume of the STNO. Although these two phase diagrams look very similar, it is interesting to note that it is possible to directly convert the MRFM data into resistance only when the thin layer precesses at low current with an angle θ. In this simple case, the variation of resistance is $\Delta R = \Delta R_{GMR}(1-\cos\theta)/2$ and $(1-\cos\theta) = \Delta M_z/M_s$. Thus, one has simply $\Delta R = \Delta R_{GMR}\Delta M_z/(2M_s) = \Delta R_{GMR}p$, with p the normalized power measured by MRFM. In figure 6.3, we have plotted the experimentally measured ΔR together with this conversion of the MRFM signal. An excellent agreement is obtained, which means that the independent calibration of the mechanical signal ΔM_z is correct. Another interesting point is the better signal to noise ratio of the MRFM data compared to the data obtained by dc transport. A very nice feature of our MRFM setup is its dynamic range: with the same settings, it can detect signal as small as $1G/\sqrt{Hz}$ and as large as 10 kG. To improve the transport measurements, we add to I_{dc} a small signal of amplitude 0.1 mA modulated at a low frequency f_c, and lock-in detect the differential resistance dV/dI. Simultaneously, it is possible to measure by MRFM the small variation dM_z/dI induced by this modulation. The obtained phase diagrams are presented in appendix (A).

Finally, a comparison between these experimental results and a micromagnetic simulation incorporating the STT [150] calculated using continuous random matrix theory [151] reveals good qualitative agreement. All of the static and dynamical states seen experimentally are observed in the simulation, with the correct relative positions. Notice that, when I_{dc} reaches large negative values (for large positive current see Appendix (B))

the dynamics become more complex, with both thin and thick layers. We will come back on these results in details in section 6.3.

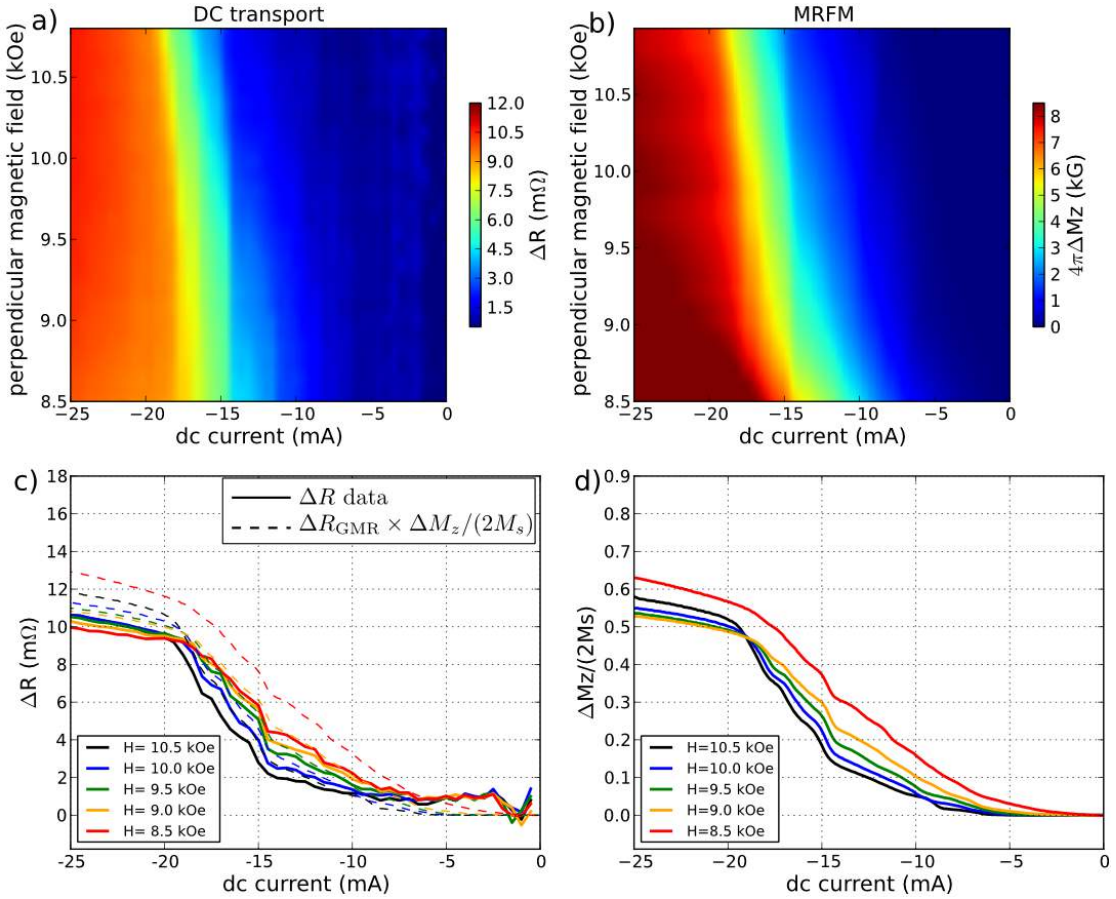

Figure 6.3.: *Experimental phase diagrams of the variation of dc resistance R_{dc} (a) and of longitudinal magnetization ΔM_z (b) as a function of the bias dc current and the perpendicular magnetic field H_{ext}. c) and d) are some cuts at fixed H_{ext} vs. I_{dc} of respectively a) and b). The dashed lines in c) correspond to the data of normalized power p plotted in d), converted into resistance change.*

6.1.1.2. Identification of the auto-oscillating mode

In this subsection we report a quantitative analysis of the sub-critical regime by using the nonlinear auto-oscillator theory of microwave generation by a spin-polarized current which already presented on chapter 3 . Let us concentrate on the spin transfer dynamics in the thin layer at $I_{dc} < 0$. We first introduce the number of spins in the thin layer $\mathcal{N} = V\mathcal{M}_s/(g\mu_B)$ where V is its volume, g the Landé factor, μ_B the Bohr magneton. Within the stochastic dynamics of the STNO described in section 3.3.2 of chapter 3, the average power in the sub-critical regime ($I_{dc} < I_{th}$), directly measured by MRFM, is given by:

$$p = \frac{\Delta\mathcal{M}_z}{2\mathcal{M}_s} = \frac{k_B T}{\mathcal{N}\hbar\omega}\,\frac{1}{1 - I_{dc}/I_{th}}\,, \tag{6.2}$$

where

$$I_{th} = 2\alpha\omega\mathcal{N}e/\epsilon\,, \tag{6.3}$$

is the threshold current for auto-oscillation of the SW mode with frequency ω. In this expression, α is the Gilbert damping constant in the thin layer, ϵ the spin-polarization efficiency, and e the electron charge. In equation (6.2), the prefactor

$$\eta \equiv k_B T/(\mathcal{N}\hbar\omega)\,, \tag{6.4}$$

is the noise power which is the ratio between the thermal energy (k_B is the Boltzmann constant, T the temperature) and the maximal energy stored in the SW mode with frequency ω ($\hbar$ is the Planck constant over 2π).

From equation (6.2), the inverse power is linearly dependent on the bias current I_{dc} in the sub-critical region. As shown in figure 6.4 (a), one can obtain the threshold current I_{th} and the noise power η from the linear fit of $2\mathcal{M}_s/\Delta\mathcal{M}_z$ vs. I_{dc}. The dependencies of ϵ, I_{th} and η on the perpendicular magnetic field are plotted in figures 6.4 (b), (c) and (d), respectively. The parameters V, $\mathcal{M}_s$, g (hence, $\mathcal{N} \simeq 6.3 \times 10^6$) and α of the thin layer have been previously reported in Table 5.1, as well as the dispersion relations $\omega_\nu(\mathcal{H}_{ext}) = \gamma(\mathcal{H}_{ext} - \mathcal{H}_\nu)$ of the SW modes in the thin layer disk ($\gamma = g\mu_B/\hbar = 1.87 \times 10^7$ rad.s^{-1}.G^{-1} is the gyromagnetic ratio and $\mathcal{H}_\nu$ the Kittel field associated to the mode ν). By replacing

ω by $\omega_\nu(H_{ext})$ in equation (6.3), it is found that the threshold current depends linearly on the perpendicular bias field:

$$I_{th} = \frac{2\alpha\mathcal{N}e}{\epsilon}\gamma(H_{ext} - H_\nu)\,, \tag{6.5}$$

as observed in figure 6.4 (c) for $H_{ext} > 8.8$ kOe, which corresponds to the saturation field of the thick layer (see Table 5.1). The linear fit of I_{th} vs. H_{ext} yields $H_\nu = 6.80 \pm 0.15$ kOe and $\epsilon = 0.299 \pm 0.005$. In this axially symmetric case, the identification of the eigenmodes in our STNO are reported in table 5.2 of chapter 5. From the comparison with the SW modes of the thin layer (see black symbols in figure 6.4 (b), it is found that the fitted value of H_ν precisely corresponds to the Kittel field of the $(\ell, n) = (0, 0)$ mode. Therefore, the analysis performed in figure 6.4 (c) unambiguously demonstrates that the first mode to auto-oscillate is the fundamental, most uniform precession mode of the thin layer. Moreover, it also provides an accurate determination of the spin-polarization efficiency (see figure 6.4 (b)) found to be in good agreement with the values measured in similar STNO stacks $\epsilon = 30\%$[151].

To gain further insight in our analysis of the sub-critical regime, now by injecting the dispersion relations ω_ν of various SW modes in equation (6.4), one can also observe in figure 6.4 (d) that the fluctuations of the STNO power are dominated by those of the $(\ell, n) = (0, 0)$ SW mode. This can be explained by the fact that it is the lowest energy mode, hence, with the lowest damping rate $\alpha\omega_{00}$, and therefore, the most affected by spin transfer. It also confirms that the single mode assumption made to derive equation (6.2) is a good approximation in the highly symmetric case $\theta_H = 0°$ [22]. Moreover, due to the relatively large volume of the thin layer and the high mode frequency (5–11 GHz in the investigated field range), the oscillator energy is far greater than the thermal energy, so the noise power is only a few 10^{-4}.

Now if we confine our attention to figure 6.4 (c) and (d), we can see systematic deviation from the expected curve for smaller perpendicular fields. We can explain this behavior by the fact that inside the saturation regime, the dispersion relation of the spin-wave mode is linear with the perpendicular field, and we do not observe any systematic deviation. Closer to the saturation field, the dispersion relation softens, and ω_{00} goes to zero faster than linear, which explains why the data points are systematically slightly above the theoretical prediction. To be complete on this point, this effect is less due here to the saturation of the thin layer itself (8 kOe), than to the one of the thick layer, whose

saturation field is $4\pi M_s = 8.8$ kOe. Below this value, the thick layer deviates from the exact perpendicular orientation, and therefore, its strayfield on the thin layer decreases, so ω_{00} of the thin layer.

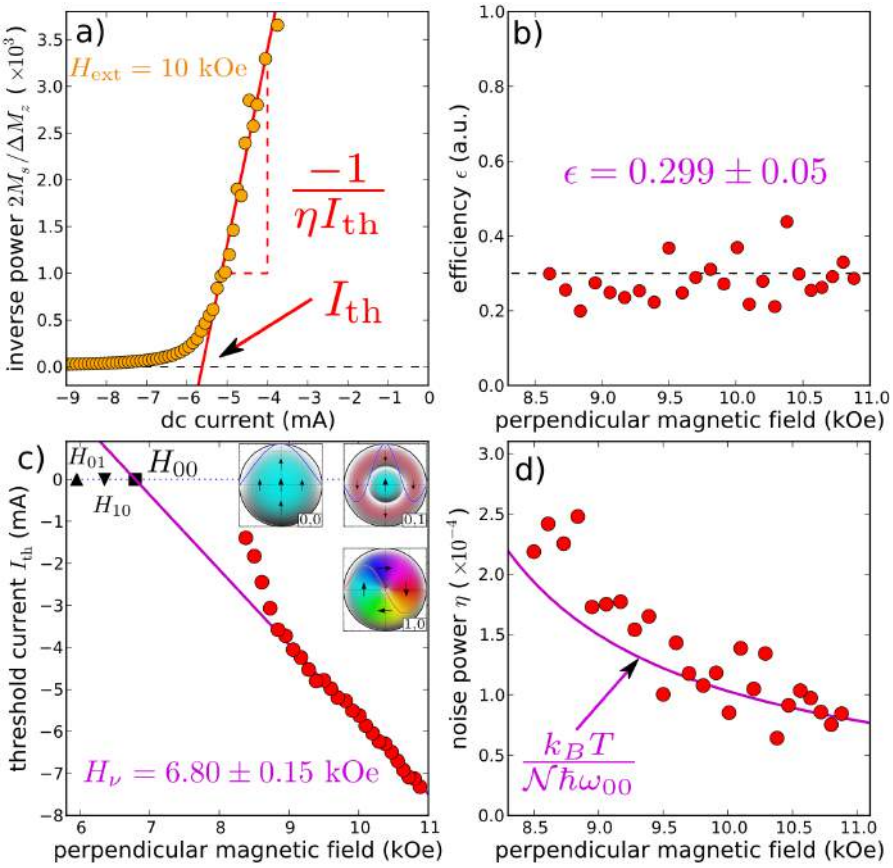

Figure 6.4.: *(a) Determination of the threshold current I_{th} and noise power η at $H_{ext} = 10$ kOe, from the linear fit of the inverse power measured by MRFM in the subcritical regime. (b) Determination of spin torque efficiency (c) Dependence of the threshold current on the perpendicular magnetic field. The pink line is a fit to the data using equation (6.3).(d) Dependence of the noise power on the magnetic field. The pink line is the prediction from equation (6.4) with no fitting parameter. In (c) the modes are indexed by a pair of integers $\nu = (\ell, n)$, with ℓ and n respectively the azimuthal and radial modes indices, these different SW modes are extracted from [41]. (see figure 5.6 of previous chapter) The inset shows the precession profiles across the thin layer and the code color show the dynamics in this layer. In this coding scheme, the hue indicates the phase (or direction) of the transverse component of the magnetization $\boldsymbol{m}$, and the brightness indicates the amplitude of the longitudinal component, M_z.*

6.1.2. Forced regime

Now that the auto-oscillating SW mode has been identified, beside this, we discuss its synchronization to an external signal [94, 90, 95, 96, 99]. Using the two different microwave circuits, we shall compare the ability of the auto-oscillating mode to phase-lock either to the uniform microwave field $h_{\rm rf}$ generated by the antenna or to the microwave current $i_{\rm rf}$ flowing through the nanopillar. The dependence on $I_{\rm dc}$ and $H_{\rm ext}$ of the SW modes excited by $h_{\rm rf}$ ($i_{\rm rf}$) is presented in figure 6.5a (6.5b). In these experiments, field-sweep MRFM spectra are acquired at fixed microwave frequency and $I_{\rm dc}$ is decreased from 0 to -8.25 mA by steps of 50 μA. The color code shows the change in the longitudinal component ΔM_z produced by the amplitude modulation at f_c of the microwave source.

As aforementioned, in the exact perpendicular configuration, $h_{\rm rf}$ selectively probes the $\ell = 0$ SW modes, whereas due to the orthoradial symmetry of the induced microwave Oersted field, $i_{\rm rf}$ couples to the $\ell = +1$ SW modes [41]. The three main peaks of the MRFM spectra obtained at $I_{\rm dc} = 0$ in figures 6.5 (a) and 6.5 (b) are labeled according to the SW mode identification see table 5.2 . $B_{\ell n}$ peaks correspond to SW modes dominated by the thick Py$_B$ layer, while A_{00} and A_{10} are the fundamental harmonics of the thin Py$_A$ layer with azimuthal indices $\ell = 0$ and $\ell = +1$, respectively. The resonant fields of these two modes are similar, due to the different excitation frequencies used for $h_{\rm rf}$ (8.1 GHz) and $i_{\rm rf}$ (9.2 GHz), *i.e.*, A_{10} is 1.1 GHz higher in frequency than A_{00} [41].

Below the threshold current for the thin layer determined in Fig.6.4 c (indicated by the magenta lines in Fig.6.5), the observed behaviors of the $\ell = 0$ and $\ell = +1$ modes are similar: a small negative dc current slightly attenuates the thick layer SW modes $B_{\ell n}$, while it promotes quite rapidly the SW modes A_{00} and A_{10} of the thin layer, in agreement with STT [41]. On the contrary, there is a clear qualitative difference between the modes A_{00} and A_{10} beyond $I_{\rm th}$. Although both peaks shift similarly towards lower field as $|I_{\rm dc}|$ is increased, A_{00} gets strongly distorted, with the appearance of a negative dip on its high field/large current side, in contrast to A_{10}, which remains a positive peak.

A negative MRFM signal means that the precession angle in the thin layer is reduced in the presence of the microwave excitation, see figure 6.6. This effect can be associated to the synchronization of the auto-oscillating mode to the external signal [44], here $h_{\rm rf}$ (and *not* $i_{\rm rf}$). In the so-called phase-locking range, its amplitude adapts ($\Delta M_z > 0$: increases, $\Delta M_z < 0$: decreases), so that the frequency of the auto-oscillation remains equal to the

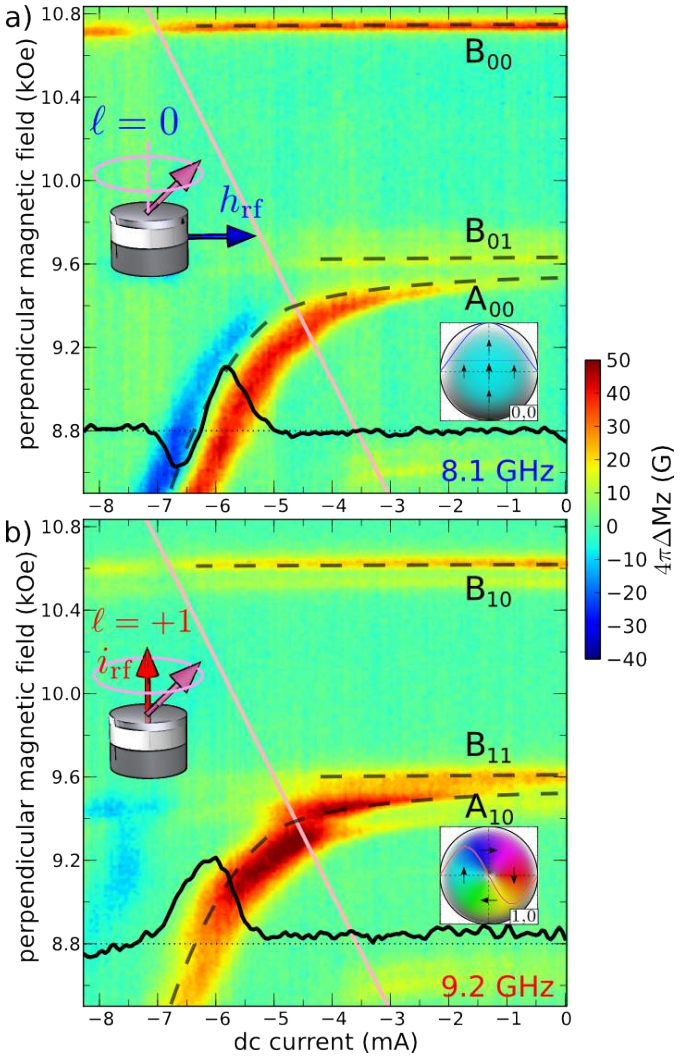

Figure 6.5.: *(Color online). Dependence on I_{dc} and H_{ext} of the $\ell = 0$ and $\ell = +1$ SW modes, excited respectively by the uniform field h_{rf} generated by the antenna at 8.1 GHz (a) and by the orthoradial Oersted field produced by the current i_{rf} flowing through the nanopillar at 9.2 GHz (b). The black traces are cuts of the MRFM signal vs. I_{dc} at H_{ext} = 0.88 T. The magenta oblique lines show the location of the threshold current determined in figure 6.4 (b). The black dashed lines are guides to the eye.*

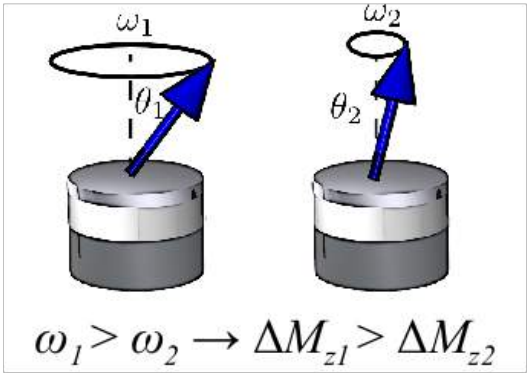

Figure 6.6: *Schematic representation of the auto-oscillation adapting its precession angle to match the external frequency. Above the critical current, the fundamental mode auto-oscillates with a precession angle $\theta_1 > 0$, and it is possible to reduce it to $\theta_2 < \theta_1$ by turning on the rf power*

frequency of the external source, here fixed at 8.1 GHz. This is made possible by the large nonlinear frequency shift in the perpendicular configuration, $N = 4\pi M_s \simeq 48$ GHz [22], which can be used to estimate the phase-locking bandwidth in our experiment (where the excitation amplitude is only $h_{\rm rf} \simeq 1.9$ G), $B = N\Delta M_z/M_s \simeq 200$ MHz.

The fact that the $i_{\rm rf}$ excitation cannot synchronize at all the auto-oscillating mode in figure 6.5 (b) might appear surprising. Indeed, it has been shown in various works that the microwave current can phase-lock spin transfer driven oscillations [94, 90, 95, 96]. This can be explained by the fact that in these studies, the STT microwave component, which is not zero due to the misalignment of the thick and thin layers [44, 45, 41], is efficient to synchronize the auto-oscillating mode (still, less than a uniform microwave field in general [22, 99]). In the exact perpendicular configuration, this STT microwave component vanishes, and $i_{\rm rf}$ can only excite $\ell = +1$ SW modes [41]. Therefore, it has the wrong symmetry to couple to the auto-oscillating mode, which bares the azimuthal index $\ell = 0$, as demonstrated above. We add that in our exact axially symmetrical case, no phase-locking behavior is observed with the even synchronization index $r = 2$ (r is the ratio of the external frequency to the STNO frequency) , neither with $i_{\rm rf}$, nor with $h_{\rm rf}$, which is due to the perfectly circular STNO trajectory.

6.2. Broken axial symmetry

We have shown in the previous sections the experimental data and their analysis in the high symmetry perpendicular configuration. We have identified the auto-oscillating mode which is the lowest energy, most uniform SW mode of the thin layer. In addition we have demonstrated that only a microwave magnetic field is efficient to synchronize this auto-oscillating mode. Moreover we have seen that only $\ell = +1$ modes are excited by the RF current flowing through the nano-pillar, due to the orthoradial symmetry of the induced RF Oersted field produced by the rf current. Because there is no overlap between this particular excitation symmetry and the uniform azimuthal symmetry of the $\ell = 0$ modes, the latter do not couple to the RF current excitation. Naletov et al. [41] demonstrated that the MRFM spectra excited by RF current change by introducing a small angle θ_H between the applied field and the normal to the nano-pillar. In fact this change is seen by the appearance of resonance peaks at the positions of $\ell = 0$ modes. It means that the latter can be excited by the rf current if the applied field is tilted away from the normal to the nano-pillar. An open question in this case arises: what is the influence of the polar angle θ_H on the auto-oscillating mode? Is there some characteristic spectral features of this mode with the breaking of the axial symmetry?

In the following, we review the main experimental results that have been obtained when a small misalignment angle $\theta_H = 2°$ is introduced between the applied filed and the normal to the layers. First, we experimentally report on the appearance of two modes when the sample is excited by a dc current flowing through the nano-pillar. Second, we have cheeked what happens if one of these two modes is interacting with an external source. Here it contains both MRFM data and spectrum analyzer (SATM) (measurement of the voltage oscillations in the frequency domain) in order to report a comprehensive analysis of the data.

6.2.1. Autonomous regime

As already mentioned, stimulated emission favors the occurence of a single mode of oscillation. Thus, only one mode is believed to auto-oscillate at the same time, this coincides with the basic assumption of the universal oscillator model, although jumps between several auto-oscillating modes have been reported [152, 130, 131]. In the following we shall show that mode competition can exist and there are situations where two modes auto-oscillate at the same time in our STNO. In fact, as in a laser, a multimode emission can occur, but this requires that the modes are phase decoupled. In our case, we will show that this condition is met for modes differring by their azimuthal index ℓ.

Let us first focus on figure 6.7, which compares the MRFM spectra excited by a uniform RF magnetic field at 8.1 GHz to the one excited by an RF current flowing through the nano-pillar at same frequency. Theses spectra are acquired at different angle from the exact perpendicularity and at current I_{dc}=0 (passive regime). Two important features are clearly visible, first, the $\ell = 0, 1$ SW modes spectrum are shifted towards lower field as θ_H increases. Second, it is clear that the mode $\ell = 0$ is excited by the RF current. These two effects have been explained in details in Reference [41]. To summarize, the resonance peaks at $\theta_H = 2°$ are labeled according to the SW modes precession profiles and reported in Table 6.1.

①	②	③	④
10.24 kOe	9.20 kOe	9.06 kOe	8.19 kOe
B_{00}	B_{01}	B_{00}	B_{01}
❶	❷	❸	❹
10.24 kOe	9.77 kOe	8.72 kOe	8.62 kOe
B_{00}	B_{10}	B_{11}	B_{10}

Table 6.1.: *The resonance fields values for the spin wave modes. The shown in blue (red) is the location of the SW modes measured experimentally in the figure 6.7 ($\theta_H = 2°$) . Second line are the experimental field peaks measured at f=8.1 GHz by sweeping the field.*

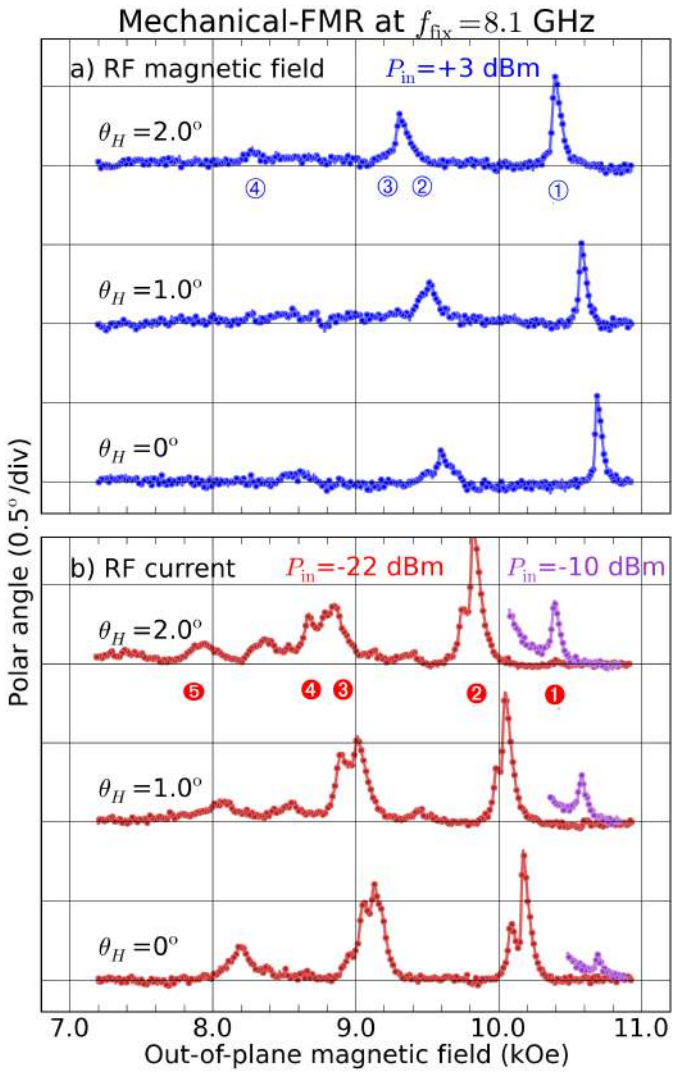

Figure 6.7.: ***Eigen modes at*** $\theta_H = 2°$. *Dependence of the mechanical-FMR spectra excited by a uniform RF magnetic field (a) and by an RF current flowing through the nano-pillar (b) on the polar angle* θ_H *between the applied field and the normal to the layers. Superposed (in violet) is the behavior of the high field peak at larger power to reveal the effect better.*

We have already mentioned that at $\theta_H = 2°$ it is possible to measure the auto-oscillations with a SATM technique, this is due to the small change of relative angle between thick and thin layers while the latter is precessing.

Now we will take advantage of this, and we will measure our sample by SATM technique. We recall here that, we are able to measure this simultaneously to the acquisition of the MRFM signal. In figure 6.8, the evolution of the auto-oscillation as a function of the bias dc current I_{dc} is presented, the bias field being fixed to H_{ext}= 9.14 kOe. The positions of the linear frequencies of modes $\ell = 0$ and $\ell = 1$ at this field are determined by standard MRFM measurements in the linear regime see table 6.1. f_0 = 6.78 +/- 0.12 GHz and f_1= 7.95 +/- 0.2 GHz are indicated by the horizontal blue and red rectangles, together with the associated mode profiles. Here, we drop the radial index n in the mode labeling ($n = 0$). From MRFM measurements, it is possible to follow the position of these two modes as a function of $I_{\rm dc}$ from the linear regime to the auto-oscillation regime, (same as shown before but with angle $\theta_H = 2°$) and to demonstrate that the two auto-oscillation peaks observed in figure 6.8 between -6.5 and -8 mA indeed correspond to these two lowest energy modes $\ell = 0$ and $\ell = 1$ (see figure 6.11 in subsection 6.2.2).

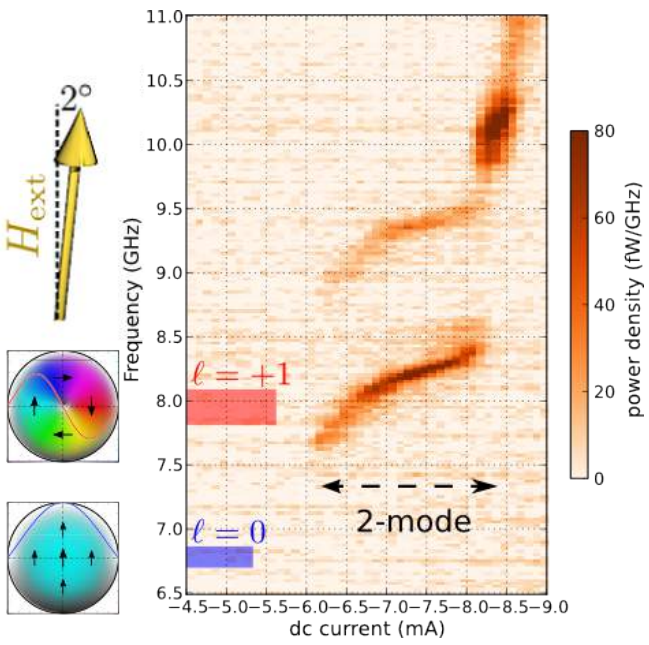

Figure 6.8.: *Power density spectrum as a function of current and applied magnetic field. Here a dc current is injected to excite the thin layer via spin transfer. the two mode $\ell = 0$ and $\ell = 1$ have different critical current.*

Two main features can be noticed in the power spectrum of figure 6.8. The first one is that the threshold current for the two modes are different : the first peak, which correspond to the mode $\ell = 0$ visible until -6 mA. Starting from -6.5 mA the mode $\ell = 1$ at GHz is visible. The second interesting feature is that beyond -8 mA, a simple one-mode generation regime is established in the system. At the moment, there is no clear understanding of the process leading to this transition. Here we will focus in the bi-modal region. For this,

it is important to note that we cannot tell anything about the relative powers p_0 and p_1 from the SA analyzer data, even if the modes do coexist. This is because for the same excitation amplitude of these two modes, $a_0 = a_1$, the voltage detection should yield a larger signal for the most uniform mode. Due to the mirror symmetry, there should not be any high frequency voltage produced at f_1 by the mode $\ell = 1$. However, one should remember that due to the breaking of axial symmetry by the applied field, the $\ell = 1$ mode profile is actually slightly asymmetric (one precession lobe is larger than the other), and also, that due to the Oersted field produced by the dc current flowing through the pillar, both the thick and thin Py layers should adopt a slightly curling configuration. This could explain why a signal is actually detected. So to detect the total power generated by the STNO, we use now the MRFM technique. Figure 6.9 displays the measurement of the STNO power vs. I_{dc}, measured by MRFM for the same total bias field as in figure 6.8 (taking into account the strayfield of the MRFM probe). For comparison, we have plotted together with the data at $\theta_H = 2°$ those obtained at $\theta_H = 0°$. It is quite remarkable that breaking the axial symmetry with the small tilt of the bias magnetic field leads to such a qualitative change. Here we measure all the power produced by the device. The problem is that we can't separate the power generated by either mode ($p = p_0 + p_1$). But if we look to the range of the applied currents [-6 mA , -8 mA] we can see that the behavior of the power change his slope, this is the signature of the presence of two mode generation.

To make this more clear, we compare qualitatively the obtained measurements of the generated power in our nanopillar with a recent theoretical results [135]. Recently Slobodianiuk [135] has presented a theory of microwave generation in STNOs in which the influence of increasing the thermal noise is taken into account. This theory shows that an increase of thermal noise level is responsible of mediating a two-mode generation regime in STNO. The results of calculations performed using his model are presented in figure 6.9 (a). Here the power are calculated numerically for a value of constant proportional to the temperature $\chi = 1.2$ and the following parameters $4\pi\gamma M_s = 9500$ G, $\nu_0 = 60$ MHz abd $\nu_1 = 1.05\ \nu_0$. As we can see if we compare the experimental measurements presented in figure 6.9 with the obtained theoretical results (figure 6.9), it is possible to describe the change of slope in the power generated by the STNO in the range of bias current (-6 and -8 mA) by starting the second mode. Indeed, as it's clear from figure 6.9 by the addition of the two analytical expression obtained previously (red and blue curves) gives a qualitative estimate of the observed power generated by the STNO. Then, we note here that this formalism description was done as a first step

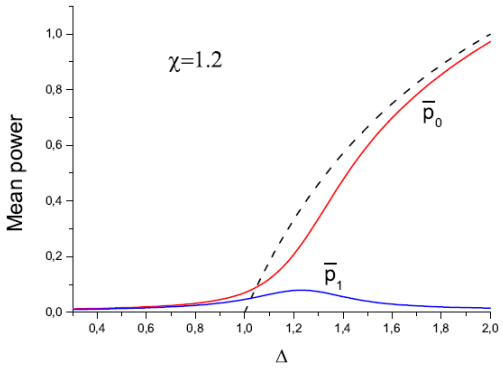

(a) Mean powers calculated as a function of supercriticalities [135].

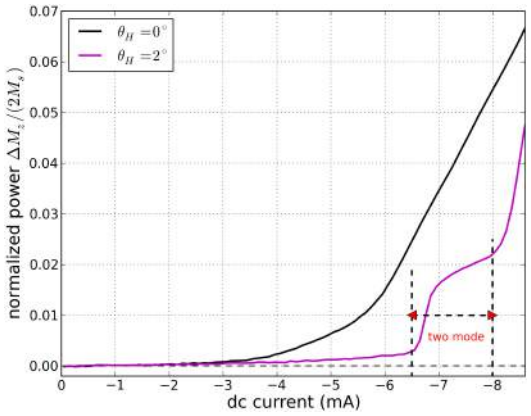

(b) Total power p emitted by the STNO as a function of the bias dc current, measured by MRFM at $\theta_H = 0°$ and $\theta_H = 2°$.

Figure 6.9.: *Qualitative Comparison between theoretical and experimental results*

to determine the origin of the two mode observed experimentally in our device. The coupled equations are very important and very rich So we have only begun to explore the behaviors of the power distribution in our STNO. Not doubt that future work will unravel with quantitive comparaison with the theory

To close this section on the autonomous dynamics of the bi-modal regime, we present in figure 6.10 a more efficient way to distinguish the features of current induced bi-modal excitations. This can be done by keeping the current constant and sweeping the applied field instead. By doing we represent in figure 6.10 the experiment obtained at constant bias current $I_{dc} = -7mA$, by varying the bias magnetic field between 8.5 and 9.6 kOe. This makes it possible to tune the auto-oscillation frequencies f_0 and f_1 on a wider range than what can be done at fixed field by varying the current. In particular,

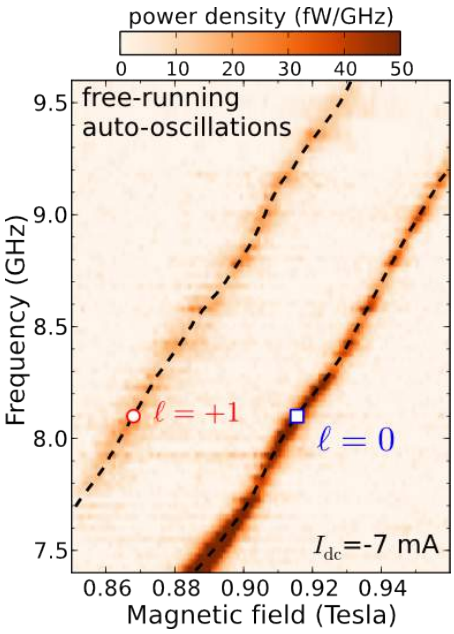

Figure 6.10.: *Frequency evolution of the free running oscillations induced by spin transfer at $I_{dc} = -7$ mA as a function of the magnetic field showing evidence that two modes auto-oscillate ($\ell = 0, 1$).*

it is also worth to mention at this point that the fact that the frequency of the auto-oscillating modes strongly depends on the perpendicular field is an indication of non-linear damping. In fact, without a non-linear contribution to the damping, the generated frequency should remain constant (the larger the field, the smaller the precession angle, therefore the smaller the non-linear frequency shift).

6.2.2. Forced regime

The above experiments clearly show the presence of two modes. An open question arises: are there interactions between them? is it possible to promote one of these two modes by acting on the system with an external source and what happens?

First to investigate the non-autonomous dynamics in the previously identified bi-modal regime, we take advantage of our sample design, that allows us to add to the bias current I_{dc} either an in-plane homogenous RF field hrf or an RF current irf flowing through the layers. So we use now the external source h_{rf} and i_{rf} , while detecting the dynamics with MRFM. In figure 6.11 we have measured the spectral deformations produced on the SW spectra of figure 6.7 when a finite negative current is injected in the nanopillar, we recall that a negative dc current destabilizes the thin layer. Here the offset field from the MRFM magnetic probe has been subtracted and the amplitude of h_{rf} is equal to 1.9 Oe and i_{rf} is equal to 125 μA (which corresponds to an Oersted field of 2.8 Oe at the periphery of the nano-pillar).

The main feature can be observed in the evolution of the SW spectra as I_{dc} varied is an increase of the modes associated to the thin layer. (we remember here that similar study in the exact perpendicular geometry for $-4 < I_{\mathrm{dc}} < 4$ mA have been reported in reference [41]. The negative ΔM_z means that the precession angle is smaller when the RF is on than when it is off, which is associated to lock-in to the external source. Based on the study discussed above (see figure 6.7) in the sub-critical regime, these two modes are identified as the lowest energy spin-wave eigen-modes of the free layer with azimuthal numbers ℓ=0 and ℓ=+1. The fact that these two modes (ℓ=0 and ℓ=+1) can auto-oscillate at the same time is made possible by the fact that each mode is living in his own space due to different spatial symmetry. The mutually exclusive nature of the responses to the uniform and orthoradial symmetry excitations is a property of the preserved axial symmetry, where the azimuthal index ℓ is here a good quantum number, i.e., different ℓ-index modes are not mixed and can be excited separately.

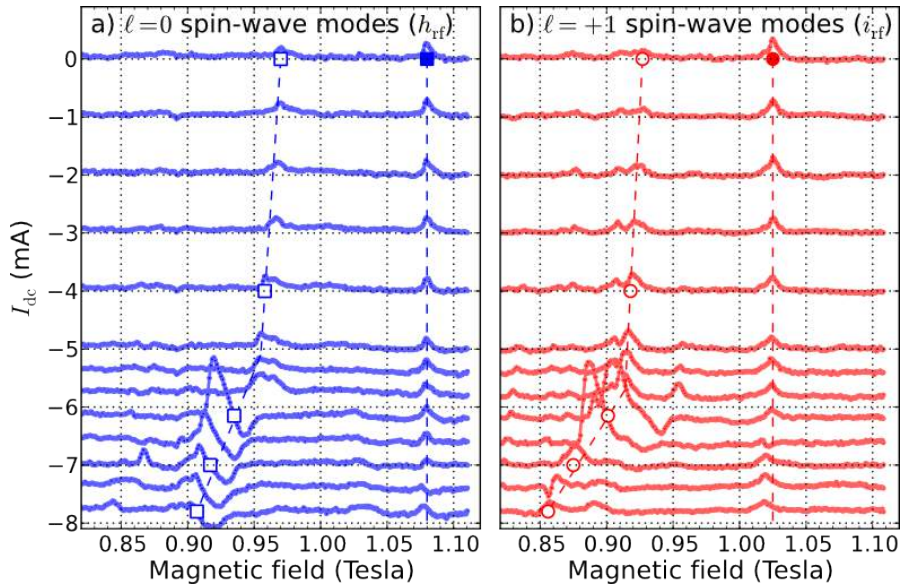

Figure 6.11.: *a) Evolution of the $\ell = 0$ SW modes excited by a uniform RF magnetic field and b) of the $\ell = +1$ SW modes excited by an RF current flowing through the nano-pillar as a function of the negative dc current bias. The FMR spectra are acquired by MRFM at fixed frequency $f = 8.1$ GHz by sweeping the applied magnetic field. The open (close) symbols indicate SW modes associated to mainly the thin (thick) layer, and the dashed lines are guides to the eye.*

To gain further insight about how above the threshold the two free-running modes are affected by an external source. In figure 6.12, we present the experimental data obtained in the same conditions as we present in figure 6.10 , plus with the external source $h_{\rm rf}$ at f=8.1 GHz (figure 6.12 (a)) and $i_{\rm rf}$ at f=9.2 GHz (figure 6.12 (b)). In both cases, one observes clearly that the auto-oscillating modes can be locked to an external source having the appropriate symmetry and a frequency close to the free-running frequency light blue (light red) line in figure 6.12 (a) (figure 6.12 (b)). The striking result here is that the external signal does not affect only the auto-oscillating mode which has its free-running frequency close to the external frequency and the appropriate spatial symmetry, but also the other auto-oscillating mode, in a quite similar way. It is particularly clear on figure 6.12 (a), where the external RF field synchronizes the $\ell = 0$ auto-oscillating mode between 9 kOe and 9.3 kOe at f=8.1 GHz: at the same time, the frequency of the $\ell = 1$ mode becomes almost constant at slightly more than 9.2 GHz (see partially transparent light red line). Note that in contrast, $h_{\rm rf}$ does not affect directly the $\ell = 1$ mode at 8.1 GHz, around H=8.7 kOe, because it has the wrong spatial symmetry. The influence of the RF current at f=9.2 GHz on the power density map of figure 6.12 (c) looks quite more complicated, but clearly, the behavior of mode $\ell = 0$, whose free-running

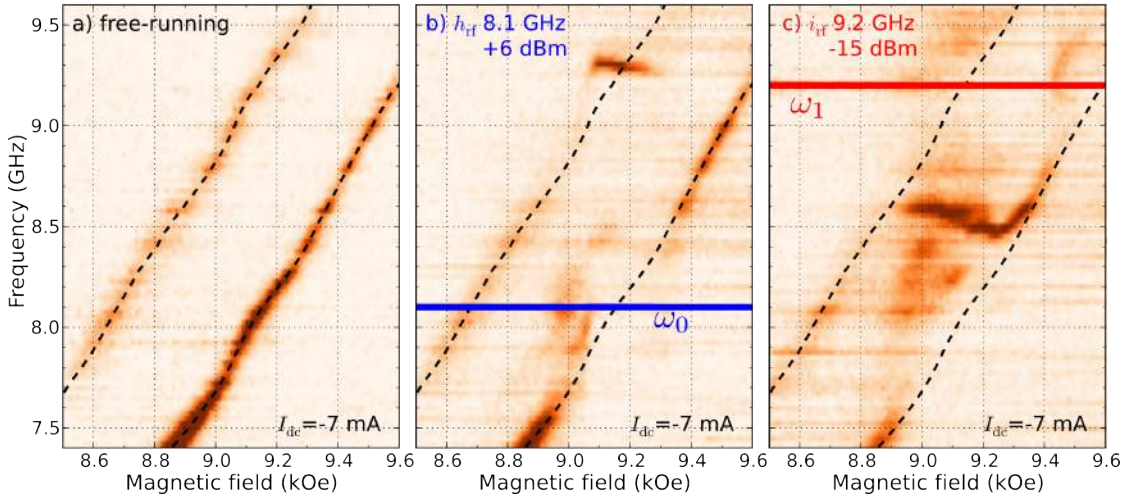

Figure 6.12.: *a) Behavior of the auto-oscillations at $I_{dc} = -7$ mA in the free running oscillation and b) in the presence of the uniform RF field generated by the external antenna at 8.1 GHz ($h_{rf} = 2.7$ G, thick blue line) and c) of the RF current flowing through the nano-pillar at 9.2 GHz ($i_{rf} = 350$ μA, thick red line).*

frequency is about 1 GHz below the external source, is strongly affected on a broad range of magnetic field. Here, when one tries to synchronize the $\ell = 1$, the mode $\ell = 0$ at f_0 locks to an intermediate frequency between f_0 and f_1. To clarify this situation, it should be remember that there is a asymmetric between rf field and rf current excitation. In particular, the rf current excitation excites the $\ell = 0$ mode at $\theta_H = 2°$, while the inverse is not true: the rf magnetic field does not excite the $\ell = 1$ mode at $\theta_H = 2°$. The difference is explained above in the previous subsection. Thus when a rf current is injected inside the $\ell = 0$ mode will try to also synchronize with the f_1 frequency. It thus shall move up in frequency by $\sqrt{(f_1 - f_0)^2 - \Delta^2}$, where Δ expresses on the strength of the ST-FMR.

The evolution of the $\ell = 0, 1$ modes as the power increases are also investigated. The spectral analysis of the mode $\ell = 1$ is presented in figure 6.13a (frequency), 6.13b (linewidth) and 6.13c (amplitude). We can see how the pseudo-synchronization of the mode $\ell = 1$ evolves: its range increases with power (same as the $\ell = 0$ mode), but at the same time, the pseudo-synchronization frequency also increases. A striking reduction of the linewidth of the $\ell = 1$ mode can also be observed, as it drops from almost 200 MHz down to less 50 MHz. A natural explanation would be some kind of mode cooling mechanism: by phase-locking the mode $\ell = 0$ with the external source, its frequency, hence its amplitude, gets stabilized. As a result, its influence on the linewidth of mode $\ell = 1$ through nonlinear cross-terms is suppressed. Hence, mode $\ell = 1$ exhibits its intrinsic linewidth, with the contribution of only self nonlinear interactions. See figure 6.14 for a

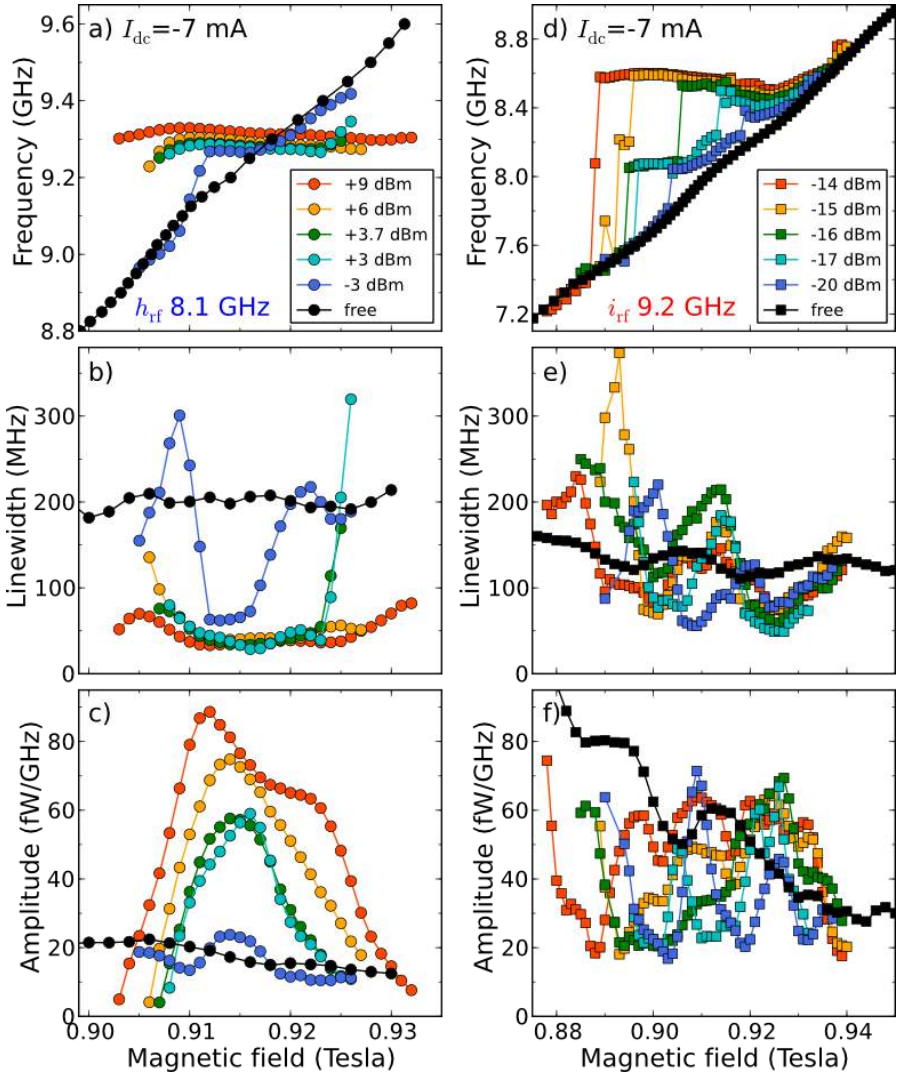

Figure 6.13.: *a-c) Emission characteristics of the mode $\ell = +1$ as a function of the amplitude of the uniform RF field used to lock the mode $\ell = 0$ at 8.1 GHz (as in figure 6.12 (a)): center frequency, linewidth, and amplitude, from top to bottom. e-f) Emission characteristics of the mode$\ell = 0$ as a function of the amplitude of the RF current used to lock the mode$\ell = +1$ at 9.2 GHz (as in 6.12 (b))*

direct experimental evidence of this mode cooling in the frequency domain.

As already stated before, the behavior of auto-oscillations in the bi-modal regime in the presence of the external source i_{rf} looks more complex. But looking at the power dependence in figure 6.13 (d) to (f) does help a little bit to understand what is going on. In fact, it is clear that the frequency of the mode $\ell = 0$ would like to jump to some constant frequency branch somewhere around 8.5 GHz, in between the two auto-oscillating modes. At low power, it does not do it in one step, but reather in two, as it is clear from figure 6.13 (d). It is difficult to comment on the variation of the linewidth and of the amplitude, which are plotted in figure 6.13 (e) and (f), as the previously mentioned steps introduce some broadening, and also, there are some weak broad features at lower frequency than the main peak. At the same time, it is hard to see what is happening with mode $\ell = 1$. It looks like it almost disappears from the power map, still there is some weak broad feature above the external frequency f=9.2 GHz. Finally, we recall here that the SA measurements do not permit to follow the auto-oscillations in the close vicinity of the external frequency, because the latter is adding a huge signal to the STNO's emission, which is hidden under the thick blue and red continuous lines in figure (6.12).

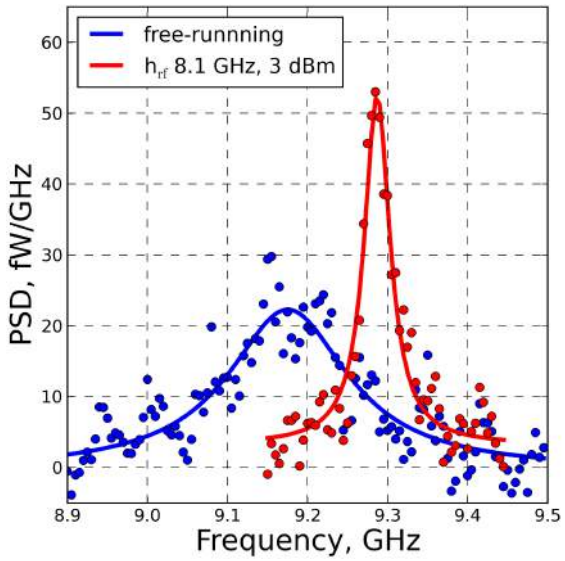

Figure 6.14: Mode cooling *introduced in the discussion of figure 6.13. We remind the striking result here: the linewidth of the mode $\ell = 1$ that auto-oscillates at 9.2 GHz decreases by more than a factor 4 (here, from 183 to 39 MHz) when the $\ell = 0$ mode, which auto-oscillates at a frequency 1.1 GHz below the mode $\ell = 1$, gets phase-locked to the external uniform RF field. The upward frequency shift (100 MHz) which accompanies this mode cooling is also clearly recorded.*

6.2.3. Synchronization: SATM data vs. MRFM data

We have already mentioned that our experimental setup allows to monitor the ac voltage produced across the nano-pillar by the precession of the magnetization in the bi-layer structure. A spectrum analyzer is used to measure the ac voltage across the nano-pillar when the I_{dc} current pass through the sample. This can be done *simultaneously* to the acquisition of the MRFM signal, in the exact same conditions. Taking advantage of this, one can compare the auto-oscillation frequency in the free (black squares in figure 6.15 (a)) and forced regimes (blue dots). The resulting frequency shift (blue dots in 6.15 (b)) can then be quantitatively compared to the MRFM signal, that has a characteristic shape with a positive and negative lobes around the center frequency (black line , which is a cut at constant current $I_{dc} = -7mA$ of figure 6.11 (a)). From this, we can also again confirm that in the so-called phase-locking range, the STNO amplitude adapts ($\Delta M_z > 0$: increases, $\Delta M_z < 0$: decreases), so as to maintain its frequency equal to the frequency of the source, here fixed at 8.1 GHz (see figure 6.6). This comparison also allows to estimate the phase-locking bandwidth, found to be as large as 0.2 GHz despite the small amplitude of the external signal. From this, one can determine the nonlinear frequency shift N = $\Delta M_z/(M_s B) \simeq 85$ GHz. This value is much larger than $N = 4\gamma M_s$. In fact the nonlinear frequency shift N strongly depends on the angle of the applied field. Its largest value is reached in the exact perpendicular

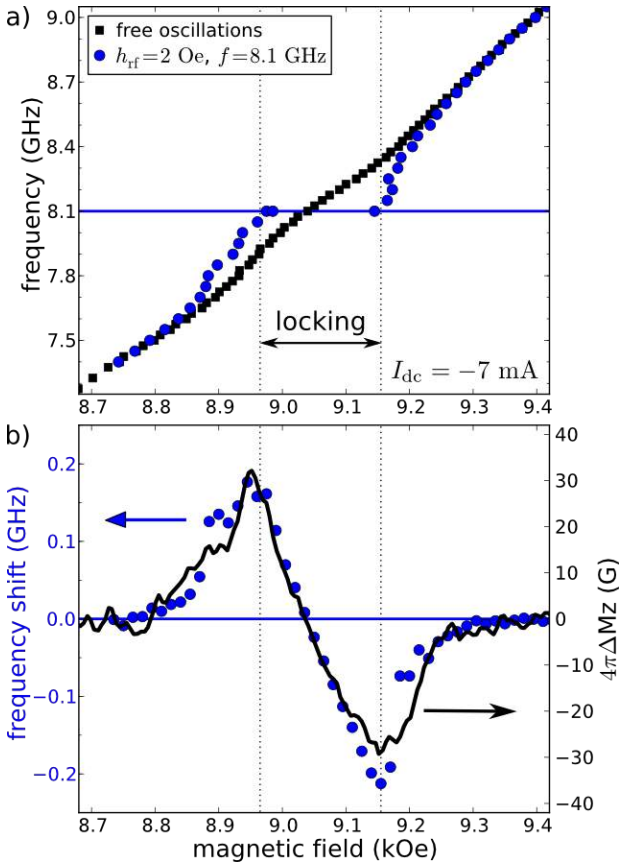

Figure 6.15.: *a) Magnetic field dependence of the STNO frequency in the free and forced regimes (the external source at 8.1 GHz is h rf). b) Comparison between the STNO frequency shift deduced from (a) and the MRFM signal.*

configuration ($\theta_H = 0°$) , which corresponds to the largest demagnetizing effect. For our sample parameters, this maximal value is close to 48 GHz. At ($\theta_H = 2°$), it drops to a value that ranges between 25 and 40 GHz, depending on the exact bias magnetic field (see figure 6.1). Therefore, to explain this apparent nonlinear frequency shift N so large (75-85 GHz, instead of 25-40 GHz) it is important to recall that the expression of N plotted in figure 6.1 is given for a uniform precession profile in an infinite layer. Due to finite size effects, both the internal field and the mode profiles are non-uniform in the nanopillar, which results in a larger N coefficient [153] .

6.3. Spin transfer dynamics at large applied current

In this section we perform a comparitive study between the auto-oscillation mode of the thin layer at low current ($I_{\rm dc} < |15|$ mA) and the coupled oscillations mode between thick and thin layers observed at larger current. In fact at sufficiently high currents we excite dynamical mode involving motion of the thin layer magnetic moment as well as the thick-layer moment. This mode is characterized by very narrow peak linewidth in the frequency spectrum of oscillations compared to the thin-layer mode which excited by low current, and the frequency of this mode is lower that the thin-layer mode.

6.3.1. Excitation of coupled dynamics modes

Here we use SATM technique to extend to high current characterization of dynamical coupled mode between the thin and the thick layer observed previously in [121, 154]. The orientation of the magnetic field in this measurement is perpendicular to the sample, with 2° of tilt toward the easy axis of the layers. We have previously determined the type of magnetic dynamics associated with ΔM_z and resistance changes, specially one of the thin layer, now we will show other mode excited when a large dc current injected in the same STNO presented previously. The full dependence of the power spectra on $I_{\rm dc}$ is shown for value of $H_{\rm ext}$ = 8.2 Oe in figure 6.16. This field is greater than the effective $4\pi M_s = 8\ kOe$ for the thin magnetic layer, so for $I_{\rm dc}$=0 the thin layer moment is aligned along $H_{\rm ext}$, while the thick layer moment is titled several degree out of plane (for thick layer $4\pi M_s = 8.8kOe$). As a function of increasing $I_{\rm dc}$, we have shown before that the angle precession of the free layer increase. Then from the data in figure 6.16 it is evident that at $H_{\rm ext}$ = 8.2 kOe the peak in the microwave signal observed at f=10 GHz for $I_{\rm dc}$

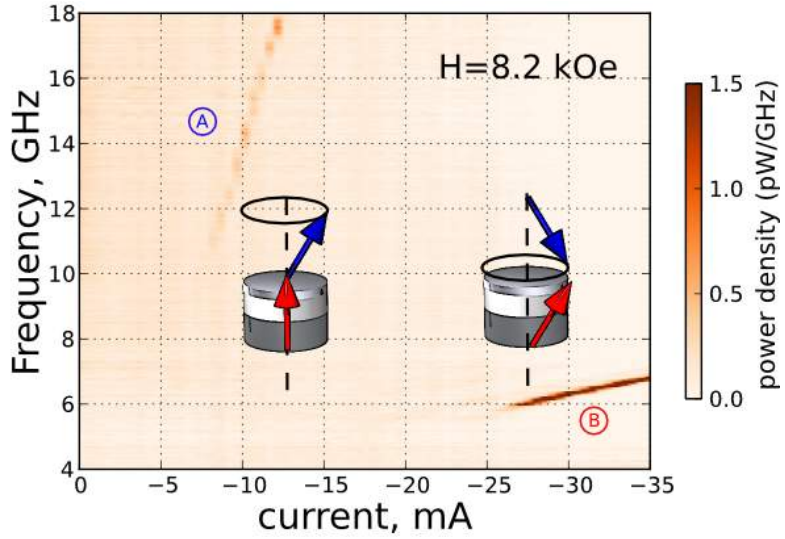

Figure 6.16.: *Microwave power density as a function of frequency and current, measured for an external magnetic field H_{ext} = 8.2 Oe. The frequency of the mode of the thin layer grows linearly as a function of current. At I_{dc}=-20mA the mode drops from free layer mode to a coupling mode between the thin and the thick layer.*

as small as -8 mA, correspond to small angle precession of the thin layer (this mode is labeled as Ⓐ). After as function of increasing I_{dc} up to -8 mA, the frequency of the microwave signal increases. This behavior was observed previously in figure 6.8 and it was identified with the increasing of ΔM_z i.e power. Here the maximum frequency at which our amplifier is working is 18 GHz, this is why the microwave signal is shown in this range of frequency (4 - 18 GHz). For larger I_{dc}, at approximately -25 mA, the microwave signal exhibits a dramatic drop to a frequency 6 GHz with a simultaneous jump in power density (mode labeled as Ⓑ). This step can be explained by a reversal of the free layer's precession axis to anti-parallel to the thick layer. Indeed, the large negative currents apply a torque on the thin and thick layers which are strongly coupled by their spin transfer torques as well as by dipolar coupling between the layers. Then the resulting is a coupling mode between the thin and the thick layers, which correspond to a precession of the thick layer, likely coupled to the thin layer.

6.3.2. Characterization of coupled dynamics modes

Our main objective is to compare the output rf signal characteristics for the cases of a dynamics free layer mode and a dynamics coupled thin and thick mode. For this

purpose, an analysis of the dependence of the frequency (a), linewidth (b) and power (c) on the current for these modes are presented in figure 6.17.

Let us first consider the frequency of mode Ⓐ and Ⓑ as a function of I_{dc}. In figure 6.17 (a) we plot the positions of the frequencies of all of the steps in I_{dc}. The blue (red) symbols illustrate the frequencies that are observed for mode Ⓐ (Ⓑ). Mode Ⓐ grows as a function of I_{dc} with a slope of 1.8 GHz/mA, but Ⓑ grows with a slope of 0.12 GHZ/mA. This change of slope of frequency versus current may be interpreted as a reduction of the nonlinear frequency shift(we will explain the physical origin of this effect later) in a STNO where the generation frequency is linked to this parameter. Regarding the linewidth of modes (see figure 6.17 (b)), it has been observed that the linewidth is reduced almost by factor of 10 in the region with thick-thin layers dynamics which correspond to increase of the quality factor ($F/\Delta F$) of our oscillator from 40 to 500. The change in linewidth is related to several effects: the first one is that the linewidth is affected by thermal fluctuations (when the temperature is increased the linewidth becoming broader [155, 88]). Then by increasing the volume of the system, there dynamics should be influenced less by thermal fluctuation, this is why the linewidth of the mode Ⓑ (thin+thick layers) is 10 times narrower than the mode Ⓐ (thin layer). The second effect, it's because the coupling between the thin and the thick layers caused by spin-transfer torques can lead to the reduction of the dimensionless non-linear parameter ν [39]. In fact we recall here that the generation linewidth in a STNO is given by this expression:

$$\Delta F = \frac{k_B T}{E_s} \frac{\Gamma_+}{2\pi} (1 + \nu^2) \,, \tag{6.6}$$

It's therefore natural to observe a reduction in linewidth when ν decreases. But this reduction is to the detriment of tunability which is connected to the nonlinear frequency shift N such as $\nu = N p_0 / \Gamma_{eff}$. It deserves to be mentioned here that in reference [39] the authors considered only the interlayer spin transfer torque coupling via the current. But we believe that in our system the dipolar interaction between the layers exist and it leads to the reduction of the coupled mode linewidth. Finally we also observed a significant difference in power output between mode Ⓐ with a single precession layer compared to mode Ⓑ with coupling precession layers. Figure 6.17 (c) shows that the power in Ⓑ was clearly greater than Ⓐ. This change in power is related to the increase in total energy of the magnetization oscillation which is refered as $E_s = \mathcal{N} \hbar \omega$ so by increasing the volune ($\mathcal{N} = V M_s / (g \mu_B)$) so, the energy should increase. Furthermore, because

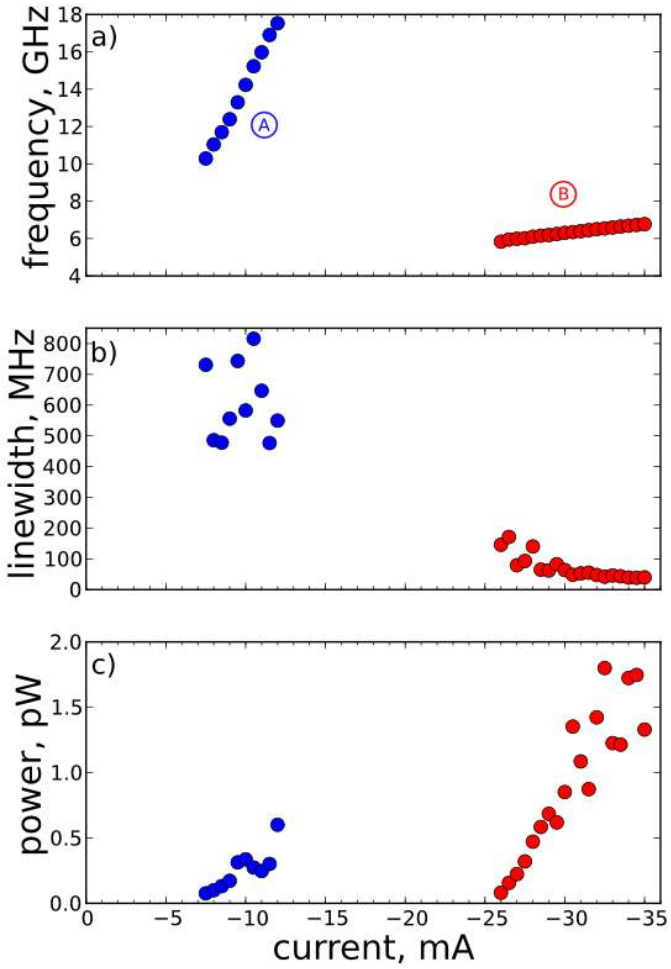

Figure 6.17.: *Spectral analysis on the full range of bias dc current. The blue color is used to highlight the auto-oscillating mode of the thin layer, while the red color highlights the collective mode between thin and thick layers.*

these oscillations occur at large current values, they can produce larger microwave signal than the thin layer oscillations.

6.4. Conclusion

The nature of the auto-oscillating mode in a spin transfer nano-oscillator based on normally magnetized nano-pillar has been investigated using the MRFM and SATM technique. In particular, we considered the high symmetric case between the applied field and the axis of the nano-pillar, as this configuration coincides with the quantitative model proposed by Slavin et al. [22], as well as asymmetric cases by tilting the applied field 2° from the sample normal. Our results show that:

i) **The auto-oscillating mode in high symmetric case consists of the lowest energy mode $(\ell = 0, n = 0)$ dominated by the thin layer.**

ii) **Only a spatially homogenous microwave magnetic field is efficient to synchronize this auto-oscillating mode.**

iii) **Two modes can be excited in the asymetric case $(\ell = 0, n = 0)$ and $(\ell = 1, n = 0)$.**

iv) **Evidence of a non-linear coupling between these two modes which are auto-oscillating at the same time has been experimentally demonstrated.**

v) **The coupled mode involving both the thin and thick layers excited at large current has improved microwave characteristics (linewidth, power) compared to the single mode dominated by the thin layer. We ascribe this mainly to a decrease of non-linearities, as evidenced by the reduction of tunability in the case of coupled mode.**

CHAPTER 7

Nano-pillar in the double-vortex state

This chapter is dedicated to the study of a spin valve nano-pillar structure with coupled magnetic vortices. The sample investigated in the previous chapter is reconsidered, thus, now with nucleation of two vortices, one in each ferromagnetic layer. Indeed, the STNO presented previously can also sustain gyrotropic vortex motion, with generated frequencies below 2 GHz, and is capable of operating under zero applied magnetic field. After, the microwave signal emitted by the STNO will be measured by SATM technique in order to investigate the non-linear characteristics of this device in the vortex state. Moreover, the influence of an external source on the microwave signal generated by this STNO will be highlighted.

7.1. Introduction

We have already presented the spin transfer nano-oscillators based on the excitation of the quasi uniform precession mode. In these experiments high external magnetic fields were required to observe microwave output signals. In 2007 Pribiag et al. have demonstrated that spin torque can also drive a magnetic vortex into gyration [33]. The microwave frequency oscillations of magnetic vortex have been observed both in nano-pillar [33, 35] and nano-contact geometry [156, 79]. Recently it has also been demonstrated that such vortex based STNO might work in absence of external field [85]. Therefore, these results allow considering the magnetic vortex motion as an important configuration of the spin torque nano-oscillator. Then, it became very interesting to study the vortex configuration not only from fundamental point of view but also as a promising class of new generation of nano-scale functional microwave devices . In particular, very narrow linewidths [40] and large TMR output signal [35] are promising for the applications. In this section, we will introduce the particular case of STNO based on coupled magnetic vortices [40].

Dynamics of two coupled vortices in STNO

As mentioned previously, the integration of STNOs in high frequency circuits depends on various conditions. The important parameters are the linewidth, and the generated power signal. Further research efforts are being devoted to optimization of these parameters. Recently, to increase the power of the signal of the STNO based vortex, a new device was proposed by A. Dussaux et al.[35]. The device is circular shape nanopillar with a radius of 85 nm patterned from the whole magnetic stack : synthetic anti-ferromagnet MgO (1.075 nm)/NiFe (15 nm)/capping. In this configuration, the vortex dynamics is converted into a microwave signal thanks to the large magneto-resistive ratio of the Tunnel Magnetoresistance effect (TMR) leading to microwave emissions combining large power (5 nW). But the linewidth in this device is limited to 1 MHz. In order, to improve the spectral linewidth of the vortex oscillator. One solution proposed in a metallic system is to use a spin transfer nano-oscillator driven dynamics of coupled vortices. Indeed, recently Locatelli et al.[40] demonstrated that two coupled vortices in a metallic nanopillar can reduce the linewidth of the microwave signals, see figure 7.1 (c). It has been also shown that, using injected current and external magnetic field, it is possible to independently control and discriminate vortex chiralities and polarities

in this system which contains two vortices, one in each magnetic layer. Figure 7.1 (a) shows the dependence of the resistance of the nanopillar device[1] on current at zero field. At I = +30 mA, the two chiralities are parallel and positive, as the current is decreased, a jump of resistance is observed I_{dc} = −3 mA, which is associated to the transition from parallel to anti-parallel chiralities (here, the Oersted field reverses the chirality of the vortex in thin Py layer). This state is conserved up to -18 mA, when a drop of resistance corresponding to the parallel chiralities is observed again (here, the large Oersted field reverses the chirality of the vortex in thick Py layer). Note that as the current is then swept back similar features are observed. Then, through the application of an external perpendicular field it is possible to control the polarities of each vortex. An important result, shown by the authors is that a microwave signal is observed only when the two polarities are opposite. Figure 7.1 (b) shows the evolution of the frequency of the signal peak as a function of applied field at I_{dc} = +20mA, for configurations with parallel positive chiralities and opposite polarities. As can be seen, the dependence of the frequency on magnetic field is linear, with the sign of the slope related to the orientation of the core polarity which indicates that the dynamical behavior is governed by the vortex in the thick layer. A highly coherent signal linewidth down to 46 kHz can be observed (see figure 7.1 (c)) for current and bias field conditions. An open question is raised here: What's the origin of this narrow linewidth? Therefore, the next section is dedicated to study this trilayer structure where both ferromagnetic layers are found to be in a vortex state in order to give the answer to this question.

Before closing this section, we would like to give a very recent example of successful idea to improve the STNO microwave signal. Indeed, Lebrun et al. proposed a device based on more complex hybrid structure, a Magnetic Tunnel Junction (MTJ) beneath a GMR spin-valve having a vortex in each magnetic layer (one thin and one thick) that are coupled by dipolar interaction. The purpose is to take advantage of having both a large emitted power due to large TMR ratio and a good quality factor due the mode excitation of coupled vortices. It permits to combine narrow linewidth (around 100 kHz) and large power (up to a few hundred of nanowatts) at zero external magnetic field and room temperature [157].

[1] Here this device has the same structure of our device i.e. a circular nanopillar of nominal diameter 200 nm patterned from a (Cu60|Py_B15 |Cu10|Py_A4|Au25) stack, where thicknesses are in nm and Py=$Ni_{80}Fe_{20}$

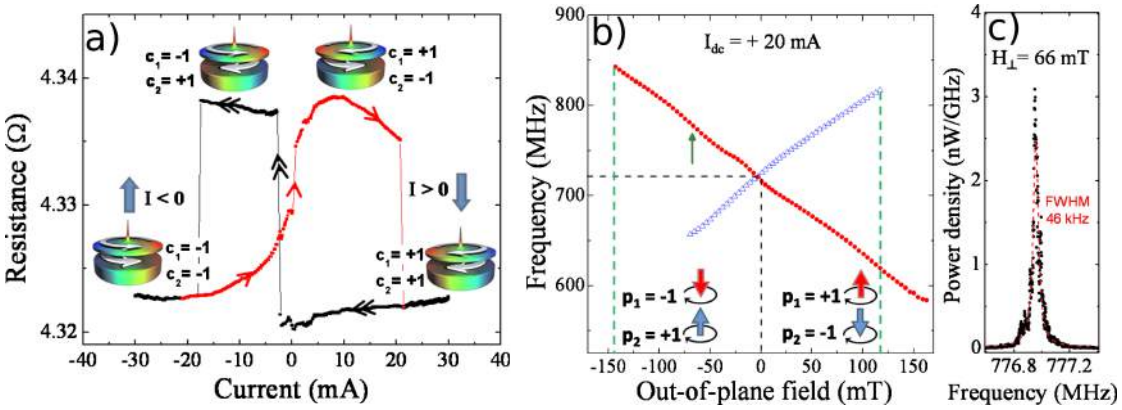

Figure 7.1.: *Resistance evolution versus dc-current, measured at zero external magnetic field. Schematics represent the magnetic configuration in thin Py(4nm) and thick Py(15nm) layers, big arrows correspond to vortices chiralities. Low resistance is associated to the observation of two-vortices state with identical chiralities, whereas hight resistance is associated to the observation of two-vortices state with opposite chiralities. Here, the increase of resistance associated with Joule heating was subtracted. (b) Dependence of microwave frequencies on perpendicular magnetic field for I=20 mA and configurations with positive chiralities and opposite polarities. The red circles show experimental data obtained for $p_1 = +1$ and $p_2 = 1$. The blue triangles show the symmetric case. (c) Microwave peak with ΔF = 46 kHz for H = 66 mT and I = 20 mA. The continuous red line is a Lorentzian fit to the data. Figures taken from reference [40]*

7.2. Autonomous regime: analysis of linewidth and tunability

A particularity of STNOs compared to other oscillators is their strong nonlinear properties, which are inherited from the equation of motion of magnetization [22]. On one hand, they confer interesting properties to STNOs, as for instance their large frequency tunability [120, 158]. On the other hand, they lead to a severe broadening of the generation linewidth [23]: due to nonlinear phase-amplitude coupling, the phase noise of STNOs is indeed rather large [24, 25], which is the main limiting factor to their practical applications.

As we mentioned previously, some of the best microwave characteristics have been reported for STNOs in which spin transfer torque (STT) excites the gyrotropic mode of a magnetic vortex [33]. It results in microwave emission in the range 100 MHz –2 GHz characterized by a narrow linewidth (about 1 MHz) and large output power in the case of TMR devices [35]. Moreover, the oscillation frequency of vortex-based STNOs can be rapidly modified between different values using the bias current, which demonstrates their high agility and tunability in current [159]. Recently, Locatelli et al. have reported a record high spectral purity (quality factor $Q > 15000$) in a spin-valve nano-pillar where

STT drives the dynamics of two coupled vortices (one in each ferromagnetic layer) [40]. In such a STNO, the generation linewidth at fixed dc current I_{dc} displays strong variations (from 40 kHz to 1 MHz) on the applied perpendicular field $H_\perp$. At the same time, its frequency tunability $dF/dI_{dc} \simeq 7$ MHz/mA remains almost constant which points out that spectral purity and tuning sensitivity are not necessarily correlated. In this section, we aim at understanding the physical origin of these peculiar behaviors, as this will give hints to optimize the characteristics of STNOs.

7.2.1. High frequency properties

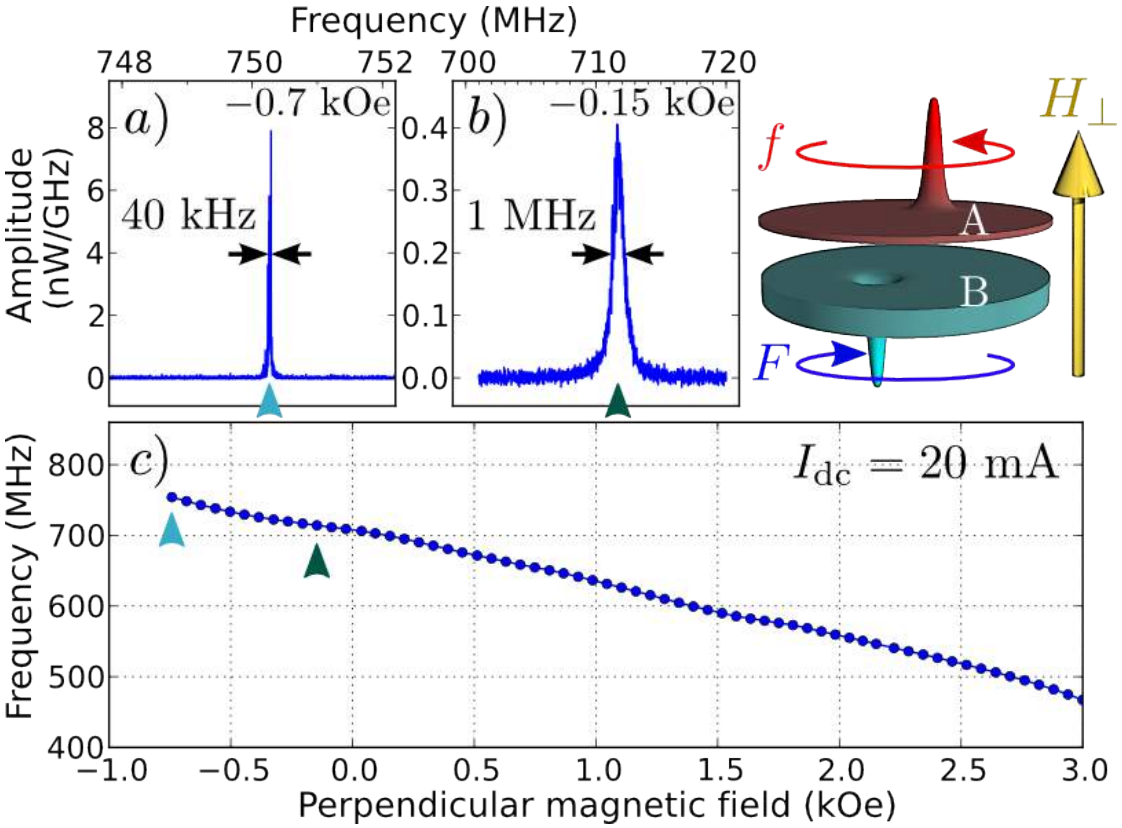

Figure 7.2.: *Upper right sketch: STNO based on coupled vortices. (a) Power density spectra measured at I_{dc} = 20 mA and a perpendicular magnetic field $H_\perp$ = −0.7 kOe and (b) $H_\perp$ = −0.15 kOe. (c) Dependence of the fundamental oscillation frequency on $H_\perp$.*

Here, the studied STNO is the same sample investigated in the previous chapter, but, now with the non-uniform magnetization profile of both layers i.e two vortices, one in each ferromagnetic layer. Indeed, our STNO can sustain the double vortex configuration

[40, 160]. We remember that a current $I_{dc} > 0$ is injected through the STNO using the bottom Cu and top Au electrodes, which corresponds to electrons flowing from the thick Py_B to the thin Py_A layer. In both Py layers, the vortex chiralities are parallel to the orthoradial Oersted field produced by I_{dc}. We use a magnetic field $H_\perp$ perpendicular to the sample plane in order to control the relative orientation of the vortex core polarities $p_A$and p_B. As shown in Ref.[40], we observe a narrow microwave signal only in the case when they are opposite, $p_A p_B = -1$, and when I_{dc} exceeds a threshold current $I_{th} \simeq 8$ to 11 mA depending on $H_\perp$. The spontaneous microwave emission branch at $I_{dc} = 20$ mA for which $p_A = +1$ and $p_B = -1$ is displayed in figure 7.2 (c). The oscillation frequency linearly decreases with increasing $H_\perp$, as expected for a gyrotropic mode dominated by the thick layer vortex, whose polarity is antiparallel to the applied field [61]. The observed emission frequency, which decreases from 750 MHz to 450 MHz as $H_\perp$ increases from −0.7 kOe to 3 kOe, agrees well [40] with the expected gyrotropic frequency for the thick Py_B layer augmented with the contributions of the Oersted field [76, 83] and of the dipolar coupling to the thin Py_A layer [161]. The boundaries of the frequency branch shown in figure 7.2 (c) result from the combined action of $H_\perp$ and STT to reverse the vortex cores in the Py layers [162].

7.2.2. Origin of narrow linewidth

Our aim is to understand why the linewidth of our oscillator can increase by more than a factor 20 (up to 1 MHz), and moreover what is the necessary condition to obtain the highest spectral purity. For this purpose, let's first concentrate on the dependence of the generation linewidth on $H_\perp$, which is plotted in figure 7.3 (a) using dark blue symbols (ΔF_1). It displays minima down to 40 kHz ($F_1/\Delta F_1 \simeq 19000$) and maxima up to 1 MHz ($F_1/\Delta F_1 \simeq 700$), *i.e.*, a decrease of spectral purity by more than a factor 25 by changing $H_\perp$ from −0.7 kOe [figure 7.2 (a)] to −0.15 kOe [figure 7.2 (b)]. We first note that the strong variations of the linewidth observed at $I_{dc} = 20$ mA cannot be attributed to changes of the nearly constant supercriticality ($I_{dc}/I_{th} \simeq 2$) or integrated power (0.32 pW at $H_\perp = -0.7$ kOe vs. 0.4 pW at $H_\perp = -0.15$ kOe (see figures .7.2 (a) and (b)). As already mentioned, the generation linewidth of a nonlinear auto-oscillator can be written as [23]:

$$\Delta F_g = \frac{k_B T}{E_s} \frac{\Gamma_+}{2\pi} (1 + \nu^2) , \tag{7.1}$$

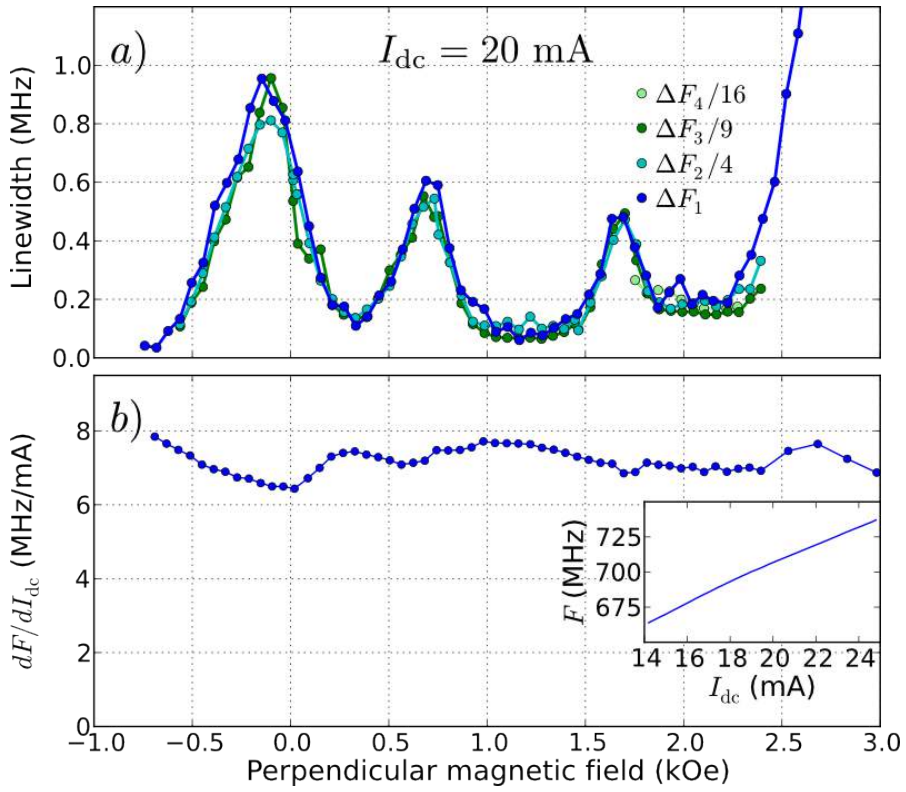

Figure 7.3.: *(a) Generation linewidths of harmonics $n = 1$ to 4 divided by n^2 as a function of $H_\perp$. (b) Frequency tunability vs. $H_\perp$. Inset: dependence of the oscillation frequency on I_{dc} measured at $H_\perp = 0$ kOe.*

we recall here that, k_B is the Boltzmann constant, T the temperature, E_s the energy stored in the auto-oscillation, Γ_+ the natural energy dissipation rate, and ν the nonlinear phase-amplitude coupling parameter. The latter is defined as $\nu = N_p/\Gamma_p$, the dimensionless ratio between the nonlinear frequency shift N multiplied by the normalized oscillation power p and divided by the damping rate of amplitude fluctuations Γ_p [22].

Since the spectral linewidth ΔF_g depends quadratically on ν, the dependence of this parameter on $H_\perp$ should be evaluated. For this, we analyze the linewidth of the harmonics of the auto-oscillation signal. It was shown in Reference [163] that the linewidth ΔF_n of the n^{th} harmonics is related to the fundamental one (ΔF_1) by:

$$\frac{1}{n^2} = \Delta F_1 \left(\frac{1+\nu^2}{\Delta F_n} - \nu^2 \frac{1 - \exp\left(-2\Gamma_p/\Delta F_n\right)}{2\Gamma_p} \right). \tag{7.2}$$

We have plotted in figure 7.3 (a) the evolution of $\Delta F_n/n^2$ (n = 2 to 4) together with the one of ΔF_1. It is clear from this graph that independently of $H_\perp$, $\Delta F_n \simeq n^2 \Delta F_1$, which means that our STNO is quasi-isochronous and from equation (7.2), that $\nu \simeq 0$ in the full field range. Therefore, one can also exclude that the strong variations of linewidth observed in figure 7.3 (a) are due to some changes of ν with $H_\perp$. Moreover, we can estimate the generation linewidth from equation (7.4) when $\nu = 0$. For the vortex gyrotropic mode with angular frequency ω, $E_s = \frac{1}{2} G \omega \mathcal{X}^2$, where $G = 2\pi L M_s/\gamma$ is the gyrovector and $\mathcal{X}$ the gyration radius of the core and $\Gamma_+ = \eta\alpha\omega$ [77]. For the thick Py_B layer (L = 15 nm), M_s = 764 emu.cm^{-3}, $\gamma = 1.87 \cdot 10^7$ rad.s^{-1}.Oe^{-1} and the damping coefficient $\alpha = 0.008$ were determined by mechanical ferromagnetic resonance [41], and the topological renormalization of damping is $\eta = 1.7$ [76]. From micromagnetic simulations [164], the radius of gyration under bias conditions close to the experimental ones is found to be $\mathcal{X} \simeq 40$ nm (corresponding to $p = (\mathcal{X}/R)^2 \simeq 0.1$). Hence, at room temperature, $k_B T/E_s \simeq 0.003$ and $\Gamma_+/(2\pi)$ = 9.5 MHz, which yields ΔF_g = 29 kHz, a value close to the narrow linewidth of 40 kHz observed at H_{ext} = −0.7 kOe [figure 7.2 (a)], which thus almost coincides with the intrinsic linewidth of our oscillator. In sum, the absence of nonlinear broadening and the large energy stored in the auto-oscillation in comparison to the thermal energy explain the low minimal values (< 100 kHz) of the linewidth in figure 7.3a.

7.2.3. Origin of tunability

Before seeking further the origin of the variations of linewidth, we first investigate possible physical causes of quasi-isochronicity. Despite the fact that the nonlinearity ν of our STNO is nearly zero, it exhibits a large frequency tunability, $dF/dI_{\text{dc}} \simeq 7$ MHz/mA, see figure 7.3 (b). This can be explained by the linear contribution of the Oersted field to the oscillation frequency. In fact, the tunability can be decomposed as follows:

$$\frac{dF}{dI_{\text{dc}}} = \frac{\partial F}{\partial p}\frac{\partial p}{\partial I_{\text{dc}}} + \frac{\partial F}{\partial I_{\text{dc}}} = \mathcal{N}\frac{\partial p}{\partial I_{\text{dc}}} + \mathcal{A}_{\text{Oe}} I_{\text{dc}} \,. \tag{7.3}$$

In the vortex state, the Oersted field participates to the confinement potential of the vortex core [76, 83], and for our STNO parameters, it is predicted to be about $\mathcal{A}_{\text{Oe}} \simeq 12.5$ MHz/mA. Therefore, a nonlinear frequency shift $\mathcal{N} \neq 0$ is not required to obtain a large tuning sensitivity in equation (7.3). Here, the measured tunability is comparable with the one expected for the Oersted field alone. We attribute the somewhat smaller experimental value to the fact that the auto-oscillating mode does not only involve the

thick Py layer, but also the thin one [40], which is not taken into account in the calculation of $\mathcal{N}_{\mathrm{Oe}}$.

For the gyrotropic mode, $\mathcal{N}$ is the sum of the nonlinearities $\mathcal{N}_{\mathrm{ms}}$ and $\mathcal{N}_{\mathrm{Oe}}$ of the magnetostatic and the Oersted field confinement potentials, respectively. An analytical model [165] predicts that the exact value of $\mathcal{N}_{\mathrm{ms}}$ is positive and depends on the aspect ratio of the magnetic dot in the vortex state, as confirmed by recent micro-magnetic simulations [83] and experiments [166]. On the contrary, $\mathcal{N}_{\mathrm{Oe}}$ is negative when the vortex chirality is parallel to the Oersted field. Therefore, the two contributions can compensate each other (see figure 3 of Ref.[83]): using our STNO parameters, $\mathcal{N} = \mathcal{N}_{\mathrm{ms}} + \mathcal{N}_{\mathrm{Oe}} = 0$ for $I_{\mathrm{dc}} = 23$ mA. Experimentally, we find that $\nu \simeq 0$ is robust from 18 mA up to 25 mA by analyzing the linewidths of harmonics as in figure 7.3a. By using equation (7.2), we can be more quantitative [163]: in the full window of field and current, we extract that $\nu < 0.5$ and that $\mathcal{V}_p$ ranges between 2 and 10 MHz. Hence, the intrinsically small $\mathcal{N}$ with respect to $\mathcal{V}_p/p \simeq 10 \cdot \mathcal{V}_p$ in our STNO is probably responsible for $\nu < 0.5$ [167]. Moreover, as mentioned before, the auto-oscillating mode in our sample involves both the thick and thin vortex Py layers with opposite core polarities. Several non-conservative STT terms are thus involved in the dynamics [80], which could be another cause of quasi-isochronicity: micro-magnetic simulations have indeed shown that such terms can substantially reduce the nonlinear phase-amplitude coupling [39].

7.2.4. Influence of other modes

At this stage, we have explained the origin of the narrow linewidth. In order to elucidate the linewidth broadenings observed in figure 7.3 (a), it should be noticed that in addition to the gyrotropic mode dominated by the thick $\mathrm{Py_B}$ layer excited by STT, there is a gyrotropic mode dominated by the thin $\mathrm{Py_A}$ layer, which for $I_{\mathrm{dc}} > 0$ is overdamped by STT [80]. In order to probe this mode, we use the microwave antenna deposited on top of the sample which produces a microwave field h_{rf} in the plane of the Py layers, and detect the dc voltage generated through the nanopillar when the vortex gyrotropic dynamics is excited at resonance by $h_{\mathrm{rf}} = 3.6$ Oe [168]. We have reported the measured resonant frequency associated to the thin layer vortex mode as a function of $\mathcal{H}_\perp$ in figure 7.4 (a) using red dots. The detailed analysis of the observed behavior will be reported in the next section (7.2.5). For the following demonstration, it is sufficient to use a linear approximation of it (red straight line). As expected, the gyrotropic mode frequency f dominated by $\mathrm{Py_A}$ is lower and has an opposite slope vs. $\mathcal{H}_\perp$ than the one F_1 dominated

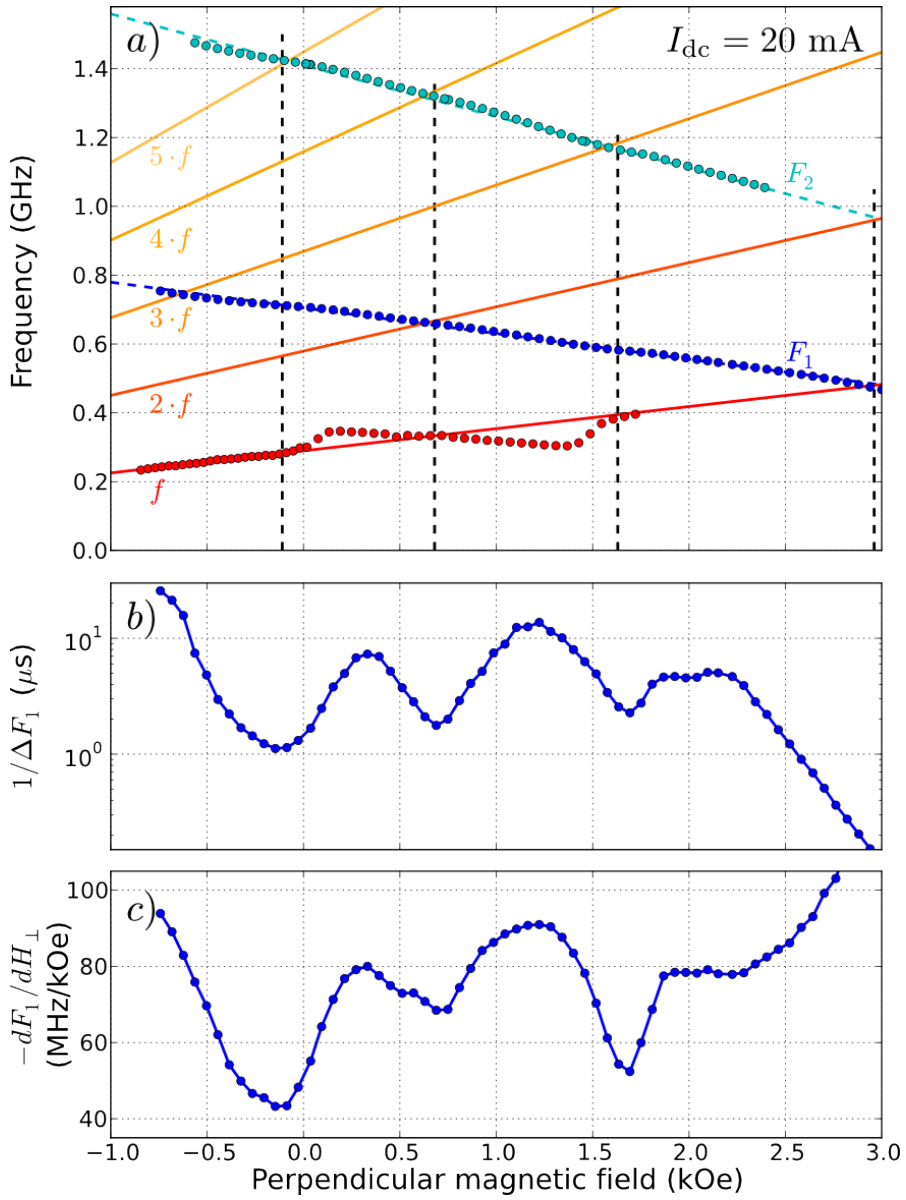

Figure 7.4.: *(a) Blue dots: fundamental frequency F_1 and harmonics F_2 of the auto-oscillating mode dominated by the thick layer (vortex core polarity $p_B = -1$) as a function of $H_\perp$. Red dots: frequency f of the overdamped mode dominated by the thin layer (polarity $p_A = +1$). Red tone straight lines are guides to the eye and show successive harmonics of f. (b) Evolution of the inverse generation linewidth. (c) Slope of the oscillation frequency F_1 vs. $H_\perp$.*

by Py_B, due to smaller thickness ($L_A < L_B$) and opposite core polarity ($p_A = +1 = -p_B$) [61]. We also note that the linewidth of this mode ranges between 80 and 100 MHz, which is about 8 times larger than its natural linewidth, in agreement with the increase

of relaxation of the thin layer due to STT.

Using red tone lines in figure 7.4 (a), we have plotted its harmonics n = 2 to 5 together with the measured fundamental frequency F_1 and harmonics F_2 of the auto-oscillation signal (blue dots). We have also reported in figures 7.4 (b) and (c) the inverse generation linewidth (logarithmic scale) and the slope $-dF_1/dH_\perp$ of the oscillation frequency vs. $H_\perp$, respectively. At magnetic fields where the frequencies of the auto-oscillating and overdamped modes are commensurable, $pF_1 = qf$, with $p, q \in \mathbb{N}$ (dashed vertical lines in figure 7.4 (a)), a decrease of $-dF_1/dH_\perp$ concomitant with a decrease of the inverse linewidth is observed. We attribute this behavior to the interaction between the eigenmodes of the STNO. When they cross each other, their frequency dispersions soften [100] and some energy can be transferred from the auto-oscillating mode to the overdamped mode. As a result, this additional channel of relaxation leads to a decrease of the coherence time of the auto-oscillation (this effect is not taken into account in equation (7.4), which was derived in a single mode approximation [22]). Here, the dynamic dipolar interaction [169, 170] is an obvious source of coupling between modes, but we stress that the dissipative STT terms at play in the double vortex configuration can also be important [80]. More theoretical work would be required to describe the multi-mode autonomous dynamics of our STNO [130]. Still, the main finding reported in figure 7.4 can be expressed in general terms, valid for all STNOs: the ratio of energy stored to energy lost in the system decreases when the auto-oscillating mode becomes degenerate with the overdamped mode. Since the coupling strength depends on the difference in energy between the modes, we emphasize that the STNO should better be operated under conditions where large frequency gaps exist between the auto-oscillating mode and other modes in the system [88, 111, 112].

7.2.5. Self parametric excitation

Parametric excitations of magnetization oscillations have been largely considered in the field of ferromagnetic resonance [171, 172]. These interesting phenomena are excited when the cycle of modulation of the oscillation is repeated twice during one period T_0 of natural oscillations in the elementary system, i.e., when the frequency Ω of parametric modulation is twice the natural frequency Ω_0 of the system. The first observation of parametric excitation of an STNO is given by Urazhdin et al.[173]. The authors have demonstrated that a microwave magnetic field, applied at frequency equal to twice the resonance frequency of the nano-contact STNO where the magnetic free layer is

uniformly magnetized leads to parametric resonance. Recently, Bortolotti et al.[174], have demonstrated that a microwave current flowing through a vortex-based MTJ STNO provided enough Oersted field to parametrically excite the vortex gyration. In addition, the same phenomena have been investigated in the case of a uniformly magnetized free layer at room-temperature where parametric excitation can also be obtained of the non-vortex high-frequency modes in MTJ STNOs by using a microwave current [175].

In this section, based on our experimental observations, we suggest the concept of *self-parametric* excitation in a STNO having one vortex in each magnetic layer. It is a case of *self-parametric* because the field used to modulate the frequency of magnetization oscillations isn't generated by an external source. It is instead produced by the auto-oscillation of the vortex in the thick layer. Indeed, when the frequency of the vortex in the thick layer comes close to twice the frequency of the lowest frequency mode present in the thin layer with vortex ground state, parametric excitation of this damped layer can be achieved. These studies are aimed for understanding the physical source of the peculiar behaviors on the frequency of the thin layer observed in figure 7.4 (a) in the previous subsection.

7.2.5.1. Spectral measurement

First, the dependence of the frequencies of the 2 gyrotropic modes on the external magnetic field of the microwave signal emitted by the STNO are reported again in figure 7.5. We recall here that there are two gyrotropic modes in our system, the first one is dominated by the thick Py_B layer (blue) which is excited by STT (this dynamical mode is characterized by measurement of auto-oscillation induced at bias current $I > I_{th}$ in the absence of the external driving signal). The second mode is dominated by the thin Py_A layer (red), which for $I_{dc} > 0$ is $overdamped$ by STT. In order to excite this mode, we have used microwave antenna deposited on top of the sample which produces a microwave field h_{rf} in the plane of the thin layer, and we have detected the dc voltage generated through the nanopillar when the vortex gyrotropic dynamics is excited at resonance by h_{rf} = 3.6 Oe [168].

The main features of the voltage spectra are modified when the frequency f of the thin layer is close to the half of the frequency of the thick layer i.e. f=F/2. In the insets of figure 7.5, we present the voltage signal as a function of the frequency of the external microwave signal source. As shown in inset [i] the spectrum measured at $H_\perp = -50\ Oe$

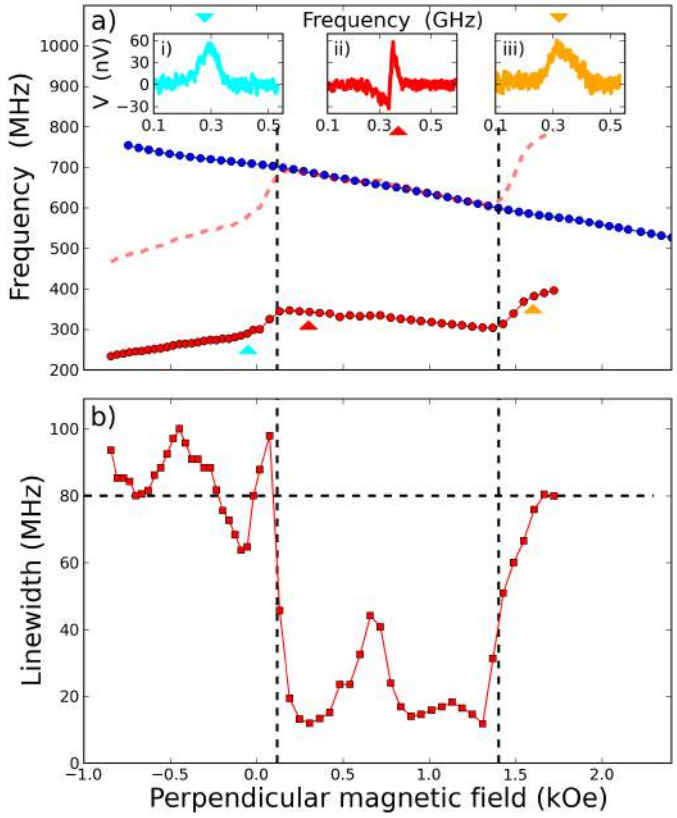

Figure 7.5: *(a) Blue dots: fundamental frequency F of the auto-oscillating mode dominated by the thick layer (vortex core polarity $p_B = -1$) as a function of $H_\perp$. Red dots: frequency f of the overdamped mode dominated by the thin layer (polarity $p_A = +1$). Red dots lines are guides to the eye and show 2*f. Insets: Spectroscopic detection at I_{dc} = +20 mA of the thin layer vortex spectrum excited by a uniform RF magnetic field. (b) Evolution of the generation linewidth of the thin layer.*

can be fitted by a Lorentzian distribution. The corresponding linewidth of this spectrum is 80 MHz, which is about 8 times larger than the natural linewidth, in agreement with the increase of relaxation of the thin layer due to STT. In fact in the vortex state, the damping multiplier $\eta = (1/2)\ln(R/(2L_E)) + 5/8$, where $L_E = 6$ nm is the exchange length in Py, equals $\eta = 1.7$ for both Py layers [76]. For simplification, we neglect the coupling between the thin and thick Py layers, *i.e.*, we assume that the overdamped and auto-oscillating modes only involve the thin and thick layers, respectively. In that case, $\Gamma_{+,A}/(2\pi) = \eta\alpha_A\omega_A/(2\pi) = 7.1$ MHz and $\Gamma_{+,B}/(2\pi) = \eta\alpha_B\omega_B/(2\pi) = 9.6$ MHz at $H_{perp} = 0$ kOe. Below the threshold current I_{th}, the linewidth is given by [22]:

$$\Delta\omega = 2\Gamma_+\left(1 - \frac{I_{dc}}{I_{th}}\right). \tag{7.4}$$

The threshold current for the mode dominated by the thin layer is about $I_{th,A} = -3$ mA. Therefore, at $I_{dc} = 20$ mA, the linewidth of the overdamped mode is predicted to be $\Delta f = 2 \cdot \Gamma_{+,A}/(2\pi) \cdot (1 + 20/3) \simeq 108$ MHz, in good agreement with the measured value (80 – 100 MHz).

The shape of the spectrum changes drastically in a large window of $H_\perp$ between 0.1 and 1.5 kOe. A striking example of such feature is displayed in the second inset [ii] for a perpendicular magnetic field equal to $H_\perp = 0.3kOe$. We find that the voltage spectrum is completely changed in this range, in which the signal associated with the vortex excitation becomes negative and positive and the spectral linewidth reduces significantly from 80 to 10 MHz. In this range, the vortex frequency $decreases$ linearly with $H_\perp$ and is strictly equal to F/2. For $H_\perp$ outside this range, the voltage spectra is again Lorentzian shape with linewidth 80 MHz. To show the drastic improvement of the linewidth of the signal, we plot in figure 7.5 (b) the linewidth of the peak detected as a function of perpendicular magnetic field. As we can see, when f is equal to F/2, the linewidth of the signal decreases. The minimum fitted linewidth reaches 11 MHz. These measurements are consistent with the effect observed on the linewidth the ones presented by Urazhdin et al. [173] for the case of uniform magnetization under a parametric rf field. Further proof of self-parametric excitation is provided by the observation of microwave signal in the SA at a frequency close to F/2 . In figure 7.6 , we present two typical spectra measured for $H_\perp = 1.3$ and $H_\perp = 1.8$ kOe. Indeed, a signal appears from the background level only when $0.1 < H_\perp < 1.5$ kOe , which corresponds to a frequency about twice the natural frequency F of the vortex oscillation in the thick layer. It is not possible to observe a parametrically excited signal for a magnetic field out of this range.

In order, to explain this observation of the self-parametric excitation STNO, we have estimated analytically the average dynamical dipolar field induced by the vortex gyration of the thick layer on the thin layer in the case of our STNO geometry. We find that the amplitude of the dipolar field for a radius of gyration under bias conditions close to $R \simeq 40$ nm is about 200 Oe, which is sufficiently large to excite parametrically the vortex in the thin layer. In fact, at resonance, a large dipolar field must be generated on the thin layer by the thick layer to make the vortex in the thin move periodically 'oscillate' at frequency F/2 [174].

As a final comment, in contrast to previous studies [2] presented by Urazhdin et al. , we found a significant increase from 11 MHz to 30 MHz of the linewidth close to the point when f should be equal exactly F/2. We speculate that the reason here for this feature is the same that described previously in section 7.2.4, where we have shown that the linewidth of a STNO increases at the crossing of modes.

[2] Here the authors shows that minimum linewidth is observed near to zero detuning i.e, when the frequency of the STNO is equal to the frequency of the external source divided by two

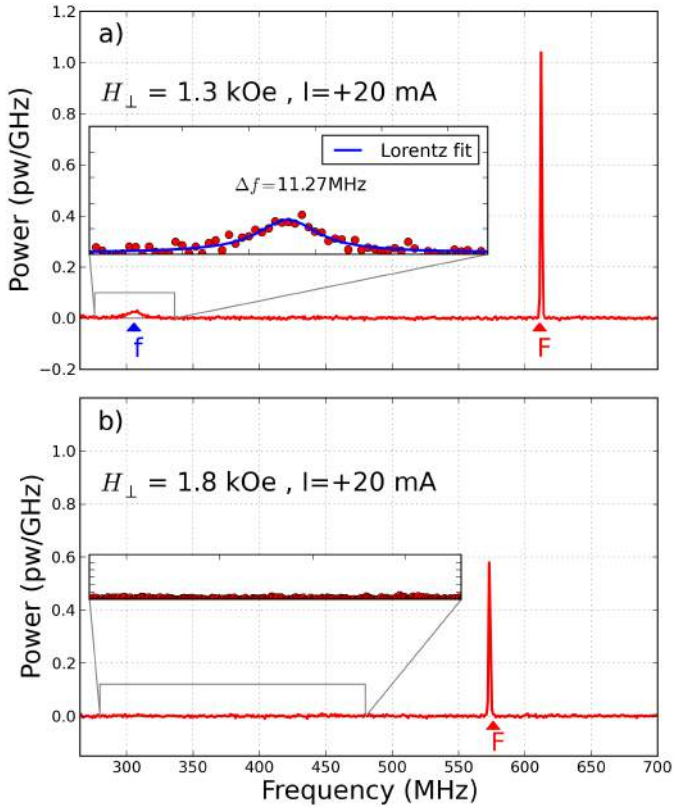

Figure 7.6: *(a) Self-parametric exitation of the vortex in the thin layer at I_{dc} = 20 mA measured by the SA. The measured spectra for $H_\perp$ =1.3 kOe shows 2 peaks one at F = 610 MHz and another at F/2 which corresponds to the excitation of the thin layer. The inset shows a zoom. (b) Measured spectra for I_{dc} = 20 mA and $H_\perp$=1.8 kOe . Only one pics at F=575 MHz is observed.*

7.2.5.2. Threshold and bandwidth of self-parametric excitation

Parametric resonance is possible only when a threshold is exceeded, that is, when the increment of energy during a period caused by the parametric variation is larger than the amount of energy spread out during the same time. To meet this requirement, the depth of modulation must past some critical value. This threshold value of the depth of modulation depends on the damping in the material [171, 173, 174]. Nevertheless, if the threshold is exceeded, the frictional losses of energy cannot restrict the growth of the amplitude. Moreover, one of the most interesting features of parametric resonance is the possibility of exciting oscillations not only at exactly 2F, but also in intervals of frequencies lying on either side of the values 2F (in the range of instability). This bandwidth becomes wider as the range of parametric variation is extended, that is, as the amplitude of modulation is increased. Usually in parametric excitation studies the driving amplitude is controlled by the external source, while in our experiment we can tune the amplitude via the DC current injected in the device. When we increase (decrease) the current the amplitude of the oscillation increases (decreases), as a result

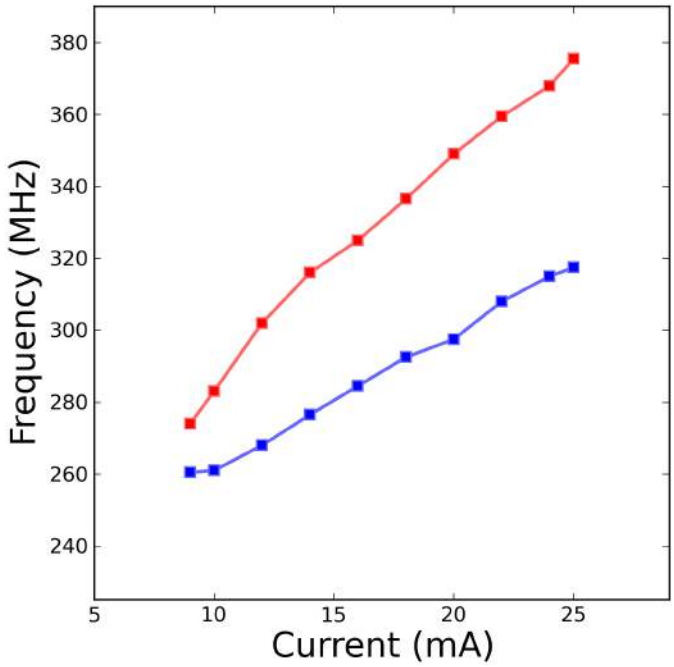

Figure 7.7.: *Frequency boundaries of the self-parametric excitation region vs I_{dc}.*

the dipolar field increase (decrease). The dependence of the self-parametrically induced oscillation spectra on the current is summarized in figure 7.7. The blue and red squares in this plot mark the boundaries of the instability region for the given pumping current, which are defined by the condition that the oscillation frequency of the thin layers is equal to F/2. The width of the *instability region* increases with the increase of the current, and vanishes when I_{dc} approaches the threshold value I_{th} determined by the dynamic magnetic damping in the Py disk and the amplitude of oscillation of the vortex in the thick layer. Our data demonstrate that self-parametric excitation cannot be achieved in the thin layer at I_{dc}= 9 mA without oscillation of the vortex in the thick layer. The frequency range of the self-parametrically excited oscillations increases approximately linearly with increasing I_{dc}, confirming that this variation is dominated by the amplitude of the dipolar field generated by the thick layer which grows linearly with the current [83].

7.3. Forced regime

Synchronization to an external periodic signal and mutual phase-locking of several STNOs have been suggested as a way to increase the emitted power and reduce the phase noise of STNOs. It has been successfully demonstrated that phase locking of an arrays of Josephson junctions [3] leads to increase the power as a squares of the numbers of junctions [93], and it is a general assumption that the ocillating coherently of $\mathcal{N}$ oscillators, reduce the phase noise by a factor of about $\mathcal{N}$ [176]. It has also been proposed that synchronized arrays of STNOs could be operated as associative memories [177]. So far, mutual phase-locking has been achieved using spin wave coupling between nanocontacts [27, 28, 30] and 2D arrays of vortices and anti-vortices [29]. It is also predicted to occur using the common microwave current emitted [97, 26] or the dipolar interaction between adjacent STNOs [178, 179]. To demonstrate the efficiency of these two types of coupling, synchronization to an external microwave current passing through the device [94, 90, 96, 95] or to a microwave field produced by an external antenna [99, 158] have been studied.

Two key characteristics to analyze the quality of the synchronization are the locking range and the generation linewidth in the phase-locked regime, which are respectively related to the coupling efficiency and the response to noise of the oscillator. In a single vortex-based tunneling magnetoresistance (TMR) device, it was shown that using an external microwave current, the locking range could reach up to one third of the oscillator frequency, and the linewidth be reduced by 3 orders of magnitude, from a few MHz down to 3 kHz [95].

We have discussed the microwave signal generated by the dynamics of two coupled vortices in a spin-valve oscillators in detail. In this section, we investigate the case when such a system is subjected to a external microwave source. For this purpose, the microwave emissions are recorded on the spectrum analyzer and injection locking experiments are performed by adding a microwave field from an external source. The characteristics of the signal will be measured in the phase-locked regime and we will show experimentally and analytically the influence of the linewidth on the coupling between the signal emitted by the STNO and an external microwave signal.

[3] The josephson junction is a system very close to the STNO

7.3.1. Synchronization at fundamental frequency

We have shown that above a current of about +10 mA, a narrow microwave emission peak is observed on the spectrum analyzer, which corresponds to the spin transfer driven dynamics of the two coupled vortices. At fixed I_{dc}, the microwave characteristics of this auto-oscillation peak (frequency and linewidth) can be tuned by varying $H_\perp$. In this study, all measurements were carried out at room temperature. The dc current injected through the nanopillar was fixed to I_{dc} = 15 mA or varied by ±4% around this value when specified. The maximal output power from the synthetizer (source frequency F_s) injected into the microwave antenna was +10 dBm, corresponding to h_{rf} = 6.3 Oe.

In the first experiment, the perpendicular field is set to $H_\perp$ = 1 kOe. Under these bias conditions, the oscillator frequency is F_0 = 586 MHz and the generation linewidth ΔF_0 = 142 kHz. In figure 7.8, we present a map of the power density recorded on the spectrum analyzer when the frequency F_s of the external microwave field is swept from 540 MHz to 630 MHz and the driving field amplitude is set to h_{rf} = 2 Oe. When F_s comes closer to F_0, the frequency of the oscillator is pulled towards the source frequency. When $F_s \simeq 574$ MHz, there is a single frequency peak in the spectrum, meaning that the auto-oscillation is synchronized to the external source. At this point, it is not possible to separate the signal of the gyrotropic auto-oscillation and that of the source, which prevents measuring the generation linewidth in the phase-locked regime. This situation is observed until $F_s \simeq 597$ MHz, above which the auto-oscillation frequency comes back to its free running value F_0.

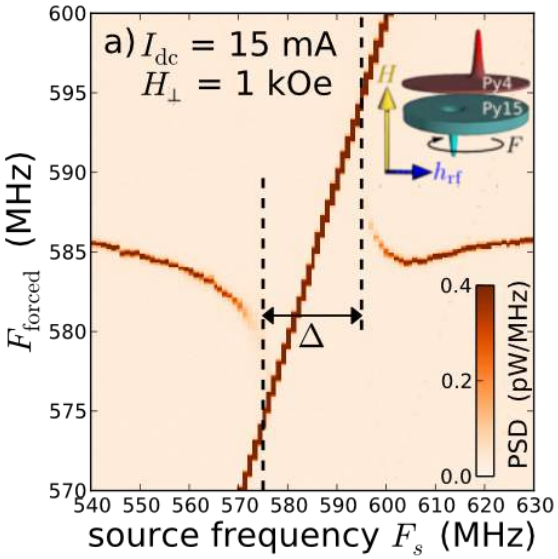

Figure 7.8.: *Power spectrum map of the STNO at I_{dc} = 15 mA and H_0 = 1 kOe vs. the frequency F_s of the external microwave field h_{rf} = 2 Oe.*

The locking range Δ measured experimentally is plotted vs. the

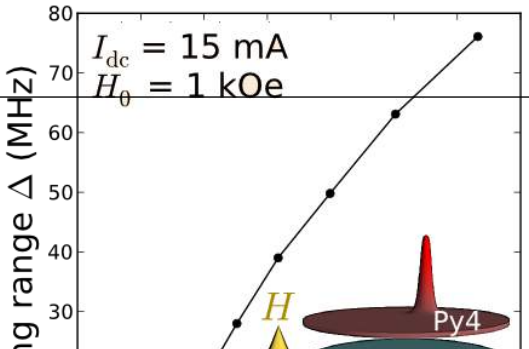

driving field amplitude h_{rf} in figure 7.9. As expected [22], it increases linearly with h_{rf} at low driving amplitude ($h_{\mathrm{rf}} < 1.5$ Oe). The behavior observed at larger h_{rf} is presumably due to some nonlinearities of the system. We point out that at $h_{\mathrm{rf}} = 6.3$ Oe, the locking range $\Delta = 75$ MHz corresponds to 13% of the oscillator frequency F_0. Moreover, we emphasize that there is no synchronization to the external microwave current i_{rf} passing through the STNO based on coupled vortices, in contrast to the situation presented in figure 7.8, where the microwave field h_{rf} is very efficient to phase-lock the signal. A similar behavior was observed in the saturated state of the same device and ascribed to symmetry reasons [158].

7.3.2. Fractional synchronization

Since the peaks observed at F when the oscillator is synchronized at the fundamental frequency F are dominated by the parasitic coupling to the driving external source signal. We have performed a second measurement in which the microwave signal generated by the oscillator is locked to the source when its frequency F_s is equal to some fractions of F_0. Figure 7.10 shows the PSD map of the output voltage for the STNO frequency F_0 versus the driving frequency F_s. It is clear that the frequency F_0 of the driven STNO follows the driving frequency F_s not only in the vicinity of the point $F_s = F_0$ but also the locking is observed near to the points F_s=3F_0/2,F_s=2F_0 and F_s=3F_0. We note here that these fractional synchronization are not related to the source nonlinearity, because we have checked that no subharmonics were emitted by the source, in particular, at $1/3F_s$, $1/2F_s$ and $2/3F_s$. Moreover, the power emitted in the second and third harmonic of the source is 40 dB smaller than the power emitted at the main frequency.

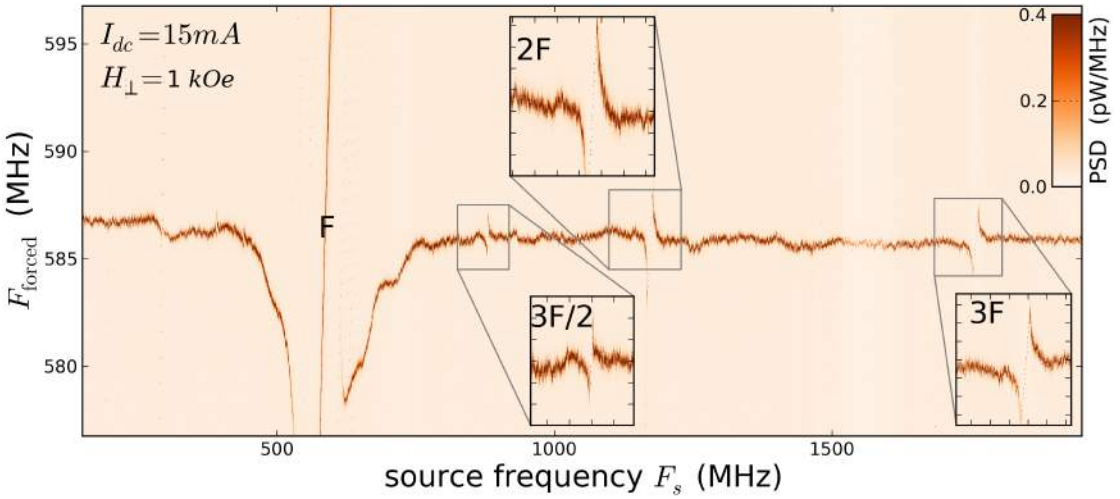

Figure 7.10.: *Power spectrum map of the STNO at I_{dc} = 15 mA and H_0 = 1 kOe vs. the frequency F_s of the external microwave field h_{rf} = 6.3 Oe. The source frequency F_s is swept from 200 MHz to 1850 MHz, the insets are zoom for the synchronization showing 3/2 F_s, 2F_s and 3 F_s.*

7.3.3. Perfect and robust synchronization

In order to caracterize quatitativly the linewidth of the oscillator signal when its frequency is locked, an example when the source frequency F_s is swept around $2F_0$ is show in figure 7.11 (a). Here, we plot the frequency shift $F_{\text{forced}} - F_0$ of the oscillator when it is forced by the microwave field of amplitude h_{rf} = 6.3 Oe as a function of F_s varying from 1150 MHz to 1190 MHz. As in figure 7.11 (a), we observe the characteristic behavior of synchronization to the external source, except that it is now at twice the oscillator frequency and the oscillation signal is not hindered by the source signal. Hence, we can analyze the dependence of the generation linewidth on F_s, which is plotted in figure 7.11 (b). The striking observation is a dramatic reduction of the generation linewidth within the locking range. As shown in the inset of figure 7.11 (b), the measured linewidth is indeed limited by the 1 Hz minimal RBW of the spectrum analyzer, *i.e.*, the auto-oscillation is perfectly phase-locked to the external source. This corresponds to an improvement of the signal coherency by a factor greater than 10^5 with respect to the free running case. The increase of the generation linewidth up to 1 MHz observed at the boundaries of the locking range is attributed to successive synchronization-unsynchronization events occurring at the timescale of the measurement [95].

To gain further insight, we investigate the robustness of this perfect phase-locking.

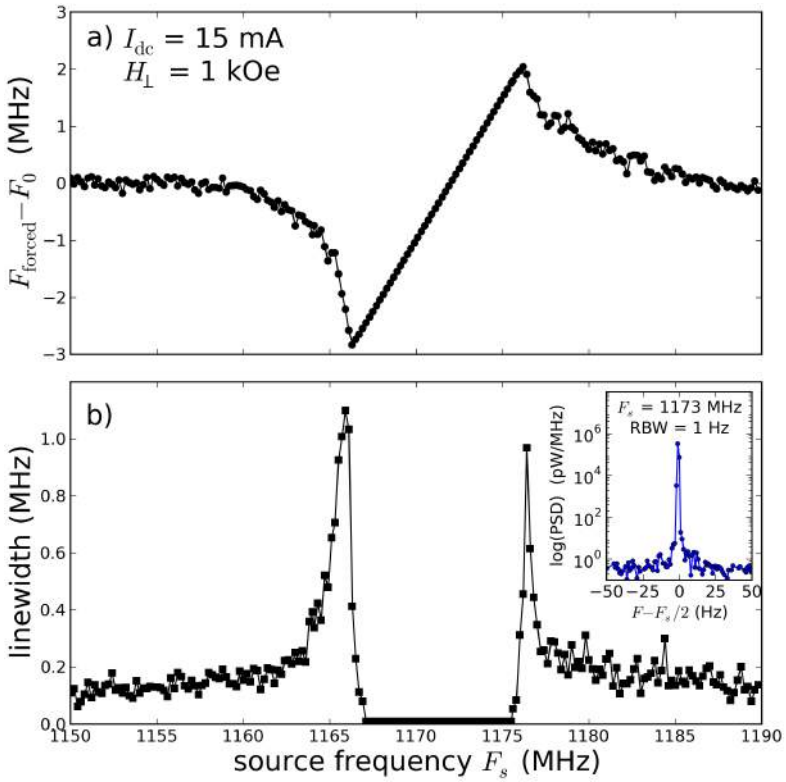

Figure 7.11.: *Current dependence of the (a) STNO frequency and (b) generation linewidth in the free (black dots) and forced regimes (blue dots)*

We now measure the auto-oscillation signal as a function of I_{dc}, which is swept from 14.6 mA to 15.6 mA. In the free regime (external source turned off), the generation frequency increases linearly from 584 MHz to 592 MHz, while the linewidth is nearly constant around $\Delta F_0 = 142$ kHz, as shown by the black dots in figures 7.12 (a) and (b), respectively. The tunability observed in our vortex-based STNO, $dF_0/dI_{dc} \simeq 8$ MHz/mA, results from the Oersted field created by the dc current [76]. In the forced regime with the external source turned on at $F_s = 1175$ MHz and $h_{rf} = 6.3$ Oe (see blue dots in figure 7.12 (a)), the auto-oscillation frequency is pulled towards half the source frequency $F_s/2$ for $I_{dc} < 14.9$ mA and $I_{dc} > 15.4$ mA, and constant and equal to $F_s/2$ in between these boundaries, which define the locking range. The associated decrease of the generation linewidth is spectacular, as shown by the logarithmic scale in figure 7.12 (b). The measured linewidth is limited by the RBW = 1 Hz for $14.93 < I_{dc} < 15.35$ mA, which means that the phase-locking to the external source is perfect within this range of current. The latter corresponds to a variation by 4 MHz of the auto-oscillation frequency in the

free regime. These features demonstrate the robustness of the synchronization observed in our sample, as it means that even if the external source frequency deviates from the oscillator frequency by more than ten times the free running linewidth, perfect phase-locking can still occur.

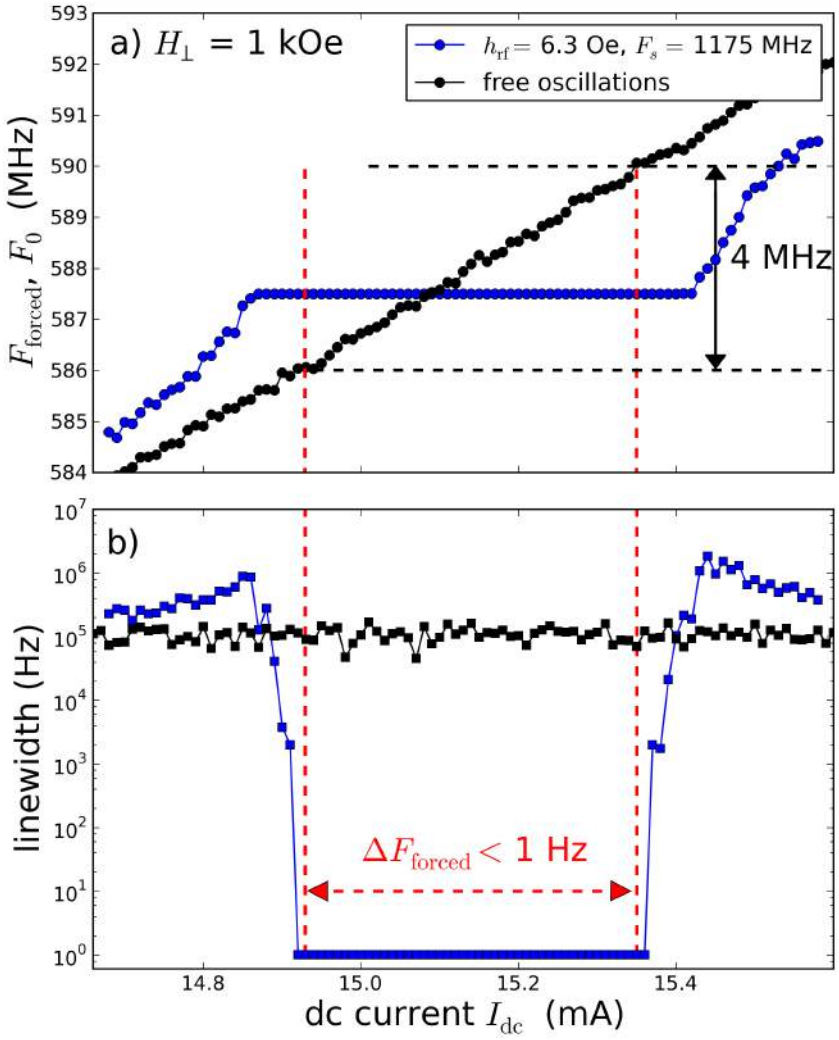

Figure 7.12.: *Current dependence of the (a) STNO frequency and (b) generation linewidth in the free (black dots) and forced regimes (blue dots).*

7.3.4. Role of noise in phase-locking phenomena

Another issue to investigate is the influence of fluctuations on the actual characteristics of our vortex oscillator when it is phase-locked. To do that, we compare the synchronization of auto-oscillation signals having different generation linewidths. We use two different applied fields, $H_\perp^0$ = +1 kOe and $H_\perp^1$ = −0.27 kOe, at which the emission frequencies at $I_{\rm dc}$ = 15 mA slightly differ (F_0 = 586 MHz and F_1 = 684 MHz, respectively), and the generation linewidth varies by more than a factor seven, from ΔF_0 = 142 kHz to ΔF_1 = 1.05 MHz (see inset of figure .7.13 (a)). Using blue and red dots at $H_\perp^0$ and $H_\perp^1$, respectively, we plot the experimental frequency mismatch $F_{\rm forced} - F_s/2$ (figure .7.13 (a)) and the linewidth in the forced regime (figure .7.13 (b)) as a function of the detuning $F_{0,1} - F_s/2$ between the natural oscillator frequency and half the source frequency. The strong differences observed in the characteristics of the synchronization at these two fields reveal the role played by the fluctuations in the phase dynamics of STNOs. When the latter are weak (narrower generation linewidth at $H_\perp^0$), the locking range is large (more than 4 MHz) and the synchronized signal acquires the spectral quality of the source (less than 1 Hz). When the noise is larger (broader generation linewidth at $H_\perp^1$), it competes against the coupling to the external source, which results in a smaller apparent locking range and a poorest spectral quality of the forced oscillation. Here, increasing the linewidth by a factor $\Delta F_1/\Delta F_0 \simeq 7$ has a huge influence on the signal coherency in the phase-locked regime since its improvement with respect to the free running case drops from a factor 10^5 to only 10.

In order to model these experimental results, we employed the theory from reference [90, 91]. According to this model, the mismatch $F_{forced} - F_s/2.$ of a noisy oscillator is related to the detuning frequency $\Delta F_{Det} = F_0 - F_s/2.$ via the locking strength ε in the following expression:

$$F_{forced} - F_s = -\Delta F_{Det} - \varepsilon Im\left[\frac{1}{2\frac{i\Delta F_{Det}-w^2}{\varepsilon} + \frac{1}{2\frac{i\Delta F_{Det}-2w^2}{\varepsilon}+\ldots}}\right]. \tag{7.5}$$

Where w^2 is the noise of the oscillator, expressed as its natural linewidth. Now One can use equation 7.5 and compare it to the experimental observation.The influence of phase fluctuations on the frequency mismatch has been shown by continuous lines in figure .7.13 (a). Using the measured linewidths ΔF_0 and ΔF_1 in the equation 7.5, the

only fitting parameter is the coupling strength of the external microwave source to the oscillator (equal to half the locking range in the case of zero fluctuations), which is found to be ε = 2.5 MHz both at H_0 and H_1.

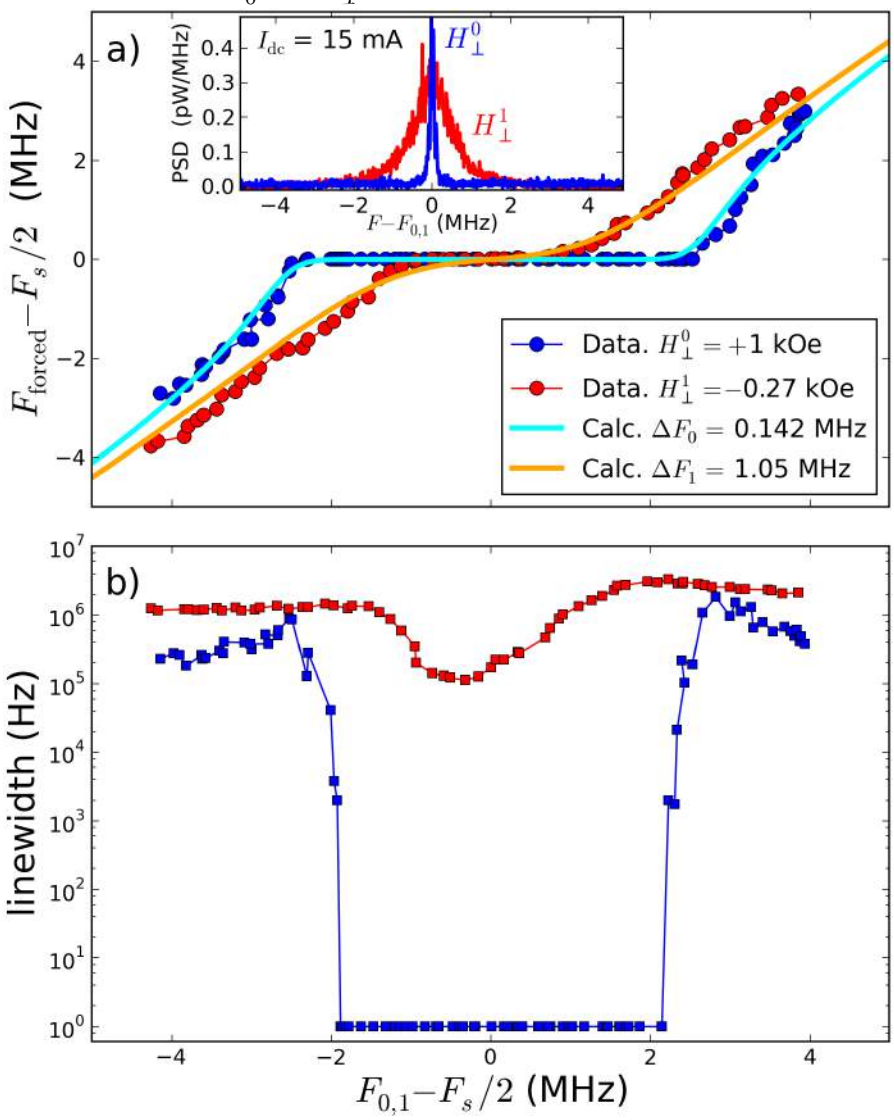

Figure 7.13.: *(a) Variation of the frequency mismatch $F_{forced} - F_s/2$ as a function of the detuning $F_{0,1} - F_s/2$ at $H_\perp^0$ = +1 kOe (blue dots) and $H_\perp^1$ = −0.27 kOe (red dots). The external source amplitude is set to h_{rf} = 6.3 Oe. Continuous lines are fits using Eq.(5) of Ref.[90] yielding a coupling strength ε = 2.5 MHz. The inset shows the emission spectra at $H_\perp^0$ and $H_\perp^1$ in the free running regime. (b) Dependence of the emission linewidth on the frequency detuning at $H_\perp^0$ and $H_\perp^1$.*

7.4. Conclusion

In this chapter, we have investigated the microwave characteristics of a spin transfer nano-oscillator based on coupled vortices as a function of the perpendicular magnetic field $H_\perp$. By analyzing the harmonic content of the spectrum, we find that our STNO is quasi-isochronous independently of $H_\perp$, which suppresses the severe nonlinear broadening usually observed in STNOs. Still the generation linewidth displays strong variations on $H_\perp$ (from 40 kHz to 1 MHz), while the frequency tunability in current remains almost constant (7 MHz/mA). This demonstrates that isochronicity does not necessarily imply a loss of frequency tunability, which is here governed by the current induced Oersted field. It is not sufficient either to achieve the highest spectral purity in the full range of magnetic field. We show that the observed linewidth broadenings are due to the excited mode interacting with a lower energy overdamped mode, which occurs at the successive crossings between harmonics of these two modes.

We have also reported that the strong dynamic dipolar field induced by the spin transfer driven excitation of the mode dominated by the thick layer is able to parametrically excite the damped mode dominated by the thin layer. The excitation bandwidth increases with the dc current, which is consistent with our interpretation. These results are important not only to understand the behavior of the freqeuncy of the thin layer in our system, but also for the synchronization of STNO arrays.

In addition, we have also studied the synchronization of this spin transfer driven vortex dynamics to an external source. Phase-locking to the microwave field h_{rf} occurs in a range larger than 10% of the oscillator frequency for drive amplitudes of only a few Oersteds. Using fractional synchronization at the double frequency, we analyzed the behavior of the generation linewidth. It is found to decrease by more than 5 orders of magnitude in the phase-locked regime (down to 1 Hz, limited by the resolution bandwidth of the spectrum analyzer) in comparison to the free running regime (140 kHz). We find that the phase-locking remains perfect for frequency detunings as large as 2 MHz, which proves its robustness. We also analyzed how the phase noise in the free running regime influences the characteristics of the synchronization.

CHAPTER 8

Dipolar coupling between adjacent STNOs

We have studied in detail the synchronization of a STNO to an external microwave source. Here we extend these ideas to more interesting situations when two STNO are interacting through dynamic dipolar coupling. In this chapter, we study the behavior of the coupled vortex based STNOs. We start with giving the device structure and characterization. Then we illustrate some features of synchronization of these STNOs pair and briefly discuss synchronization properties.

8.1. Introduction to mutual synchronization

We have already demonstrated that in the saturated state, there is a very efficient coupling of the auto-oscillations to an RF field (external antenna), and no coupling to the RF current flowing through the device. We have also verified experimentally in the previous chapter that the same synchronization rules apply to the double vortex STNO structure. Therefore, we have identified a coupling mechanism to obtain mutual synchronization between $\mathcal{N}$ STNOs, namely, the dipolar field. Indeed, to date, three different possible coupling mechanisms between STNOs have been proposed: $spin\ wave$ coupling, $electrical$ coupling and $dipolar$ coupling . In the electrical coupling design, the STNOs are electrically connected in series or parallel. Thus, the mechanism to couple several comes from the common microwave current emitted by and shared through the devices [26]. In this mechanism, the STNOs have to be connected to the same electrical circuit, so the constraint on the separation between individual devices in the network isn't required. The requirement to achieve self-synchronization is only on the amplitude of the emitted microwave current, which depends on the magnetoresistance ratio and on the type of magnetization dynamics that is excited. So far, there has been no experimental proof of self-synchronization using this global coupling, but individual STNOs have successfully been phase-locked to an external source [94, 95, 90, 96]. There are others designs that are based on local couplings which arise from exchange and dipolar energies, and are mediated by spin waves and dipolar fields between closest neighbors in an array of STNOs. Due to the exponential attenuation of propagating spin waves with distance d and $1/d^3$ decay of dipolar fields, these two types of coupling are effective below a typical length scale of 1 μm, which is much larger than the separation that can be defined by lithography between adjacent STNOs (~50 nm). Mutual synchronization of STNOs has been achieved for the first time using two adjacent nano-contacts patterned on a common ferromagnetic layer, acting as a medium for propagating spin waves [28, 27]. Pairwise synchronization by the spin wave mechanism in devices with four nano contacts has also been demonstrated [30]. A theoretical work combining micro-magnetic simulations and analytical calculations performed by demonstrated that this dipolar interaction is also very efficient to synchronize several STNOs in the vortex state [178]. Regarding mutual synchronization of vortex state auto-oscillations we have decided to perform a first experimental study [80] of dipolar coupling using only a pair of STNOs placed nearby laterally. This study has been carried out in collaboration with the group CNRS/Thales (Nicolas Locatteli, Vincent Cros), Palaiseau, France.

8.2. Device structure and characterization

8.2.1. Device structure

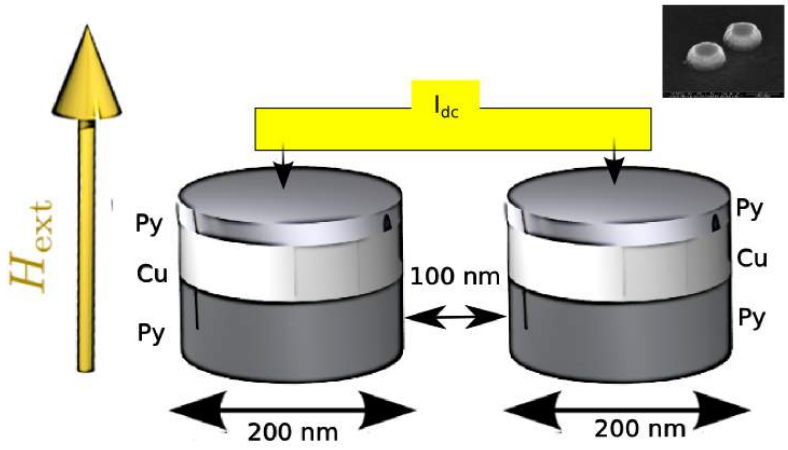

Figure 8.1.: *Schematic representation of a pair of STNOs. Each pillar is composed by a thin magnetic Py layers, a non magnetic spacer, and a thick Py layer. Yellow arrows indicate the direction of the external magnetic field. The nanopillars have a diameter 200 nm and are separated by a distance of 100 nm. The inset is a SEM image of the device.*

In order to perform this study on dipolar coupling between two STNOs, a new device was built. It consists of two identical nanopillars with diameters 200 nm, connected in parallel, each of them is composed of a thick (15 nm) and thin (4 nm) Py layers separated by nonmagnetic spacer Cu. The samples are fabricated using the procedure described in section 5.1 of chapter 5. The originality of our design is that the two STNOs are very close to each other, the edge-to-edge separations is s = 100 nm which leads to dipolar coupling between the STNOs. In fact the coupling strength Ω depends strongly on the STNO's distance. This parameters can be estimated as $\Omega \sim \gamma h_{1\to 2} h_{2\to 1}$, where $h_{i\to j}$ is the microwave magnetic field created at the location of the i-th STNO by the microwave oscillations of the j-th STNO [97] (see section 2.4.2).

8.2.2. DC transport characterization of double STNOs

In figure 8.2 we compare measurements of the GMR in current-perpendicular tp plane (CPP) geometry as the magnetic field is swept in the direction of the long axis of

the sample cross section (θ_{plane} = 0°), and in the perpendicular in-plane direction the (θ_{plane} = 90°).

Let's first concentrate in figure 8.2 (a) where we display the variation of the device resistance ΔR with in-plane measured at I_{dc} = 1 mA. For $H^{0°}_{plane}$ = 1 kOe, both thin and thick magnetization directions in each pillar are parallel. Upon decreasing $H^{0°}_{plane}$, the low resistance state is conserved until $H^{0°}_{plane}$ = 0.4 kOe. Below this value, the dipolar coupling between layers of pillars is large enough to reverse the magnetization of the thins Py layers. These transitions from parallel to anti-parallel directions is associated with a sharp jump of the resistance equal to about $0.0085R_0$ (R_0=4.690Ω) . Then this quasi-uniform onion state occurs when the field is reduced to 0.1 kOe after a vortex is nucleated in each thick layer. At $H^{0°}_{plane}$ = -0.4 kOe the vortex is distorted and then annihilated in each layers leading to stabilization of a quasi-uniform parallel state. When $H^{0°}_{plane}$ is swept back from -1 to 1 kOe, similar features corresponding to magnetization direction switches and vortex nucleation are detected.

The GMR of the sample recorded for $H^{90°}_{plane}$ in-plane (hard axis) is shown in figure 8.2 (b). The maximum ΔR is 40 mΩ which gives the same value as before for $\theta_{plane} = 0^{circ}$. As we have noted previously, the dipolar coupling between layers of the pillars causes the switching of the magnetic thin layer in each pillar before field inversion occurs. Then, as the magnetic field is swept in the direction of the hard axis of the sample cross section, we observe switching of the thin magnetic layers between parallel and anti- parallel alignments at $H^{90°}_{plane}$= 0.6 kOe . For H in-plane the passage from the parallel to the antiparallel layers for 0° and 90° is different, this is an indication that we are measuring two pillars. Indeed, when we change the in-plane field direction we change the dipolar interaction between the layers.

The experimental study of transport curves based on a planar field R (H) allowed us to confirm the presence of two pillars and the vortex magnetic configuration in each thick layer of pillar. We note here that we have shown the DC measurement showing the evolution of the resistance of the pair of pillars versus in-plane magnetic field for low current. In these experiment the current amplitude is not large enough to generate sufficiently large Oersted field that could favor the nucleation of a vortex in the thin layer of each pillar. We have checked with DC measurements at higher current that the GMR curves obtained for this value show more features [80]. This probably due to the presence of four vortices: one in each layer.

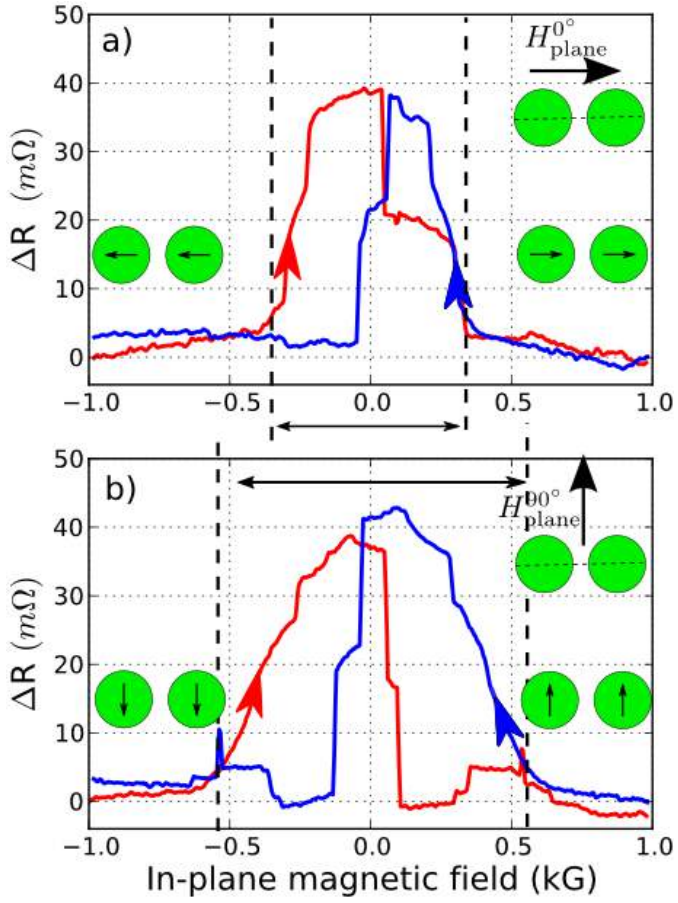

Figure 8.2.: ***GMR curves***: *Δ R as a function of magnetic field for the same device for fields (a) along the easy-axis direction and (b) along the in-plane hard axis and with a DC current of 1 mA.*

8.3. Advantage of vortex-state over saturated state for the synchronization through dipolar coupling

In reality, from the nano-fabrication point of view, it is rather impossible to reach a nanometer precision for the pillars diameter, so there is always some manufacturing difference among STNOs. This leads to a frequency difference between the two nano-pillars. This gap in frequency has to be compensated by a sufficiently strong dipolar coupling. Our goal is to be able to couple the pair of STNOs in the saturated and in the vortex state through the dipolar interaction. Even if the strength of the dipolar interaction is similar in the two cases (saturated and vortex) [100, 116], our experiments revealed the real complexity to synchronize the two STNOs in the saturated state see appendix (D). In spite of the same current density flowing through the two STNOs as shown in figure 8.1, each STNO will generate a different frequency because there may be different diameters between the layers. For similar sample to sample dispersion (e.g., 10%), the frequency dispersion in the saturated state is $\Delta\omega_S = 0.1\omega_S \sim 500$ MHz is stronger than in the vortex state $\Delta\omega_V = 0.1\omega_V \sim 50$ MHz. This difference between the free-running frequencies between the STNO's is the main parameter that controls the phase-locking behavior of this two oscillators. In fact, the condition for synchronizing these two STNOs is $\Delta\omega < \Omega$. Then, if the strength of the dipolar interaction is similar in the saturated case and in the vortex state (100 MHz in good cases) [100, 116] it's clear that the conditions for synchronization are reached more easily in the vortex state than in the saturated state.

8.4. Experimental results on a pairs of STNOs in the vortex states

Considering the smaller volume of the thin 4 nm layers and the small magnetization oscillation amplitude in the thin layer for the gyrotropic mode dominated by the thick layer, their influence on the dynamic dipolar coupling can be neglected. The coupling between the STNOs will only be considered through the mutual influence of the vortices excited in the two thick 15 nm layers. Thus, the thin layers will be considered as fixed polarizing layers, and their shallow dynamics will be neglected. The polarities of the thick layer's vortices will be further referred to as P_1 and P_2 as for 1st and 2nd pillar. The two nano-pillars are connected with common bottom and top electrodes, then it

is not possible to independently access to the signals from each of the pillars. As a consequence, observing two independent peaks on the spectrum analyzer is the only proof supporting the fact that the condition for vortex auto-oscillations is attained in both pillars. Any synchronization phenomenon will be then easily highlighted when observing a transition between two independent peaks associated to each auto-oscillator, and a single peak associated to the synchronized auto-oscillators. However, when a single peak is observed in the power spectrum, it is a priori impossible to determine whether the two oscillators oscillate at a common frequency, or whether one of the two oscillators is excited. Then a crucial point is to find an external knob to couple and uncouple our pairs of oscillators. In other words: to have the possibility to perform the following experiment. We firstly separate the two STNOs frequencies and measure their frequencies F_1 and F_2. Having done this, we use the external knob to tune continuously, and differentially, the frequency of the vortex gyro-mode in each thick layer of the pair STNOs. To do this experiment there are three available options:

- *Perpendicular magnetic field*: In our experiment, we can tune the frequency of our device by varying the external perpendicular magnetic field $H_\perp$. The key idea is to take advantage from the small slope in $dF/dH_\perp$ between the two pillars, which allow us to act on this difference. If the vortices have opposite polarities the variations $dF/dH_\perp$ have even opposite signs which makes it ideal. The application of a perpendicular field then allow us to easily change the gap between the two frequencies. Moreover, it allows us to prove how the interaction depends on relative vortex polarities in the thick layers.

- *Current*: Even if the two nano-pillars are connected with common bottom and top electrodes, the small different in diameter leads to different slope in dF/dI_{dc}. It is also possible to change the coupling strength between the two oscillators by changing the current. Indeed, the reduction of the radii gyration of the two vortices will effectively reduce the average energy of interaction which reduce the stability of the synchronization. Then, by increasing the current I_{dc}, we can envisage to modify slightly the radii of gyration which makes it possible to observe a transition between desynchronized and synchronized states.

- *In plane magnetic field (amplitude and angle)*: We have seen in the GMR curve that when we change the angle in plane θ_{plane} we change the coupling between the layers, then in our experiment it is possible to do this not only to change the

frequency of each oscillator but also to change the coupling strength Ω between layers (see appendix (C)).

8.4.1. Synchronization versus applied field

Same polarities

In the first experiment, a constant DC current of 38 mA is applied through the device, i.e. about 19 mA in each STNO. The upper panel of figure 8.3 shows the evolution of the auto-oscillation peaks measured on the spectrum analyzer as a function of the perpendicular applied magnetic field. This color map clearly shows that two auto-oscillation peaks can coexist. The polarities of the vortex cores in each thick layers of the two STNO are parallel, because the dependence of frequencies exhibited by each oscillator on perpendicular magnetic field have the same sign of slope. However, a slight difference exists in the slope for each oscillator due to their manufacturing difference. When the frequency of one STNO approaches the other one, the dynamic dipolar interaction causes the oscillator to lock together. Figure 8.3 (b) plots the evolution of the combined spectrum from both STNOs as magnetic field increases. As $H_\perp$ increases from 1 to 1.55 kOe, two signals are visible. The frequency of theses signals decreases with $H_\perp$ owing to the vortex polarity of each thick layer is opposite to the perpendicular magnetic field. The power spectrum from $H_\perp$=1.6 kOe shows that both STNOs frequency-lock. We assume that here direct evidence of mutual synchronization is given because the spectrum of the locked state shows a single peak with much larger amplitude. Morever, we have checked that this process is reversible, therefore we cannot attribute that transition from two peaks to one peak to some magnetization switching. This mutual synchronization phenomenon is often described in terms of coincidence of frequencies as locking : if two nonidentical oscillators having their own frequencies F_1 and F_2 are coupled together, they may start to oscillate with a common frequency F. Whether they synchronize or not depends on two terms: the coupling strength and the frequency detuning ΔF. The first term describes how strong the interaction is. In our experimental it is not clear how to measure this quantity since it depends on several factors (damping of ferromagnetic layer, oscillator amplitude , vortex radius). In order to characterize the synchronization it is possible to measure ΔF which quantifies the two critical frequencies differences before locking. In contrast to the coupling strength, in our experiments with two oscillators the detuning can be easily measured. Indeed, one can tune the frequency of an oscillator by

the external magnetic field, we can find out how the results of the interaction depends on the frequency mismatch. Here for the configuration of parallel polarity, we have measured a Δ_P = 17MHz.

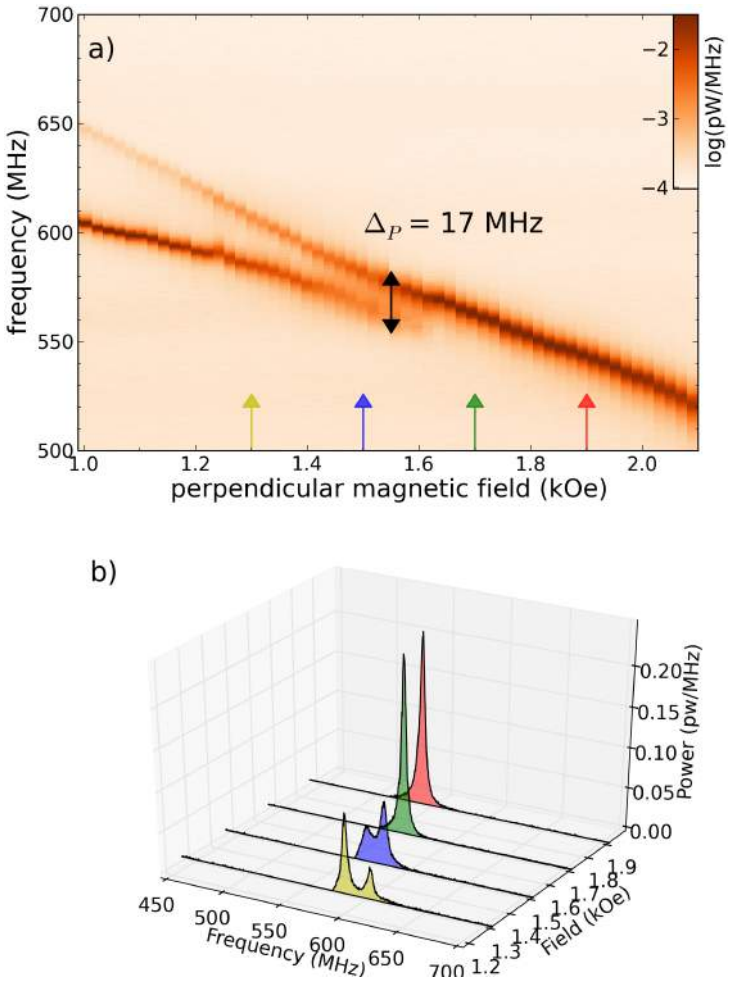

Figure 8.3.: ***Mutual synchronization in a pair of STNOs.*** *Power spectrum maps of a pair of spin transfer vortex oscillators separated from center to center by 300 nm. The maps are recorded as a function of the perpendicular bias magnetic field for a common current $I_{\rm dc}$ = 38 mA injected through the two STVOs in parallel. (**a**) Mutual synchronization when the vortex core polarities in the two Permalloy 15 nm layers are parallel, P (and opposite to the bias field). (**b**) Typical power spectra of the STNOs for different external perpendicular magnetic field.*

Opposite polarities

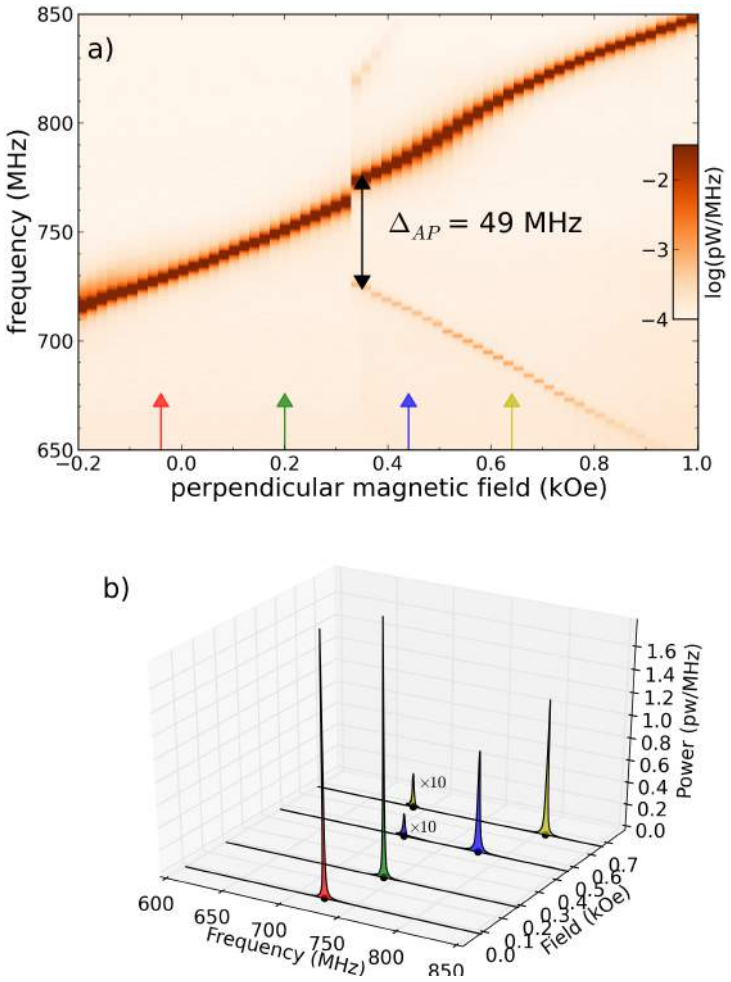

Figure 8.4.: ***Mutual synchronization in a pair of STVOs.*** *Power spectrum maps of a pair of spin transfer vortex oscillators separated from center to center by 300 nm. The maps are recorded as a function of the perpendicular bias magnetic field for a common current I_{dc} = 38 mA injected through the two STNOs in parallel. (**a**) Mutual synchronization when the vortex core polarities in the two Permalloy 15 nm layers are anti-parallel, AP. (**b**) Typical power spectra of the STNOs for different external perpendicular magnetic field.*

We have already presented in figure 7.1 (b) that parallel and anti-parallel to the field core polarities in the thick layer lead to opposite slope frequency field relations. In this experiment, we purposely prepared a state where the vortex core polarities in the thick layers of each STNO are opposite. The same constant DC current of 38 mA is applied through the device in order to compare this opposite polarities with parallel polarities

configurations. As illustrated in figure 8.4 for $H_\perp$ decreasing from 1 to 0.35 kOe, two signals are visible, The frequency of theses signals changes with $H_\perp$, one of the frequency increases when the second one decreases. Then when the two oscillating frequencies get closer at $H_\perp$ =0.32 kOe, the dynamical dipolar interaction, and it eventually leads to the synchronization of the vortex oscillations, as indicated here by the fact that only one large amplitude peak subsists, again, this transition is reversible. In this experiment, there is obviously a strong attraction between the two oscillation peaks and we have found that the differences in frequency before synchronization is about Δ_{AP}=49 MHz. Then it's clear that in the configuration of anti-parallel polarities, we measure a Δ much larger than for the parallel configuration. The physical reasons of this difference will be explained in the next section 8.5.1. A surprising feature observed in this experiment is the fact that a significant difference in power output between nano-pillars with a vortex polarity +1 compared to nano-pillar with a vortex polarity -1.

8.4.2. Synchronization versus DC current

Here, we study the dependence on bias current of the high-frequency dynamics of the pair of vortex-based STNO. The bias perpendicular field is fixed to 0.32 kOe, and the vortex cores in each of the thick layers of the two STNO are parallel to the applied field. In figure 8.5 (a), we observe two auto-oscillating peaks of similar amplitude at low current (20 mA). These two separate peaks then exhibit a reversible transition to a single peak above current $I_{\rm dc}$ > 24 mA, indicating that the STNOs have phase-locked. Figure 8.5 (d) shows the corresponding output power. The black stars are for the single peak at $I_{\rm dc}$ between 24 mA and 37 mA, while red circles and blue squares are the individual powers in the two peaks at $I_{\rm dc}$ below 24 mA and above 37 mA, with the red circles (blue squares) showing the data for the lower (higher) frequency peak of these two. We have measured an average total power of 2 fW/mA^2 and 0.5 fW/mA^2 just below the transition at $I_{\rm dc}$ = 30 mA, as compared to 3 fW/mA^2 in the single peak at higher current. This power increase is an additional indication that the two STNOs have phase-locked.Figure 8.5 (e) illustrates the linewidth, which decreases across the transition, from , ~ 3 / 5 MHz for each of the two peaks at low $I_{\rm dc} < 20mA$, narrowing to 500 kHz for the single peak at $I_{\rm dc}$ =26 mA.

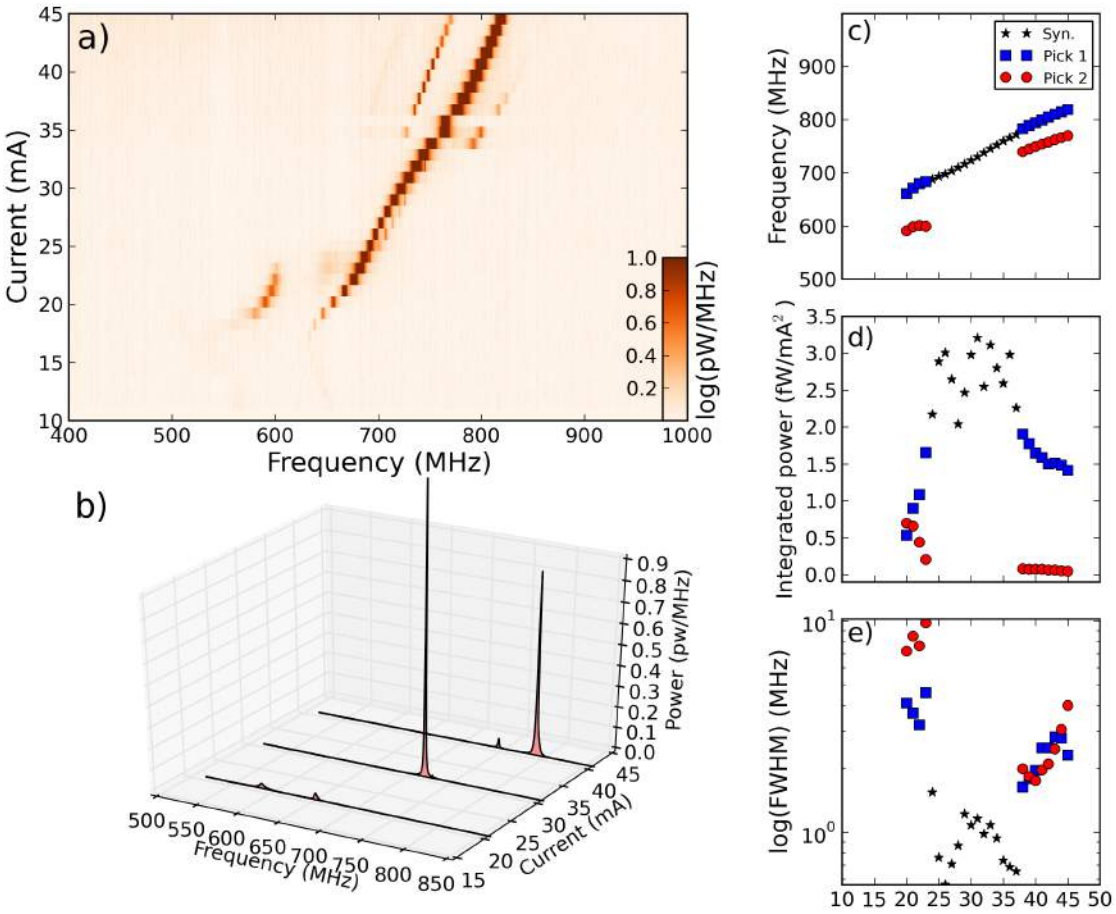

Figure 8.5.: ***Mutual synchronization in a pair of STNOs versus current.*** *(a) Power spectrum PSD versus frequency and applied current bias I_{dc} for perpendicular magnetic field of 0.32 kOe and when the vortex core polarities in the two Permalloy layers are parallel. Two peaks were observed at I_{dc} below 24 mA and above 40 mA, and only a single peak was observed for I_{dc} between 24 and 40 mA.(c), (d) and (e) frequency, power and linewidth versus I_{dc}. The data below and above the synchronization is given by the red circles and blue squares. Black stars show the data for the single peak observed. The transition from two peaks to one are accompanied by an increase in the power and reduction in linewidth, indicating that mutual synchronization between the pair STNOs has occurred.*

8.4.3. Discussion

In collaboration with UMR CNRS Thales, we measured several devices and repeatedly observed the trend in figures 8.4 and 8.5. Only one device showed strikingly different results which are presented in Appendix(C). We have also observed that the common frequency after synchronization was sometimes close to the lowest frequency, and sometimes to the highest. This observation can be linked to the existence of disparities between the two auto-oscillators. Indeed, the ability for each of them to adapt its frequency in order to match the second one is defined by non-linearities around their equilibrium orbit. Small size mismatch, difference in the polarizer shapes, as well as small current mismatch can imply an asymmetry that will allow one of the STNOs to take over and drive the second one.

One of the goal of building arrays of STNOs is to reduce the linewidth of the microwave emission. We haven't tell anything about the linewidth in the part of synchronization versus perpendicular field $H_\perp$. Indeed , we have seen in the previous chapter that even for a single oscillator, the linewidth strongly varies versus perpendicular field (see figure 7.3 (a)). It must be noted that our experimental results have demonstrated that synchronization can be achieved for frequency mismatches as big as 10% of the gyrotropic frequency in the case of opposite polarities. A more physical question can be answered which is why the coupling is more efficient to induce synchronization when the two vortex-auto-oscillators have opposite polarities?

8.5. Theoretical analysis and numerical simulations

8.5.1. Synchronization efficiency: P vs. AP polarities

In order to give an answer to this question and understand the different between the efficient coupling observed in the two synchronization experiments versus $H_\perp$ presented above, it is quite convenient to analyze how the dipolar interaction varies over a precession period. For simplification, we only consider the dipolar interaction between the thick layers, which is dominant here. We recall, that the strong Oersted field induced by the DC current forces the chiralities in each layer to be parallel. When both core polarities are parallel, the two vortices gyrate in the same direction (see figure 8.6), while when they are anti-parallel, they gyrate in opposite directions (because the sign of

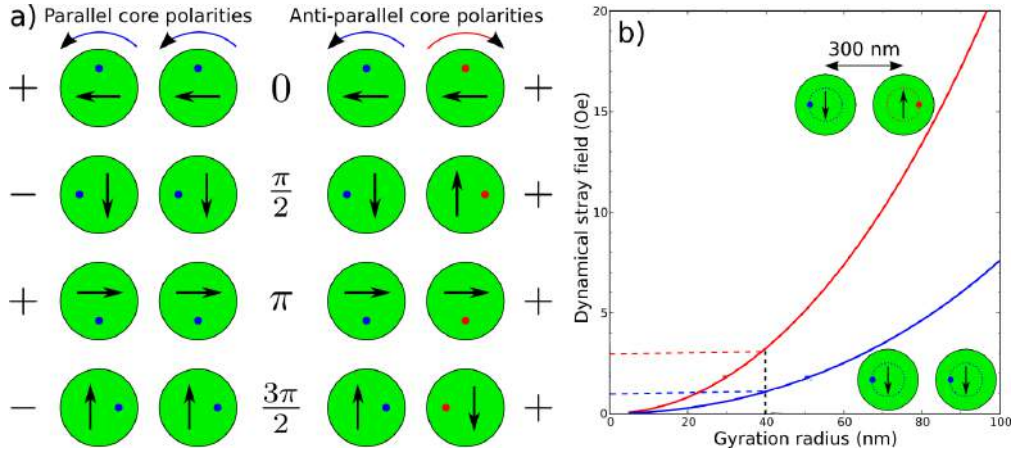

Figure 8.6.: ***Mutual dipolar coupling mechanism.*** *(a) Sketches showing the evolution of the dipolar coupling over a precession period in a pair of adjacent disks in the vortex state having parallel and anti-parallel core polarities. The sign of the mutual interaction is displayed on each side of the sketches. (b) Calculation of the dynamical stray field averaged over a precession period in both cases, as a function of the gyration radius of the vortex core. The red and blue dashed lines correspond to the amplitudes of the microwave field indicated in figure 1(b).*

gyrovector $\mathcal{G}$ is opposite, see equation 1.16). These two situations are not equivalent: contrary to the latter case, the dipolar interaction is not always minimized in the former case, as depicted by "+" and "-" signs in figure 8.6 (a) . Therefore, the dipolar interaction averaged over one period of precession is larger when the core polarities are anti-parallel, which should then favor synchronization.

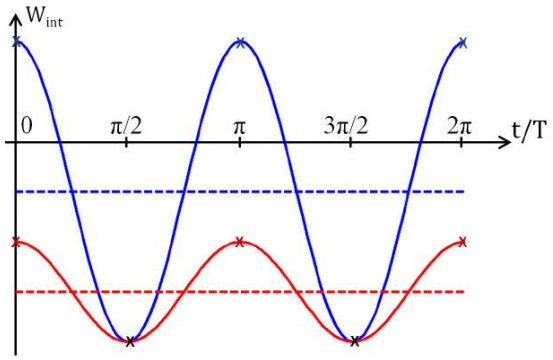

Figure 8.7.: *Dipolar energy (W_{int}) evolution of two interacting dipoles. The blue curve shows the evolution of the in phase oscillating regime (parallel polarities) and the red one the anti-phase case (anti-parallel polarities). The dashed colored lines represent the corresponding mean value of the coupling energies. The coupling is 3 times stronger for the anti-phase oscillating case.*

Now to be quantitative and to explain why the coupling is$three$ times more efficient to induce synchronization when the two vortex-auto-oscillators have different polarities, and are hence gyrating in opposite directions, it is possible to calculate the dynamical stray field averaged over a precession period in both cases, as a function of the gyration radius of the vortex core (see figure 8.6 (b)). As seen in figure 8.6 (b) the mean dynamical stray field is 3 times larger for anti-parallel case than that for the parallel one for a radius gyration of 40 nm. It is also possible to calculate the interaction energy (W_{int}) between these two configurations by using a macro-dipole approximation (see equation (8.3)). As seen graphically in figure 8.7 the mean interacting energy is three times larger for the anti-phase (red) oscillating case than for the in phase one (blue).

8.5.2. Theoretical modeling

The general theoretical modeling and numerical study of phase locking dynamics of dipolarly coupled vortex-based spin transfer nan-oscillators, is presented in details in references [178, 180] and in the thesis of Nicolas Locatelli [80]. Below, we briefly recall the general idea of this model.

The global interaction between the two vortices is very complex as it includes the contributions from the in-plane (body) and out-of-plane (core) magnetizations. As already stated, the shallow dynamics of the thin 4 nm layers can be neglected, and will not substantially contribute to the coupling. Moreover, since the size of the core is very small compared to the dot size (of the order of the exchange length), the dominating interaction is the one between the in-plane magnetizations of the thick 15 nm layers. As the vortex is gyrating, its mean in-plane magnetization describes a full rotation. We will then consider a simple model of two rotating macro-dipoles at the disks center positions. In the following, we will cautiously consider all the polarities and chiralities configuration, as P_1 and C_1 will relate to the first STNO and P_2 and C_2 to the second one.

The proposed model is based on coupled Thiele equations. As we have shown previously the so called Thiele equation is a collective variable equation describing the whole vortex self-sustained gyrotropic motion through the motion of the vortex core. In the following set of equations, a supplementary term was added to account for the dipolar coupling:

$$\vec{G}_{1,2} \times \dot{\vec{X}}_{1,2} - k_{1,2}(X_{1,2})\vec{X}_{1,2} - D\dot{\vec{X}}_{1,2} + \vec{F}_{STT} + \vec{F}_{int} = 0\,. \tag{8.1}$$

In these equations and for each auto-oscillator: $\vec{X}_i$ is the vortex core position (both vortices are considered centered at equilibrium position $\vec{X}_i = 0$) ; $\vec{G}_i = -P_i G\vec{e_z} = -2\pi P_i L\frac{M_s}{\gamma}\vec{e_z}$ is the vortex gyrovector (L: layer thickness, M_s saturation magnetization, γ : gyro-magnetic ratio) ; $W_i(\vec{X}_i) = \frac{1}{2}k_i X_i^2$ is the shifted vortex energy, with $k_i(X_i) = \omega_{i_0} G\left(1 + a_i(X_i/R)^2\right)$ including both the magneto-static and the Oersted field contributions (R : pillar radius); $-D\dot{\vec{X}}_{1,2}$ with $D = -\alpha\eta G$ is the damping force accounting for the dissipative phenomena opposing the motion (α: Gilbert damping coefficient, $\eta = \frac{1}{2}ln\frac{R}{2b} - \frac{1}{8}$: damping factor, b: vortex core radius) ; $\vec{F}_{STT}$ accounts for the total spin-transfer force acting on the vortex and $\vec{F}_{int} = \frac{\partial \varepsilon_{int}}{\partial \vec{X}_i}$ accounts for the dipolar interaction.

$\vec{F}_{STT} = -P_i\lambda J\vec{e_\chi}$. In the specific case of a vortex polarizer [80], it was demonstrated that the spin transfer force acting on the gyrating vortex is constant as a function of gyration radius. As a consequence, it is not expected to have significant influence on the synchronization process.

In a first approximation, the net in-plane magnetization of the shifted vortex grows linearly as a function of the core distance to the center of the dot : $\mu_0 M_i = C_i\xi\left(\vec{X}_i \times \vec{e_z}\right)$ where $\xi = 2/3$ is determined analytically [34]. In a simple macro-dipole model, the interaction energy can be expressed as :

$$W_{int}^{md} = V^2\left(\frac{\vec{M}_1 \cdot \vec{M}_2}{D_{12}^3} - \frac{3(\vec{M}_1 \cdot \vec{D}_{12})(\vec{M}_2 \cdot \vec{D}_{12})}{D_{12}^5}\right) \tag{8.2}$$

$$= C_1C_2\left(-\mu_{(+)}X_1X_2cos(\varphi_1 - \varphi_2) + \mu_{(-)}X_1X_2cos(\varphi_1 + \varphi_2)\right) \tag{8.3}$$

where (X_1, φ_1) and (X_2, φ_2) are the polar coordinates of the first and second vortices cores respectively, and $\vec{D}_{12}$ is a vector connecting the two dots centers. The coupling coefficient then rewrites as $\mu_{(+)} = \frac{1}{2}\frac{\xi^2V^2}{D_{12}^3} < 0$ and $\mu_{(-)} = \frac{3}{2}\frac{\xi^2V^2}{D_{12}^3} > 0$ so that $\mu_{(-)} = 3\mu_{(+)}$

At this point, it must be emphasized that the gyration direction of the vortex oscillator is governed by its core direction (polarity). As a major consequence, the contribution of the two terms to the interaction energy will be dramatically different as the polarity are identical or opposite. To account for this, we rewrite the phase evolution for the two auto-oscillators as : $\varphi_{1,2} = P_{1,2}\omega_{1,2}t + \varphi_{i_0}$ where $\omega_{1,2} > 0$. This reveals that the first term associated to $\mu_{(+)}$ oscillates in time at a frequency $P_1\omega_{1,2} - P_{1,2}\omega_2$ where the second

one associated to $\mu_{(-)}$ oscillates at a frequency $P_1\omega_{1,2} - P_{1,2}\omega_2$. For two STNOs with close frequencies $\omega_1 \sim \omega_2$, depending on the relative polarities, one term will beat at high frequency while the other will be slowly varying in time as compared to the oscillators' gyrotropic frequencies. When considering the phase locking dynamics for synchronization, only the slowly varying term will contribute as the second one will be averaged out. For identical polarities, only the $\mu_{(+)}$ term remains, when the $\mu_{(-)}$ term remains for opposite polarities.

The two cases are illustrated on figure is the ideal condition of frequency locking $\omega_1 = \omega_2 = \omega$. When the vortices gyrates in the same direction (identical polarities), the interaction energy shows large oscillations at frequency 2ω around a mean energy $\langle \mathcal{W}_{int} \rangle |_P = -\mu_{(+)} \mathcal{M}_1 \mathcal{M}_2$, whereas when they gyrate in opposite direction (opposite polarities) the interaction energy varies with lower amplitude but has a mean energy $\langle \mathcal{W}_{int} \rangle |_A \; P = -\mu_{(-)} \mathcal{M}_1 \mathcal{M}_2$, three times lower. From this study it also appears that the sign of relative chiralities, despite changing the sign of the interaction coefficient, will not affect its amplitude. Such change in the sign of the coupling will simply affect the synchronization equilibrium phase, being whether close to $\Delta\varphi = 0$ or π. Then, in the following, we will focus on the case of identical chiralities $C_1 C_2 = +1$. Starting from the coupled equations, we then study the synchronization phenomenon by deriving the dynamics of the signed phase shift $\Psi = P_1\varphi_1 - P_2\varphi_2$. Under the assumption of relatively small disparities between the two oscillators and small coupling, its evolution can be summarized by the differential equation (see Nicolas thesis for details of the calculation):

$$\dot{\Psi} = \Delta\omega - \frac{2\mu_{\pm}}{\alpha\eta} sin\Psi \,, \tag{8.4}$$

where $\mu_{(\pm)}$ stands for $\mu_{(+)}$ in case of identical polarities and $\mu_{(-)}$ in case of opposite polarities. This equation is similar to the well-known Adler equation for the synchronization of coupled oscillators [124]. A stable equilibrium phase-shift can only exist at the condition:

$$\Delta\omega < \frac{2\mu_{\pm}}{\alpha\eta} \,. \tag{8.5}$$

8.5.3. Discussion

This analytical result and the experimental measurements appear to be in good agreement, the critical frequency difference for synchronization being three times bigger in the case of identical polarities than in the case of identical ones. However, it must be noted that this model does not take into account the influence of the temperature. Thermal noise can indeed reduce the synchronization region or even prevent the synchronization if the coupling is too weak when pillars are too far away from each other. To get a hint of the limitation of dipolar coupling to achieve the synchronization of STNOs, we present a numerical evaluation of the mean interaction [178]. On figure 8.8 we plot the mean interaction energy between two identical vortex auto-oscillators with diameter 200 nm as a function of the center-to-center distance, extracted from full micro-magnetic simulations [178]. These values are extracted by studying the synchronization dynamics between the two identical oscillators at zero temperature and zero field, hence with no frequency difference. This specific case allowed us to monitor the synchronization phenomenon whatever the amplitude of the coupling. In the figure 8.8, we identify again the factor three between P and AP polarities cases, and can compare both associated energies to the thermal energy at room temperature. It confirms that for a 100 nm inter-dots distance (D_{12} = 300nm), coupling energy is high enough to overcome thermal energy, allowing to observe synchronization in both AP and P polarities configurations. But, it appears that when edge-to-edge distance exceeds the pillar diameter, thermal fluctuation may prevent synchronization, starting with the less efficient P configuration.

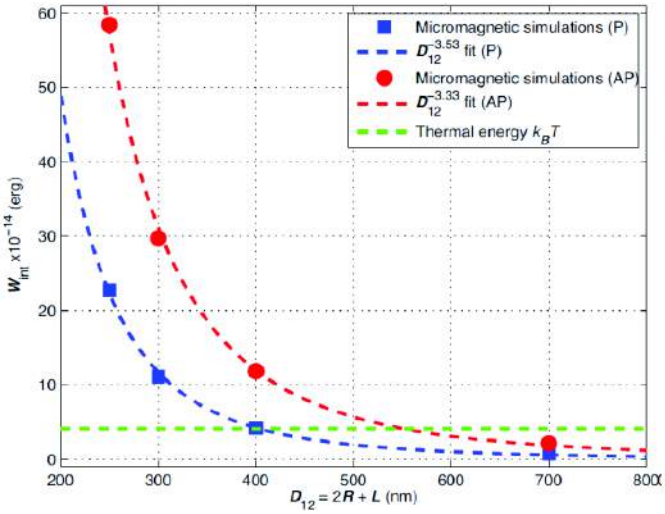

Figure 8.8.: *Absolute values of interaction energy W_{int} as a function of inter-dot separation distance $D_{12} = 2R + L$ obtained from the micro-magnetic simulations (dots) and from the macro-dipole model (line) in the case for parallel polarities (blue) and opposite polarities (red).*

8.6. Conclusion

We have investigated the synchronization of spin transfer nano-oscillators that are interacting through dynamical dipolar coupling. We have experimentally measured a system composed of two STNOs with diameter 200 nm separated by a L=100 nm edge-to-edge distance. In this experiment, both pillars are supplied through the same electrodes and the current flowing in each pillar cannot be tuned independently.

We have observed that when the frequencies of the two oscillators are brought closer, they eventually merge into a single peak, demonstrating the first experimental synchronization through magneto-dipolar coupling. Reproducing the experiment, we measured and compared the experimental values of the synchronization range for core polarities being parallel or anti-parallel. A good agreement is demonstrated between experiments and analytical/numerical predictions. Namely, the coupling efficiency and the associated locking-range is tripled when the interacting vortices have opposite polarities instead of identical ones. Combined with the control of vortex polarities, this work open the path for coupling control of interaction in networks of oscillators, which can be of great interest in applications.

Conclusion and perspectives

General summary

The main goal of this thesis was to contribute to a better understanding of the microwave properties of STNOs, a prerequisite to optimize their performance in particular in terms of tunability by a current and spectral purity at the level of single device or several mutually coupled oscillators. My studies have focused on two classes of configurations which are characterized by different excitation modes that lead to different frequency ranges and dynamic properties. The first configuration is the normally magnetized state of a circular nanopillar. I have studied the spin transfer driven excitation modes when the magnetization of both layers are out-of-plane, saturated by a strong external magnetic field $H_\perp$. I have also investigated another important configuration of the same device, which is the double vortex state. I have focused on the lowest energy mode excited by spin transfer which is the coupled gyrotropic mode where the vortex cores in each magnetic layer are orbiting on a circular trajectory around the equilibrium position.

Our first original contribution was to identify the nature of the auto-oscillating mode in a spin transfer nano-oscillator. The spectroscopic identification of the auto-oscillating mode is usually a challenge, as a large variety of dynamic modes can be excited in STNOs, and their nature can change depending on the geometry, magnetic parameters and bias conditions. Thus, an accurate identification has important consequences regarding the

optimization of the performance of STNOs, because it allows to understand the details symmetry of the mode. The MRFM was of great interest for this identification since it can directly monitor the power emitted by our archetype STNO. In the first step, we have studied our STNO in the most simple configuration: a nanopillar saturated by a strong magnetic field applied along its normal. Then from the power behavior in the sub-critical region of the autonomous dynamics, we have obtained a quantitative measurement of the threshold current and of the noise level. Their field dependence directly yields both the spin torque efficiency acting on the thin layer and the nature of the mode which first auto-oscillates: the lowest energy, spatially most uniform spin-wave mode. From the MRFM behavior in the forced dynamics, it is then demonstrated that in order to phase-lock this auto-oscillating mode, the external source must have the same spatial symmetry as the mode profile, i.e., a uniform microwave field must be used rather than a microwave current flowing through the nanopillar.

The influence of broken the axial symmetry of the perpendicular field on the auto-oscillating mode was also investigated. Interestingly, we have measured excitations in a STNO nanopillar, revealing the occurrence of the two-mode generation regime. These two modes were identified as the lowest energy spin-wave eigen-modes of the free layer with different azimuthal numbers $\ell = 0$ and $\ell = +1$. Then, we have experimentally demonstrated that these two mode can be phase-locked to an external source having the appropriate symmetry. As one of these two modes is synchronized to the external source, the emission characteristics of the other one are also strongly affected, which can be understood in terms of the mutual non-linear interaction between the two modes. In particular, a reduction of the linewidth by a factor up to five was observed on the $\ell = 1$ mode when the mode $\ell = 0$ was phase locked. Nevertheless, a full theoretical description of this phenomenon is missing at this time.

We have then taken the advantage of the sample design to investigate the microwave characteristics of the same spin transfer nano-oscillator (STNO) based on coupled vortices as a function of the perpendicular magnetic field $H_\perp$. Interestingly, we found that our vortex-based oscillator is quasi-isochronous independently of $H_\perp$ and for a DC current ranging between 18 and 25 mA. It means that the severe nonlinear broadening usually observed in STNOs can be suppressed on a broad range of bias. Still the generation linewidth displays strong variations on $H_\perp$ (from 40 kHz to 1 MHz), while the frequency tunability in current remains almost constant ($\simeq$ 7 MHz/mA). This demonstrates that isochronicity does not necessarily imply a loss of frequency tunability, which is here governed by the current induced Oersted field. It is not sufficient either

to achieve the highest spectral purity in the full range of $H_\perp$. We have shown that the observed linewidth broadenings are due to the excited mode interacting with a lower energy overdamped mode, which occurs at the successive crossings between harmonics of these two modes. These findings open new possibilities for the design of STNOs and the optimization of their performance. In fact, our tunability is almost $\sim 80 MHz/mA$ at $H_\perp$ = $0.7kOe$, the sweet point for spectral purity (see Fig. 2), which corresponds to about 200 times the linewidth in 1 mA.

From a practical point of view, it was demonstrated that the microwave signal generated by a STNO based on coupled vortices can be efficiently synchronized to an external microwave field. The relative locking range indeed exceeds 10% for small drive amplitudes ($h_{\mathrm{rf}} \simeq 5$ Oe) and the auto-oscillation signal acquires the spectral purity of the source, corresponding to an improvement of its coherency by a factor greater than 10^5. Moreover, this perfect phase-locking is robust, as it survives even when the external frequency deviates from the oscillator frequency by more than ten times of its linewidth.

The last main achievement of this thesis is the demonstration of the synchronization of two STNOs coupled by the dipolar interaction. We have observed that when the frequencies of the two oscillators are brought closer, they eventually merge into a single peak, demonstrating the first experimental synchronization through magnetostatic coupling. Reproducing the experiment, we have measured and compared the experimental values of the synchronization range for core polarities being parallel or anti-parallel. A good agreement was demonstrated between the experiment results and the analytical/numerical predictions. Namely, the coupling efficiency and the associated locking-range is tripled when the interacting vortices have opposite polarities instead of identical ones. Coupled to already demonstrated control of vortex polarities, this work open the path for coupling control of interaction in networks of oscillators, which is of great interest for many applications.

Outlook

From this thesis, a novel approach can be proposed to tackle the issue of spectral purity which is to focus on spin transfer induced collective or coupled magnetic excitations for microwave generation in particular in the vortex state. It can be done by using advanced multilayers made of magnetic/non magnetic stacks where consecutive ferromagnetic layers are coupled via exchange, dipolar fields and spin momentum transfer. Further

improvement of the microwave performance will be expected via dipolar coupling of individual spintronics devices in an array. Indeed, some important knowledge of fundamental physics on device level was acquired in this thesis, like the role of the coupling mechanisms and coupling strengths between two oscillators. After our experimental observation, we believe that the dipolar coupling mechanism between individual STNOs should be efficient to synchronize $\mathcal{N}$ STNO. This can expand the possible applications of spintronics devices e.g. associative memories [177].

Finally, I hope that the knowledge gaps presented in this thesis will be filled by progressing in understanding the fundamental mechanisms governing the microwave properties in STNOs. Moreover, there are many other systems in which spin momentum transfer should generate new physics and applications [181]. In particular, it was demonstrated to be very interesting in diverse situations : chaos [182], droplet solitons [183], skyrmions [184, 185], pure spin currents [186, 187], and magnetic insulators [188].

Appendices

APPENDIX A

Differential phase diagrams

In this appendix, we show experimental phase diagrams, with better signal to noise ratio of the MRFM and transport data. To improve the measurements, we add to I_{dc} a small signal of amplitude I_{pp} = 0.1 mA modulated at the frequency of the cantilever, then it is possible to measure by MRFM the small variation dM_z/dI induced by this modulation and we have used a lock-in to detect the differential resistance dV/dI simultaneously. The obtained phase diagrams, presented in figure A.1 (a), look like the derivative of those presented in chapter 6 (see figure 6.3). Here we have measured these phase diagrams in the exact perpendicular configuration $\theta_H = 0°$ and at $\theta_H = 2°$ where θ_H represent the angle between the external magnetic field and the normal to the free layer. Using the conversion from MRFM data to resistance, we can also quantitatively compare MRFM to transport measurements. Two striking features can be observed in these diagrams. First, the succession of sharp peaks in dV/dI and dM_z/dI, which indicate a succession of steps in R_{dc} and M_z. Second, the qualitative difference between $\theta_H = 0°$ and at $\theta_H = 2°$ in the region of onset of the auto-oscillations: there is a peak at $\theta_H = 2°$ (see white arrows), absent at $\theta_H = 0°$.

The succession of sharp peaks should be related to the frequency jumps of the auto-oscillations observed in the transport spectrum analyzer data see figure 6.8. Rather

than a smooth opening of the precession angle in the thin layer as the supercriticality increases, we observe successive jumps, where the precession angle abruptly increases. This is not only observed at $\theta_H = 2°$, but also at $\theta_H = 0°$ (where no SA data are available). However, when the supercriticality is small ($\xi < 1.5$), we do observe a quite smooth increase of resistance and ΔM_z at $\theta_H = 0°$ (whose detailed analysis have been already presented in chapter 6) and is related to the excitation of a bi-modal regime when $\theta_H = 2°$, contrary to the case $\theta_H = 2°$. This qualitative difference was already pointed out in the discussion in chapter 6. In figure A.1, one can also note that whereas the threshold current monotonously increases with the bias field at $\theta_H = 0°$, it first decreases at $\theta_H = 2°$, before it starts to increase above 9.6 kOe (white arrows).

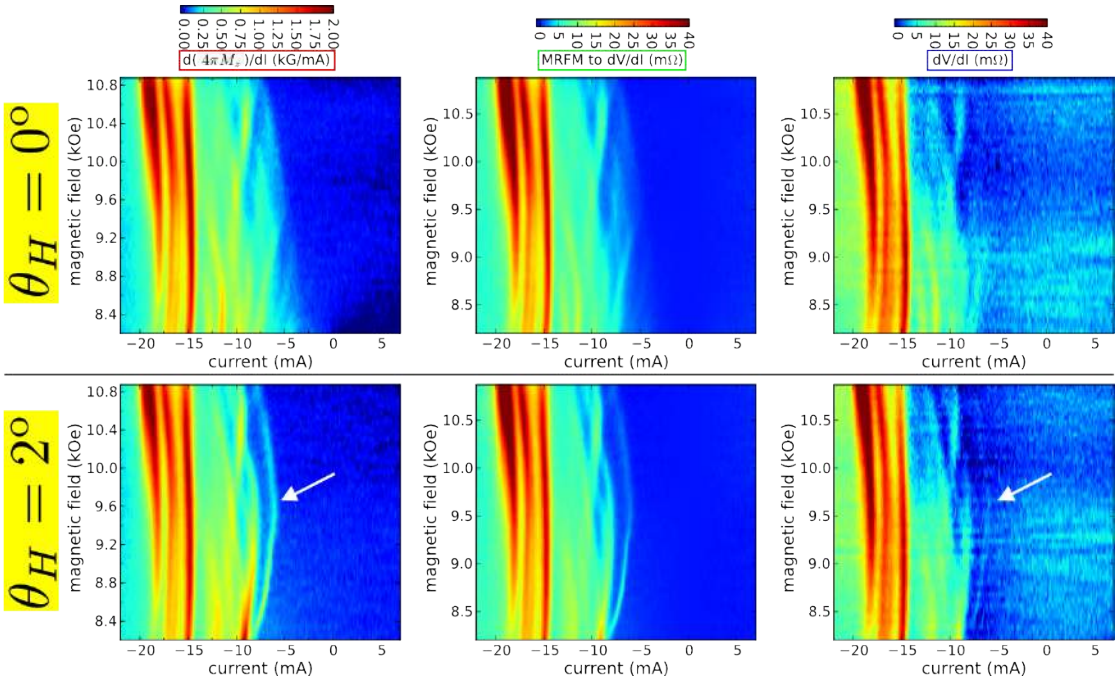

Figure A.1.: *Differential phase diagrams obtained at $\theta_H = 0°$ (top row) and at $\theta_H = 2°$ (bottom row). The peak-to- peak current amplitude is $I_{pp} = 0.1mA$. The left column shows the raw MRFM data, the middle one, its conversion into differential resistance dV/dI, and the right one, the measured dV/dI using a lock-in amplifier.*

APPENDIX B

STNO power at large **positive** current

In this appendix we display the measurement of the STNO $\Delta M_z/M_s$ versus high (positive and negative) current, measured by MRFM for a bias field $H_\perp$ = 10 kOe. In fact, we find that the spin-transfer torque can also excite the magnetic thick layer in our STNO for large positive current. One can see that in region (1) (red), the current starts exciting the precession of the thick layer. As a small precession angle opens, the ΔM_z increases slightly (the MRFM signal starts to smoothly increase). Notice that since the critical current depends on the thickness of the layer (see equation 1.9 in chapter 1), then for the thick layer the critical at this field is about 22 mA which is ~ 4 times greater that for the thin layer.

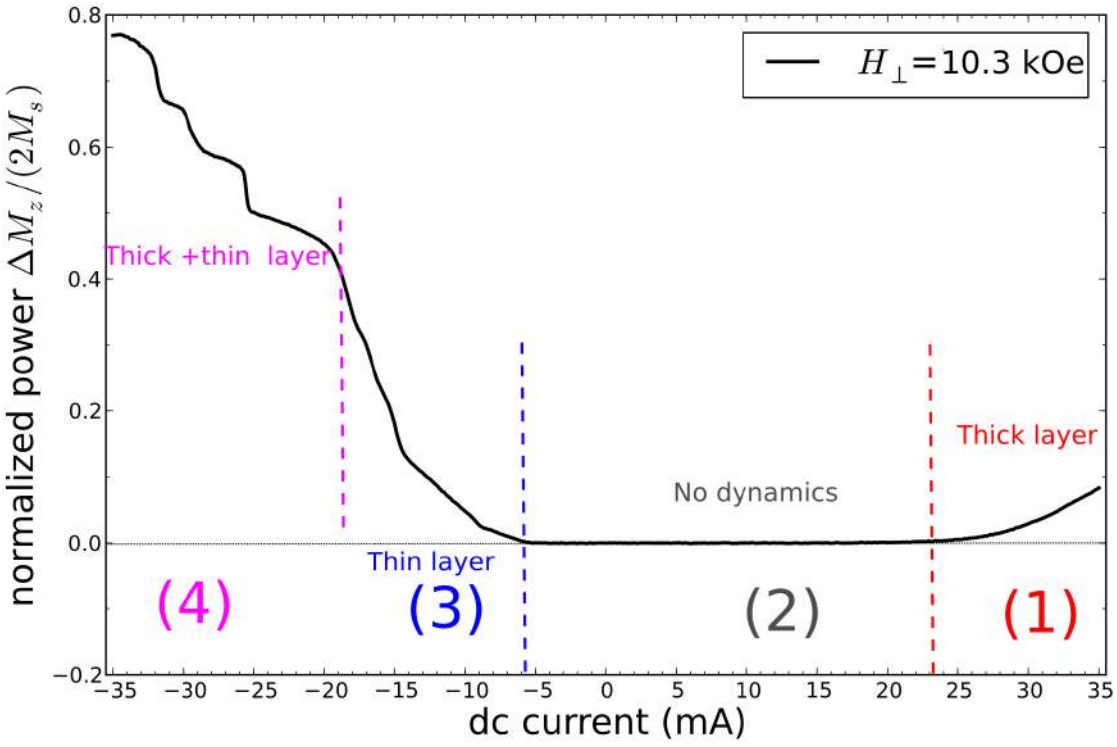

Figure B.1.: *Total power p emitted by the STNO as a function of the bias I_{dc} current $-35 < I_{dc} < 35mA$, measured by MRFM when a external magnetic field$(H_\perp = 10.3kOe)$ is applied along the normal of the sample $(\theta_H = 0°)$. We can distinguish 4 regions with different dynamics. Region (1): precession of only the thick layer; region (2) No dynamics i.e. both the layers are aligned with $H_\perp$; region (3): precession of the thin layer; regions (4): magnetization reversal of the thin and precession of both layers (see the text for the description of region 1 and see section 6.1.1.1 for regions 2,3,4).*

APPENDIX C

Strongly mutually coupled oscillators

In this appendix, we show intersting results of mutual synchronization in a pair of STNOs obtained in one device which is taken from the same batch of samples (see section 5.1.2).

In the first experiment, a constant DC current of 35 mA is applied through the device, i.e. about 17.5 mA in each STNO. The top panel of figure C.1 shows the evolution of the auto-oscillation peaks measured on the spectrum analyzer as a function of the perpendicular applied magnetic field. Here we purposely prepared a state where the vortex core polarities in the thick layers of each STNO are opposite. We can clearly see that when the auto-oscillation peaks are close enough in frequency, a strong **pulling** occurs, that makes them meet each other (synchronize). The frequency of each oscillator is analyzed in the bottom graph, where the data (in red) correspond to the synchronized regime. Contrary to what is observed in figure 8.4 of chapter 8, the synchronization in this case is not accompanied by a jump of the frequencies. It is instead close to the synchronization phenomena observed in the pair of nano-contacts see figure 3.7 (a) of chapter 3. One can also note the appearance of signals at mixing values of the two oscillating frequencies in the pulling regime at field above -0.9 kOe (before the vortices

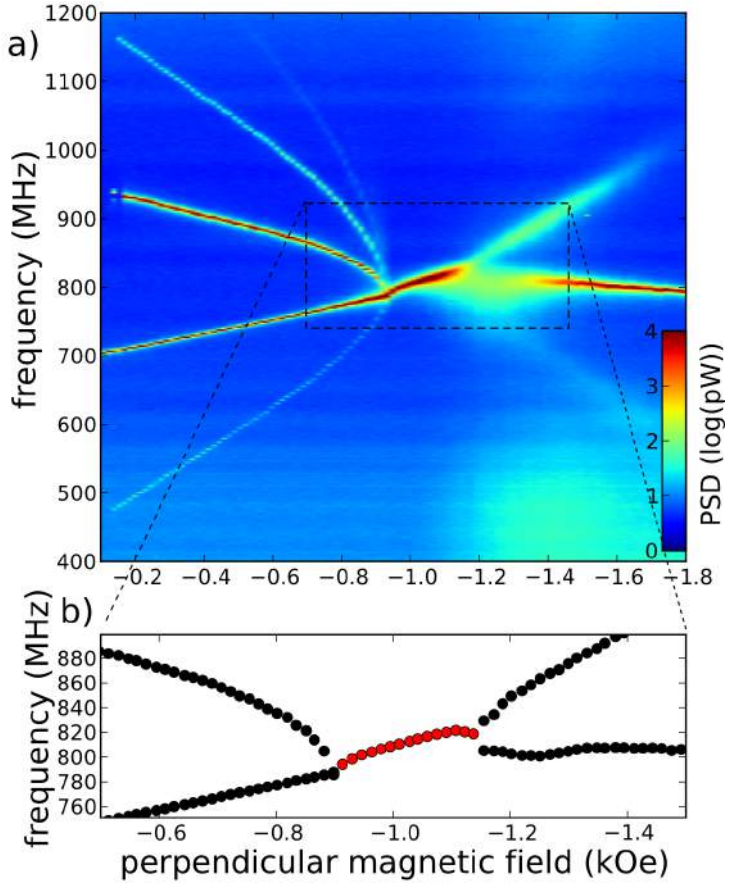

Figure C.1.: *(a) PSD map of a pair of STNOs separated from center to center by 300 nm. The map are recorded as a function of the perpendicular bias magnetic field for a common current I_{dc} = 35 mA injected through the two STNOs in parallel. Strong mutual synchronization is observed when the vortex core polarities in the thick layers are anti-parallel. (b) Device signal frequency as a function of magnetic field.*

phase-lock their motion). This is also observed when we synchronize a single vortex STNO to an external source (the rf field produced by an external microwave antenna).

In addition, we have also studied the dependence on bias current of the high-frequency dynamics of this device. In this experiment the bias perpendicular field is fixed to $H_\perp$ = 1 kOe, and the vortex cores in each of the thick layers of the two STNOs are parallel to the applied field. At low current (14 mA), one can observe two auto-oscillating peaks of similar amplitude. As the current increases, the frequencies of both oscillators increase. As both STNOs are not exactly similar (or the bias DC current that flows in each of them is slightly uneven), it happens that the two oscillator frequencies can cross each other. The crossing observed in this case is not accompanied by any pulling or jump of the two

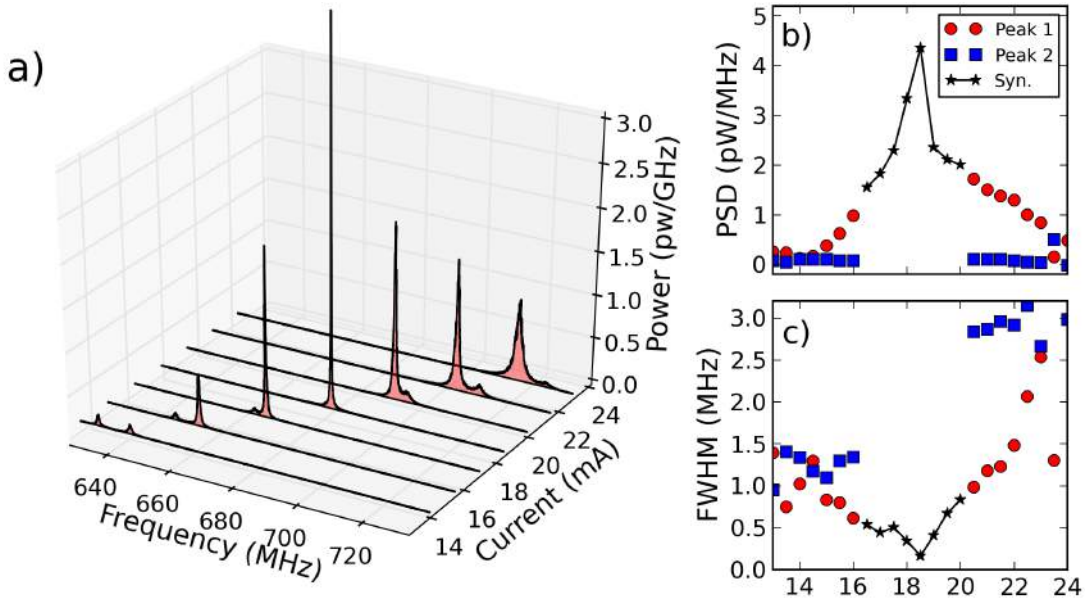

Figure C.2.: *Power spectrum PSD versus frequency and applied current bias I_{dc} for perpendicular magnetic field of 1 kOe and when the vortex core polarities in the two thick Permalloy layers are parallel. (b) and (c) Linewith and power versus I_{dc}. The data below and above the synchronization is given by the red circles and blue squares. Black stars show the data for the single peak observed. The transition from two peaks to one are accompanied by an increase in the power and reduction in linewidth.*

frequencies, in contrary to what was observed in the previous experiment (see figure 8.5 of chapter 8). Here, the phase-locking manifests itself by a strong reduction of the linewidth (see figure C.2 (c)) and by a large increase of the amplitude (see figure C.2 (b)).

Finally we have performed a measurement versus the in-plane magnetic field angle $\theta_\measuredangle$. In this experiment an external magnetic field of small constant magnitude (30 Oe) is applied to the sample at an angle $\theta_\measuredangle$ with respect to the axis through the center of both STNOs. As explained in section 8.4 that when we change $\theta_\measuredangle$ we can change the coupling between the layers, and the frequency of each oscillator because the vortex cores are displaced in the magnetic layers. Figure C.3 shows the angular dependence of the microwave spectrum at a constant current I_{dc} = 24 mA. We observe two distinct signals for $\theta_\measuredangle = 0°$. The frequencies of these two signals differ by about 20 MHz, and then start to approach each other up to an angle $\theta_\measuredangle = 50°$ where the lower frequency signal disappears, which is probably the signature of synchronization. The two distinct signals appear again for values of $\theta_\measuredangle = 100°$ but now the two signals differ in frequencies by only about a few MHz. It's clear that the coupling strength is changed and for this

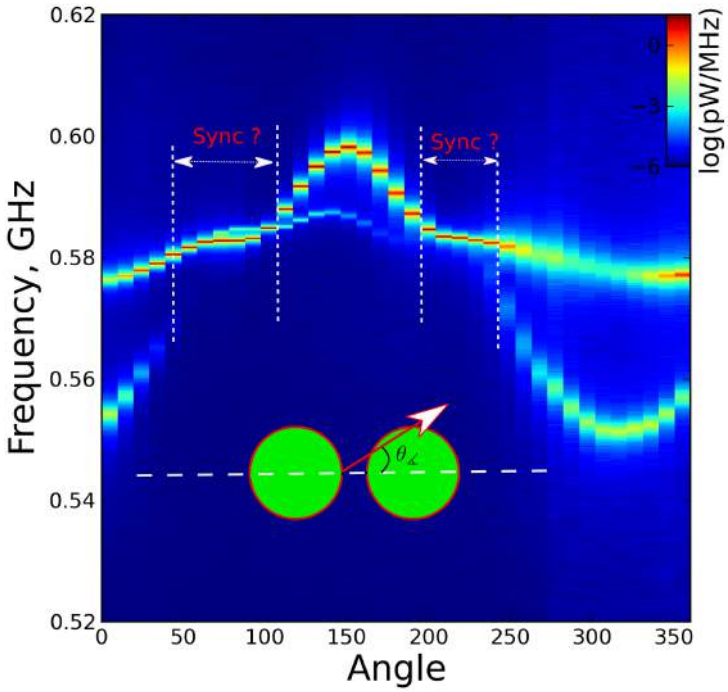

Figure C.3.: *Map of power spectrum amplitude versus frequency and an applied in plane field angle $\theta_\measuredangle$ at I_{dc} = 24 mA and H_{ext} = 30 Oe.*

angle ($\theta_\measuredangle = 100°$) the value of the coupling strength should be very small. Finally the general behavior of the dependence of the microwave frequencies (two signals, one signal) is "pseudo-periodic" with increasing the value of $\theta_\measuredangle$. The important information that we can conclude here that it's possible to $adjust$ the couplings between the STNOs by changing the in plane angle of the external magnetic field.

Discussion

The features of the mutual synchronization observed in this device are very different from the one presented in chapter 8. We believe that the particular double STNO device presented in this appendix might have major nano-fabrication defects. Maybe the two nano-pillars are touching each other, and have quite different shapes, as supported by the large frequency difference ($> 200 MHz$) observed at $H_\perp \sim 0\ kOe$ in figure C.1

APPENDIX D

Pair STNOs in the saturated state

Mutual synchronization of devices with pair of STNOs was not observed in the saturated state. In contrast, pairwise synchronization was seen in vortex state. Figure D.1 shows the measured frequency spectrum versus I_{dc} in the saturated state for the same device which was presented in chapter 8 (2 nano-pillars with diameter 200 nm and edge-to-edge spacings of 100 nm). The data in this measurement was taken at a magnetic field of 8 kOe applied perpendicular to the plane of the sample. In Figure D.1 (a), we observe the onset of one auto-oscillation peak for I_{dc} = -18 mA followed by a second peak of comparable amplitude for I_{dc} = -20 mA. Then, the two peaks evolve nearly parallel in frequency versus I_{dc}. For negative current it was identified that the dynamics here corresponds to the precessional state of the thin layer in each oscillator. One can also see from figure D.1 that the gap in frequency between the two oscillator is about ~ 1.5 GHz which is much larger than observed in the vortex state (< 50 MHz). Thus, the strength of the dipolar interaction between the two thin layers (a few tens of MHz) is not sufficient to synchronize our two oscillators in the saturated state.

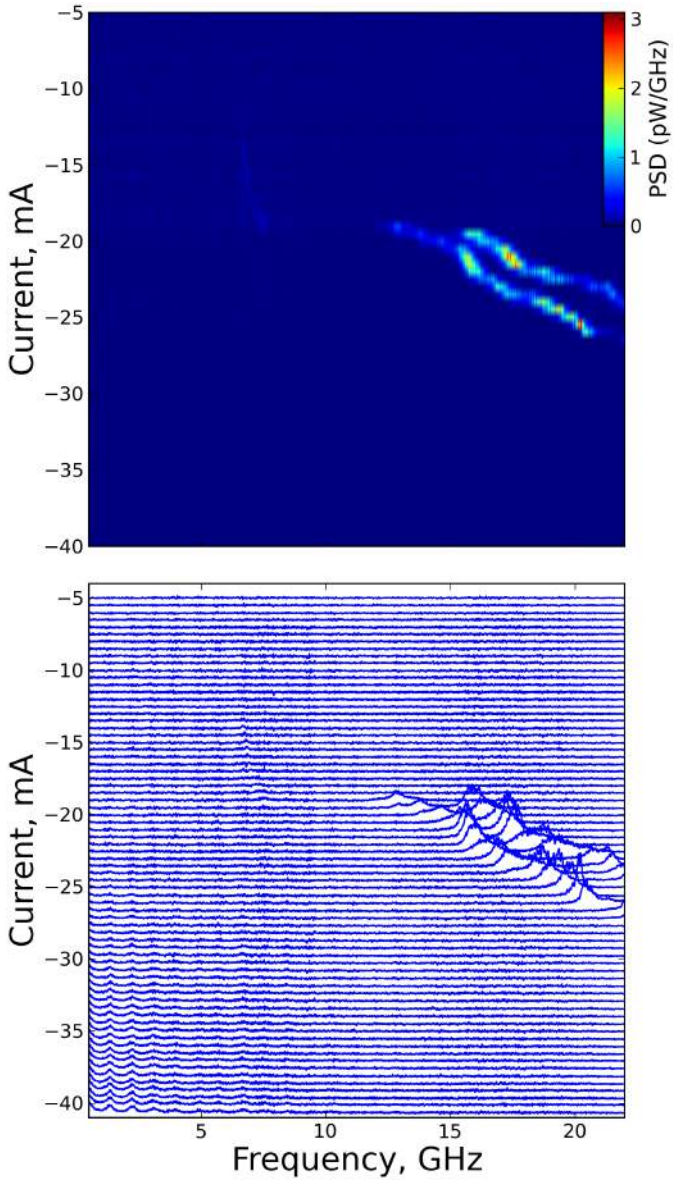

Figure D.1.: *Power spectrum map versus frequency and applied current bias I_{dc}. Two peaks are observed above I_{dc} = -20 mA,then they move approximately parallel in frequency with I_{dc} in the whole range [-20 ; -25] mA.*

APPENDIX E

Résumé substantiel en Français

Introduction

Les récents progrès technologiques dans la fabrication de nanostructures hybrides incorporant des matériaux magnétiques ont permis l'émergence de la spintronique. Ce domaine de recherche est basé sur le degré de liberté de l'électron [1] de spin: courants de spin sont générés et manipulés à l'échelle nanométrique afin de parvenir à de nouvelles fonctionnalités.

Un dispositif élémentaire de l'électronique de spin est constitué de deux couches magnétiques séparées par une couche non-magnétique. Il présente l'effet de magnétorésistance géante (GMR) [2, 3], c'est que la résistance dépend de l'angle relatif entre les couches magnétiques. Aujourd'hui, cette propriété utile est largement utilisé dans les capteurs magnétiques [4, 5]. L'effet inverse est un courant continu qui peut transférer moment angulaire de spin entre deux couches magnétiques séparées soit par un métal normal ou une couche mince isolante [**?**, 7]. Plus généralement, un courant de spin exerce sur un matériau ferromagnétique, un couple de transfert de spin, qui peut compenser l'amortissement et conduire à la déstabilisation du moment magnétique [8]. Les applications pratiques sont la possibilité de contrôler l'information numérique

dans les mémoires magnétiques (MRAM) [9, 10] ou pour produire des signaux à haute fréquence dans à transfert de spin nano-oscillateurs (STNOs) [11, 12].

En raison de leur accordabilité, l'agilité, compacité, et intégrabilité, les STNOs sont des candidats prometteurs pour diverses applications à haute fréquence tels que génération de fréquence [13, 14], détection de fréquence [15, 16], traitement du signal [17, 18] et l'enregistrement dynamique [19, 20, 21]. En ce qui concerne les applications micro-ondes, la pureté spectrale et la sensibilité de réglage sont deux caractéristiques clés pour STNOs. Une particularité de ces dispositifs par rapport aux autres oscillateurs est leurs fortes propriétés non linéaires, qui sont héritées de l'équation du mouvement de l'aimantation [22]. D'une part, ils confèrent des propriétés intéressantes pour STNOs, comme par exemple leur grande accordabilité fréquence [11, 12, 13, 14]. D'autre part, elles conduisent à un élargissement sévère de la génération du largeur de raie [23]: en raison du couplage phase-amplitude non linéaire, le bruit de phase de STNOs est en effet assez grandes [24, 25], qui est le principal facteur limitant pour les applications pratiques. Par conséquent, les non-linéarités affectent à la fois l'agilité et la pureté spectrale d'une manière de telle sorte que les deux quantités ne peuvent être optimisées de facon indépendante et un compromis doit être trouvé. En outre, étant les STNOs sont des générateurs de micro-ondes à l'échelle nanométrique, leur puissance émise est trèes petite, typiquement de l'ordre de pico ou nano-Watts. Dans ce contexte, mutuelle synchronisation de plusieurs STNOs a été proposée comme un moyen de réduire le bruit de phase et augmenter la puissance de ces oscillateurs [26, 22]. À ce jour, il ya quelques réalisations expérimentales de cette idée, basés sur des systèmes spécifiques avec $2 \leq N \leq 4$ STNOs mutuellement synchronisés [27, 28, 29, 30]. Les principales limites dans le développement de grands réseaux de STNOs synchronisés sont: la dispersion des propriétés dynamiques en raison des incertitudes dans le processus de fabrication, la force du couplage dynamique, et sa symétrie, ce qui pourrait empêcher la synchronisation de grands réseaux. Par exemple, pour la même raison pour laquelle le couplage dipolaire seul ne peut pas être responsable d'une aimantation spontanée (ferromagnétisme), on ne peut pas construire un tableau 3D fermée remplie de synchronisation des oscillateurs à travers le couplage dipolaire.

Ce travail de thèse a été motivée pour mieux comprendre les propriétés de micro-ondes de STNOs, une prérequis si on veut optimiser leurs performances au niveau d'un dispositif unique ou plusieurs oscillateurs couplés entre eux. Pour atteindre cet objectif, un outil spectroscopique a été adopté, parce que la connaissance du spectre du modes propres d'onde de spin dans les nanostructures magnétiques hybrides, leurs symétries,

les énergies, les taux de relaxation, et leurs propriétés non linéaires, est crucial dans de nombreux aspects. D'un cté, les énergies des ondes de spin, les taux de relaxation, et des propriétés non linéaires déterminent les fréquences et les largeur du raie spectrale qui peuvent émettre [22] par un STNO. D'un autre cté, la symétrie spatiale des modes donne une idée fondamentale de leurs règles de sélection (la façon dont ils se coupler à des sources externes) et sur les mécanismes de couplage mutuel qui peuvent exister intra-ou inter-STNOs.

Les modes propres d'onde de spin peuvent être considérés comme une empreinte d'une nanostructure magnétique et ils sont liés à son état fondamental [31, 32]. En outre, en raison des interactions entre les différentes couches magnétiques dans un STNO (par exemple, l'interaction dipolaire), ces modes propres ont souvent un caractère collectif, c'est à dire, ils impliquent plusieurs couches dans l'empilement. Il ya quelques années, il a été montré expérimentalement que le couple de transfert de spin pourrait exciter le mode gyrotropique d'un vortex magnétique [33], qui est le mode de plus basse énergie de cet configuration [34]. Les largeurs de raies remarquablement étroites génération (environ 1 MHz ou moins) et la grande puissance de sortie dans le cas de jonctions tunnel magnétiques (MTJ) démontré par l'UMR CNRS/Thales en collaboration avec l'AIST (Japon) [**?**], sont extrêmement prometteur pour des application[1].En parallèle, il a été réalisé dans le laboratoire du CEA Spintec que l'excitation des modes couplés dans JTMs standards uniformément magnétisés pourrait améliorer la largeur de raie jusqu'à un ordre de grandeur [38, 39]. Peu de temps avant le début de cette thèse, mon laboratoire dans CEA/SPEC et l'UMR CNRS/Thales a combiné ces deux idées pour réduire encore plus la largeur de raie d'auto-oscillation. En op érant un STNO basé sur deux vortex couplés dans un spin-valve nanopilier, ils ont obtenu un largeur de raie de $\Delta f = 46$ kHz (pour une fréquence généré $f \simeq 780$ MHz, *ie.* , $f/\Delta f \simeq 17\,000$) [40]. Important encore pour les applications, une grande cohérence a été maintenue, même à champ magnétique nul, et une grande accordabilité de la fréquence sur le courant continu ($\simeq environ 10$ MHz / mA) a été mesurée.

Afin de définir une stratégie visant à optimiser les caractéristiques de micro-ondes (en particulier la cohérence) de STNOs individuels et à quelques efficacement plusieurs STNOs ensemble, les questions suivantes doivent être adressées:

1. Quelle est la nature de la mode propre (s) auto-oscillant d ans un STNO?

[1] récemment, jusqu'à quelques micro-Watts ont été signalés dans les pilliers optimisés ayant un grand rapport de magnétorésistance [36],Le faible bruit de phase en vortex JTM a également été directement mesurés et analysés [**?**].

2. Quelle est l'influence des autres modes dans le système sur la largeur de raie?

3. Quelles sont les non-linéarités dans le système? Quels sont les autres propriétés peuvent influer sur la largeur spectrale et la accordabilité?

4. Quel est le mécanisme de couplage optimal à verrouillage de phase la auto-oscillation à une source externe?

5. Quelle est la meilleure stratégie pour synchroniser mutuellement plusieurs STNOs d'une manière évolutive?

L'objectif de cette thèse est d'apporter des connaissances à ces différents points, avec une attention particulière pour comprendre les propriétés intéressantes de STNOs basé sur des vortex magnétiques. En particulier, l'interaction entre les différentes non-linéarités et des limitations à ce jour a été largement étudié dans le cas de l'état magnétisé uniformément. Le rle de la configuration magnétique et son influence sur les propriétés non-linéaires étaient encore une question ouverte au début de ma thèse.

Méthode expérimentale

Pour s'attaquer à ces questions ouvertes, une approche expérimentale a été suivie. Par conséquent, des études détaillées à haute fréquence de STNOs bien caractérisés doivent être menées. Si l'on veut être en mesure de comprendre avec suffisamment de précision leurs propriétés à micro-ondes, il est donc important de travailler avec des échantillons STNOs de conception simple et de haute symétrie. Alors, Les travaux ont été concentrée sur une nanopilier circulaire (de rayon R=120 nm) composée de seulement deux couches ferromagnétiques ayant des épaisseurs différentes et séparées par une couche de métal normal (NiFe15 nm—Cu10 nm—NiFe4 nm). L'échantillon est aimanté par un champ magnétiques appliqué perpendiculairement le long de sa normale, afin de conserver la symétrie axiale de cette STNO pour avoir une identification simplifiée de modes propres d'onde du spin [41]. De plus, le même dispositif présente une configuration de double vortex (avec un vortex dans chaque couche magnétiques) avec des propriétés de micro-ondes en suspens [40]. Cet échantillon, un archétype de STNO, est donc particulièrement adapté pour apporter des réponses utiles aux questions soulevées par les motivations de cette thèse. Pour être cohérent avec notre feuille de route, le même dispositif de STNO, mais en double, sera utilisée dans les études de synchronisation mutuelle.

Une originalité de ce travail est son point de vue spectroscopique. Il faut donc des outils spectroscopiques pour étudier la dynamique de l'aimantation dans STNOs. Un moyen naturel pour sonder les modes d'onde de spin dans les nanostructures hybrides consiste à utiliser les propriétés de magnétorésistance [42, 43, 44, 45, 46]. Depuis sa première application pour STNOs [11], analyse spectrale des signaux émis a répandu. Cependant, ces techniques de transport à haute fréquence ne sont pas sensibles à tous les modes d'onde de spin, car certains peuvent être cachés à eux en raison de règles de sélection [41]. De plus, ils ne fournissent pas un accès direct à des profils de mode spatial. Des méthodes expérimentales indépendantes des transports ont récemment apporté des informations utiles à la dynamique de l'aimantation dans les nanostructures hybrides [47, 48, 49, 50, 51, 52]. En particulier, les techniques optiques telles que la résolution temporelle magnéto-optique Kerr microscopie (TR-MOKE) [53], micro Brillouin Light Scattering (μ BLS) [54], ou X-ray circulaire magnétiques dichrosme (XMCD) [55] ont récemment été appliquée avec succès à sonder transfert de spin dynamique parcourus. Cependant, ces techniques expérimentales nécessiten un accès optique à la partie active de l'échantillon. cet égard, microscopie de force à résonance magnétique (MRFM) [56, 57, 58, 59, 60], qui est basé sur l'interaction dipolaire entre l'échantillon et une sonde magnétique fixée à l'extrémité libre d'un cantilever souple, est bien adapté à l'étude des STNOs [41]. En fait, cette technique très sensible permet de détecter la dynamique de l'aimantation dans les nanostructures enterrées sous des électrodes métalliques épaisses [61], surtout que dans les STNOs sont couvrée par des électrodes qui sont necessaire pour passer des grandes densités de courant nécessaires pour compenser l'amortissement. Par ailleurs, il est sensible à tous les modes d'ondes de spin, parce qu'il mesure directement la composante longitudinale de l'aimantation ΔM_z[62].

Dans cette thèse, on a utilisés les deux techniques de MRFM et de transport à haute fréquence pour detecter la dynamique de l'aimantation dans un STNO o dans les couches magnétiques soit dans le saturé et ou à l'état de vortex. Ces deux techniques apporteront des informations complémentaires pour répondre aux questions ouvertes proposées ci-dessus.

STNO dans l'état saturé

Dans cette partie nous avons étudié la dynamique d'auto-oscillations de l'aimantation dans un nano-oscillateur à transfert de spin dans l'état saturé. La technique MRFM

nous a permis d'étudier les effets de transfert de spin dans une configuration de haute symétrie permettant une identification simplifiée des modes propres du système, quand les mesures standards de transport haute fréquence ne le permettent pas. L'originalité de notre expérience est de se coupler directement à la variation d'aimantation longitudinale dans le nano-pilier ΔM_z, directement proportionnelle à la puissance émise par le STNO. Cette étude d'un STNO nous a d'abord permis de définir les lignes critiques qui séparent les différents états stables du système qui sont nécessaires pour comprendre ses propriétés dynamique (figure E.1). En particulier, une analyse quantitative du seuil critique du mode de plus basse énergie dans la couche fine a été menée dans le cadre du modèle universel d'un auto-oscillateur à amortissement compensé [22]. Ensuite, nous avons identifié le mode d'auto-oscillation dans la couche fine. En utilisant deux circuits micro-onde différents, nous avons pu sélectivement sonder les modes d'indice ℓ=0 et ℓ=1 dans le nano-pilier. Les premiers sont excités par le champ micro-onde uniforme h_{rf} généré par une antenne, tandis que les seconds se couplent au champ d'Oersted créé par un courant micro-onde i_{rf} traversant l'échantillon. Nous avons observé une différence de comportement qualitative entre les modes ℓ=0 et ℓ=1 de la couche fine en fonction du courant continu. Les spectres MRFM du mode ℓ=0 se distordent, avec l'apparition d'un lobe négatif, alors que cela n'est pas observé pour le mode ℓ=1 (figure E.2). Cet effet est associé à la synchronisation du mode qui auto-oscille à la source externe, ici h_{rf} : sur la gamme de phase locking, l'amplitude de ce mode s'adapte de façon à ce que sa fréquence reste constante et égale à celle de la source (figure). Cette observation permet de montrer que le mode auto-oscillant, qui est le mode portant l'index azimutal ℓ=0 de plus basse énergie de la couche fine, susceptible de se coupler à la symétrie uniforme de l'excitation. Au contraire, on a observé que l'excitation par un courant ne provoque pas d'effet de synchronisation, en raison de sa symétrie azimutale (ℓ=1) incompatible avec le mode qui auto-oscille. Dans le cas particulier de la configuration de haute symétrie que nous avons étudié, il apparat donc que le couplage dipolaire entre STNOs voisins peut être très efficace pour synchroniser un réseau, alors que le courant RF ne l'est pas.

STNO dans L'état vortex

Notre oscillateur a ensuite été étudié sous faible champ perpendiculaire. En fait, en fonction des conditions de champ magnétique appliqué et de courant traversant le pillier, il est possible d'y exciter une grande variété de modes magnétiques par transfert de spin. Toutefois, lorsqu'aucun champ magnétique extérieur n'est appliqué, les deux couches

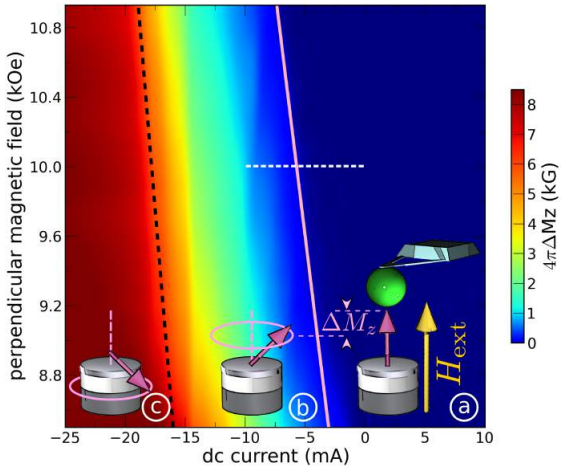

Figure E.1.: *Diagramme de phase expérimental qui représente ΔM_z en fonction du courant et du champ appliqué. Il est divisé en 3 régions. La région 1: les 2 couches sont alignées avec le champ magnetique appliqué, région 2: seule la couche fine qui précesse, région 3: reversement de l'aimantation de la couche fine et précession couplée de 2 couches.*

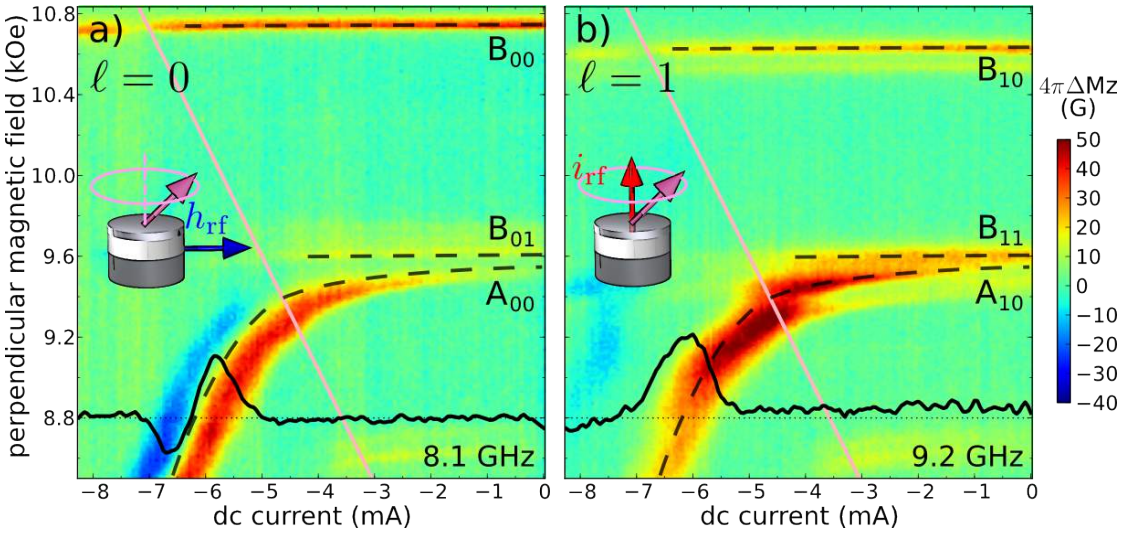

Figure E.2.: *Diagrammes de synchronisation du mode qui auto-oscilleà la source externe. (a) le mode ℓ=0 est excité par le champ magnétique micro-onde uniforme, (b) le mode ℓ=1 est excité par le champ d'Oersted généré par un courant micro-onde traversant l'échantillon. Un spectre MRFM est tracé sur chacun des diagrammes pour un champ Ht, pour le mode l=0 (a) le spectre se distorde avec l'apparition d'un lobe négatif. Alors cela n'est pas observé pour les modes l=1(b).A l'extrémité gauche du chaque diagramme en représente évolution de spectre d'ondes du spin pour identifier les modes excités.*

magnétiques se trouvent à la rémanence dans l'état vortex. Il est alors possible d'exciter un mode de grande cohérence: la dynamique couplée des deux vortex (une précession

couplée des coeurs de vortex appelée mode gyrotropique), induite par transfert de spin [40]. L'état magnétique doit néanmoins être préparé de façon à avoir deux vortex de chiralités identiques et de polarités opposées dans chacune des deux couches. Dans une premiére étude en analysant le contenu harmonique du spectre, nous avons déterminé que le couplage non-linéaire amplitude-phase du mode excité est quasi nul, ce qui explique la grande pureté spectrale observée, et qu'en parallèle, la fréquence d'oscillation reste ajustable sur une grande gamme grâce au champ d'Oersted créé par le courant injecté. Dans une dexiéme étude, nous avons concentré sur la dynamique de mode couplé generer par l'oscillateur en présence d'une source extérieure. Sur la figure E.3, nous présentons une mesure effectuée sur le STNO soumis à un champ magnétique micro-onde alternatif uniforme d'amplitude h_{rf}= 2.5 Oe dont la fréquence F_s est balayée. Le courant injecté dans l'oscillateur est égal à 15 mA, et la fréquence libre des oscillations est F_o=585 MHz, (mode gyrotropique dominé par la couche épaisse). Lorsque F_s est suffisamment proche de F_o, l'oscillateur s'écarte de sa fréquence propre pour se synchroniser sur la fréquence de la source. On relève alors la dépendance de la fenêtre de synchronisation Δ (locking range) en fonction de l'amplitude de la source, que nous présentons sur la figure E.3 (b): Δ peut atteindre plus de 10 $\%$ de F_o pour une faible amplitude h_{rf} =6 Oe. On souhaite ensuite étudier l'évolution de la largeur de raie du signal relevé aux bornes de l'oscillateur (caractérisant la cohérence des oscillations) lors du verrouillage de phase du STNO. Cependant, il n'est pas possible d'étudier le comportement de la largeur de raie de l'oscillateur lorsque F_s=F_0 car le signal directement issu de la source masque le signal issu du STNO. Pour y remédier, nous avons étudié la synchronisation du STNO à F_s=2F_o et F_s=2F_o. La forte diminution de la largeur de raie de l'oscillateur lorsqu'il se synchronise à la source peut alors être observée: pour un champ appliqué hors du plan de 1 kOe, la largeur de raie décroit même de 100 kHz à moins de 1 Hz, c'est-à-dire que le STNO se synchronise parfaitement à la source externe. Il est finalement à noter que pour des raisons de symétrie, le mode gyrotropique couplé de notre STNO ne se synchronise qu'au champ uniforme h_{rf}, et pas du tout à un courant i_{rf}. Il apparat donc que de nouveau que le couplage magnéto-dipolaire entre STNOs à base de vortex est très prometteur pour obtenir une synchronisation mutuelle, le cham p dipolaire rayonné par un STNO sur ses voisins jouant alors le rle de la source h_{rf} dans cette étude.

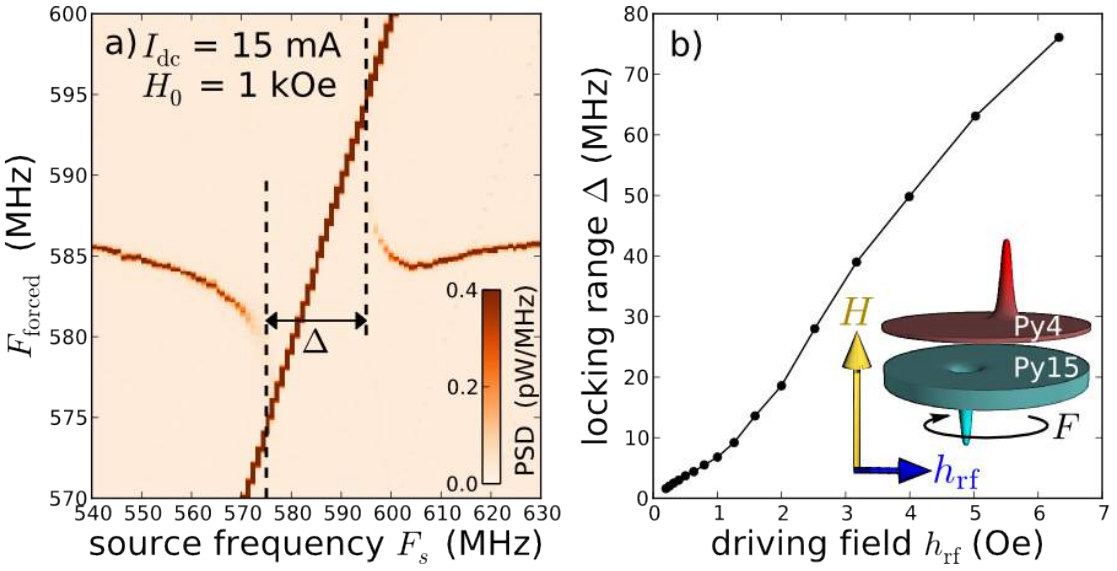

Figure E.3.: *(a) Évolution de la fréquence d'auto-oscillation en fonction de la fréquence de la source h_{rf} = 2.5 Oe. Δ représente le locking range. (b) Locking range en fonction de l'amplitude du champ appliqué. Dans les deux cas I_{dc}=15 mA.*

Synchronisation mutuelle

Un des objectifs de cette partie est de démontrer s'il est possible d'observer un phénomène de synchronisation mutuelle entre les oscillations de deux STNOs. Nous avons pour cela réalisé des échantillons constitués de deux piliers de diamètre D=200nm gravés dans un meme empilement de celle presenter avant et séparés d'une distance s=100nm bord-à-bord. Les deux STNOs sont alimentés en courant par une électrode commune.

L'étape suivante a été de mesurer expérimentalement ce système de deux STNOs, dans différentes configurations de polarités des vortex. Sur la figure E.4, nous représentons les évolutions des caractéristiques de la fréquence des deux oscillateurs en fonction d'un champ extérieur appliqué selon l'axe des piliers. On peut faire varier l'écart en fréquence des deux oscillateurs grâce à l'application d'un champ perpendiculaire. Nous présentons sur la figure E.4 (a) (figure E.4 (b)) le cas expérimental de deux vortex de polarités opposées (parallèle). La réduction (augmentation) du champ magnétique appliqué permettra de réduire progressivement l'écart en fréquence jusqu'à observer le phénomène de synchronisation. En fait et nous avons pu observer le phénomène de synchronisation dans le cas de vortex de polarités parallèle et anti-parallèles En dessous

d'un écart en fréquence de critique, les deux signaux issus de chacun des oscillateurs ne font plus qu'un : ils oscillent maintenant à la même fréquence. Ces résultats constituent la première démonstration expérimentale à température ambiante de synchronisation d'oscillateurs à transfert de spin par couplage dipolaire.

Ces observations ont pu être répétées pour plusieurs échantillons et dans différentes configurations des vortex. Finalement la synchronisation s'est montrée être beaucoup plus efficace dans la configuration de polarités opposées, pour laquelle nous avons pu observer une synchronisation pour un écart en fréquence d'environ 50 MHz, soit 8 % de la fréquence d'oscillation gyrotropique. Ce pourcentage représente potentiellement la dispersion maximale en fréquence permettant d'observer la synchronisation d'une assemblée d'oscillateurs.

Ces résultats extrêmement intéressants ouvrent la perspective de la fabrication de réseauxd'oscillateurs spintroniques couplés, qui permettront de renforcer la puissance et la cohérence des signaux dont ils seront à l'origine.

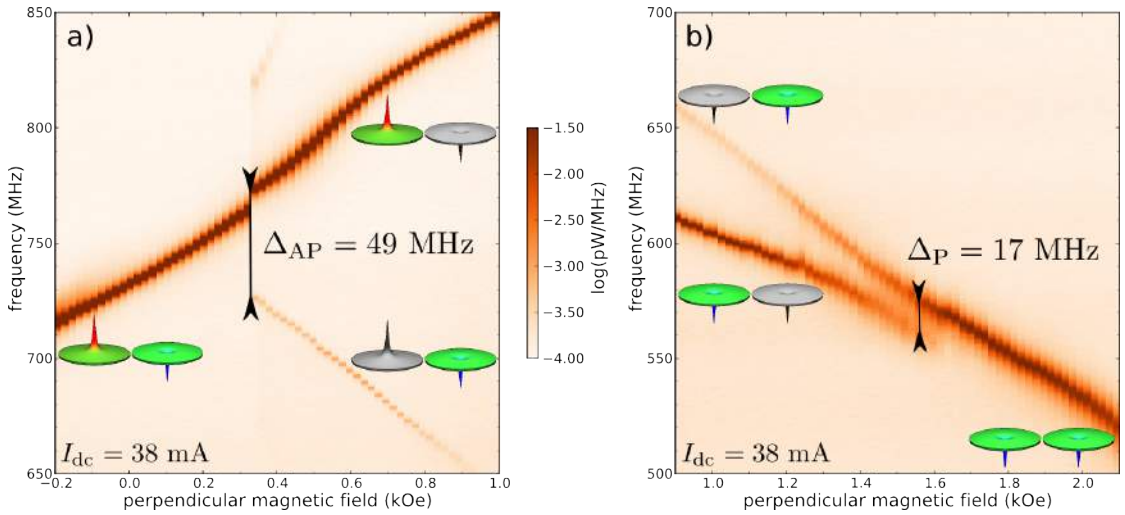

Figure E.4.: ***Phénomène de synchronisation*** *Cartographie du spectre en tension aux bornes des deux piliers, montrant le phénomène de synchronisation. Les mesures sont enregistrées en fonction du champ magnétique perpendiculaire à un courant $I_{dc} = 38$ mA injecté par les deux STNOs en parallèle. (**a**) Synchronisation mutuelle dans les cas pour lesquels les polarités des vortex dans la couche épaisse de Py sont anti-parallèles. (**b**) parallèles*

References

[1] S. Wolf, D. D. Awschalom, R. A. Buhrman, J. Daughton, S. von Molnar, M. L. Roukes, A. Y. Chtchelkanova and D. M. Treger, *Spintronics: A Spin-Based Electronics Vision for the Future*, Science **294**, 1488 (2001).

[2] M. N. Baibich, J. M. Broto, A. Fert, F. N. V. Dau, F. Petroff, P. Etienne, G. Creuzet, A. Friederich and J. Chazelas, *Giant magnetoresistance of (001)Fe/(001)Cr magnetic superlattices*, Phys. Rev. Lett. **61**, 2472 (1988).

[3] G. Binasch, P. Grunberg, F. Saurenbach and W. Zinn, *Enhanced magnetoresistance in layered magnetic structures with antiferromagnetic interlayer exchange*, Phys.Rev.B **39**, 4828 (1989).

[4] B. Dieny, V. Speriosu, B. Gurney, S. Parkin, D. Wilhoit, K. Roche, S. Metin, D. Peterson and S. Nadimi, *Spin-valve effect in soft ferromagnetic sandwiches*, Journal of Magnetism and Magnetic Materials **93**, 101 (1991).

[5] M. Pannetier, C. Fermon, G. Le Goff, J. Simola and E. Kerr, *Femtotesla Magnetic Field Measurement with Magnetoresistive Sensors*, Science **304**, 1648 (2004).

[6] J. C. Slonczewski, *Current-driven excitation of magnetic multilayers* , J. Magn. Magn. Mater. **159**, 1 (1996).

[7] L. Berger, *Emission of spin waves by a magnetic multilayer traversed by a current*, Phys. Rev. B **54**, 9353 (1996).

[8] D. Ralph and M. Stiles, *Spin transfer torques*, Journal of Magnetism and Magnetic Materials **320**, 1190 (2008).

[9] F. J. Albert, J. A. Katine, R. A. Buhrman and D. C. Ralph, *Spin-polarized current switching of a Co thin film nanomagnet*, Applied Physics Letters **77**, 3809 (2000).

[10] J. Grollier, V. Cros, A. Hamzic, J. M. George, H. Jaffres, A. Fert, G. Faini, J. B. Youssef and H. Legall, *Spin-polarized current induced switching in Co/Cu/Co pillars*, Applied Physics Letters **78**, 3663 (2001).

[11] S. I. Kiselev, J. C. Sankey, I. N. Krivorotov, N. C. Emley, R. J. Schoelkopf, R. A. Buhrman and D. C. Ralph, *Microwave oscillations of a nanomagnet driven by a spin-polarized current*, Nature **425**, 380 (2003).

[12] W. H. Rippard, M. R. Pufall, S. Kaka, S. E. Russek and T. J. Silva, *Direct-Current Induced Dynamics in $Co_{90}Fe_{10}/Ni_{80}Fe_{20}$ Point Contacts*, Phys. Rev. Lett. **92**, 027201 (2004).

[13] D. Houssameddine, U. Ebels, B. Delat, B. Rodmacq, I. Firastrau, F. Ponthenier, M. Brunet, C. Thirion, J.-P. Michel, L. Prejbeanu-Buda, M.-C. Cyrille, O. Redon and B. Dieny, *Spin-torque oscillator using a perpendicular polarizer and a planar free layer*, Nature Mater. **6**, 447 (2007).

[14] S. Bonetti, P. Muduli, F. Mancoff and J. Akerman, *Spin torque oscillator frequency versus magnetic field angle: The prospect of operation beyond 65 GHz*, Appl. Phys. Lett. **94**, 102507 (2009).

[15] A. A. Tulapurkar, Y. Suzuki, A. Fukushima, H. Kubota, H. Maehara, K. Tsunekawa, D. D. Djayaprawira, N. Watanabe and S. Yuasa, *Spin-torque diode effect in magnetic tunnel junctions*, Nature **438**, 339 (2005).

[16] J. Zhu, J. A. Katine, G. E. Rowlands, Y.-J. Chen, Z. Duan, J. G. Alzate, P. Upadhyaya, J. Langer, P. K. Amiri, K. L. Wang and I. N. Krivorotov, *Voltage-Induced Ferromagnetic Resonance in Magnetic Tunnel Junctions*, Phys. Rev. Lett. **108**, 197203 (2012).

[17] P. K. Muduli, Y. Pogoryelov, S. Bonetti, G. Consolo, F. Mancoff and J. Åkerman, *Nonlinear frequency and amplitude modulation of a nanocontact-based spin-torque oscillator*, Phys. Rev. B **81**, 140408 (2010).

[18] Y. Pogoryelov, P. K. Muduli, S. Bonetti, E. Iacocca, F. Mancoff and J. Åkerman, *Frequency modulation of spin torque oscillator pairs*, Appl. Phys. Lett. **98**, 192501 (2011).

[19] P. M. Braganca, B. A. Gurney, B. A. Wilson, J. A. Katine, S. Maat and J. R. Childress, *Nanoscale magnetic field detection using a spin torque oscillator*, Nanotechnology **21**, 235202 (2010).

[20] K. Mizushima, K. Kudo, T. Nagasawa and R. Sato, *Signal-to-noise ratios in high-signal-transfer-rate read heads composed of spin-torque oscillators* , Journal of Applied Physics **107**, 063904 (2010).

[21] J.-G. Zhu and Y. Wang, *Microwave Assisted Magnetic Recording Utilizing Perpendicular Spin Torque Oscillator With Switchable Perpendicular Electrodes*, IEEE Trans. Magn. **46**, 751 (2010).

[22] A. Slavin and V. Tiberkevich, *Nonlinear Auto-Oscillator Theory of Microwave Generation by Spin-Polarized Current*, IEEE Transactions on Magnetics **45**, 1875 (2009).

[23] J.-V. Kim, V. Tiberkevich and A. N. Slavin, *Generation Linewidth of an Auto-Oscillator with a Nonlinear Frequency Shift: Spin-Torque Nano-Oscillator*, Phy.Rev.Let. **100**, 017207 (2008).

[24] M. W. Keller, M. R. Pufall, W. H. Rippard and T. J. Silva, *Nonwhite frequency noise in spin torque oscillators and its effect on spectral linewidth*, Phys. Rev. B **82**, 054416 (2010).

[25] M. Quinsat, D. Gusakova, J. F. Sierra, J. P. Michel, D. Houssameddine, B. Delaet, M.-C. Cyrille, U. Ebels, B. Dieny, L. D. Buda-Prejbeanu, J. A. Katine, D. Mauri, A. Zeltser, M. Prigent, J.-C. Nallatamby and R. Sommet, *Amplitude and phase noise of magnetic tunnel junction oscillators*, Appl. Phys. Lett. **97**, 182507 (2010).

[26] J. Grollier, V. Cros and A. Fert, *Synchronization of spin-transfer oscillators driven by stimulated microwave currents*, Phys. Rev. B **73**, 060409 (2006).

[27] S. Kaka, M. R. Pufall, W. H. Rippard, T. J. Silva, S. E. Russek and J. A. Katine, *Mutual phase-locking of microwave spin torque nano-oscillators*, Nature **437**, 389 (2005).

[28] F. B. Mancoff, N. D. Rizzo, B. N. Engel and S. Tehrani, *Phase-locking in double-point-contact spin-transfer devices*, Nature **437**, 393 (2005).

[29] A. Ruotolo, V. Cros, B. Georges, A. Dussaux, J. Grollier, C. Deranlot, R. Guillemet, K. Bouzehouane, S. Fusil and A. Fert, *Phase-locking of magnetic vortices mediated by antivortices*, Nature Nanotech. **4**, 528 (2009).

[30] S. Sani, J. Persson, S. Mohseni, Y. Pogoryelov, P. Muduli, A. Eklund, G. Malm, M. Kll, A. Dmitriev and J. Akerman, *Mutually synchronized bottom-up multi-nanocontact spin-torque oscillators*, Nature Communications **4**, 2731 (2013).

[31] M. Bailleul, R. Hollinger and C. Fermon, *Microwave spectrum of square Permalloy dots: Quasisaturated state*, Physical Review B (Condensed Matter and Materials Physics) **73**, 104424 (2006).

[32] M. Bailleul, R. Höllinger, K. Perzlmaier and C. Fermon, *Microwave spectrum of square permalloy dots: Multidomain state*, Physical Review B (Condensed Matter and Materials Physics) **76**, 224401 (2007).

[33] V. S. Pribiag, I. N. Krivorotov, G. D. Fuchs, P. M. Braganca, O. Ozatay, J. C. Sankey, D. C. Ralph and R. A. Buhrman, *Magnetic vortex oscillator driven by d.c. spin-polarized current*, Nature Phys. **3**, 498 (2007).

[34] K. Y. Guslienko, *Magnetic Vortex State Stability, Reversal and Dynamics in Restricted Geometries*, J. Nanosci. Nanotechnol. **8**, 2745 (2008).

[35] A. Dussaux, B. Georges, J. Grollier, V. Cros, A. Khvalkovskiy, A. Fukushima, M. Konoto, H. Kubota, K. Yakushiji, S. Yuasa, K. Zvezdin, K. Ando and A. Fert, *Large microwave generation from current-driven magnetic vortex oscillators in magnetic tunnel junctions*, Nat. Commun. **1**, 8 (2010).

[36] S. Tsunegi, H. Kubota, K. Yakushiji, M. Konoto, S. Tamaru, A. Fukushima, H. Arai, H. Imamura, E. Grimaldi, R. Lebrun, J. Grollier, V. Cros and S. Yuasa, *High emission power and Q factor in spin torque vortex oscillator consisting of FeB free layer*, Applied Physics Express **7**, 063009 (2014).

[37] E. Grimaldi, A. Dussaux, P. Bortolotti, J. Grollier, G. Pillet, A. Fukushima, H. Kubota, K. Yakushiji, S. Yuasa and V. Cros, *Response to noise of a vortex based spin transfer nano-oscillator*, Phys. Rev. B **89**, 104404 (2014).

[38] D. Houssameddine, J. F. Sierra, D. Gusakova, B. Delaet, U. Ebels, L. D. Buda-Prejbeanu, M.-C. Cyrille, B. Dieny, B. Ocker, J. Langer and W. Maas, *Spin torque*

driven excitations in a synthetic antiferromagnet , Applied Physics Letters **96**, 072511 (2010).

[39] D. Gusakova, M. Quinsat, J. F. Sierra, U. Ebels, B. Dieny, L. D. Buda-Prejbeanu, M.-C. Cyrille, V. Tiberkevich and A. N. Slavin, *Linewidth reduction in a spin-torque nano-oscillator caused by non-conservative current-induced coupling between magnetic layers*, Appl. Phys. Lett. **99**, 052501 (2011).

[40] N. Locatelli, V. V. Naletov, J. Grollier, G. de Loubens, V. Cros, C. Deranlot, C. Ulysse, G. Faini, O. Klein and A. Fert, *Dynamics of two coupled vortices in a spin valve nanopillar excited by spin transfer torque*, Appl. Phys. Lett. **98**, 062501 (2011).

[41] V. V. Naletov, G. de Loubens, G. Albuquerque, S. Borlenghi, V. Cros, G. Faini, J. Grollier, H. Hurdequint, N. Locatelli, B. Pigeau, A. N. Slavin, V. S. Tiberkevich, C. Ulysse, T. Valet and O. Klein, *Identification and selection rules of the spin-wave eigenmodes in a normally magnetized nanopillar*, Phys. Rev. B **84**, 224423 (2011).

[42] S. Petit, C. Baraduc, C. Thirion, U. Ebels, Y. Liu, M. Li, P. Wang and B. Dieny, *Spin-Torque Influence on the High-Frequency Magnetization Fluctuations in Magnetic Tunnel Junctions*, Phys. Rev. Lett. **98**, 077203 (2007).

[43] A. Helmer, S. Cornelissen, T. Devolder, J.-V. Kim, W. van Roy, L. Lagae and C. Chappert, *Quantized spin-wave modes in magnetic tunnel junction nanopillars* , Phys. Rev. B **81**, 094416 (2010).

[44] J. C. Sankey, P. M. Braganca, A. G. F. Garcia, I. N. Krivorotov, R. A. Buhrman and D. C. Ralph, *Spin-Transfer-Driven Ferromagnetic Resonance of Individual Nanomagnets*, Phys. Rev. Lett. **96**, 227601 (2006).

[45] W. Chen, J.-M. L. Beaujour, G. de Loubens, A. D. Kent and J. Z. Sun, *Spin-torque driven ferromagnetic resonance of Co/Ni synthetic layers in spin valves*, Appl. Phys. Lett. **92**, 012507 (2008).

[46] N. Biziere and C. Fermon, *High-frequency giant magnetoresistance measurement to study the dynamics of a micron-scale spin-valve sensor*, Physical Review B (Condensed Matter and Materials Physics) **78**, 064408 (2008).

[47] V. E. Demidov, S. O. Demokritov, B. Hillebrands, M. Laufenberg and P. P. Freitas, *Radiation of spin waves by a single micrometer-sized magnetic element*, Appl. Phys. Lett. **85**, 2866 (2004).

[48] G. Woltersdorf, O. Mosendz, B. Heinrich and C. H. Back, *Magnetization Dynamics due to Pure Spin Currents in Magnetic Double Layers*, Phys. Rev. Lett. **99**, 246603 (2007).

[49] G. de Loubens, V. V. Naletov, O. Klein, J. B. Youssef, F. Boust and N. Vukadinovic, *Magnetic Resonance Studies of the Fundamental Spin-Wave Modes in Individual Submicron Cu/NiFe/Cu Perpendicularly Magnetized Disks*, Physical Review Letters **98**, 127601 (2007).

[50] G. Gubbiotti, M. Madami, S. Tacchi, G. Carlotti, H. Tanigawa and T. Ono, *Spin dynamics of multilayered nanoelements with different shapes studied by Brillouin light scattering technique*, J. Phys. D: Appl. Phys. **41**, 134023 (2008).

[51] P. S. Keatley, P. Gangmei, M. Dvornik, R. J. Hicken, J. R. Childress and J. A. Katine, *Large amplitude magnetization dynamics and the suppression of edge modes in a single nanomagnet*, Applied Physics Letters **98**, 082506 (2011).

[52] H. T. Nembach, J. M. Shaw, C. T. Boone and T. J. Silva, *Mode- and Size-Dependent Landau-Lifshitz Damping in Magnetic Nanostructures: Evidence for Nonlocal Damping*, Phys. Rev. Lett. **110**, 117201 (2013).

[53] J.-Y. Chauleau, H. G. Bauer, H. S. Körner, J. Stigloher, M. Härtinger, G. Woltersdorf and C. H. Back, *Self-consistent determination of the key spin-transfer torque parameters from spin-wave Doppler experiments*, Phys. Rev. B **89**, 020403 (2014).

[54] V. E. Demidov, M. Buchmeier, K. Rott, P. Krzysteczko, J. Münchenberger, G. Reiss and S. O. Demokritov, *Nonlinear Hybridization of the Fundamental Eigenmodes of Microscopic Ferromagnetic Ellipses*, Phys. Rev. Lett. **104**, 217203 (2010).

[55] Y. Acremann, J. P. Strachan, V. Chembrolu, S. D. Andrews, T. Tyliszczak, J. A. Katine, M. J. Carey, B. M. Clemens, H. C. Siegmann and J. Stöhr, *Time-Resolved Imaging of Spin Transfer Switching: Beyond the Macrospin Concept*, Phys. Rev. Lett. **96**, 217202 (2006).

[56] Z. Zhang, P. C. Hammel and P. E. Wigen, *Observation of ferromagnetic resonance in a microscopic sample using magnetic resonance force microscopy*, Applied Physics Letters **68**, 2005 (1996).

[57] K. Wago, D. Botkin, C. S. Yannoni and D. Rugar, *Paramagnetic and ferromagnetic resonance imaging with a tip-on-cantilever magnetic resonance force microscope*, Appl. Phys. Lett. **72**, 2757 (1998).

[58] V. Charbois, V. V. Naletov, J. B. Youssef and O. Klein, *Influence of the magnetic tip in ferromagnetic resonance force microscopy*, Applied Physics Letters **80**, 4795 (2002).

[59] O. Klein, G. de Loubens, V. V. Naletov, F. Boust, T. Guillet, H. Hurdequint, A. Leksikov, A. N. Slavin, V. S. Tiberkevich and N. Vukadinovic, *Ferromagnetic resonance force spectroscopy of individual submicron-size samples*, Phys. Rev. B **78**, 144410 (2008).

[60] H.-J. Chia, F. Guo, L. M. Belova and R. D. McMichael, *Nanoscale Spin Wave Localization Using Ferromagnetic Resonance Force Microscopy*, Phys. Rev. Lett. **108**, 087206 (2012).

[61] G. de Loubens, A. Riegler, B. Pigeau, F. Lochner, F. Boust, K. Y. Guslienko, H. Hurdequint, L. W. Molenkamp, G. Schmidt, A. N. Slavin, V. S. Tiberkevich, N. Vukadinovic and O. Klein, *Bistability of Vortex Core Dynamics in a Single Perpendicularly Magnetized Nanodisk*, Physical Review Letters **102**, 177602 (2009).

[62] G. de Loubens, V. V. Naletov and O. Klein, *Reduction of the spin-wave damping induced by nonlinear effects*, Phys. Rev. B **71**, 180411(R) (2005).

[63] E. M. Landau, L. D. .and Lifshitz, *On the theory of the despersion of magnetic permeability in ferromagnetic bodies*, Sov. Phys. **8**, 153 (1935).

[64] T. L. Gilbert, *A lagrangian formulation of the gyromagnetic equation of the magnetization field*, Phys. Rev. **100**, 1243 (1955).

[65] K. L. Metlov and K. Y. Guslienko, *Stability of magnetic vortex in soft magnetic nanosized circular cylinder*, Journal of magnetism and magnetic materials **242**, 1015 (2002).

[66] N. A. Usov and S. E. Peschany, *Magnetization curling in a fine cylindrical particle*, J.Magn.Magn.Mater. **118**, L290 (1993).

[67] K. Y. Guslienko and K. L. Metlov, *Evolution and stability of a magnetic vortex in a small cylindrical ferromagnetic particle under applied field*, Physical Review B **63**, 100403 (2001).

[68] M. Hehn, K. Ounadjela, J.-P. Bucher, F. Rousseaux, D. Decanini, B. Bartenlian and C. Chappert, *Nanoscale magnetic domains in mesoscopic magnets*, Science **272**, 1782 (1996).

[69] R. P. Cowburn, D. K. Koltsov, A. O. Adeyeye, M. E. Welland and D. M. Tricker, *Single-Domain Circular Nanomagnets*, Phys. Rev. Lett. **83**, 1042 (1999).

[70] K. L. Metlov and K. Y. Guslienko, *Quasiuniform magnetization state in soft ferromagnetic nanocylinders*, Phys. Rev. B **70**, 052406 (2004).

[71] K. Y. Guslienko, V. Novosad, Y. Otani, H. Shima and K. Fukamichi, *Field evolution of magnetic vortex state in ferromagnetic disks*, Applied Physics Letters **78**, 3848 (2001).

[72] K. Y. Guslienko, V. Novosad, Y. Otani, H. Shima and K. Fukamichi, *Magnetization reversal due to vortex nucleation, displacement, and annihilation in submicron ferromagnetic dot arrays*, Phys. Rev. B **65**, 024414 (2002).

[73] A. Fernandez, M. Gibbons, M. Wall and C. Cerjan, *Magnetic domain structure and magnetization reversal in submicron-scale Co dots*, Journal of Magnetism and Magnetic Materials **190**, 71 (1998).

[74] S. Urazhdin, C. Chien, K. Y. Guslienko and L. Novozhilova, *Effects of current on the magnetic states of permalloy nanodiscs*, Physical Review B **73**, 054416 (2006).

[75] A. A. Thiele, *Steady-State Motion of Magnetic Domains*, Phys. Rev. Lett. **30**, 230 (1973).

[76] A. V. Khvalkovskiy, J. Grollier, A. Dussaux, K. A. Zvezdin and V. Cros, *Vortex oscillations induced by spin-polarized current in a magnetic nanopillar: Analytical versus micromagnetic calculations*, Physical Review B (Condensed Matter and Materials Physics) **80**, 140401 (2009).

[77] K. Y. Guslienko, *Low-frequency vortex dynamic susceptibility and relaxation in mesoscopic ferromagnetic dots*, Appl. Phys. Lett. **89**, 022510 (2006).

[78] B. A. Ivanov and C. E. Zaspel, *Excitation of Spin Dynamics by Spin-Polarized Current in Vortex State Magnetic Disks*, Physical Review Letters **99**, 247208 (2007).

[79] Q. Mistral, M. van Kampen, G. Hrkac, J.-V. Kim, T. Devolder, P. Crozat, C. Chappert, L. Lagae and T. Schrefl, *Current-Driven Vortex Oscillations in Metallic Nanocontacts*, Phys. Rev. Lett. **100**, 257201 (2008).

[80] N. Locatelli, Thèse de doctorat, Université Paris Sud, 2012.

[81] K. Y. Guslienko, S. O. Demokritov, B. Hillebrands and A. N. Slavin, *Effective dipolar boundary conditions for dynamic magnetization in thin magnetic stripes*, Physical Review B (Condensed Matter and Materials Physics) **66**, 132402 (2002).

[82] K. Y. Guslienko, G. R. Aranda and J. Gonzalez, *Spin torque and critical currents for magnetic vortex nano-oscillator in nanopillars*, Journal of Physics: Conference Series **292**, 012006 (2011).

[83] A. Dussaux, A. V. Khvalkovskiy, P. Bortolotti, J. Grollier, V. Cros and A. Fert,*Field dependence of spin-transfer-induced vortex dynamics in the nonlinear regime*, Phys. Rev. B **86**, 014402 (2012).

[84] M. Tsoi, A. G. M. Jansen, J. Bass, W.-C. Chiang, M. Seck, V. Tsoi and P. Wyder, *Excitation of a Magnetic Multilayer by an Electric Current*, Phys. Rev. Lett. **80**, 4281 (1998).

[85] T. Devolder, J.-V. Kim, P. Crozat, C. Chappert, M. Manfrini, M. van Kampen, W. V. Roy, L. Lagae, G. Hrkac and T. Schrefl, *Time-resolved zero field vortex oscillations in point contacts*, Appl.Phys.Lett. **95**, 012507 (2009).

[86] A. Dussaux, E. Grimaldi, B. Rache Salles, A. S. Jenkins, A. V. Khvalkovskiy, P. Bortolotti, J. Grollier, H. Kubota, A. Fukushima, K. Yakushiji, S. Yuasa, V. Cros and A. Fert, *Large amplitude spin torque vortex oscillations at zero external field using a perpendicular spin polarizer*, Applied Physics Letters **105**, 022404 (2014).

[87] W. H. Rippard, M. R. Pufall and S. E. Russek, *Comparison of frequency, linewidth, and output power in measurements of spin-transfer nanocontact oscillators*, Phys. Rev. B **74**, 224409 (2006).

[88] J. C. Sankey, I. N. Krivorotov, S. I. Kiselev, P. M. Braganca, N. C. Emley, R. A. Buhrman and D. C. Ralph, *Mechanisms limiting the coherence time of spontaneous magnetic oscillations driven by dc spin-polarized currents*, Phys. Rev. B **72**, 224427 (2005).

[89] J.-V. Kim, Q. Mistral, C. Chappert, V. S. Tiberkevich and A. N. Slavin, *Line Shape Distortion in a Nonlinear Auto-Oscillator Near Generation Threshold: Application to Spin-Torque Nano-Oscillators*, Phys. Rev. Lett. **100**, 167201 (2008).

[90] B. Georges, J. Grollier, M. Darques, V. Cros, C. Deranlot, B. Marcilhac, G. Faini and A. Fert, *Coupling Efficiency for Phase Locking of a Spin Transfer Nano-Oscillator to a Microwave Current*, Physical Review Letters **101**, 017201 (2008).

[91] M. R. A. Pikovsky and J. Kurths., in *Synchronization. A universal concept in nonlinear sciences.*, hrsg. v. C. N. S. Series (Cambridge University Press, ADDRESS, 2001).

[92] M. Madami, S. Bonetti, G. Consolo, S. Tacchi, G. Carlotti, G. Gubbiotti, F. B. Mancoff, M. A. Yar and J. kerman, *Direct observation of a propagating spin wave induced by spin-transfer torque*, Nature Nanotechnology **6**, 635638 (2011).

[93] K. Wan, A. K. Jain and J. E. Lukens, *Submillimeter wave generation using Josephson junction arrays*, Applied Physics Letters **54**, 1805 (1989).

[94] W. H. Rippard, M. R. Pufall, S. Kaka, T. J. Silva, S. E. Russek and J. A. Katine, *Injection Locking and Phase Control of Spin Transfer Nano-oscillators*, Phys. Rev. Lett. **95**, 067203 (2005).

[95] A. Dussaux, A. V. Khvalkovskiy, J. Grollier, V. Cros, A. Fukushima, M. Konoto, H. Kubota, K. Yakushiji, S. Yuasa, K. Ando and A. Fert, *Phase locking of vortex based spin transfer oscillators to a microwave current*, Appl. Phys. Lett. **98**, 132506 (2011).

[96] M. Quinsat, J. F. Sierra, I. Firastrau, V. Tiberkevich, A. Slavin, D. Gusakova, L. D. Buda-Prejbeanu, M. Zarudniev, J.-P. Michel, U. Ebels, B. Dieny, M.-C. Cyrille, J. A. Katine, D. Mauri and A. Zeltser, *Injection locking of tunnel junction oscillators to a microwave current*, Appl. Phys. Lett. **98**, 182503 (2011).

[97] A. N. Slavin and V. S. Tiberkevich, *Nonlinear self-phase-locking effect in an array of current-driven magnetic nanocontacts*, Phys. Rev. B **72**, 092407 (2005).

[98] Z. Li, Y. C. Li and S. Zhang, *Dynamic magnetization states of a spin valve in the presence of dc and ac currents: Synchronization, modification, and chaos*, Physical Review B (Condensed Matter and Materials Physics) **74**, 054417 (2006).

[99] S. Urazhdin, P. Tabor, V. Tiberkevich and A. Slavin, *Fractional Synchronization of Spin-Torque Nano-Oscillators*, Phys. Rev. Lett. **105**, 104101 (2010).

[100] B. Pigeau, C. Hahn, G. de Loubens, V. V. Naletov, O. Klein, K. Mitsuzuka, D. Lacour, M. Hehn, S. Andrieu and F. Montaigne, *Measurement of the Dynamical Dipolar Coupling in a Pair of Magnetic Nanodisks Using a Ferromagnetic Resonance Force Microscope*, Phys. Rev. Lett. **109**, 247602 (2012).

[101] R. Verba, G. Melkov, V. Tiberkevich and A. Slavin, *Collective spin-wave excitations in a two-dimensional array of coupled magnetic nanodots*, Phys. Rev. B **85**, 014427 (2012).

[102] B.Pigeau, Thèse de doctorat, Université Paris Sud - Paris XI, 2012.

[103] K. Y. Guslienko, A. N. Slavin, V. Tiberkevich and S.-K. Kim, *Dynamic Origin of Azimuthal Modes Splitting in Vortex-State Magnetic Dots*, Phys. Rev. Lett. **101**, 247203 (2008).

[104] B. A. Ivanov and G. M. Wysin, *Magnon modes for a circular two-dimensional easy-plane ferromagnet in the cone state*, Phys. Rev. B **65**, 134434 (2002).

[105] K. Y. Guslienko and A. N. Slavin, *Boundary conditions for magnetization in magnetic nanoelements*, Phys. Rev. B **72**, 014463 (2005).

[106] B. A. Ivanov and C. E. Zaspel, *High Frequency Modes in Vortex-State Nanomagnets* , Physical Review Letters **94**, 027205 (2005).

[107] M. Buess, T. Haug, M. R. Scheinfein and C. H. Back, *Micromagnetic Dissipation, Dispersion, and Mode Conversion in Thin Permalloy Platelets*, Phys. Rev. Lett. **94**, 127205 (2005).

[108] K. Vogt, O. Sukhostavets, H. Schultheiss, B. Obry, P. Pirro, A. A. Serga, T. Sebastian, J. Gonzalez, K. Y. Guslienko and B. Hillebrands, *Optical detection of vortex spin-wave eigenmodes in microstructured ferromagnetic disks*, Phys. Rev. B **84**, 174401 (2011).

[109] J. P. Park and P. A. Crowell, *Interactions of Spin Waves with a Magnetic Vortex*, Physical Review Letters **95**, 167201 (2005).

[110] V. Castel, J. Ben Youssef, F. Boust, R. Weil, B. Pigeau, G. de Loubens, V. V. Naletov, O. Klein and N. Vukadinovic, *Perpendicular ferromagnetic resonance in soft cylindrical elements: Vortex and saturated states*, Phys. Rev. B **85**, 184419 (2012).

[111] Q. Mistral, J.-V. Kim, T. Devolder, P. Crozat, C. Chappert, J. A. Katine, M. J. Carey and K. Ito, *Current-driven microwave oscillations in current perpendicular-to-plane spin-valve nanopillars*, Appl. Phys. Lett. **88**, 192507 (2006).

[112] J. F. Sierra, M. Quinsat, F. Garcia-Sanchez, U. Ebels, I. Joumard, A. S. Jenkins, B. Dieny, M.-C. Cyrille, A. Zeltser and J. A. Katine,*Influence of thermal fluctuations on the emission linewidth in MgO-based spin transfer oscillators*, Appl. Phys. Lett. **101**, 062407 (2012).

[113] G. Gubbiotti, M. Kostylev, N. Sergeeva, M. Conti, G. Carlotti, T. Ono, A. N. Slavin and A. Stashkevich, *Brillouin light scattering investigation of magnetostatic modes in symmetric and asymmetric $NiFe/Cu/NiFe$ trilayered wires*, Phys. Rev. B **70**, 224422 (2004).

[114] O. Dmytriiev, T. Meitzler, E. Bankowski, A. Slavin and V. Tiberkevich, *Spin wave excitations of a magnetic pillar with dipolar coupling between the layers*, Journal of Physics: Condensed Matter **22**, 136001 (2010).

[115] O. V. Sukhostavets, J. M. Gonzalez and K. Y. Guslienko, *Magnetic Vortex Excitation Frequencies and Eigenmodes in a Pair of Coupled Circular Dots*, Applied Physics Express **4**, 065003 (2011).

[116] O. V. Sukhostavets, J. González and K. Y. Guslienko, *Multipole magnetostatic interactions and collective vortex excitations in dot pairs, chains, and two-dimensional arrays*, Phys. Rev. B **87**, 094402 (2013).

[117] D. Ham, W. Andress and D. Ricketts, *Phase noise in oscillators*, International workshop on SiP/SoC intergration of MEMS and passive components with RF-ICs (2004).

[118] B.Raquet, *Electronic noise in magnetic materials and devices*, Edited by M. Ziese and M. J. Thonton (Springer-Verlag, Berlin) **569**, 232 (2001).

[119] V. Tiberkevich, A. Slavin and J.-V. Kim, *Microwave power generated by a spin-torque oscillator in the presence of noise*, Applied Physics Letters **91**, 192506 (2007).

[120] W. H. Rippard, M. R. Pufall, S. Kaka, T. J. Silva and S. E. Russek, *Current-driven microwave dynamics in magnetic point contacts as a function of applied field angle*, Phys. Rev. B **70**, 100406 (2004).

[121] S. I. Kiselev, J. C. Sankey, I. N. Krivorotov, N. C. Emley, M. Rinkoski, C. Perez, R. A. Buhrman and D. C. Ralph, *Current-Induced Nanomagnet Dynamics for Magnetic Fields Perpendicular to the Sample Plane*, Physical Review Letters **93**, 036601 (2004).

[122] M. Covington, M. AlHajDarwish, Y. Ding, N. J. Gokemeijer and M. A. Seigler, *Current-induced magnetization dynamics in current perpendicular to the plane spin valves*, Phys. Rev. B **69**, 184406 (2004).

[123] K. V. Thadani, G. Finocchio, Z.-P. Li, O. Ozatay, J. C. Sankey, I. N. Krivorotov, Y.-T. Cui, R. A. Buhrman and D. C. Ralph, *Strong linewidth variation for spin-torque nano-oscillators as a function of in-plane magnetic field angle* , Phys. Rev. B **78**, 024409 (2008).

[124] R. Adler, *A Study of Locking Phenomena in Oscillators*, Proceedings of the IRE **34**, 351 (1946).

[125] S. Bonetti, *Magnetization Dynamics in Nano-Contact Spin Torque Oscillators: Solitonic bullets and propagating spin waves*, (2010).

[126] A. Slavin and V. Tiberkevich, *Theory of mutual phase locking of spin-torque nanosized oscillators*, Physical review B **74**, 104401 (2006).

[127] P. K. Muduli, O. G. Heinonen and J. Åkerman, *Decoherence and Mode Hopping in a Magnetic Tunnel Junction Based Spin Torque Oscillator*, Phys. Rev. Lett. **108**, 207203 (2012).

[128] P. K. Muduli, O. G. Heinonen and J. Åkerman, *Temperature dependence of linewidth in nanocontact based spin torque oscillators: Effect of multiple oscillatory modes*, Phys. Rev. B **86**, 174408 (2012).

[129] R. K. Dumas, E. Iacocca, S. Bonetti, S. R. Sani, S. M. Mohseni, A. Eklund, J. Persson, O. Heinonen and J. Åkerman, *Spin-Wave-Mode Coexistence on the Nanoscale: A Consequence of the Oersted-Field-Induced Asymmetric Energy Landscape*, Phys. Rev. Lett. **110**, 257202 (2013).

[130] O. Heinonen, P. Muduli, E. Iacocca and J. Akerman, *Decoherence, Mode Hopping, and Mode Coupling in Spin Torque Oscillators*, Magnetics, IEEE Transactions on **49**, 4398 (2013).

[131] E. Iacocca, O. Heinonen, P. K. Muduli and J. Åkerman, *Generation linewidth of mode-hopping spin torque oscillators*, Phys. Rev. B **89**, 054402 (2014).

[132] F. M. de Aguiar, A. Azevedo and S. M. Rezende, *Theory of a two-mode spin torque nanooscillator*, Phys. Rev. B **75**, 132404 (2007).

[133] V.Tiberkvich and A.Slavin, *Two-mode oscillation regimes of a STNO*, 12th joint MMM-Intermag conference **Abstact**, EF (2012).

[134] G. Melkov, D. Slobodianiuk, V. Tiberkevich, G. de Loubens, O. Klein and A. Slavin, *Nonlinear Ferromagnetic Resonance in Nanostructures Having Discrete Spectrum of Spin-Wave Modes*, Magnetics Letters, IEEE **4**, 4000504 (2013).

[135] D.V.Slobodianiuk, *Transition from one- to two-mode generation regime in spin-torque nano-oscillator mediated by thermal noise*, Condensed Matter Physics **17**, 13801 (2014).

[136] F. Sanches, V. Tiberkevich, K. Guslienko, J. Sinha, M. Hayashi, O. Prokopenko and A. Slavin, *Current-driven gyrotropic mode of a magnetic vortex as a nonisochronous auto-oscillator*, Physical Review B **89**, 140410 (2014).

[137] J. H. B. Hillebrands, *Investigation of spin waves and spin dynamics by optical techniques*, Handbook of Magnetism and Advanced Magnetic Material **3**, (2007).

[138] K. Perzlmaier, M. Buess, C. H. Back, V. E. Demidov, B. Hillebrands and S. O. Demokritov, *Spin-Wave Eigenmodes of Permalloy Squares with a Closure Domain Structure*, Phys. Rev. Lett. **94**, 057202 (2005).

[139] M. Buess, R. Höllinger, T. Haug, K. Perzlmaier, U. Krey, D. Pescia, M. R. Scheinfein, D. Weiss and C. H. Back, *Fourier Transform Imaging of Spin Vortex Eigenmodes*, Phys. Rev. Lett. **93**, 077207 (2004).

[140] J. C. Sankey, P. M. Braganca, A. G. F. Garcia, I. N. Krivorotov, R. A. Buhrman and D. C. Ralph, *Spin-Transfer-Driven Ferromagnetic Resonance of Individual Nanomagnets*, Physical Review Letters **96**, 227601 (2006).

[141] Z. Zhang, P. C. Hammel and P. E. Wigen, *Ferromagnetic Resonance Force Microscopy on Microscopic Co Single Layer Films*, Appl. Phys. Lett. **68**, 2005 (1996).

[142] A. Jander, J. Moreland and P. Kabos, *Micromechanical detectors for local field measurements based on ferromagnetic resonance (invited)*, Journal of Applied Physics **89**, 7086 (2001).

[143] V. Charbois, V. V. Naletov, J. Ben Youssef and O. Klein, *Mechanical detection of FMR spectrum in a normally magnetized YIG disk*, J. Appl. Phys. **91**, 7337 (2002).

[144] V. Charbois, V. V. Naletov, J. B. Youssef and O. Klein, *Influence of the magnetic tip in ferromagnetic resonance force microscopy*, Applied Physics Letters **80**, 4795 (2002).

[145] G. de Loubens, Thèse de doctorat, Université Paris Sud - Paris XI, 2005.

[146] D. Rugar, C. S. Yannoni and J. A. Sidles, *Mechanical detection of magnetic resonance*, Nature **360**, 563 (1992).

[147] D. Rugar, O. Züger, S. Hoen, C. S. Yannoni, H. M. Vieth and R. D. Kendrick, *Force detection of Nuclear Magnetic Resonance*, Science **264**, 1560 (1994).

[148] H. Lavenant, V. V. Naletov, O. Klein, G. De Loubens, C. Laura and J. M. De Teresa, *Mechanical magnetometry of Cobalt nanospheres deposited by focused electron beam at the tip of ultra-soft cantilevers*, Nanofabrication **1**, 65 (2014).

[149] P. W. Anderson and H. Suhl, *Instability in the motion of ferromagnets at high microwave power levels*, Phys.Rev. **100**, 1788 (1955).

[150] S.Borlenghi, Thèse de doctorat, Université Paris 6, Paris, France, 2011.

[151] V. S. Rychkov, S. Borlenghi, H. Jaffres, A. Fert and X. Waintal, *Spin Torque and Waviness in Magnetic Multilayers: A Bridge between Valet-Fert Theory and Quantum Approaches*, Phys. Rev. Lett. **103**, 066602 (2009).

[152] A. Eklund, S. Sani, S. Mohseni, J. Persson, B. Malm and J. Akerman, in *Noise and Fluctuations (ICNF), 2013 22nd International Conference on* (PUBLISHER, doi=10.1109/ICNF.2013.6578965, 2013), Seiten 1–4.

[153] V. V. Naletov, V. Charbois, O. Klein and C. Fermon, *Quantitative measurement of the ferromagnetic resonance signal by force detection*, Appl. Phys. Lett. **83**, 3132 (2003).

[154] S. I. Kiselev, J. C. Sankey, I. N. Krivorotov, N. C. Emley, A. G. F. Garcia, R. A. Buhrman and D. C. Ralph, *Spin-transfer excitations of Permalloy nanopillars for large applied currents*, Phys. Rev. B **72**, 064430 (2005).

[155] S. E. Russek, S. Kaka, W. H. Rippard, M. R. Pufall and T. J. Silva, *Finite-temperature modeling of nanoscale spin-transfer oscillators*, Phys. Rev. B **71**, 104425 (2005).

[156] M. R. Pufall, W. H. Rippard, M. L. Schneider and S. E. Russek, *Low-field current-hysteretic oscillations in spin-transfer nanocontacts*, Phys. Rev. B **75**, 140404 (2007).

[157] R. Lebrun, N. Locatelli, F. Abreu Araujo, H. Kubota, S. Tsunegi, K. Yakushiji, A. Fukushima, J. Grollier, S. Yuasa and V. Cros, *Nonlinear behavior and mode coupling in spin transfer nano-oscillators*, arXiv **1407**, 6901 (2014).

[158] A. Hamadeh, G. de Loubens, V. V. Naletov, J. Grollier, C. Ulysse, V. Cros and O. Klein, *Autonomous and forced dynamics in a spin-transfer nano-oscillator: Quantitative magnetic-resonance force microscopy*, Phys. Rev. B **85**, 140408 (2012).

[159] M. Manfrini, T. Devolder, J.-V. Kim, P. Crozat, N. Zerounian, C. Chappert, W. V. Roy, L. Lagae, G. Hrkac and T. Schrefl, *Agility of vortex-based nanocontact spin torque oscillators*, Appl.Phys.Lett. **95**, 192507 (2009).

[160] V. Sluka, A. Kákay, A. M. Deac, D. E. Bürgler, R. Hertel and C. M. Schneider, *Quenched Slonczewski windmill in spin-torque vortex oscillators*, Phys. Rev. B **86**, 214422 (2012).

[161] K. Y. Guslienko, K. S. Buchanan, S. D. Bader and V. Novosad, *Dynamics of coupled vortices in layered magnetic nanodots*, Appl. Phys. Lett. **86**, 223112 (2005).

[162] N. Locatelli, A. E. Ekomasov, A. V. Khvalkovskiy, S. A. Azamatov, K. A. Zvezdin, J. Grollier, E. G. Ekomasov and V. Cros, *Reversal process of a magnetic vortex core under the combined action of a perpendicular field and spin transfer torque*, Appl. Phys. Lett. **102**, 062401 (2013).

[163] M. Quinsat, V. Tiberkevich, D. Gusakova, A. Slavin, J. F. Sierra, U. Ebels, L. D. Buda-Prejbeanu, B. Dieny, M.-C. Cyrille, A. Zelster and J. A. Katine, *Linewidth of higher harmonics in a nonisochronous auto-oscillator: Application to spin-torque nano-oscillators*, Phys. Rev. B **86**, 104418 (2012).

[164] A. V. Khvalkovskiy, J. Grollier, N. Locatelli, Y. V. Gorbunov, K. A. Zvezdin and V. Cros, *Nonuniformity of a planar polarizer for spin-transfer-induced vortex oscillations at zero field*, Appl. Phys. Lett. **96**, 212507 (2010).

[165] K. L. Metlov, *Vortex precession frequency and its amplitude-dependent shift in cylindrical nanomagnets*, arXiv:1308.0240 .

[166] O. V. Sukhostavets, B. Pigeau, S. Sangiao, G. de Loubens, V. V. Naletov, O. Klein, K. Mitsuzuka, S. Andrieu, F. Montaigne and K. Y. Guslienko, *Probing the Anharmonicity of the Potential Well for a Magnetic Vortex Core in a Nanodot*, Phys. Rev. Lett. **111**, 247601 (2013).

[167] P. M. Braganca, O. J. Lee, O. Ozatay, L. Liu, G. Finocchio, D. C. Ralph and R. A. Buhrman, *Coherent and incoherent spin torque oscillations in a nanopillar magnetic spin-valve*, Appl. Phys. Lett. **102**, 252402 (2013).

[168] S. Kasai, Y. Nakatani, K. Kobayashi, H. Kohno and T. Ono, *Current-Driven Resonant Excitation of Magnetic Vortices*, Phys. Rev. Lett. **97**, 107204 (2006).

[169] S. Sugimoto, Y. Fukuma, S. Kasai, T. Kimura, A. Barman and Y. Otani, *Dynamics of Coupled Vortices in a Pair of Ferromagnetic Disks*, Phys. Rev. Lett. **106**, 197203 (2011).

[170] P. S. Keatley, P. Gangmei, M. Dvornik, R. J. Hicken, J. Grollier and C. Ulysse, *Isolating the Dynamic Dipolar Interaction between a Pair of Nanoscale Ferromagnetic Disks*, Phys. Rev. Lett. **110**, 187202 (2013).

[171] M. Sparks, *Ferromagnetic relaxation theory* (McGraw-Hill, New York, 1964).

[172] A. G. Gurevich and G. A. Melkov, *Magnetization Oscillations and Waves* (CRC Press, ADDRESS, 1996).

[173] S. Urazhdin, V. Tiberkevich and A. Slavin, *Parametric Excitation of a Magnetic Nanocontact by a Microwave Field*, Phys. Rev. Lett. **105**, 237204 (2010).

[174] P. Bortolotti, E. Grimaldi, A. Dussaux, J. Grollier, V. Cros, C. Serpico, K. Yakushiji, A. Fukushima, H. Kubota, R. Matsumoto and S. Yuasa, *Parametric excitation of magnetic vortex gyrations in spin-torque nano-oscillators*, Phys. Rev. B **88**, 174417 (2013).

[175] P. Durrenfeld, E. Iacocca, J. Akerman and P. K. Muduli, *Parametric excitation in a magnetic tunnel junction-based spin torque oscillator*, Applied Physics Letters **104**, 052410 (2014).

[176] H.-C. Chang, X. Cao, U. K. Mishra and R. York, *Phase noise in coupled oscillators: theory and experiment*, Microwave Theory and Techniques, IEEE Transactions on **45**, 604 (1997).

[177] T. Shibata, R. Zhang, S. Levitan, D. Nikonov and G. Bourianoff, in *Cellular Nanoscale Networks and Their Applications (CNNA)* (13th International Workshop, pages 1-5, 2012).

[178] A. D. Belanovsky, N. Locatelli, P. N. Skirdkov, F. A. Araujo, J. Grollier, K. A. Zvezdin, V. Cros and A. K. Zvezdin, *Phase locking dynamics of dipolarly coupled vortex-based spin transfer oscillators*, Phys. Rev. B **85**, 100409 (2012).

[179] S. Erokhin and D. Berkov, *Robust synchronization of an arbitrary number of spin-torque-driven vortex nano-oscillators*, Phys. Rev. B **89**, 144421 (2014).

[180] A. Belanovsky, N. Locatelli, P. Skirdkov, F. A. Araujo, K. Zvezdin, J. Grollier, V. Cros and A. Zvezdin, *Numerical and analytical investigation of the synchronization of dipolarly coupled vortex spin-torque nano-oscillators*, Applied Physics Letters **103**, 122405 (2013).

[181] N. Locatelli, V. Cros and J. Grollier, *Spin-torque building blocks*, Nature materials **13**, 11 (2014).

[182] S. Petit-Watelot, J.-V. Kim, A. Ruotolo, R. M. Otxoa, K. Bouzehouane, J. Grollier, A. Vansteenkiste, B. V. de Wiele, V. Cros and T. Devolder, *Commensurability and chaos in magnetic vortex oscillations*, Nature Physics **8**, 686 (2012).

[183] S. M. Mohseni, S. R. Sani, J. Persson, T. N. A. Nguyen, S. Chung, Y. Pogoryelov, P. K. Muduli, E. Iacocca, A. Eklund, R. K. Dumas, S. Bonetti, A. Deac, M. A. Hoefer and J. Akerman, *Spin Torque-Generated Magnetic Droplet Solitons*, Science **339**, 1295 (2013).

[184] J. Sampaio, V. Cros, S. Rohart, A. Thiaville and A. Fert, *Nucleation, stability and current-induced motion of isolated magnetic skyrmions in nanostructures*, Nature Nanotechnology **8**, 839 (2013).

[185] A. Fert, V. Cros and J. Sampaio, *Skyrmions on the track*, Nature Nanotechnology **8**, 152 (2013).

[186] V. E. Demidov, S. Urazhdin, E. R. J. Edwards, M. D. Stiles, R. D. McMichael and S. O. Demokritov, *Control of Magnetic Fluctuations by Spin Current*, Phys. Rev. Lett. **107**, 107204 (2011).

[187] V. Demidov, S. Urazhdin, H. Ulrichs, V. Tiberkevich, A. Slavin, D. Baither, G. Schmitz and S. O. Demokritov, *Magnetic nano-oscillator driven by pure spin current*, Nature Materials **11**, 1028 (2012).

[188] Y. Kajiwara, K. Harii, S. Takahashi, J. Ohe, K. Uchida, M. Mizuguchi, H. Umezawa, H. Kawai, K. Ando, K. Takanashi, S. Maekawa and E. Saitoh, *Transmission of electrical signals by spin-wave interconversion in a magnetic insulator*, Nature **464**, 262 (2010).